



# NEURAL NETWORKS ON FRETTING FATIGUE

REDES NEURAS NA FADIGA POR FRETTING

GIORGIO ANDRÉ BRITO OLIVEIRA

TESE DE DOUTORADO EM CIÊNCIAS MECÂNICAS  
DEPARTAMENTO DE ENGENHARIA MECÂNICA

FACULDADE DE TECNOLOGIA  
UNIVERSIDADE DE BRASÍLIA

Universidade de Brasília  
Faculdade de Tecnologia  
Departamento de Engenharia Mecânica

## Neural Networks on Fretting Fatigue

Giorgio André Brito Oliveira

TESE DE DOUTORADO SUBMETIDA AO PROGRAMA DE PÓS-GRADUAÇÃO  
EM CIÊNCIAS MECÂNICAS DA UNIVERSIDADE DE BRASÍLIA COMO PARTE  
DOS REQUISITOS NECESSÁRIOS PARA A OBTENÇÃO DO GRAU DE DOC-  
TOR.

APROVADA POR:

---

Prof. José Alexander Araújo, D.Phil. (UnB)  
(Orientador)

---

Prof. Raimundo Carlos Silverio Freire Júnior, Ph.D. (UFRN)  
(Co-orientador)

---

Prof. Reza Hojjati Talemi, Ph.D. (KU Leuven)  
(Examinador Externo)

---

Prof. Jesús Vázquez Valeo, Ph.D. (Universidad de Sevilla)  
(Examinador Externo)

---

Prof. Fábio Comes de Castro, Ph.D. (UnB)  
(Examinador Interno)

Brasília/DF, Outubro de 2024.

## FICHA CATALOGRÁFICA

BRITO OLIVEIRA, GIORGIO ANDRÉ

Neural Networks on Fretting Fatigue. [Brasília/DF] 2024.

xxx, nnp., 210 x 297 mm (ENM/FT/UnB, Doctor, Tese de Doutorado, 2024).

Universidade de Brasília, Faculdade de Tecnologia, Departamento de Engenharia Mecânica.

Departamento de Engenharia Mecânica

- |                            |                               |
|----------------------------|-------------------------------|
| 1. Fretting Fatigue        | 2. Artificial Neural Networks |
| 3. Multiaxial Fatigue      | 4. Aeronautical Alloys        |
| 5. Finite Element Analysis | 6. Overhead conductors        |
| I. ENM/FT/UnB              | II. Doutorado                 |

## REFERÊNCIA BIBLIOGRÁFICA

BRITO OLIVEIRA, G. A. (2024). Neural Networks on Fretting Fatigue. Tese de Doutorado, Publicação PCMEC.Outubro/2024, Departamento de Engenharia Mecânica, Universidade de Brasília, Brasília, DF, 283p.

## CESSÃO DE DIREITOS

AUTOR: Giorgio André Brito Oliveira

TÍTULO: Neural Networks on Fretting Fatigue.

GRAU: Doctor ANO: 2024

É concedida à Universidade de Brasília permissão para reproduzir cópias desta Tese de Doutorado e para emprestar ou vender tais cópias somente para propósitos acadêmicos e científicos. O autor reserva outros direitos de publicação e nenhuma parte desta tese de doutorado pode ser reproduzida sem autorização por escrito do autor.

---

Giorgio André Brito Oliveira

Universidade de Brasília (UnB) - Campus Darcy Ribeiro

Faculdade de Tecnologia - FT

Departamento de Engenharia Mecânica(ENM)

Brasília - DF CEP 70919-970

*"Cloudless, everyday you fall upon my waking eyes,  
inviting and inciting me to rise"*  
– **Pink Floyd**

*"You keep on learning and learning, and pretty soon  
you learn something no one has learned before."*  
– **Richard Feynman**

*"Le hasard n'est que la mesure de notre ignorance; il  
est ainsi souvent la forme de l'inconnu."*  
– **Henri Poincaré**

*"Trabalha e serve sempre, alheio à recompensa, que  
o trabalho, por si, é a glória que condensa o salário  
da Terra e a bênção do Infinito."*  
– **Múcio Teixeira**

*"There is nothing outside of yourself that can ever  
enable you to get better, stronger, richer, quicker,  
or smarter. Everything is within. Everything exists.  
Seek nothing outside of yourself."*  
– **Miyamoto Musashi**

# Acknowledgements

I express my gratitude firstly to God, for health and for the opportunities granted to come to Brasília and carry out this work. To the Fatigue, Fracture, and Materials Group (GFFM), an internationally recognized group, for welcoming me and passing on invaluable knowledge that greatly contributed to the research endeavor.

To my supervisor, Professor Alex, who not only guided me through my research but also provided support in my personal life during this period. His influence, advice, and friendship have been, are, and undoubtedly will remain significant on my journey. I also extend my thanks to my co-supervisor, Professor Raimundo, who consistently encouraged me and offered enlightening discussions, guiding me toward paths I could not discern alone. His friendship expanded the horizons of my limitations.

I am grateful to the Research Support Foundation of the Federal District (FAPDF), the Coordination for the Improvement of Higher Education Personnel (CAPES), the National Council for Scientific and Technological Development (CNPq), and the Foundation for Scientific and Technological Enterprises (FINATEC) for their support and provision of scholarships that aided in sustaining this research over the years.

I am sincerely thankful to the support and friendship of Professor Raphael Cardoso, whose assistance greatly influenced my research in numerical simulation. His partnership was fundamental in my achievements. I also thank Professor Edgar Mamiya, who primarily assisted me in awakening to the necessary mathematical formalism in the field of Mechanical Sciences. I must also acknowledge the contributions of professors Jorge, Fábio, and Doca, who also played a role in my academic development. To technician Wesley, for all his support and frank conversations. To Mrs. Raimunda, Mrs. Bia, and Mr. Reginaldo, for their dedication and camaraderie.

Regarding my colleagues at work: Remy, Gabriel, Danilo, Lucas, Miguel, André Novelino, Rodrigo, Nathália Manes, Nélio, Márcio, Karoline, Natália Torres, Roberto, Ricardo, André

Pinto, Ian, Pedro, and Felipe Maganha, who were part of this stage of my life, I am immensely grateful for everything. Each played an important role in this journey, not only in theoretical collaborations but especially in fostering a healthy and relaxed environment, fundamental aspects in completing a doctorate.

I would like to extend special thanks to those who were more directly involved in this thesis. I am grateful to Dr. Gabriel Juvenal for his invaluable assistance and insights during the experiments, and to Dr. Pedro Rocha and Dr. Ian Matos for their support in the computational aspects. These collaborations were essential to the success of this thesis.

I also thank my more distant friends: Alex, Gabriel, Diego, Jordy, Wisashi, Marquinhos, Paulo, among many others who I know support me, for their understanding and camaraderie during this time when I was more distant.

Last but certainly not least, to my partner Larissa, for all the support, involvement, love, and understanding so crucial during this stage. To my mother, Augusta, my father, Élidon, and my sister, Lorena, who form my moral foundations and have always supported me unconditionally. Obrigado por tudo!

# Abstract

This thesis proposes a novel approach for analyzing fretting fatigue using data-driven models, specifically artificial neural networks (ANNs). Fretting fatigue occurs when there are micro-slips between contact mechanical components under fatigue loading, commonly found in overhead conductors, turbines, fuselages, and brake discs. Although ANNs have existed since the 1940s, their application to fretting fatigue is recent and innovative. In this setting, this work is divided into four parts. The first part explores the use of analytical equations to compute stresses, which are physically related to the crack initiation process, to be used as inputs for the ANN model, incorporating the effect of nonzero mean bulk stress in estimating fretting fatigue life. In the second part, the generalization capability of these models is further explored with finite element analysis. New stress parameters are used as inputs, allowing the model to extrapolate fretting fatigue life to new materials, loadings, and geometries never seen during training. The third part of this work has a more applied focus, based on the new methodology proposed in parts 1 and 2. Three different fretting cases are addressed, involving variable shear loading amplitude and applications in overhead conductor fatigue. The fourth and final part has a more experimental profile, with new fretting fatigue experiments performed under non-usual loading conditions and analyzed through fracture analysis and various life prediction models. Specifically, a new loading inspired by the conditions experienced by an aircraft fuselage is reproduced. This analysis demonstrated the importance of a deeper understanding of the physics of the problem, which differs significantly from classical fretting fatigue experiments, to achieve reasonable life estimates. In all parts of the study, comparative analyses were conducted, with other fatigue models being appropriately calibrated and tested for the materials under investigation. Nevertheless, the proposed data-driven methodology consistently demonstrated clear advantages in all scenarios. Overall, in parts 1, 2, and 3, most of the estimates fell within the two-band width, with a minority within the 3-band range. In part 4, however, the estimations were around the 4-band width. This discrepancy is primarily due to the crack propagation

effect not being considered in the proposed new loading conditions. The broad applicability of this new data-driven modeling approach is discussed throughout the thesis, highlighting its practical and innovative potential in predicting fretting fatigue.

**Keywords:** Fretting fatigue, Neural networks, Aeronautical alloys, Overhead Conductors, Complex loadings

# Resumo

Esta tese propõe uma nova abordagem para a análise da fadiga por fretting utilizando modelos de machine learning, especificamente redes neurais artificiais (RNA). A fadiga por fretting é um fenômeno que ocorre quando há microdeslizamentos entre componentes em contato mecânico sob carregamento de fadiga, comum em cabos de energia, turbinas, fuselagens e discos de freio. Embora as RNAs existam desde os anos 40, sua aplicação na fadiga por fretting é recente e inovadora. Neste contexto, este trabalho divide-se em quatro partes. A primeira parte explora o uso de equações analíticas para o cálculo das tensões, que estão fisicamente relacionadas com o processo de iniciação de trincas, para serem usadas como entradas para o modelo de RNA, incorporando o efeito da tensão média na estimativa da vida à fadiga por fretting. Na segunda parte, a capacidade de generalização destes modelos é explorada com a análise de elementos finitos. Novos parâmetros de tensão são utilizados como entradas, permitindo ao modelo extrapolar a vida em fadiga por fretting para novos materiais, carregamentos e geometrias nunca vistas durante o processo de treinamento. A terceira parte deste trabalho tem um foco mais aplicado, baseado na nova metodologia proposta nas partes 1 e 2. São abordados três casos diferentes de fretting, envolvendo amplitude de carga de cisalhamento variável e aplicações na fadiga de cabos condutores. A quarta e última parte tem um perfil mais experimental, com novos experimentos de fadiga por fretting realizadas sob condições de carga não usuais e avaliadas através de análise de fratura e também sob vários tipos de modelos de previsão de vida em fadiga. Especificamente, é reproduzido um novo carregamento inspirado nas condições experimentadas pela fuselagem de um avião. Esta análise demonstrou a importância de uma compreensão mais profunda da física do problema, que difere significativamente dos ensaios clássicos de fadiga por fretting, para então se obter estimativas de vida razoáveis. Em todas as partes do estudo, também foram efetuadas análises comparativas, de modo que outros modelos de fadiga multiaxial foram devidamente calibrados e testados para os materiais em estudo. No entanto, a metodologia proposta, baseada em ciência de dados, demonstrou consistentemente

claras vantagens em todos os cenários estudados. De um modo geral, nas partes 1, 2 e 3, a maioria das estimativas situou-se dentro das bandas de dois, com uma minoria dentro da banda de três. No entanto, na parte 4, as estimativas de vida situaram-se em torno da banda de quatro. Esta discrepância deve-se principalmente ao fato de não ter-se considerado o efeito de propagação de trincas no novo carregamento proposto. A ampla aplicabilidade desta nova abordagem baseada em redes neurais é discutida ao longo da tese, destacando o seu potencial prático e inovador na previsão e estudo da fadiga por fretting.

**Palavras-chave:** Fadiga por fretting, Redes Neurais Artificiais, Ligas Aeronáuticas, Cabos condutores, Carregamento complexo

# Journal Articles and Conference Papers

## PEER REVIEWED JOURNAL PUBLICATIONS AND SUBMISSIONS

1. [BRITO OLIVEIRA, G. A.](#); FREIRE JÚNIOR, R. C. S.; VELOSO, L. A. C. M.; ARAÚJO, J. A. A hybrid ANN-multi-axial fatigue nonlocal model to estimate fretting fatigue life for aeronautical Al alloys. *International Journal of Fatigue*, v. 162, November 2021, p. 107011, 2022. DOI: [10.1016/j.ijfatigue.2022.107011](https://doi.org/10.1016/j.ijfatigue.2022.107011).
2. [BRITO OLIVEIRA, G. A.](#); CARDOSO, R. A.; FREIRE JÚNIOR, R. C. S.; ARAÚJO, J. A. A generalized ANN-multi-axial fatigue nonlocal approach to compute fretting fatigue life for aeronautical Al alloys. *Tribology International*, v. 180, November 2022, p. 108250, 2023a. DOI: [10.1016/j.triboint.2023.108250](https://doi.org/10.1016/j.triboint.2023.108250)
3. [OLIVEIRA, G. A. B.](#); CARDOSO, R. A.; FREIRE JÚNIOR, R. C. S.; DOCA, T.; ARAÚJO, J. A. On the generalization capability of artificial neural networks used to estimate fretting fatigue life. *Tribology International*, v. 192, n. December 2023, p. 109222, 2024. DOI: [10.1016/j.triboint.2023.109222](https://doi.org/10.1016/j.triboint.2023.109222)
4. [OLIVEIRA, G. A. B.](#); MATOS, I. M.; ROCHA, P. H. C.; CASTRO, F. C.; FREIRE JÚNIOR, R. C. S.; ARAÚJO, J. A. On the life estimation of wires using non-local ANN methodology. **In process of submission.**
5. [OLIVEIRA, G. A. B.](#); ROCHA, P. H. C.; MATOS, I. M.; CASTRO, F. C.; LANGLOIS, S.; FREIRE JÚNIOR, R. C. S.; ARAÚJO, J. A. On the fatigue life prediction of overhead conductors using neural networks. **In process of submission.**
6. [OLIVEIRA, G. A. B.](#); ALMEIDA, G. M. J.; CARDOSO, R. A.; GARCIA, M. A.; FREIRE JÚNIOR, R. C. S.; ARAÚJO, J. A. Complex fretting fatigue tests and analysis with Al 7075-T651. **In process of submission.**

## PEER REVIEWED PAPERS IN CONFERENCE PROCEEDINGS

1. [BRITO OLIVEIRA, G. A.](#); CARDOSO, R.A.; FREIRE JÚNIOR, R.C.S.; ARAÚJO, J. A. A Hybrid ANN Multiaxial Fatigue Model for the Assessment of Fretting Fatigue under Variable Amplitude Shear Loading. *Procedia Structural Integrity*, v. 57, 2024, p. 228-235, 2024b. DOI: [10.1016/j.prostr.2024.03.025](https://doi.org/10.1016/j.prostr.2024.03.025)

## CONFERENCE ORAL PRESENTATIONS

1. [BRITO OLIVEIRA, G. A.](#); CARDOSO, R.A.; FREIRE JÚNIOR, R.C.S.; ARAÚJO, J. A. A generalized ANN-multiaxial fatigue nonlocal approach to compute fretting fatigue life for aeronautical alloys. 10th International Symposium of Fretting Fatigue (ISFF10). Leuven, Belgium. 19-21 September, 2022. ([Official site](#))
2. [BRITO OLIVEIRA, G. A.](#); CARDOSO, R.A.; CARDOSO, R.A.; FREIRE JÚNIOR, R.C.S.; ARAÚJO, J. A. A Hybrid ANN Multiaxial Fatigue Model for the Assessment of Fretting Fatigue under Variable Amplitude Shear Loading. 10th Edition of Fatigue Design Hybrid International Conference on Material Fatigue (FD10). Cetim Selins, France. 29-30 November, 2023. ([Official site](#))

# Contents

<b>Contents</b>	<b>i</b>
<b>List of figures</b>	<b>iv</b>
<b>List of Tables</b>	<b>xi</b>
<b>Nomenclature and symbols</b>	<b>xiv</b>
<b>Abbreviations</b>	<b>xviii</b>
<b>Chapter 1 – Introduction</b>	<b>1</b>
1.1 Context and motivations of the study . . . . .	2
1.2 Fretting fatigue review . . . . .	3
1.2.1 ANN modelling of fretting fatigue . . . . .	8
1.3 Aims and scope . . . . .	12
1.4 Structure of the work . . . . .	13
<b>Chapter 2 – Research Methods &amp; Theory</b>	<b>17</b>
2.1 Fretting Fatigue . . . . .	18
2.1.1 Understanding material fatigue . . . . .	18
2.1.1.1 The nature of fatigue damage . . . . .	20
2.1.1.2 Factors influencing the fretting fatigue phenomenon . . . . .	21
2.1.2 Miner cumulative damage model . . . . .	23
2.1.3 Multiaxial fatigue approaches . . . . .	24
2.1.3.1 Stresses in any surface element . . . . .	24
2.1.3.2 Smith, Watson and Topper model . . . . .	29
2.1.3.3 The Modified Wöhler Curve Method . . . . .	30
2.1.3.4 The Crossland criterion . . . . .	31
2.1.4 Basics of Fracture Mechanics . . . . .	32
2.1.4.1 Paris’s law . . . . .	34
2.1.4.2 The theory of critical distances . . . . .	35
2.1.5 Mechanics of elastic contacts . . . . .	37
2.1.5.1 Cylindrical-on-plane contact . . . . .	38
2.1.5.2 Sphere-on-plane contact . . . . .	46
2.1.6 Numerical methodologies in fretting fatigue . . . . .	52
2.1.7 Fretting fatigue experimental testing . . . . .	60
2.1.7.1 Four actuators fretting fatigue machine test . . . . .	62
2.1.7.2 Overhead conductors fatigue test . . . . .	63
2.1.8 Neural networks in the fretting fatigue context . . . . .	66
2.1.8.1 Machine learning models . . . . .	68
2.1.8.2 Artificial neural networks . . . . .	73

<b>Chapter 3 – A hybrid ANN-multiaxial fatigue non-local model</b>	<b>85</b>
3.1 Overview . . . . .	86
3.2 Fretting Fatigue Analysis . . . . .	86
3.2.1 Computing the equivalent stresses . . . . .	87
3.2.2 Choosing the input parameters . . . . .	87
3.3 Materials and datasets . . . . .	88
3.4 ANN modeling . . . . .	89
3.4.1 ANN architecture . . . . .	93
3.5 Results and discussion . . . . .	96
3.5.1 ANN models . . . . .	97
3.5.2 Comparative analysis . . . . .	100
3.6 Partial Conclusions . . . . .	101
<b>Chapter 4 – A generalized ANN-multiaxial fatigue nonlocal numerical approach</b>	<b>103</b>
4.1 Overview . . . . .	104
4.2 Nonlocal multiaxial stress methodology . . . . .	105
4.2.1 Input parameters considered for the ANNs . . . . .	106
4.3 Materials and datasets . . . . .	108
4.3.1 Axial and torsional fatigue data . . . . .	109
4.3.2 Fretting fatigue data . . . . .	112
4.4 Simulation developments . . . . .	120
4.4.1 Finite element models . . . . .	120
4.4.2 Neural networks based models . . . . .	125
4.4.2.1 Development of the models . . . . .	129
4.5 Results and discussions . . . . .	131
4.5.1 Part 1 - Aluminium Article . . . . .	131
4.5.1.1 Calibration of the multiaxial models . . . . .	131
4.5.1.2 ANN results . . . . .	131
4.5.1.3 Comparative analysis . . . . .	133
4.5.1.4 Discussions . . . . .	137
4.5.2 Part 2 - Titanium Article . . . . .	138
4.5.2.1 ANN training results . . . . .	139
4.5.2.2 Ti-6Al-4V results . . . . .	140
4.5.2.3 Out-of-phase loading results . . . . .	143
4.5.2.4 Further discussions . . . . .	149
4.6 Partial conclusions . . . . .	150
<b>Chapter 5 – Applications and insights of ANN models</b>	<b>153</b>
5.1 Overview . . . . .	154
5.2 Part I – Fretting fatigue under variable shear amplitude . . . . .	154
5.2.1 Fretting fatigue under variable amplitude data . . . . .	154
5.2.2 Modelling framework . . . . .	157
5.2.2.1 Damage rule model . . . . .	157
5.2.3 Results and discussions (Part I) . . . . .	158
5.2.4 SHEAR model + LSM-Miner rule approach results . . . . .	159
5.2.4.1 SHEAR model + ANN-damage rule approach results . . . . .	161
5.2.4.2 SHEAR model + Pinto-damage rule approach results . . . . .	161
5.2.4.3 SHEAR model + Miner rule approach results . . . . .	161
5.3 Part II – On the life estimation of wires using non-local ANN methodology . . . . .	162
5.3.1 Methodology (Part II) . . . . .	163
5.3.1.1 The ANN_NORMAL model . . . . .	164

5.3.2	Experimental data and FE analysis . . . . .	166
5.3.3	Results and discussions (Part II) . . . . .	168
5.3.3.1	Wires under constant amplitude loading . . . . .	168
5.3.3.2	Variable amplitude loading . . . . .	170
5.4	Part III – Nominal stress -ANN approach for life estimation of overhead conductors	171
5.4.1	The machine learning-based modeling approach . . . . .	172
5.4.1.1	A brief theoretical background . . . . .	173
5.4.1.2	The choice of the input parameters . . . . .	174
5.4.2	Training and test of the machine learning models . . . . .	176
5.4.2.1	Fatigue data on wire against wire . . . . .	176
5.4.2.2	Training and testing the models . . . . .	177
5.4.2.3	Determining the weights matrices of the ANN model . . . . .	181
5.4.3	Application of the ML model to estimate overhead conductors' fatigue life	183
5.4.3.1	Overhead conductors' experimental data . . . . .	183
5.4.3.2	Finite element modelling . . . . .	184
5.4.4	Results and Discussions (Part III) . . . . .	187
5.4.4.1	Overhead conductors' life estimation . . . . .	187
5.4.4.2	Location fracture prediction . . . . .	189
5.5	Partial Conclusions . . . . .	190
<b>Chapter 6 – Extended load conditions - Experimental design</b>		<b>192</b>
6.1	Overview . . . . .	193
6.2	Test design . . . . .	194
6.2.1	Test specimens and machine apparatus . . . . .	194
6.2.2	Flight fretting fatigue tests . . . . .	196
6.2.3	Test configuration . . . . .	197
6.2.4	Fretting machine programming . . . . .	197
6.3	Experimental results and investigation . . . . .	200
6.3.1	Experimental campaign . . . . .	200
6.3.2	Cracks during tests . . . . .	201
6.3.3	Post-failure analysis . . . . .	203
6.3.3.1	Confocal and SEM analysis . . . . .	204
6.4	Analytical and numerical frameworks . . . . .	208
6.4.1	Multiaxial fatigue models calibration . . . . .	210
6.4.2	Data-driven model . . . . .	211
6.4.3	Finite element analysis . . . . .	214
6.5	Results and Discussions . . . . .	216
6.5.1	Life estimates . . . . .	217
6.5.2	The stress intensity factor range response . . . . .	219
6.6	Partial conclusions . . . . .	220
<b>Chapter 7 – Conclusions</b>		<b>223</b>
7.1	Main conclusions . . . . .	224
7.2	Future works . . . . .	225
<b>References</b>		<b>227</b>

# List of Figures

1.1	Number of fretting fatigue documents published over the years. . . . .	7
1.2	The four parts of the doctoral thesis. . . . .	13
1.3	Equivalence of the experimental tests. . . . .	14
2.1	Some factors to consider when analysing (A) fatigue and (B) fretting. . . . .	22
2.2	A body subjected to a system of external forces and a reference point. . . . .	26
2.3	Stresses acting on a plane within a three-dimensional coordinate system. . . . .	27
2.4	Maximum Rectangular Hull (MRH) method for a shear stress path $\Omega$ in a surface element $\Xi$ . . . . .	28
2.5	Basis of the physical interpretation of the SWT (A) and MWCM (B) model. . . . .	29
2.6	Scheme of the $da/dN$ vs $\Delta K$ in log-log diagram. . . . .	36
2.7	Example of a incomplete contact. . . . .	37
2.8	Representation of the cylinder-on-plane contact configuration. . . . .	39
2.9	Pressure and shear traction profiles considering $Q/fP = 0.5$ . . . . .	41
2.10	Shear load ( $Q$ ) over the time. . . . .	42
2.11	Shear traction distributions during a tangential cycle, $Q_{max}/fP = 0.6$ . . . . .	42
2.12	Subsurface distribution of the $\sigma_{xx}/p_0$ for a cylindrical-on-plane configuration under fretting fatigue ( $Q/fP = 0.6$ , $\sigma_{B,a}/fp_0 = 0.4$ , $\nu = 0.33$ , $f = 0.5$ ). . . . .	46
2.13	Sphere on-plane fretting fatigue set-up. . . . .	47
2.14	Sphere-on-plane configuration fretting fatigue normalized stress curves: (A), (B), and (C) under the x-contact surface and (D), (E), and (F) under the y-contact surface ( $p_0 = 200$ MPa, $\sigma_{B,a} = 150$ MPa, $Q/P = 0.5$ , $f = 0.8$ , and $\nu = 0.33$ ). . . . .	53

2.15	Sphere-on-plane configuration fretting fatigue stress fields: (A), (B) and (C) under the x-z plane and (D) and (E) under the x-y plane, both normalized. (F) shows all normalized stress components at the contact trailing edge, inward the surface ( $p_0 = 200$ MPa, $\sigma_{B,a} = 150$ MPa, $Q/P = 0.5$ , $f = 0.8$ , and $\nu = 0.33$ ). . . . .	54
2.16	Comparison between the analytical and numerical solutions for the normalized normal and shear tractions, over the normalized contact position ( $P = 50$ N, $Q = 30$ N, $R = 25.4$ mm, $\sigma_{B,a} = 225$ MPa). . . . .	56
2.17	CSHEAR distribution example in the contact interface, for the spheric-on-plane numerical model ( $P = 50$ N, $Q = 30$ N, $R = 25.4$ mm, $\sigma_{B,a} = 225$ MPa). . . . .	56
2.18	Comparison of numerical and analytical solutions for the aluminium alloy Al 4%Cu and 7075-T6, analysing the effect of the $h_s/2a$ ratio. . . . .	58
2.19	Example of a numerical model used for the stress solutions of the sphere-on-plane contact configuration. . . . .	59
2.20	Commonly used types of fretting fatigue experimental testing (A) Bridge-type, (B) Grip-type and (C) Single clamp. . . . .	61
2.21	Schematic representation of the high-temperature fretting fatigue rig with four actuators at the University of Brasilia (ALMEIDA <i>et al.</i> , 2022). . . . .	64
2.22	Schematic representation of the resonance fatigue test bench for testing overhead conductors. . . . .	64
2.23	Stages of fatigue development, adapted from Wang <i>et al.</i> (2023b). . . . .	67
2.24	Classification of the machine learning models. . . . .	70
2.25	Development of a data-driven model based on supervised learning. . . . .	71
2.26	Example of a nonlinear model of a neuron, labeled k. . . . .	75
2.27	Example of a multi-layered ANN architecture. . . . .	76
2.28	Examples of sigmoid and tanh functions along with their derivatives. . . . .	79
2.29	Pseudocode for training an ANN . . . . .	84
3.1	Fretting fatigue set-up scheme. . . . .	87
3.2	Representation of the ANN architecture with (A) Two inputs, and, (B) Three inputs. . . . .	96

3.3	Flowchart demonstrating all data processing with the ANN cross validation training. . . . .	97
3.4	ANN (M3I model) estimated vs experimental fretting fatigue lives. . . . .	98
3.5	S-N curve for the $\sigma_{N,max}$ vs $N_f$ fretting fatigue life ( $N_f$ ) in function of the $\sigma_{N,max}$ for a constant $\tau_{a,critic}$ (143 MPa in this case), for two aluminum alloys: 2024-T351 and 7050-T7451 . . . . .	99
3.6	Comparative logarithmic fretting fatigue life diagram, for M3I model and the model constructed with (NOWELL; NOWELL, 2020) parameters, using (ROSSINO <i>et al.</i> , 2009; ARAÚJO; CASTRO, 2012) data. . . . .	101
4.1	Example of a simple-layered ANN architecture. . . . .	107
4.2	Uniaxial fatigue data for the 2024-T3 Al alloy (a), and for the 7075-T6 Al alloy (b). . . . .	110
4.3	Axial and torsional fatigue data for the Ti-6Al-4V alloy (A), Al 7050-T7451 alloy (B), and ASTM A743 CA6NM alloy. . . . .	111
4.4	Experimental fretting fatigue life range for all aluminum alloys considered. . . . .	113
4.5	Cylinder on-plane fretting fatigue experimental set-up scheme (a), sphere on-plane fretting fatigue experimental set-up scheme (b), and a schematic of loading history (c). . . . .	121
4.6	Finite element model used to simulate the cylinder on-plane fretting fatigue experiments. . . . .	122
4.7	Finite element model used to simulate the sphere on-plane fretting fatigue experiments. . . . .	123
4.8	Comparison between the analytical and the numerical contact surface stresses for the cylinder-on-plane model. . . . .	125
4.9	Comparison between the analytical and the numerical stress field for the sphere on-plane model: (a) on the contact surface and (b) inward the contact surface (trailing edge). . . . .	126
4.10	ANN architecture based on the parameters of the MWCM model (a) and on the parameters of the SWT model (b), based on (BRITO OLIVEIRA <i>et al.</i> , 2023a). . . . .	127

4.11	General ANN architecture for all ANN models considered in (OLIVEIRA <i>et al.</i> , 2024).	128
4.12	Flowchart illustrating all the process to construct the ANN models	130
4.13	Summary of the considered modeling	130
4.14	SWT parameter versus fatigue life for the 2024-T3 (a) and the 7075-T6 (b) Al alloys. Modified Wohler " curve for the 2024-T3 (c) and the 7075-T6 (d) Al alloys.	132
4.15	Estimated fatigue life by the ANN_SHEAR model vs. the experimental one (a). Estimated fatigue life by the ANN_NORMAL model vs. the experimental one (b).	134
4.16	Estimated fatigue life considering all the models vs. experimental one for the 2024-T3 (a) and the 7075-T6 (b) Al alloys	136
4.17	Fatigue life surface for the 7075-T651 Al alloy by using the ANN_SHEAR model. The experimental data provided in (MARTÍN <i>et al.</i> , 2020; MUÑOZ <i>et al.</i> , 2007) are also reported.	138
4.18	Fatigue life surface for the 7075-T651 Al alloy by using the ANN_NORMAL model. The experimental data provided in (MARTÍN <i>et al.</i> , 2020; MUÑOZ <i>et al.</i> , 2007) are also reported.	139
4.19	Estimated fatigue life considering all the multiaxial fatigue models vs. experimental one for the Ti-6Al-4V alloy.	141
4.20	Estimated fatigue life vs. experimental one for the SHEAR (A), NORMAL (B) and INV (C) models for the Ti-6Al-4V alloy	144
4.21	Estimated fatigue life considering all the multiaxial fatigue models vs. experimental one for the Al 7050-T7451 alloy (A), and ASTM A743 CA6NM alloy (B).	146
4.22	Estimated fatigue life considering all the ANN models vs. experimental one for the Al 7050-T7451 alloy (A), and ASTM A743 CA6NM alloy (B).	148
4.23	Constant life curves for the Ti-6Al-4V alloy by using the SHEAR and MWCM models (A), NORMAL and SWT models (B), and INV and Crossland models (C). The experimental data are also reported.	151
5.1	Representation of the loads in (A) H-L configuration; (B) L-H configuration.	156

5.2	Fretting fatigue life vs. damage of first block (d1) showing the experimental data and (A) analytical models based on LSM and (B) ANN damage model. . . . .	160
5.3	Estimated fatigue life considering all the three models vs. experimental one for varying amplitude FF data. . . . .	162
5.4	Flowchart illustrating all the modelling conducted in Part I of this work . . . . .	165
5.5	Estimated life vs. experimental life for fretting fatigue tests on AA1120 and AA1350 wires, subjected to constant amplitude loading. . . . .	169
5.6	Estimated life vs. experimental life for fretting fatigue tests on AA6201 wires, subjected to variable amplitude loading. . . . .	171
5.7	Schematic of the machine learning model using wire fatigue data for training. . .	176
5.8	Correlation of the SWT parameter, calculated using the bulk nominal stress, with lives of fretting fatigue tests of wires made of AA6201, AA1120 and AA1350. . . . .	177
5.9	Estimated life vs. experimental life for fretting fatigue tests on learning data (AA1120 and AA1350) and validation data (AA6200). Prediction made using all the ML models (A) RF, (B) GPR, (C) XGBoost and (D) ANN. . . . .	180
5.10	ANN architecture for the ANN_Cable model. . . . .	182
5.11	Schematic of the overhead conductor fatigue test bench. Adapted from (BADIBANGA, 2017) . . . . .	183
5.12	Flowchart illustrating all the modelling procedure. . . . .	186
5.13	Estimated life vs. experimental one for overhead conductors' fatigue tests (AAAC900 and TERN), for all wire breaks considered. Estimates made using the ANN-Cable model. . . . .	187
5.14	Fatigue life surface for the conductors with AA6201 alloy by using the ANN_Cable. The experimental data provided in ref (BADIBANGA, 2017) for the AAAC 900 MCM conductor are also reported. . . . .	189
5.15	Segment of the cable with the most critical values of the Damage Life Index, highlighting the three layers from the outermost to the innermost in (a), (b), and (c), respectively. Data from the tests with Tension = 33.4 kN and $Y_b = 0.84$ . The experimental failure regions are taken from Badibanga's work (2017). . . . .	190
6.1	Specimen and pad for the fretting fatigue tests. . . . .	194

6.2	UnB's fretting fatigue rig test, zoomed view of contact region, and illustration of main forces acting on the test. . . . .	195
6.3	Schematic of the load history investigated . . . . .	198
6.4	Schematic of the programming established using block language via the Multi-purpose Elite program. . . . .	199
6.5	Shear loading amplitude for $P = 10$ kN and $P = 5$ kN vs. experimental fatigue life for the 7075-T651 specimens. . . . .	201
6.6	Crack propagation highlighted on both specimen side views revealing a distinctive triangular pattern on test T08. . . . .	202
6.7	Highlighting the evolution of crack propagation pattern over time of test T05. . . . .	202
6.8	Triangular pattern of crack propagation observed across selected specimens. . . . .	203
6.9	Post-failure analysis, featuring both parts of the fractured specimen, the fretting pad, and the fatigue-detached triangular piece. Macroscopic details of the fracture are also depicted. . . . .	204
6.10	Confocal laser microscopic images showing the cracked specimen T06, highlighting the crack initiation angles, secondary cracks, and the fretted region. . . . .	205
6.11	Highlighted confocal images of the fracture of T06, in lateral and frontal views. . . . .	206
6.12	Fractography of the specimen T06 from a top-view perspective using confocal microscopy. . . . .	207
6.13	SEM observations of the test specimen T02 at the inclined top view near contact. . . . .	208
6.14	SEM observations of the test specimens: (a) T03 (fast fracture surface), (b) T05 (triangular detached fretted piece), (c) T06 (inclined top view), (d) T06 (130x magnification), (e) T06 (430x magnification), and (f) T06 (1000x magnification). . . . .	209
6.15	Mapping using EDS, highlighting the quantity of aluminum and oxygen present at specific points (a) and across the entire analyzed surface (b) of the contact of specimen T04. . . . .	210
6.16	Wöhler curves for torsional and uniaxial fatigue under fully reversed loading ( $R_\sigma = -1$ ) (a) and modified Wöhler diagram for the same fatigue curves (b). . . . .	212
6.17	Numerical analysis of stress distribution for the test configuration T03. . . . .	215
6.18	Flowchart illustrating all the modelling proposed and conducted. . . . .	216
6.19	Estimated vs. fatigue life for all testing conditions . . . . .	217

6.20 Depth (b) vs. stress intensity factor range ( $\Delta K$ ) for the fretting cycle loading (see the Damage 2 range in Fig. 6.17) for the test configuration T06. . . . .	221
---	-----

# List of Tables

3.1	Experimental data of Al4%Cu collected from Nowell (1988). . . . .	90
3.2	Experimental data of 2024-T351 collected from Szolwinski and Farris (1998). . .	91
3.3	Experimental data of 7050-T7451 collected from Rossino et al. (2009) and Araújo and Castro (2012). . . . .	92
3.4	Proprieties and critical distance of the materials considered. . . . .	92
3.5	Processed stresses ( $\tau_{a,max}$ and $\sigma_{n,max}$ ) from MRH method for Nowell (1988) data-set. The logarithmic correspondent fatigue life is also presented. . . . .	93
3.6	Processed stresses ( $\tau_{a,max}$ and $\sigma_{n,max}$ ) from MRH method for Szlowinski and Farris (1998) data-set. The logarithmic correspondent fatigue life is also presented.	94
3.7	Processed stresses ( $\tau_{a,max}$ and $\sigma_{n,max}$ ) from MRH method for Rossino <i>et al.</i> (2009) and Araújo and Castro (2012) data-set. The logarithmic correspondent fatigue life is also presented. . . . .	95
3.8	ER values for M2I and M3I models with the respective hidden neuron's quantities.	98
4.1	Proprieties of the aluminum alloys considered. . . . .	109
4.2	Proprieties of the titanium and steel alloys considered. . . . .	109
4.3	Experimental data of Al 4%Cu collected from (NOWELL, 1988) (cylindrical contact). . . . .	113
4.4	Experimental data of 2024-T351 collected from (SZOLWINSKI; FARRIS, 1998) (cylindrical contact). . . . .	114
4.5	Experimental data of 2024-T3 collected from (HOJJATI-TALEMI <i>et al.</i> , 2014) (cylindrical contact). . . . .	115
4.6	Experimental data of 7050-T7451 collected from (ROSSINO <i>et al.</i> , 2009; ARAÚJO; CASTRO, 2012) (cylindrical contact). . . . .	115

4.7	Experimental data of 7075-T6 collected from (WITTKOWSKY <i>et al.</i> , 2000; KIRKPATRICK, 1999) (spherical contact).	115
4.8	Experimental data of 7075-T651 collected from (MARTÍN <i>et al.</i> , 2020) (cylindrical contact, 90 to 112) and (MUÑOZ <i>et al.</i> , 2007) (spherical contact, 113 to 132).	116
4.9	Experimental data of the Ti-6Al-4V collected from ref. (BELLECAVE, 2015; ARAUJO, 2000; FERRY, 2017) (cylindrical contact).	117
4.10	Experimental data of the Ti-6Al-4V collected from ref. (VENKATESH <i>et al.</i> , 2001; KIRKPATRICK, 1999) (spherical contact).	118
4.11	Experimental data of the 7050-T7451 collected from ref. (GAILLIEGUE, 2018) (cylindrical contact).	118
4.12	Experimental data of the A743 CA6NM collected from ref. (GAILLIEGUE, 2018) (cylindrical contact).	119
4.13	Geometrical and critical distance parameters for all the materials studied.	120
4.14	Empirical risk (ER) error for the ANN_SHEAR and the ANN_NORMAL models by considering their respective optimum number of neurons in the hidden layer.	133
4.15	Empirical risk (ER) error for the query data by considering all models.	135
4.16	Empirical risk (ER) error for the query data by considering all models.	140
4.17	Band Mean Error Factor (BMEF) for the Ti-6Al-4V data by considering all models.	142
4.18	Band Mean Error Factor (BMEF) for the out-of-phase data by considering all models.	149
5.1	Fretting fatigue tests under H-L and L-H loading sequence.	155
5.2	Fretting Fatigue loading configuration of each configuration.	155
5.3	Values of coefficients $v_1$ and $v_2$ for each approach considered (Model 1, 2 and 3).	159
5.4	Mean percentage error of all models considered.	162
5.5	Properties, dimensions and critical distance of the materials considered.	167
5.6	Nominal stresses, numerical critical plane stresses (at the critical distance), and the fatigue life of the AA1120 (MATOS <i>et al.</i> , 2022; VIEIRA, 2020).	167

---

5.7	Nominal stresses, numerical critical plane stresses (at the critical distance), and the fatigue life of the AA6201 (MATOS <i>et al.</i> , 2023). . . . .	167
5.8	Comparative analysis of BMEF for the AA1120 and AA6201. . . . .	169
5.9	Mechanical properties of the materials considered. . . . .	177
5.10	Fretting fatigue test parameters of wires on AA6201, AA1120 and AA1350 for Part II. . . . .	178
5.11	Comparative error analysis (ER and BMEF) for the learning and query dataset by considering the machine learning models. . . . .	179
5.12	$W$ matrice. . . . .	182
5.13	$V$ matrice. . . . .	182
5.14	Experimental data from AAAC 900 MCM overhead conductor. . . . .	184
5.15	Experimental data from AAAC 900 MCM overhead conductor. . . . .	185
5.16	BMEF for the 1 <sup>st</sup> , 2 <sup>nd</sup> and 3 <sup>rd</sup> break of both overhead conductors by considering the ANN_Cable . . . . .	188
6.1	Material and mechanical proprieties of the Al 7075-T651. . . . .	194
6.2	Experimental loading parameters and fatigue lives. . . . .	200
6.3	Dimensions of the heights of the triangles, the angles $\beta_1$ and $\beta_2$ , and their mean value. . . . .	206
6.4	Measurements of angles for other specimens. . . . .	207
6.5	Fatigue life in terms of loading blocks and the error $\psi$ values of each test. . . . .	219
6.6	Error values (ER and BMEF) for all models in study. . . . .	219

# Nomenclature and symbols

$a$	Half contact size
$A$	Composite compliance
$A_n, b_n$	Wöhler curve parameters
$a_K$	Crack length
$a_1, a_2$	Halves of the sides of the rectangular hull
ANN_Cable	ANN model for overhead conductors fatigue life
ANN_NORMAL	ANN model based on normal parameters
ANN_SHEAR	ANN model based on shear parameters
$b$	Bias on an ANN model
$B$	Bulk fatigue load
$\mathbf{b}_1, \mathbf{b}_2, \mathbf{b}_3, \mathbf{b}_4, \mathbf{b}_5$	Orthonormal basis from the deviatoric space
$c$	Maximum semi-width of the stick zone
$c'$	Semi-width of the stick zone at time
$c_1$	Fatigue strength exponent
$c_2$	Ductility exponent
$C, m$	Material constants from Paris's law
$d$	Desired-response value in the ANN training
$d_w$	Wire diameter
$da_K/dN$	Crack growth rate
$D_t$	Critical damage value
$e$	Maximum offset of the stick zone
$e'$	Offset of the stick zone at time
$e_{out}$	Error signal produced at the neuron output
$E$	Young's modulus
$E^*$	Effective modulus of elasticity
$E_1, E_2$	Young's modulus of contacting bodies.
$ER$	Empirical Risk error
$\mathbf{e}_x, \mathbf{e}_y, \mathbf{e}_z$	Orthonormal basis
$\mathbf{e}_A, \mathbf{e}_B, \mathbf{n}$	Orthonormal basis from the Cauchy tetrahedron
$\mathbf{f}_0$	System of forces
$f$	Friction coefficient
$F_0$	Constant to compute contact stresses in spherical contacts
$F_C$	Clamping force at overhead conductors
$g(x)$	Relative tangential displacement distribution
$h(x)$	Normal displacement distribution
$h_s$	Specimen's height
$h_t$	Triangle's height

$H_0$	Constant to compute contact stresses in spherical contacts
$HV_{max}$	Maximum adopted Vickers Hardness for a given material
$I_{SWT}$	SWT parameter
INV	ANN model based on invariant stress
$J$	Variable to compute contact stresses in spherical contacts
$K$	Stress intensity factor
$L$	Material critical distance size
M2I	Two-input ANN model based on the critical distance
M3I	Three-input ANN model based on the critical distance
$\mathbf{n}$	Unit normal vector
$n$	Number of data on a dataset
$N$	Number of fatigue load cycles
$N_j$	Number of cycles applied at a given stress level $\sigma_{a,j}$
$N_f$	Number of cycles to failure
$N_{block}$	Variable amplitude loading block
$N_{f,j}$	Number of cycles to failure for given stress level $\sigma_{a,j}$
$N_{f,exp}$	Experimental number of cycles to failure
$N_{f,pred}$	Predicted number of cycles to failure
$N_{f,MAX}$	Maximum number of cycles to failure between a given dataset
$N_{f,max}$	Maximum adopted failure cycles
$N_{ref}$	Number of reference cycles
NORMAL	ANN model based on normal stress
$P$	Normal load on pad
$P_{exp}$	Normalized and logarithmized experimental fatigue life
$P_{pred}$	Normalized and logarithmized predicted fatigue life
$p(x)$	Normal traction distribution
$p_0$	Peak pressure
$q(x)$	Shear traction distribution
$q'$	First perturbation term on $q(x)$
$q''$	Second perturbation term on $q(x)$
$Q$	Shear/tangential/fretting loading
$Q_{max}$	Maximum tangential loading
$Q_{min}$	Minimum tangential loading
$r$	Radial distance in spherical contacts
$r_K$	Distance from the crack tip
$R$	Pad radius
$R_1, R_2$	Radius of contacting bodies
$R_\sigma$	Fatigue load ratio
$S_a$	Deviatoric stress amplitude
$S_{B,a}$	Nominal normal stress amplitude
$S_{B,m}$	Nominal normal mean stress
$S_1, S_2, S_3, S_4, S_5$	Deviatoric stress components
$\mathbf{S}$	Deviatoric stress tensor
SHEAR	ANN model based on shear stress
$SWT_{block}$	Nominal value for the SWT parameter
$t$	Time
$T$	Tension load applied to the conductor
$T_0$	Initial tensile load applied to the conductor
$\mathbf{t}$	Stress vector

$\mathbf{t}_n$	Normal stress vector
$thk$	Specimen's thickness
$u$	Variable to compute the spherical contact stresses
$V$	Weights matrices between the hidden layer and the output layer
$V_{up}$	Updated $V$ matrix
$w$	Synaptic weights
$W$	Weights matrices between the input layer and the hidden layer
$W_{up}$	Updated $W$ matrix
$\mathbf{x}$	Input vector
$x_1, x_2, \dots, x_n$	Inputs signals
$Y_b$	Bending displacement amplitude
$\alpha$	Wires crossing angle
$\beta$	Orientation angle from MRH / Mean crack angle / Pinto's parameter
$\beta_P$	Static deflection angle with the passive end of the conductor
$\beta_0$	Static deflection angle with the active end of the conductor
$\beta_1$	Crack angle near the leading edge contact
$\beta_2$	Crack angle near the trailing edge contact
$\gamma$	Neuron activation function
$\Gamma$	Cost function in backpropagation algorithm
$\delta$	Local gradient from backpropagation algorithm
$\Delta F/2$	Force amplitude
$\Delta K$	Stress intensity factor range
$\Delta K_{th}$	Threshold stress intensity factor range
$\Delta N_i$	Number of cycles applied at a given stress level $\sigma_{a,i}$
$\Delta W, \Delta V$	Parameters to update the synaptic weights matrices
$\Delta w$	Parameter to update the synaptic weights
$\Delta$	Force amplitude
$\Delta\beta$	Variation of the sag angle in the overhead conductors
$\varepsilon_{n,a}$	Normal strain amplitude
$\varepsilon'_f$	Ductility coefficient
$\epsilon$	Damage function based on ANN
$\zeta$	Parameter to adjust tanh and sigmoid functions
$\eta$	Learning rate parameter
$\theta$	Angle between $x$ and $y$ directions in the Cauchy tetrahedron
$\vartheta$	Angle of the orthonormal basis from the deviatoric space
$\kappa, \lambda$	Crossland calibration constants
$\kappa_\tau$	Negative inverse slope in $\tau_a$ vs. $N_f$ diagrams
$\Lambda$	Parameter derived from Muskhelishvili potential analysis.
$\nu$	Poisson's coefficient
$\nu_1, \nu_2$	Poisson's coefficient of contacting bodies
$\xi$	Variable in the integral equation governing two similarly elastic bodies
$\Xi$	Material plane or surface element
$\varpi$	Phase angle for the Out-of-phase loading datasets
$\rho$	Stress ratio from MWCM
$\rho_{crit}$	Critical value of $\rho$
$\sigma_a$	Normal stress amplitude
$\sigma_{a,j}$	Stress amplitude on a certain loading block
$\sigma_{B,a}$	Bulk stress amplitude
$\sigma_{B,m}$	Mean bulk stress

$\sigma'_f$	Fatigue strength coefficient
$\sigma_{H,max}$	Maximum hydrostatic stress
$\sigma_n$	Normal component of $\mathbf{t}$ into $\mathbf{n}$ direction
$\sigma_{n,a}$	Normal stress amplitude on the critical plane
$\sigma_{n,max}$	Maximum normal stress on the critical plane
$\sigma_{n,MAX}$	Maximum normal stress between a given dataset
$\sigma_{ult}$	Ultimate tensile strength of the material
$\sigma_{xx}, \sigma_{yy}, \sigma_{zz}$	Normal stress on $x, y$ and $z$ directions, respectively
$\sigma_{xx}^N, \sigma_{yy}^N, \sigma_{zz}^N$	Normal stress of the $\boldsymbol{\sigma}^N$ on $x, y$ and $z$ directions, respectively
$\sigma_{xx}^T, \sigma_{yy}^T, \sigma_{zz}^T$	Normal stress of the $\boldsymbol{\sigma}^T$ on $x, y$ and $z$ directions, respectively
$\sigma_y$	Yield stress of the material
$\boldsymbol{\sigma}$	Cauchy stress tensor
$\boldsymbol{\sigma}_B$	Bulk fatigue stress tensor
$\boldsymbol{\sigma}^N$	Normal component stress tensor
$\boldsymbol{\sigma}^T$	Tangential component stress tensor
$\tau_{xy}, \tau_{xz}, \tau_{yz}$	Shear stress on $xy, xz$ and $yz$ planes, respectively
$\tau_{xy}^N, \tau_{xz}^N, \tau_{yz}^N$	Shear stress of the $\boldsymbol{\sigma}^N$ on $xy, xz$ and $yz$ planes, respectively
$\tau_{xy}^T, \tau_{xz}^T, \tau_{yz}^T$	Shear stress of the $\boldsymbol{\sigma}^T$ on $xy, xz$ and $yz$ planes, respectively
$\tau_a$	Shear stress amplitude
$\tau_{a,max}$	Maximum shear stress amplitude
$\tau_{a,MAX}$	Maximum shear stress amplitude between a given dataset
$\tau_{a,ref}$	$\tau_a$ for a reference number of cycles ( $N_{ref}$ )
$\tau_A$	Shear component of $\mathbf{t}$ into $\mathbf{e}_A$ direction
$\tau_B$	Shear component of $\mathbf{t}$ into $\mathbf{e}_B$ direction
$\boldsymbol{\tau}$	Shear stress vector
$\mathbf{v}_1, \mathbf{v}_2$	LSM parameters
$\varphi$	Angle between $\mathbf{n}$ and $z$ directions in the Cauchy tetrahedron
$\Phi$	Potential of Muskhelishvili
$\chi$	Variable from $\Phi$ integral equation
$\psi$	Band error factor
$\Omega$	Shear stress path
$\nabla$	Divergent operator
$\otimes$	Tensor product operator

# Abbreviations

<b>AAAC</b>	All Aluminum Alloy Conductors
<b>ACSR</b>	Aluminum Conductor Steel Reinforced
<b>ANN</b>	Artificial Neural Networks
<b>ASTM</b>	American Society for Testing and Materials
<b>BMEF</b>	Band Mean Error Factor
<b>CROSSLAND</b>	Crossland multiaxial fatigue model
<b>EDS</b>	Everyday Stress
<b>FEA</b>	Finite Element Analysis
<b>FEM</b>	Finite Element Method
<b>FEM</b>	Gauss Process Regression
<b>HCF</b>	High Cycle Fatigue
<b>HV</b>	Vickers Hardness
<b>ISFF</b>	International Symposium on Fretting Fatigue
<b>JSME</b>	Japan Society of Mechanical Engineers
<b>LCF</b>	Low Cycle Fatigue
<b>LEFM</b>	Linear Elastic Fracture Mechanics
<b>LVDT</b>	Linear Variable Differential Transformer
<b>ML</b>	Machine Learning
<b>MHR</b>	Maximum Rectangular Hull
<b>MSE</b>	Mean Squared Error
<b>MWCM</b>	Modified Wöhler Curve Method
<b>PINN</b>	Physics Informed Neural Networks
<b>SWT</b>	Smith, Watson and Topper model
<b>TBE</b>	Transmissoras Brasileiras de Energia
<b>TCD</b>	Theory of Critical Distance
<b>XGBoost</b>	Extreme Gradient Boost

# Chapter 1

## Introduction

*"This chapter provides an overview of the research topic and outlines the objectives and significance of the study."*

## 1.1 CONTEXT AND MOTIVATIONS OF THE STUDY

The analysis conducted in this document aims to contribute to the understanding of fretting fatigue, a phenomenon particularly common in mechanical couplings subjected to dynamic loads, such as parts in machinery, mechanical equipment, and structures exposed to constant vibrations. To achieve this goal, it proposes the utilization of a contemporary approach, specifically the application of machine learning-based models, with a focus on artificial neural networks (ANN).

As will be detailed further, the use of these data-driven models is increasingly expanding across all areas of engineering, including fatigue analysis. This growth is primarily due to the increase in data generation, its easy acquisition, which facilitates real-time monitoring, and the ability to address complex problems. Concurrently, advancements in computing power have also contributed to this trend. As will be discussed later, the ability to select training data in terms of variability and representativeness enhances these models' generalization capabilities, making them more robust and versatile.

It is well known that, over the years, millions of dollars have been lost due to problems related to fretting fatigue. This occurs because the phenomenon affects both high-value components, such as aircraft turbines, marine risers, and power transmission cables (where a failure can cost millions due to temporary power loss), as well as more common components that exist in large quantities, such as bolted joint hubs in gear transmissions, axle bolts in roller coasters, and connecting rod bolts, all of which are susceptible to fretting fatigue. This underscores the need for updated methodologies that are stress-based—in other words, applicable to any geometry at risk of fretting fatigue, easy to implement, and capable of providing estimates consistent with experimental observations.

Before presenting the objectives of this work, the next subsection will review fretting fatigue definitions and the historical evolution of the analysis of this phenomenon over decades of research, with a focus on key methodologies developed to date. The published articles focusing on the application of data-driven models to fretting fatigue will also be presented. The final section will outline the structure of the thesis.

## 1.2 FRETTING FATIGUE REVIEW

Fretting is a mechanical phenomenon arising from the interaction of slight oscillatory movements between surfaces in contact under pressure, causing wear, surface deterioration, and potential structural health compromise. This process involves repetitive, low-amplitude micro-motions occurring between neighboring surfaces, resulting in wear via abrasion, corrosion, and eventual fatigue failure. The fretting fatigue (FF) phenomenon occurs when there is small relative slip and fatigue loads between contacting parts, it has been extensively studied since were discovered situations where microslips between surfaces of mechanical assemblies led to a considerable decrease in fatigue life, when compared to a single component of the assembly subjected to plain fatigue. Under these circumstances, the surface contact induces localized high stress concentrations and, consequently, high stress gradients as well as complex multiaxial stress states. This phenomenon is usually encountered in many engineering systems, such as blade/disks joints of turbines (GLODEK; TALEMI, 2022; CIAVARELLA; DEMELIO, 2001) and overhead conductors (KALOMBO *et al.*, 2020; CÂMARA *et al.*, 2022). Even today, after more than half a century of investigation of the FF problem, it still remains very challenging from both experimental and modelling points of view. Therefore, gaining a deep understanding of the mechanisms and characteristics of fretting fatigue is crucial to design reliable and safe mechanical systems.

The earliest documented instance of fretting was recorded by Eden *et al.* (1911), who noted the formation of oxide debris in the steel grips of their fatigue machine when in contact with a steel specimen. Subsequent investigations by Tomlinson (1927), Warlow-Davies (1941), and McDowell (1953) unveiled a notable reduction in fatigue strength attributable to this phenomenon. Wright (1953a, 1953b) conducted extensive research on the role of oxidation in fretting, exploring the interaction between fretting and corrosion on the fatigue life and wear rate of mechanical structures. Further insights into distinct fatigue limits and the occurrence of fretting corrosion were provided by Waterhouse and Allery (1965). Additionally, Fenner and Field (1958) were the first to demonstrate that fretting significantly accelerated the crack initiation process.

A critical point in the timeline is the late 1960s when more systematic investigations into fretting fatigue parameters unfolded, notably by Nishioka and Hirakawa (1969c, 1969a, 1969b,

1969d, 1972, 1968). Their studies examined the influence of factors such as contact pressure, relative slip amplitude, environmental conditions, and materials on fretting fatigue strength. They concluded that the amount of relative slip significantly impacted fretting fatigue strength, with a sharp reduction observed at specific slip amplitudes. Micro-cracks were initiated but did not propagate to complete fracture, aligning with observations from other contemporary authors (WATERHOUSE; ALLERY, 1965; FENNER; FIELD, 1958). Addressing the mean stress effect, these Japanese researchers found it had little impact on crack initiation but that higher mean stress in the specimen reduced fatigue life. Consequently, fretting appears to govern the formation of embryo cracks, while bulk stress assumes a more substantial role in later stages of propagation.

In 1971, the first International Conference on corrosion fatigue introduced the concept of a fretting damage threshold by Hoepfner and Goss (1972). They observed that a specific degree of fretting damage was crucial before any discernible reduction in fatigue life was evident in tests involving Ti-6Al-4V and Al 7075-T6 alloys. Interestingly, eliminating the source of fretting after surpassing the fretting damage threshold had minimal impact on subsequent fatigue life. The concept of the fretting damage threshold was closely linked to the initiation of an initial crack, elevating local stress intensity beyond the threshold value within a considerably smaller number of applied cycles. Bramhall (1973) delved into the influence of varying contact sizes and discovered that fretting significantly diminished fatigue life for contact widths exceeding a critical value. Future works experimentally confirms this evidence (NOWELL, 1988; ARAUJO, 2000). Endo and Goto (1976) found that cracks in mild steel initiated on shear planes (stage I) and then quickly propagated nearly perpendicular to the contact surface (stage II) when using cylindrical pads under full slip conditions. Their work demonstrated that fretting not only accelerates crack initiation but also has a significant influence on early stages of crack propagation. This research, alongside the works of Edwards *et al.* (1977) and Hoepfner (1977), marked a pioneering application of linear elastic fracture mechanics (LEFM) in studying fretting fatigue, establishing the foundation for extensive applications of fracture mechanics in fretting fatigue studies (GOLDEN; GRANDT, 2004; CHAMBON; JOURNET, 2006; MADGE *et al.*, 2008; NAVARRO *et al.*, 2011; HOJJATI-TALEMI; WAHAB, 2013; FONTES DO RÊGO *et al.*, 2018; RANGEL *et al.*, 2022). A significant milestone in this trajectory was the publication of a major book on fretting fatigue by Waterhouse in 1981 (WATERHOUSE, 1981).

Ruiz *et al.* (1984) proposed a popular method for predicting fretting fatigue performance using empirical parameters tailored for the fretting case. They defined an energy damage parameter as the product of the local slip amplitude with the maximum shear traction ( $\tau\delta$ ) and later improved this formulation by incorporating the maximum stress component parallel to the contact surface ( $\sigma\tau\delta$ ), providing better estimations of fretting crack initiation location. This approach has been adopted by a larger number of research (BRAMHALL, 1973; HILLS *et al.*, 1988; SZOLWINSKI; FARRIS, 1998). Despite the unclear physical interpretation, this parameter often correlates well with experimental observations (CIAVARELLA *et al.*, 2001).

At this time, early applications of finite element analysis (FEA) in fretting contact problems began to take shape with contributions from Ruiz *et al.* (1984) and Stover *et al.* (1985). Consequently, numerous researchers started to apply this technique in the field of fretting fatigue. For instance, Giannakopoulos and Suresh (1998) utilized a 3D finite element model to analyze spherical-plane fretting fatigue issues, capturing the evolution of surface and sub-surface fields for various levels of partial slip, interfacial friction, and externally imposed mean stress values. Farris *et al.* (2000) combined FEA modeling and experimental observations, leading to a thermography/FEM approach for understanding the influence of fretting on fatigue failure of riveted aircraft structures. Sato (1992) calculated the contact stress pressure distribution using a boundary element method. Neu *et al.* (2000) employed the FEA approach and multiaxial fatigue criteria based on the critical plane approach to estimate the local state stress at and near the contact interface to predict fretting fatigue crack nucleation lifetime. Mutoh and Xu (2003) proposed a new FEA approach based on a singular stress field near the contact edge and on fracture mechanics to predict fretting fatigue crack propagation lifetime. Madge *et al.* (2007) developed FEA integrated wear modeling with fretting fatigue analysis to predict the effects of material removal due to fretting wear. These are just a few of the dozens of studies that arose during this period and continue to emerge to this day, encompassing various applications of this methodology (NESLÁDEK *et al.*, 2012; LI *et al.*, 2015; CARDOSO *et al.*, 2019; ARAÚJO *et al.*, 2020; WANG *et al.*, 2022a; DOCA *et al.*, 2022), including more recent approaches such as the use of the enrichment approach, as exemplified by the X-FEM framework in fretting simulations (CARDOSO *et al.*, 2018; ANJUM *et al.*, 2015; GLODEK *et al.*, 2023; PINTO *et al.*, 2021).

In this way, with the continuous evolution of contact mechanics theory over the past century (HERTZ, 1882; CATTANEO, 1938; MUSKHELISHVILI, 1977; JOHNSON, 1985; HILLS; NOWELL, 1993), analytical advancements have yielded precise insights into the mechanical fields for simple geometries commonly employed to assess the fretting fatigue phenomenon. Concurrently, owing to ongoing computational developments, several researchers have explored diverse theories to predict fretting fatigue performance. Noteworthy methodologies include the notch analogy (GIANNAKOPOULOS *et al.*, 2000; ARAÚJO *et al.*, 2007; DINI *et al.*, 2006), crack analogy (GIANNAKOPOULOS; SURESH, 1998; CIAVARELLA *et al.*, 2003), short crack arrest (ARAÚJO; NOWELL, 1999; DINI *et al.*, 2006; FOUVRY *et al.*, 2008) and more recently data-driven approaches (ORBANIĆ; FAJDIGA, 2003; MAJZOBI; KAZEMI, 2013; LIU; YUAN, 2023).

Over the years, there has been a substantial proliferation of methodologies and associated works in the fretting fatigue domain, making it practically unfeasible to comprehensively cover all these research endeavors. Consequently, various reviews have surfaced in the literature, seeking to encapsulate the primary contributions up to their respective publication dates. For instance, Bhatti and Abdel Wahab (2018) provided an overview of numerical and experimental works related to crack nucleation under fretting conditions. Hills and Dini (2004) underscored the importance of employing simple asymptotic forms to represent any type of contact, thereby facilitating the analysis of intricate practical problems. In 2018, Cardoso *et al.* (2018) published a review on short crack models and proposed a novel approach, considering available data on AISI 1034, Al4%Cu, and Ti-6Al-4V under cylindrical contacts. In a recent development, Croccolo *et al.* (2022) conducted a review on the influence of fretting fatigue in mechanical joints, specifically in press-fitted shaft hub joints, dovetail joints, and bolted joints, recognized for their susceptibility to this phenomenon. Moreover, the influence of fretting fatigue on overhead conductors, a central focus of this research, has been emphasized since the groundbreaking work of Lanteigne *et al.* (1986). This emphasis has been further deepened in the current century, as evidenced by studies such as those by Dalpe *et al.* (2008), Azevedo *et al.* (2009), Levésque *et al.* (2010), and others (FADEL *et al.*, 2012; STEIER *et al.*, 2014). These investigations have employed state-of-the-art laboratory experiments (KALOMBO *et al.*, 2015; KALOMBO *et al.*, 2017) and advanced numerical techniques (LALONDE *et al.*, 2017; MATOS *et al.*, 2020; ROCHA *et al.*, 2022; SAID *et al.*, 2023), including recent advancements in

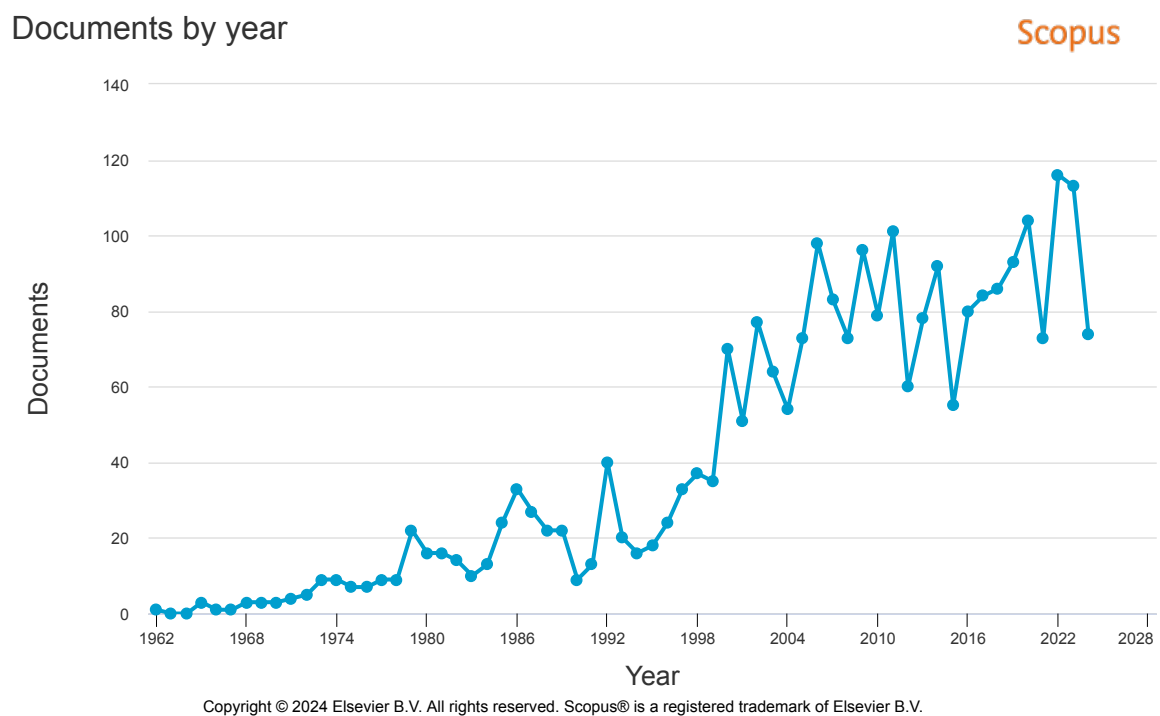


**Figure 1.1.** Number of fretting fatigue documents published over the years.

machine learning methodologies (PESTANA *et al.*, 2018; KALOMBO *et al.*, 2020; CÂMARA *et al.*, 2022). Another facet of our research, focusing on fretting fatigue with variable amplitude loading, has been under investigation since the 1980s (KANTIMATHI; ALIC, 1981) and has witnessed consistent growth over the years (MUTOH *et al.*, 1989; KINYON; HOEPPNER, 2000; KONDO *et al.*, 2006; MASSINGHAM; IRVING, 2006; GANDIOLLE; FOUVRY, 2016; KOUANGA *et al.*, 2023; PINTO *et al.*, 2023).

Finally, the enduring contributions of esteemed researchers in the field (JOHNSON *et al.*, 1971; JOHNSON, 1985; NOWELL; HILLS, 1990; WATERHOUSE, 1992; HILLS *et al.*, 1993; MUTOH, 1995; FOUVRY *et al.*, 1996; SZOLWINSKI; FARRIS, 1996; FARRIS *et al.*, 2000; ARAÚJO; NOWELL, 2002; DOMÍNGUEZ; NAVARRO, 2002; NAVARRO *et al.*, 2008; HOJJATI-TALEMI; WAHAB, 2013; VÁZQUEZ *et al.*, 2012; HILLS; NOWELL, 2014; CARDOSO *et al.*, 2018; VANTADORI *et al.*, 2020; ARAÚJO *et al.*, 2020; ALMEIDA *et al.*, 2023), emphasize the continual development and diversification of this theme in terms of new applications and methodologies across the decades. In this setting, conducting a search on Scopus, a bibliographic database containing abstracts and citations of scientific articles, books, and conference publications, reveals itself as the largest database of its kind with over 250 million publication records. Analyzing the data, it becomes evident that the topic of fretting fatigue

has seen a substantial increase over the years, as illustrated in Fig. 1.1.

As mentioned in the previous section, the core of this work is the application of models based on machine learning, more specifically artificial neural networks (ANN). In the fatigue field there are many studies in which the ANN technique has been applied in more diverse forms (PLEUNE; CHOPRA, 2000; MARQUARDT; ZENNER, 2005; FREIRE JÚNIOR *et al.*, 2009; MALEKI *et al.*, 2018; JIMENEZ-MARTINEZ; ALFARO-PONCE, 2019; DINIZ; FREIRE JÚNIOR, 2020; STROHMANN *et al.*, 2021; WANG *et al.*, 2021). Nevertheless, when it comes to fretting fatigue, only a handful of articles delve into the utilization such techniques. In the following subsection, one will discuss these authors and their research, shedding light on how this contemporary approach is gradually being explored in the field of fretting fatigue.

### 1.2.1 ANN modelling of fretting fatigue

In the literature, the first instance of applying neural networks to fretting fatigue issues dates back to 2003, in the work of Orbanić and Fajdiga (2003). The study incorporates parameters such as stress amplitude, surface pressure, material type, and surface finish conditions as inputs to the ANN, which outputs the occurrence or non-occurrence of fretting fatigue. To reduce the input variables of the ANN, the material type and surface finish conditions were combined into a single input parameter. The final model, consisting of four inputs model and trained with 114 data points, includes studies exploring the impacts of surface pressure and treatment on the fatigue life of aluminium–steel couplings under dynamic reverse bending. Subsequently, 28 previously unseen data points from the database were employed to test the ANN. The predictions demonstrated commendable alignment with experimental results, with 86% accuracy in predictions. This classification model proved to be satisfactory in detecting fretting fatigue in these scenarios.

Only a decade later, the second article in the field was published (MAJZOABI; KAZEMI, 2013). The authors, Majzoobi and Kazemi utilized artificial neural networks (ANN) to examine the impact of re-shot peening on the fretting fatigue behavior of Al 7075-T6. The inputs to the neural networks were the maximum stress levels resulting from different shot peening intensities, and the output was the total fatigue life. The predicted life values were then compared with experimental results. The outcomes indicated a significant increase in fretting fatigue life,

ranging from 390% to 410% compared to the life of virgin specimens, contingent on the stress level, with the application of shot peening. Additionally, the authors noted that the effect of re-shot peening, particularly after the third session, was not as pronounced and became negligible after the fourth shot peening. It is noteworthy that the authors demonstrated applications within a specific training range, limiting the exploration of the generalization potential of their model.

In 2018, Pestana *et al.* (2018) applied ANN models to estimate the fatigue life of overhead conductors, which also contain interwire fretting effects, under various levels of mean stresses. Until then, there has been a relatively low publication rate in the field of fretting fatigue over the years. However, from 2020 onward, there has been a gradual increase in publications. As an example, Nowell and Nowell (2020) presented a study aiming to model the effect of contact size on fretting fatigue. They employed an ANN models with four inputs, considering common variables in fretting problems. In the same year, Hafid *et al.* (2020) proposed a hybrid and applied modeling approach, incorporating machine learning. In this hybrid computation, damage resulting from fretting fatigue is assessed using a mechanical multiscale approach, wherein representative loading and scenarios are derived through machine learning techniques. Leveraging the decision-making tool developed, the authors achieved accurate predictions of conductor failures in specific areas of France, comparing favorably with field data. Concurrently, the team from the study by Kalombo *et al.* (2020), a continuation of the previously mentioned work (PESTANA *et al.*, 2018) for Aluminum Conductor Steel Reinforced (ACSR) conductors, released a new paper delving deeper into the analysis of ANN applied to overhead conductors. They utilized an ANN model with two inputs: mean stress normalized by the ultimate tensile strength and the fatigue life by a maximum fatigue life considered ( $10^7$  in this case). The output was the stress amplitude, also normalized by the ultimate stress. The model, trained with data from three S-N curves, demonstrated the ability to handle conductors with diverse values of everyday stress (EDS). Analyzing All Aluminum Alloy Conductors (AAAC) 1055 MCM cables in this study, it exhibited excellent performance across different mean stress values, using a small sample of experimental data for network training.

In the following year, Strohmman *et al.* (2021) proposed a modeling approach using digital image correlation (DIC) and convolutional neural networks (CNN) for the automatic prediction

of fatigue crack paths. The CNN was trained to predict the coordinates of crack paths and crack tips based on the displacement fields around the fatigue crack. DIC data used for training were supplemented with data from finite element calculations to increase the dataset. The authors assessed the performance of the trained CNN for different types of specimens. At the same year, continuing the efforts on ANN applied to overhead conductors, Camara *et al.* (2021) introduced a novel ANN model, basing its inputs on various physical parameters such as the specific weight and the bending stiffness of the conductors. Their results demonstrated that this new architecture was capable of estimating the fatigue behavior of a family of aluminum overhead conductors.

In 2022, Camara *et al.* (2022) returned to publish articles in the field with a more innovative model proposal. Their new ANN model was based on parameters from well-established analytical-experimental methods in the literature, such as the Poffenberger-Swart formula (POFFENBERGER; SWART, 1965). Thus, their results demonstrated that an ANN model using the Poffenberger-Swart formula produced better results and incorporated more information on the studied conductor cables when compared to older models. In the same year, researchers from Belgium and China (WANG *et al.*, 2022b) joined forces in the endeavor to utilize machine learning-based models to predict fretting fatigue crack initiation lifetime based on a restricted dataset of aluminum alloy of 2024-T351, well-established in the literature (SZOLWINSKI; FARRIS, 1998). This was the first of four articles released the following year, all with the same objective of predicting fretting fatigue initiation life, albeit changing only the type of machine learning model (WANG *et al.*, 2022b; HAN *et al.*, 2023a; HAN *et al.*, 2023b; WAHAB, 2023). Despite employing a complex modeling approach, using recent methods like deep neural networks (DNN) or physics-informed neural networks (PINN), these authors did not delve into the generalization power of their models, testing only on the limited dataset they had with this specific fretting fatigue initiation life characteristic.

In 2023, several new works in the field of monitoring related to fretting fatigue phenomena, employing data-driven approaches, began to emerge. Noteworthy among these are the works of Senavirathna *et al.* (2023) and Carboni and Zamorano (2023). The former applied the methodology to transmission lines conductors using image processing with deep neural networks. The latter monitored fretting fatigue damage in solid railway axles using acoustic

emission with unsupervised machine learning, making comparisons to non-destructive testing techniques.

Finally, we highlight the notable work of Liu *et al.* (2023), who proposed a hierarchical mechanism-informed neural network (HMNN) life prediction method. The authors considered four neural network layers, hierarchically and progressively established for proportional multi-axial fatigue, non-proportional multi-axial fatigue, notch fatigue, and fretting fatigue, respectively. According to the authors, each layer can assess the fatigue life of the previous layer based on the progressive construction of fatigue complexity. Thus, the authors provided a progressive approach to investigating complex fatigue problems. They emphasize that the reliability and stability of the ANN depend significantly on the quality and amount of data (LIU; YUAN, 2023). Extrapolation from ANN can generate incorrect results and is generally not useful for engineering applications. As points out by the authors, the introduction of physics background and boundary conditions into the ANN model can substantially improve the efficiency and applicability of the ANN approach. This observation implies that data-driven models based on physical parameters more related to the problem can enhance the generalization capabilities of these models, allowing them to perform well in regions outside the training data.

In recent years, there has been an exponential increase in interest in this subject, with increasingly complex models being employed to investigate and predict the behavior of fretting fatigue in several instances. However, despite this recent increase, several gaps in the literature were also identified, which is where this work makes its contribution. The key issue lies in exploring the generalization capability of these models, comparing them head-to-head with the classical models not only in terms of accuracy but also in terms of practicality and versatility. Overall, no previous work has dared to tackle all the major challenges of fretting fatigue at once, such as the effects of material type, contact shape, contact size, the presence of mean stress, out-of-phase loading, high temperature, among others. The modeling approach proposed in this thesis aims to address these challenges, in the next section, one will highlight the objectives of this work, emphasizing our contribution to the field.

### 1.3 AIMS AND SCOPE

As will be shown in the next section, this work is structured into four distinct parts, each aligned with a specific objective and emphasis. While employing different approaches, these segments share a common central focus: the utilization of data-driven approaches for fretting fatigue life calculation—an overarching goal of this study. Throughout the text, various types of comparative analyses, hybrid model formulations, numerical simulations, and experimental analyses are conducted. To achieve this, a foundation of mechanical science principles relevant to the subject matter is applied, such as the utilization of the theory of critical distances to account for the so-called stress gradient effect. Another example is the choice of the stress parameters that are physically linked to the crack initiation process serving as inputs for the models created, akin to their use in classical multiaxial fatigue models. One reiterates, however, that this doctoral thesis aims to establish a methodology that serves specifically to:

- Compute fretting fatigue life for various types of metallic alloys, encompassing alloys such as Al 4% Cu, 2024-T351, 7050-T7451, 7075-T651, 7075-T6, 2024-T3, Ti-6Al-4V, A743 CA6NM, Inconel 718, AA1120, AA6201, AA1350.
- Address different effects, including *(i)* nonzero mean bulk stress, *(ii)* contact geometry, *(iii)* stress gradient, *(iv)* contact size, and *(v)* high temperature on life.
- Develop a model that is methodologically robust and accessible to users, yielding estimates comparable to or surpassing the best-performing models in the literature for the same purpose.
- Extend the methodology’s applicability to the study of fatigue in overhead conductors and their wires, which also involves fretting effects.
- Accommodate complex loadings, including those with variable  $P$  normal load (ALMEIDA *et al.*, 2022; ALMEIDA *et al.*, 2023), variable  $Q$  shear load amplitude (PINTO *et al.*, 2023), and more intricate loadings which will be discussed in the penultimate chapter of this doctoral thesis. This chapter considers loadings that closely resemble real-world scenarios, such as those encountered during the cruise phase of an aircraft.

## 1.4 STRUCTURE OF THE WORK

This work is organized by first presenting an introduction (Chapter 1) to address the scope. Following that, a literature review is provided with the theory and methodology adopted (Chapter 2). As can be seen in Fig. 1.2, the core of this thesis has been structured into four parts: analytical, numerical, applied, and experimental. However, it is worthy to acknowledge that these labels are more closely tied to the emphasis of each chapter, as each part encompasses aspects of analytical approach, numerical modeling, applications, and experimental data to varying extents. Each part of this is presented in a chapter after the one that follows Chapter 2, i.e. Chapters 3, 4, 5 and 6.

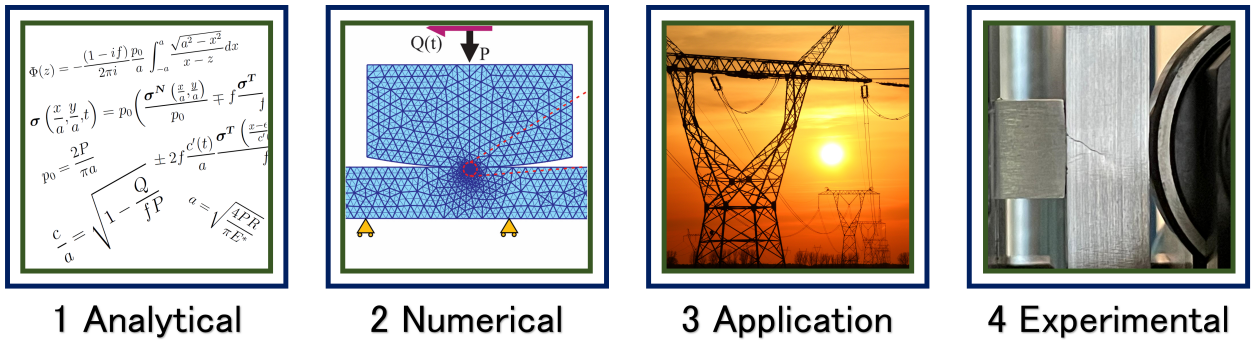


**Figure 1.2.** The four parts of the doctoral thesis.

The first part of this work (Chapter 3) was dedicated to studying fretting fatigue in classical geometries. These are geometries commonly used in analytical approaches and laboratory experiments. Not taking away their merit, it is important to note that these experiments aim to study material behavior under fretting fatigue conditions, extending this analysis from simple pad geometries in contact with test specimens to more complex configurations, such as airplane turbines, which undergo fretting fatigue, as shown in Fig 1.3 (principle of similitude). Here, a new hybrid model based on ANN and on a non-local multiaxial fatigue analysis has been proposed to predict fretting fatigue life. The inputs for the ANN were: (i) the shear stress amplitude, (ii) the maximum normal stress, both on the material critical plane, and (iii) the critical distance size. To train, validate and test the analysis available fretting fatigue data on three different aluminium alloy were chosen. The first article related to this thesis has been published and can be found here (BRITO OLIVEIRA *et al.*, 2022).

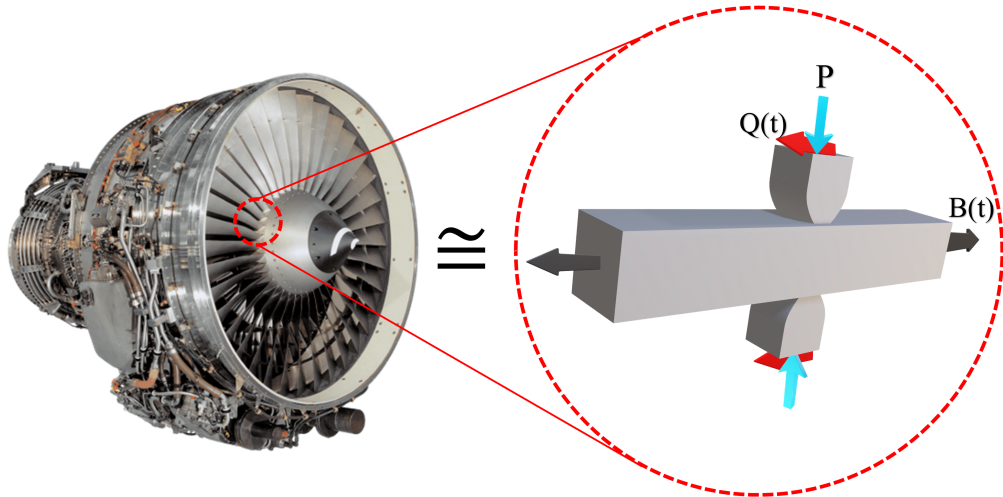


**Figure 1.3.** Equivalence of the experimental tests.

The second part of this work (Chapter 4) is connected to two subsequent articles that explore closely related themes (BRITO OLIVEIRA *et al.*, 2023a; OLIVEIRA *et al.*, 2024). In these studies, the generalization capability of the ANN model was more rigorously implemented and tested, supported by the Finite Element Method (FEM), and demonstrated high accuracy across a substantial dataset of fretting fatigue cases (over 200 instances). A key strength of this work is the ability of the developed models to handle a wide range of materials, loadings, and geometries, including those that differ significantly from the conditions on which the model was originally calibrated (or, more precisely, trained). The introduction of nonlinear inputs specific to each material allowed the model to produce predictions that had not been achieved by any previous model, even when applied to datasets that differed from the training data.

The third part of this work (Chapter 5), as the name suggests, has a more applied focus. It consists of three articles that explore different aspects of the subject. The first article addresses the application of ANN models to fretting fatigue cases involving variable shear loading amplitude. The second article involves the prediction of fretting fatigue life in wire-to-wire contact scenarios. The final article presents the application of a new model, based on nominal stresses, for estimating the fatigue life of overhead conductors.

Finally, and not less important, I emphasize the significant motivation to conduct experiments for the last part of this work (Chapter 6). These experiments aimed to push the limits of the hybrid models that had been created until then, and they were designed with the premise of introducing complexities into the loading scenarios. Inspired by the work of Professor Alex

Araújo (2000), who dealt with variable amplitude loadings and high (HCF) and low (LCF) fatigue cycle regimes, simulating the loading of aircraft subjected to aeroelastic flight effects. In the aeroplane junction regions, they undergo two types of fretting damage linked to loading conditions during different flight phases (take-off, cruise, landing): one related to changes in rotational speed during take-off and landing, causing hoop stress and relative motion, and the other resulting from high-frequency vibrational loads induced by aerodynamic forces during cruise, leading to minor relative displacements at the contact interface of their components. In this way, we were able to conclude a series of these tests. This endeavor allowed us to test the limits of this novel approach to predicting fretting fatigue life through models based on neural networks.

Subsequently, the conclusions and future works are presented. More specifically, one has:

- **Chapter 1:** A general scope is given, followed by a review of the main research progress in the field of fretting fatigue along with the neural network approach.
- **Chapter 2:** A review of the main theories and methodologies used in the thesis is conducted, relating to the topic of fretting fatigue. Basic concepts in contact mechanics, fracture mechanics, multiaxial fatigue, machine learning models, among many others, are addressed here.
- **Chapter 3:** The initial research results are presented in this chapter, highlighting the creation of an neural network based model that considers analytical equivalent stresses calculated at the critical plane and in the material critical distance.
- **Chapter 4:** This chapter deepens the previously proposed methodology for various aerospace alloys. This time, numerical models are used to compute equivalent stresses, serving as inputs for a new and robust ANN-based model. Addressing cylindrical and spherical pad contacts, this chapter emphasizes the significant generalization power of these ANN-based models.
- **Chapter 5:** A new methodology inspired by the previous approaches to address the phenomenon of fatigue in overhead conductors is discussed here.
- **Chapter 6:** This chapter addresses the application of the created methodology for less

common and more complex loadings, such as those involving variable shear loading amplitude and high temperature. Additionally, the results of new fretting fatigue experiments involving complex variable amplitude loading for the aerospace aluminum alloy 7075-T651 are presented.

- **Chapter 7:** The main conclusions obtained are highlighted in this chapter, and suggestions for future work are also addressed

## Chapter 2

# Research Methods & Theory

*"In this chapter, the theoretical foundation of the study is addressed, delineating key concepts and methodologies pertinent to the topic."*

Some parts of the text in this chapter was previously published as:

BRITO OLIVEIRA, Giorgio André; FREIRE JÚNIOR, Raimundo Carlos Silverio; VELOSO, Luís Augusto Conte Mendes; ARAÚJO, José Alexander. A hybrid ANN-multiaxial fatigue nonlocal model to estimate fretting fatigue life for aeronautical Al alloys. *International Journal of Fatigue*, v. 162, p. 107011, 2022. DOI: 10.1016/j.ijfatigue.2022.107011.

BRITO OLIVEIRA, Giorgio André; CARDOSO, Raphael Araújo; FREIRE JÚNIOR, Raimundo Carlos Silverio; ARAÚJO, José Alexander. A generalized ANN-multiaxial fatigue nonlocal approach to compute fretting fatigue life for aeronautical Al alloys. *Tribology International*, v. 180, n. November 2022, p. 108250, 2023a. DOI: 10.1016/j.triboint.2023.108250.

To ensure adherence to standard nomenclature, some symbols were adjusted from the original publication. Moreover, specific paragraphs were slightly modified to eliminate redundancy.

## 2.1 FRETTING FATIGUE

As introduced in the earlier chapter, fretting fatigue takes place when contacting parts experience both small amplitude relative slip and fatigue loads. In this case, contact loads are responsible for generating strong stress gradients near contacting surfaces, as well as induce multiaxial and nonproportional stress states, which might lead to early crack initiation. Such initiated cracks, in the presence of bulk fatigue loads, might propagate rapidly leading to catastrophic failures.

Both the fields of fatigue and fretting are inherently broad, and it is beyond the scope of this work to delve into all the intricacies of these subjects. Solely a brief fatigue history review will be covered since fatigue is the main area of this work. Therefore, our focus will be directed toward more specific topics, such as multiaxial fatigue and contact mechanics, as they form the basis for the comprehending fretting fatigue life prediction. In this setting, this section encompasses various theoretical, experimental, and numerical approaches related to the phenomenon of fretting fatigue. These approaches will serve as the foundation for the development of novel methodologies for predicting fretting fatigue life, as elaborated in the following chapters.

### 2.1.1 Understanding material fatigue

Fatigue is a complex and recurring phenomenon observed in numerous structures and materials, playing a pivotal role in the field of engineering and materials science. Its impact extends significantly not only on mechanical components but also across various sectors, ranging from aerospace industries to biomedical devices. The comprehension of fatigue as a phenomenon traces back several centuries, initially through empirical observations and documented incidents, providing initial clues to its existence. However, systematic studies began to emerge only towards the late 19th century. The initial milestone in fatigue investigation dates back to the period of the Industrial Revolution, when structural failures in metallic components, particularly in railways and machinery, began to draw the attention of engineers. This era was marked by significant incidents such as the collapse of the Broughton Bridge in 1831, prompting subsequent inquiry commissions aiming to comprehend the causes behind these catastrophic failures. In this context, Julius Albert (1837) designed a test machine for the conveyor chains

that had experienced failures while in service at the Clausthal mines, in Germany. He was known for publishing the first fatigue-test results in history.

In his remarkable review, Walter Schütz discusses the advancements in the field of fatigue up to the end of the 20th century (SCHÜTZ, 1996). The author prominently highlights the work of Wöhler, Thum, and Gassner for their invaluable contributions to the field. August Wöhler, often referred to as the father of fatigue, developed a method for testing the fatigue of materials in the laboratory. His method, known as the "Wöhler curve", is still used today to estimate the service life of components subjected to repeated loads. It's worth noting that his successor, Spangenberg (SPANGENBERG, 1875; SPANGENBERG, 1879), is credited with being the first to plot stress-life curves, as Wöhler had only presented results in tables (SCHÜTZ, 1996). The final form of these well-known S-N curves, or Wöhler curves, used today, was introduced in 1910 by Basquin (BASQUIN, 1910). This representation, which includes a logarithmic scale, can be described by the formula in Eq. 2.1. Wöhler's work inspired several great exponents of fatigue, such as Gerber (1874), Goodman (1899), Smith (1908, 1910), Moore (1921), Haigh (1912, 1915) and many others. Gassner (1939) was noted for his pioneering work in the analysis of variable amplitude fatigue, among numerous other contributions (GAßNER, 1937; GAßNER, 1942). Additionally, Thum, who published over 500 papers between 1922 and 1956, made significant contributions in various fatigue-related domains, including size effect (1938), drive shafts (1938), flame-hardening (1939), fatigue strength (1937), and shot-peening (1935).

$$\sigma_a = A_n N_f^{b_n} \quad (2.1)$$

Significant progress in understanding fatigue occurred during the 20th century, notably after the World War II. The technological race and the development of complex aircraft, ships, and structures intensified the need to comprehend and predict material fatigue under dynamic loads. This era witnessed the establishment of standardized testing methodologies, such as the Wöhler's rotary bending tests, and the emergence of fundamental theories, including the Fatigue Crack Propagation (Paris's law) and the Power Spectral Density (PSD analysis), revolutionizing the understanding and treatment of fatigue. It is worth noting that most of these investigations were predominantly focused on metallic materials, although there is currently a growing trend towards analyzing fatigue in various materials such as ceramics, polymers, and composites. Nonetheless, an estimated 80% of the economic expenses related to fractures and

their prevention involve situations where fatigue plays at least a contributory role (DOWLING, 2013). Campbell (2008) reported that nearly 90% of all mechanical service failures are attributable to fatigue. Hence, the understanding and continuous advancements in comprehending or minimizing these issues intersect economic matters significantly.

#### **2.1.1.1 The nature of fatigue damage**

When observed at a sufficiently small size scale, all materials exhibit anisotropic and inhomogeneous characteristics. For instance, engineering metals are comprised of an aggregate of small crystal grains. Inhomogeneities arise not only due to the grain structure but also owing to tiny voids or particles of different chemical compositions compared to the material's one. Consequently, as a result of such non-uniform microstructures, stresses are irregularly distributed at this size scale. In this setting, the specific behaviors at this level vary widely among different materials due to their distinct mechanical properties and microstructures.

In the case of ductile engineering metals, the material in focus of this work, crystal grains with unfavorable orientations relative to the applied stress initially develop slip bands (regions with intense deformation resulting from the shear motion between crystal planes). Under fatigue loading, additional slip bands emerge as more cycles are applied. The number of these bands may increase to the extent that the rate of formation slows down, eventually approaching a saturation level. Individual slip bands become more pronounced, and some evolve into cracks within grains, propagating into other grains and eventually merging with similar cracks, resulting in the creation of a larger crack. This initial stage is recognized as Stage I (crack initiation). As the crack length grows significantly, the crack starts propagating perpendicular to the principal stress, marking the transition to Stage II (crack propagation). In fatigue, the term 'material endurance limit' is also commonly employed. The endurance limit is defined as the stress amplitude below which microcracks can initiate but do not propagate to failure. When the cracks are sufficiently 'short', the endurance limit remains independent of the crack size, a concept known as the 'short crack' regime (KITAGAWA; TAKAHASHI, 1976). However, beyond a certain size, the endurance limit decreases as the crack grows, marking the onset of the so-called 'long crack' regime. The fatigue cracks is typically originate at free surfaces, predominantly external surfaces. Nevertheless, initiation can also occur at sub-surface locati-

ons in the presence of defects such as voids and inclusions. Common surface defects include geometric notches and surface roughness.

Material fatigue is characterized by the initiation, combination, and stable progression of these cracks that culminate in the yielding of the net section or material fracture. Hence, fatigue can be understood as the weakening of a material due to repetitive application of loads. In this way, it can be said that the nature of fatigue damage depends on several factors, including the frequency of applied loads, material properties, stress concentration, load amplitude, load ratio, and many others, which will be discussed in the next subsection. This phenomenon is commonly divided into two main categories: Low Cycle Fatigue (LCF) and High Cycle Fatigue (HCF). In LCF, components endure high loads that introduce substantial plastic deformation and have a limited service life. Conversely, in HCF, loads are sufficiently low to predominantly result in elastic deformation, enabling significantly longer lives, typically exceeding  $10^5$  cycles.

### 2.1.1.2 Factors influencing the fretting fatigue phenomenon

Fretting fatigue represents a special case of fatigue that combines the effects of bulk fatigue loading with the inherent challenges of fretting. Figure 2.1 illustrates some factors to consider for both fatigue and fretting phenomena. These factors rely on the specific context of the analysis, the material type under consideration, environmental conditions including temperature control, loading constraints, and other relevant parameters. Microstructural aspects of the material are also pivotal in altering its fatigue response. In metals, the resistance to fatigue is generally improved by minimizing the size of inclusions and voids, employing a smaller grain size, and producing a dense network of dislocations. However, achieving enhancements based on microstructure alone might not be viable if it significantly compromises the material's ductility - its ability to deform under stress without fracturing (DOWLING, 2013). Another influential factor is the presence of internal stresses or residual stresses, which mimic the effect of applied mean stress. Dobromirski (2009) identified fifty different variables that could influence the material response under fretting conditions. Regarding the experimental test procedures, Abbasi et al. (2020) highlighted the necessity of developing a new test rig equipped with sophisticated measuring instruments. They suggested that more comprehensive and realistic discussions could be provided by measuring the extent of oxide debris, exposure time to oxygen, contact

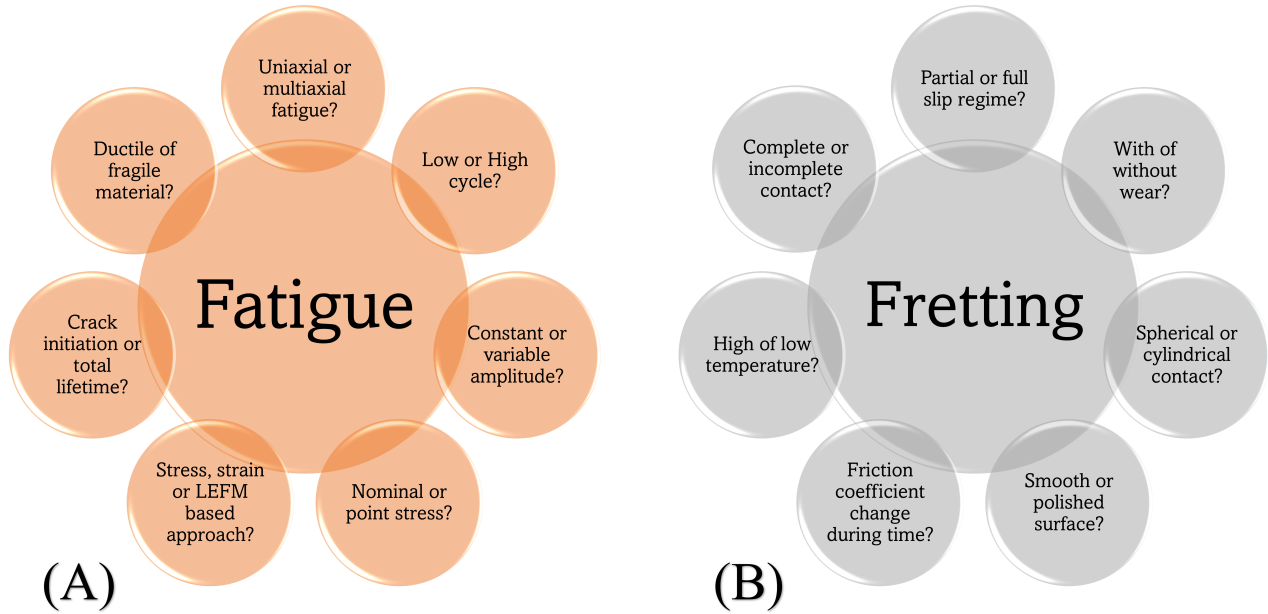


**Figure 2.1.** Some factors to consider when analysing (A) fatigue and (B) fretting.

interface temperature rise, wear rate, slip amplitude, and possible changes in the coefficient of friction. It was pointed out that any new parameter attempting to predict fretting fatigue under cyclic loading must incorporate the concept of damage accumulation over the contact region. This includes considering load interactions, wear and debris effects, frequency, and changes in the friction coefficient during cycling.

Since the mean stress effect plays a critical role in fatigue, extensive studies, as detailed by Goodman (1899), have highlighted that the presence of mean tensile stress tends to reduce the fatigue limit of materials, whereas compressive stress can increase it. This phenomenon occurs due to tensile loads tending to propagate pre-existing cracks while compressive loads tend to inhibit their growth. To address this, various models such as Soderberg, Morrow, Gerber and Walker have been proposed (DOWLING, 2013). In the context of fretting fatigue, characterized by multiaxial stress states, some researchers have proposed more intricate methodologies. For example, Araújo and Castro (2012), along with Vantadori *et al.* (2020), examined the impact of mean stress on the fretting fatigue of the 7050-T7451 aluminum alloy, utilizing the  $\Delta K$ -based short crack arrest models and the Carpinteri criterion (CARPINTERI *et al.*, 2019), respectively. Rossino *et al.* (2009) also conducted several tests investigating the mean stress effect. In their work, they considered a non-local stress-based methodology combined with a critical plane model as an alternative to evaluate the mean stress effect in fretting fatigue, but noted that

crack arrest-based models were more effective. Almeida *et al.* (2020) also investigated the behavior of the material 7050-T7451 under the influence of mean stress, particularly in fretting conditions. Their results indicated that the bulk mean stress does not have a considerable effect on altering the crack initiation angle.

In fretting fatigue, the general trend often shows a decrease in fatigue life as the slip amplitude increases up to a certain threshold value (typically 50  $\mu\text{m}$ ), followed by an increase again (VINGSBO; SÖDERBERG, 1988). One explanation for this phenomenon is that the wear debris itself forms a solid lubricant layer, thereby reducing stresses (WATERHOUSE, 1992). Size effects have also been explored in fretting fatigue literature, as a factor directly affecting the component's life (ARAÚJO; NOWELL, 2002; CARDOSO *et al.*, 2019). Finally, another notable aspect in the study of fretting fatigue is the non-local approach, attributed to the presence of stress gradients, which has been widely adopted in the literature (ARAÚJO *et al.*, 2017; WANG *et al.*, 2023a; ALMEIDA *et al.*, 2023; GLODEK *et al.*, 2023). This approach will be discussed in details in subsection 2.1.4.2. Due to all these variables, the response to fretting fatigue tends to exhibit a reasonable degree of statistical scatter. This scattering is attributed mainly due to variations in material properties between samples, differences in internal defect sizes, surface roughness, and the challenge of controlling test variables, such as humidity and specimen alignment.

## 2.1.2 Miner cumulative damage model

When dealing with variable loading in stress history, it is common to employ damage accumulation models to address this challenge. In this thesis, due to its simplicity and strong relevance to fretting fatigue problems (PINTO *et al.*, 2020; PINTO *et al.*, 2023; MATOS *et al.*, 2023) the Miner damage rule, also recognized as the Palmgren-Miner model, is adopted. Miner (1945) gained prominence for popularizing a linear cumulative damage rule that was initially proposed independently by Palmgren in 1924. This model specifies that, under  $n$  different stress states levels, fatigue failure occurs when:

$$\sum_{i=1}^n \frac{\Delta N_i}{N_{f,i}} = 1 \quad (2.2)$$

where  $\Delta N_i$  is the number of cycles applied at a given stress level  $\sigma_{a,i}$  and  $N_{f,i}$  is the number of cycles to failure at the same stress level.

In real-world applications, mechanical components experience intricate, occasionally random sequences of loads. Techniques like the rainflow counting method (MATSUISHI; ENDO, 1968) simplify these complex loading histories into a series of simple cyclic loadings. Subsequently, Miner’s rule can be applied for each stress level.

### 2.1.3 Multiaxial fatigue approaches

As it is well known, the nature of the stress field in the fretting fatigue problem is multiaxial. Besides, in most engineering applications, multiaxial stress states are more likely to occur. In this systems, steady applied loads that induce mean stresses may coincide with continuous cyclic loads. Adding complexity, distinct sources of cyclic loading might exhibit variations in phase, frequency, or even both. To tackle this problem, the fundamental concept behind multiaxial fatigue criteria is to utilize data obtained from simplified laboratory tests to design against more complex and multiaxial stress conditions. Currently, five distinct approaches can be classified for addressing the challenge of multiaxial fatigue: models based on critical plane analysis (FINDLEY *et al.*, 1956; SMITH *et al.*, 1970; FATEMI; SOCIE, 1988; MCDIARMID, 1991; SUSMEL; LAZZARIN, 2002), stress invariant methods (SINES, 1955; CROSSLAND, 1956), specific fretting parameters (RUIZ *et al.*, 1984; HATTORI *et al.*, 2003; DING *et al.*, 2011), continuum damage approaches (LEMAITRE, 1985; CHABOCHE, 1988; ZHAN *et al.*, 2019; LI *et al.*, 2022), and data-driven approaches (MAJZOABI; KAZEMI, 2013; PESTANA *et al.*, 2018; NOWELL; NOWELL, 2020; GORJI *et al.*, 2022; HAN *et al.*, 2023a; WANG *et al.*, 2023b). The following subsections will delve into some multiaxial models, specifically those grounded in the theories of the critical plane and the stress invariant. These models will be also employed in the present work. Furthermore, a concise introduction outlining the process of obtaining equivalent stresses will also be provided.

#### 2.1.3.1 Stresses in any surface element

Before delving into the definition of stress parameters commonly used in multiaxial criteria, which are typically calculated at specific critical points within the mechanical component, one intend to perform some considerations regarding the Cauchy stress tensor. Consider a solid subjected to the forces as indicated in Fig. 2.2. The stress state at point  $O$  is entirely described

by the following tensor:

$$\boldsymbol{\sigma} = \begin{bmatrix} \sigma_{xx} & \tau_{xy} & \tau_{xz} \\ \tau_{xy} & \sigma_{yy} & \tau_{yz} \\ \tau_{xz} & \tau_{yz} & \sigma_{zz} \end{bmatrix} \quad (2.3)$$

where  $\sigma_x$ ,  $\sigma_y$  and  $\sigma_z$  are the normal and  $\tau_{xy}$ ,  $\tau_{xz}$  and  $\tau_{yz}$  are the shear stress components. Considering this stress tensor based in an orthonormal basis  $\{\mathbf{e}_x, \mathbf{e}_y, \mathbf{e}_z\}$  and a unit vector  $\mathbf{n}$ , such that:

$$\mathbf{n} \cdot \mathbf{e}_i > 0 \quad (2.4)$$

In 1827, the renowned mathematician, physicist and engineer Augustin-Louis Cauchy introduced his theorem, known as 'Cauchy's Theorem,' which may be succinctly delineated, considering the example in Fig. 2.2, for any solid subjected to a system of forces ( $\mathbf{f}_0$ ) in equilibrium, by the following postulates:

- For any unit vector  $\mathbf{n}$ , the stress vector is given by:

$$t(\mathbf{n}) = \boldsymbol{\sigma} \mathbf{n}, \quad t_i(\mathbf{n}) = \sigma_{ij} n_j \quad (2.5)$$

- The Cauchy stress tensor ( $\boldsymbol{\sigma}$ ) is symmetric, i.e.:

$$\boldsymbol{\sigma} = \boldsymbol{\sigma}^T, \quad \sigma_{ij} = \sigma_{ji} \quad (2.6)$$

- From the equilibrium one gets:

$$\nabla \cdot \boldsymbol{\sigma} + \mathbf{f}_0 = 0, \quad \sigma_{ij,j} + f_{0i} = 0 \quad (2.7)$$

For the sake of simplicity, one has exclusively demonstrated the equilibrium scenario in closest alignment with the scope of our study. However, it is worthy to note that these expressions also apply to the case of a moving body. One of Cauchy's fundamental implications is that if the stress vector is known on three mutually orthogonal planes or surface elements, at a specific point, it allows for the determination of the stress state on any other plane ( $\mathbf{n}$ ).

Building upon this, to determine the stress vector ( $\mathbf{t}$ ) on any inclined surface element, consider the Cauchy tetrahedron as depicted in Fig 2.3. This tetrahedron encompasses any plane characterized by the angles  $\theta$  and  $\varphi$  and defined by a normal vector ( $\mathbf{n}$ ) located at point  $O$  in Fig. 2.2. In this context, one introduces a new basis, denoted as  $\{\mathbf{e}_A, \mathbf{e}_B, \mathbf{n}\}$ , to better represent this vector. It is essential to note that this new basis is also orthonormal, with the

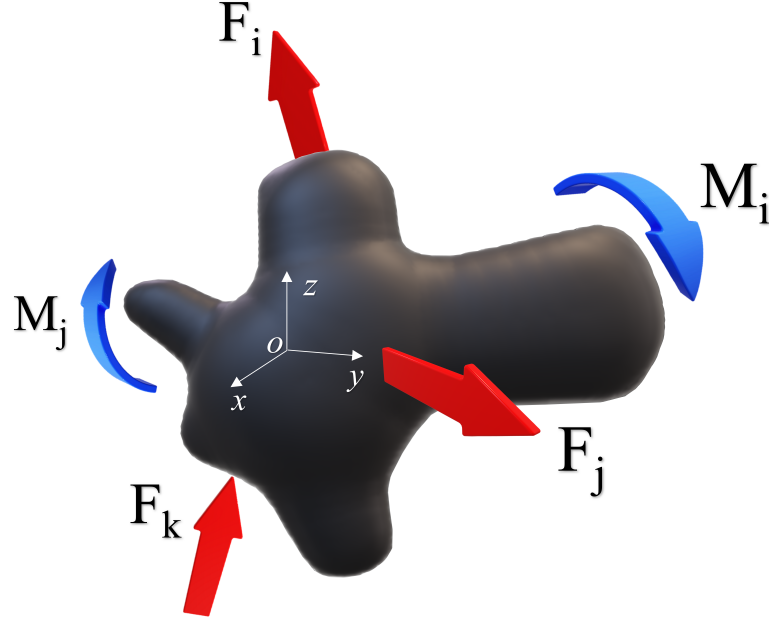


**Figure 2.2.** A body subjected to a system of external forces and a reference point.

unit vector  $\mathbf{e}_A$  aligned with the surface of the component ( $xy$ -plane), and the unit vector  $\mathbf{e}_B$  is pointed to the  $z$ -axis. Consequently, one can decompose the stress vector in terms of these angles and, in consequence, this new basis. As a result:

$$\mathbf{t}(\theta, \varphi) = \tau_A \mathbf{e}_A + \tau_B \mathbf{e}_B + \sigma_n \mathbf{n} \quad (2.8)$$

where,

$$\begin{aligned} \tau_A &= \boldsymbol{\sigma} \mathbf{n} \cdot \mathbf{e}_A, \\ \tau_B &= \boldsymbol{\sigma} \mathbf{n} \cdot \mathbf{e}_B, \\ \sigma_n &= \boldsymbol{\sigma} \mathbf{n} \cdot \mathbf{n} \end{aligned} \quad (2.9)$$

such that

$$\begin{aligned} \mathbf{e}_A &= [-\sin \theta, \cos \theta, 0]^T, \\ \mathbf{e}_B &= [-\cos \varphi \cos \theta, -\cos \varphi \sin \theta, -\sin \varphi]^T, \\ \mathbf{n} &= [\sin \varphi \cos \theta, \sin \varphi \sin \theta, \cos \varphi]^T \end{aligned} \quad (2.10)$$

It is noteworthy that the stress vector ( $\mathbf{t}$ ) can also exhibit variations in time ( $t$ ), leading to fluctuations in its components. Usually, this vector is represented by a single shear component ( $\boldsymbol{\tau}$ ) and a single normal vector component ( $\mathbf{t}_n$ ), as follows:

$$\mathbf{t} = \mathbf{t}_n + \boldsymbol{\tau} = \boldsymbol{\sigma} \mathbf{n} \quad (2.11)$$

where

$$\mathbf{t}_n = (\mathbf{n} \otimes \mathbf{n}) \mathbf{t} \quad (2.12)$$

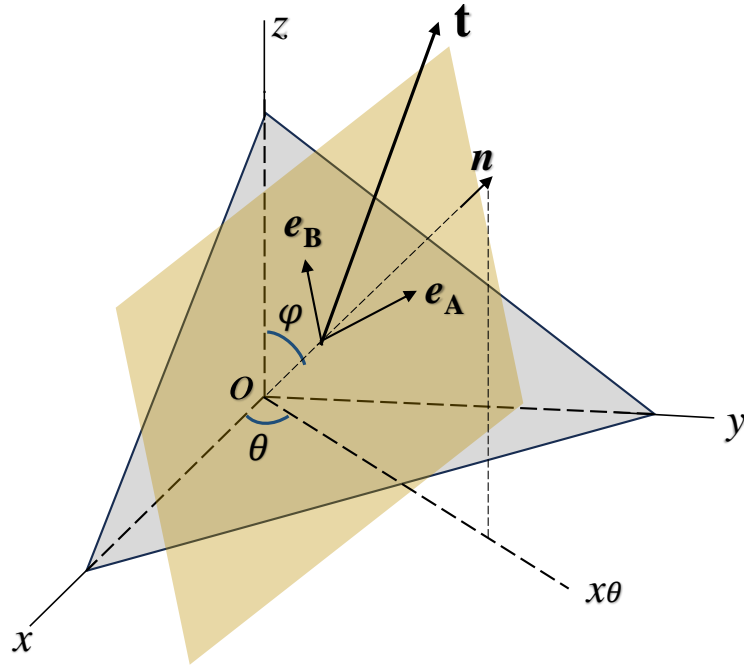


**Figure 2.3.** Stresses acting on a plane within a three-dimensional coordinate system.

$$\boldsymbol{\tau} = (\mathbf{I} - \mathbf{n} \otimes \mathbf{n})\mathbf{t} \quad (2.13)$$

where  $\mathbf{I}$  is the identity tensor and the terms  $(\mathbf{n} \otimes \mathbf{n})$  and  $(\mathbf{I} - \mathbf{n} \otimes \mathbf{n})$  transforms the stress vector ( $\mathbf{t}$ ) into the normal and shear stress vectors, respectively. Typically, in the multiaxial fatigue analysis context, scalar quantities as represented in Eq. 2.9 are often required. For instance, they are utilized in the computation of the maximum normal stress on a surface element and the maximum shear stress amplitude. One should notice that the calculation of the maximum normal stress ( $\sigma_{n,\max}$ ) is elementary (see Eq. 2.9) and defined by:

$$\sigma_{N,\max} = \max_t(\sigma_n(t)) \quad (2.14)$$

However, the shear stress amplitude ( $\tau_a$ ) is not quite straightforward, due to the shear vector history, described by  $\tau_A(t)$  and  $\tau_B(t)$  in Eq. 2.9, being able to describe a closed non-linear path ( $\Omega$ ). Various methodologies have been proposed in the literature to address this issue, including The Minimum Radius Circle (MRC) method, The Minimum F-norm Ellipse method, the Moment of Inertia (MOI) method, and the Shear Stress-Maximum Variance Method ( $\tau$ -MVM) (CASTRO *et al.*, 2009a; SUSMEL, 2010; MEGGIOLARO; CASTRO, 2015). In this thesis, one employs the methodology proposed by Araújo *et al.* (2011) which proposed the Maximum Rectangular Hull (MRH) method as a strategy to measure the amplitude of the

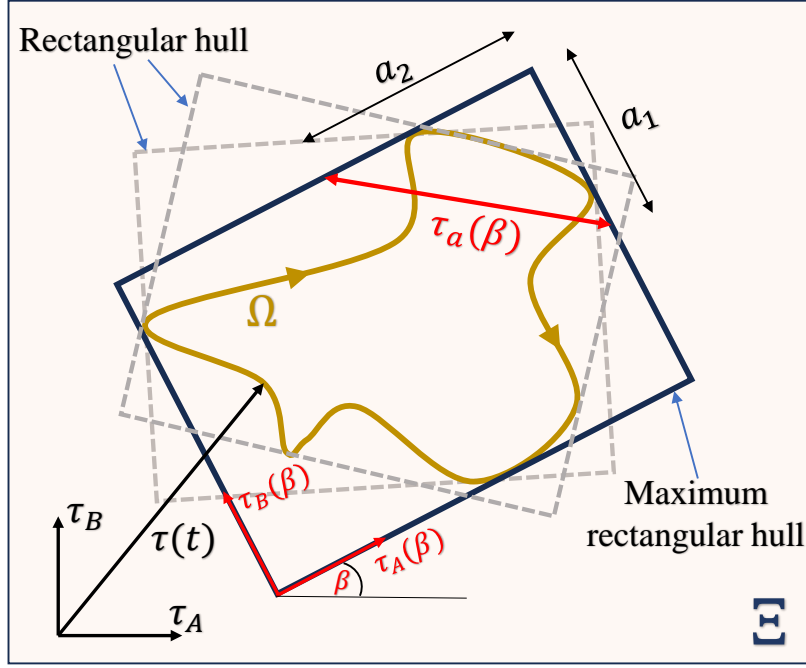


**Figure 2.4.** Maximum Rectangular Hull (MRH) method for a shear stress path  $\Omega$  in a surface element  $\Xi$ .

shear stress vector path for a given material plane ( $\Xi$ ). This method is based on finding the largest rectangular hull that circumscribes the path ( $\Omega$ ) taken by this shear stress vector in a certain Cauchy plane, as shown in Fig. 2.4. In this setting, for each  $\beta$ -oriented rectangular hull one can define its amplitude as:

$$\tau_a(\beta) = \sqrt{a_1^2(\beta) + a_2^2(\beta)} \quad (2.15)$$

such that  $a_1$  and  $a_2$  are the halves of the sides of the rectangular hull (Fig. 2.4). The equivalent maximum shear stress amplitude in this surface element is the one which maximizes Eq. 2.15, hence one gets:

$$\tau_a = \max_{\beta} \sqrt{a_1^2(\beta) + a_2^2(\beta)} \quad (2.16)$$

These equivalent stresses, among others ( $\tau_{a,med}$ ,  $\sigma_{n,a}$ ,  $S_a$ ,  $\gamma_{a,max}$ ), are commonly employed in multiaxial fatigue criteria (FINDLEY *et al.*, 1956; SMITH *et al.*, 1970; FATEMI; SOCIE, 1988; MCDIARMID, 1991; SUSMEL; LAZZARIN, 2002) for both quantitative purposes (determining fatigue life cycles) and qualitative purposes (assessing material failure under specific loading conditions).

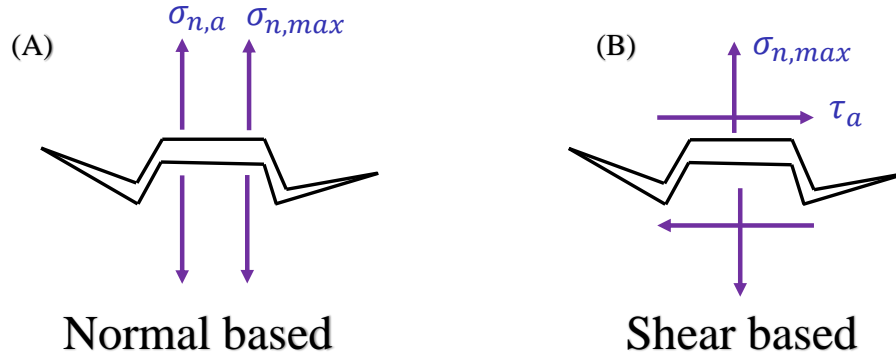


**Figure 2.5.** Basis of the physical interpretation of the SWT (A) and MWCM (B) model.

### 2.1.3.2 Smith, Watson and Topper model

The Smith, Watson and Topper (SWT) (SMITH *et al.*, 1970) criterion is a multiaxial fatigue model based on critical plane which is widely used in the FF literature (WITTKOWSKY *et al.*, 2000; LYKINS *et al.*, 2001; EKBERG, 2004; NAVARRO *et al.*, 2008; HOJJATI-TALEMI; WAHAB, 2013; O'HALLORAN *et al.*, 2016; CARDOSO *et al.*, 2019; BHATTI *et al.*, 2019; ALMEIDA *et al.*, 2020; PINTO *et al.*, 2020; RANGEL *et al.*, 2022; MATOS *et al.*, 2022; SAID *et al.*, 2023; GLODEK *et al.*, 2023). It is well-suited for materials and loading conditions where cracks propagate perpendicular to the maximum principal stress and strain direction (i.e. Mode I cracks), as shown in Fig. 2.5a. Nevertheless, it can be used for both low and high cycle fatigue and can handle non-proportional loading conditions. The classical definition for the SWT model is given by:

$$\sigma_{n,\max}\varepsilon_{n,a} = \frac{\sigma'_f}{E}(2N_f)^{2c_1} + \sigma'_f\varepsilon'_f(2N_f)^{c_1+c_2} \quad (2.17)$$

where  $\sigma_{n,\max}$  and  $\varepsilon_{n,a}$  are, respectively, the maximum normal stress and the strain amplitude on the material plane which maximizes their product. For fatigue life assessment purposes, the SWT parameter can be used in combination with Basquin and Coffin-Manson fatigue relationships as in the right-hand side of Eq. 2.17, where  $\sigma'_f$  and  $\varepsilon'_f$  are, respectively, the fatigue strength and ductility coefficients of the material, whereas  $c_1$  and  $c_2$  are their corresponding exponents. As long as plastic strains are negligible, the SWT parameter ( $I_{SWT}$ ) can be determined solely based on stress parameters, as will be accounted for in this thesis, and can be expressed in terms of the fatigue life as shown in the Eq. 2.18:

$$I_{SWT} = \sqrt{\sigma_{n,\max}\sigma_{n,a}} = A_{swt}N_f^{b_{swt}} \quad (2.18)$$

where  $\sigma_{n,a}$  is the normal stress amplitude on the critical plane which is defined as the material plane that maximizes the square root in Eq. 2.18. The constants  $A_{swt}$  and  $b_{swt}$  can be determined using a calibration process based on experimental fatigue tests, where  $N_f$  stands for the fatigue life.

### 2.1.3.3 The Modified Wöhler Curve Method

The Modified Wöhler Curve Method (MWCM) is a multiaxial fatigue model also based on the critical plane approach. This model has been extensively investigated over the past two decades within the context of fretting fatigue (ARAÚJO *et al.*, 2008; ROSSINO *et al.*, 2009; ARAÚJO *et al.*, 2011; FOUVRY *et al.*, 2014; FERRY *et al.*, 2017; KOUANGA *et al.*, 2018; GAILLIEGUE *et al.*, 2020; KOUANGA *et al.*, 2023). It postulates that cracks initiate at material planes where the maximum shear stress amplitude,  $\tau_{a,max}$ , is achieved (SUSMEL; LAZZARIN, 2002). In this case, if more than one plane present values close to maximum  $\tau_a$  (i.e., 1% tolerance), the critical plane is defined as the one which yields the maximum normal stress ( $\sigma_{N,max}$ ). Figure 2.5b illustrates the situation where material failure occurs based on the MWCM postulates, i.e. based in shear mode. Furthermore, as shown in Fig. 2.5b, this model acknowledges the crucial role, during the fatigue crack opening, of the maximum value of the stress component perpendicular to the crack initiation plane,  $\sigma_{n,max}$ . Regarding this plane, the MWCM considers the stress ratio parameter ( $\rho = \sigma_{n,max}/\tau_a$ ) which accounts the influence of the mean stress effect. Hence, for a generic stress ratio,  $\rho$ , the fatigue life ( $N_f$ ) can be estimated according to the following equation:

$$N_f = N_{ref} \left( \frac{\tau_{a,ref}}{\tau_a} \right)^{\kappa_\tau(\rho)} \quad (2.19)$$

Such that  $\tau_{a,ref}$  is the shear stress amplitude for a reference number of cycles,  $N_{ref}$ , and  $\kappa_\tau$  is the negative inverse slope of the curve  $\tau_a$  vs.  $N_f$  in a log-log diagram. Bear in mind that both terms  $\tau_{a,ref}$  and  $\kappa_\tau$  are dependent on  $\rho$ . These relationships can be obtained through a straightforward linear interpolation of two datasets, each holding the values of  $\tau_a$  vs.  $N_f$ , for different values of  $\rho$ .

### 2.1.3.4 The Crossland criterion

The Crossland invariant multiaxial fatigue model (CROSSLAND, 1956) can be used to forecast a material's fatigue life under complex loading conditions, also, it has already been thoroughly covered in FF literature (FOUVRY *et al.*, 2014; MAMIYA; ARAÚJO, 2002; POOVAKAUD *et al.*, 2020). The Crossland equation can be expressed in terms of the amplitude of the deviatoric stress tensor ( $S_a$ ) and the maximum hydrostatic stress ( $\sigma_{H,max}$ ) as shown in Eq. 2.20 (CASTRO *et al.*, 2009a; PAPADOPOULOS *et al.*, 1997):

$$\frac{S_a}{\sqrt{2}} + \kappa(N_f)\sigma_{H,max} = \lambda(N_f) \quad (2.20)$$

Such that  $\kappa(N_f)$  and  $\lambda(N_f)$  here are considered as functions of the fatigue life, that can be computed through a process of calibration which is based on two uniaxial fatigue tests with different load ratios ( $R_\sigma$ ). For instance, for load ratios ( $R_\sigma$ ) values of -1 and 0, these functions can be expressed as follows:

$$\kappa(N_f) = \frac{\sqrt{3}(A_1 N_f^{b_1} - A_2 N_f^{b_2})}{2A_2 N_f^{b_2} - A_1 N_f^{b_1}} \quad (2.21)$$

$$\lambda(N_f) = \frac{A_1 N_f^{b_1} A_2 N_f^{b_2}}{\sqrt{3}(2A_2 N_f^{b_2} - A_1 N_f^{b_1})} \quad (2.22)$$

where the constants  $A_1$  and  $b_1$  are the coefficients for the Wöhler curve with  $R_\sigma = -1$ , and  $A_2$  and  $b_2$  for the one with  $R_\sigma = 0$ .

To measure the  $S_a$  one considers the definition proposed by Mamiya *et al.* (2009) which is based on the largest prismatic hull enclosing the deviatoric stress path, also called maximum prismatic hull (MPH). In this framework, one proposed the following orthonormal basis (Eq. 2.23) in order to represent the penta-dimensional deviatoric space:

$$\begin{aligned} \mathbf{b}_1 &= \frac{1}{\sqrt{2}}(\mathbf{e}_x \otimes \mathbf{e}_x - \mathbf{e}_z \otimes \mathbf{e}_z) \\ \mathbf{b}_2 &= \frac{2}{\sqrt{6}} \left( -\frac{1}{2}(\mathbf{e}_x \otimes \mathbf{e}_x) - \frac{1}{2}(\mathbf{e}_z \otimes \mathbf{e}_z) \right) \\ \mathbf{b}_3 &= \frac{1}{\sqrt{2}}(\mathbf{e}_x \otimes \mathbf{e}_x - \mathbf{e}_y \otimes \mathbf{e}_y) \\ \mathbf{b}_4 &= \frac{1}{\sqrt{2}}(\mathbf{e}_x \otimes \mathbf{e}_z - \mathbf{e}_z \otimes \mathbf{e}_x) \\ \mathbf{b}_5 &= \frac{1}{\sqrt{2}}(\mathbf{e}_y \otimes \mathbf{e}_z - \mathbf{e}_z \otimes \mathbf{e}_y) \end{aligned} \quad (2.23)$$

where  $\otimes$  denotes the tensor product between the elements of the canonical basis ( $\mathbf{e}_x, \mathbf{e}_y, \mathbf{e}_z$ ). Based on this, the deviatoric stress tensor can be represented by a linear combination of these elements:

$$\mathbf{S} = \sum_{i=1}^5 S_i \mathbf{b}_i \quad (2.24)$$

Thus, the components ( $S_i$ ) are given in function of the time dependent stress tensor components ( $\sigma_{ij}(t)$ ):

$$\begin{aligned} S_1 &= \frac{1}{\sqrt{2}}(\sigma_{xx} - \sigma_{zz}), \\ S_2 &= \frac{1}{\sqrt{6}}(2\sigma_{yy} - \sigma_{xx} - \sigma_{zz}), \\ S_3 &= \sqrt{2}\tau_{xy}, \\ S_4 &= \sqrt{2}\tau_{xz}, \\ S_5 &= \sqrt{2}\tau_{yz}. \end{aligned} \quad (2.25)$$

Thence, let the half-sides of a prismatic hull whose axes are parallel to an inclined ( $\vartheta$ ) orthonormal basis be defined by:

$$a_i(\vartheta) = \frac{1}{2} (\max S_i(\vartheta) - \min S_i(\vartheta)), \quad i = 1 : 5 \quad (2.26)$$

where  $S_i$  (Eq. 2.26) represents the  $i$ th deviatoric stress component (Eq. 2.25) in this basis (Eq. 2.23). Therefore, based on MPH, the amplitude of the deviatoric stress tensor ( $S_a$ ) is defined as the greatest quantity among all potential orientations,  $\vartheta$ , as follows in Eq. 2.27 (MAMIYA *et al.*, 2014):

$$S_a = \max_{\vartheta} \sqrt{\sum_{i=1}^5 a_i^2(\vartheta)} \quad (2.27)$$

#### 2.1.4 Basics of Fracture Mechanics

Fracture Mechanics is a branch of engineering and materials science that investigates the behavior of materials under conditions of failure and rupture. It analyzes factors such as stress, deformation, and crack propagation to comprehend and predict structural failure, providing insights crucial for the advancement of mechanical engineering. The genesis of fracture mechanics as an engineering discipline stems from the Liberty ships during World War II, where an all-welded hull design revealed critical cracks in over 400 of the 2700 ships. In 1913, Inglis laid the groundwork for quantifying crack effects with a stress analysis of an elliptical hole in an

infinite linear elastic plate. Griffith's subsequent work in 1921 on cracked glass spheres showed the applicability of elastic analysis to describe crack propagation. George Irwin, often hailed as the "father of fracture mechanics," formalized the field in 1957 by introducing the equivalence of crack-tip stress fields and energy release parameters, establishing a foundational approach for characterizing fracture behavior (INGLIS, 1913; GRIFFITH, 1921; IRWIN, 1958).

There are some fundamental concepts necessitate exploration herein, commencing with the examination of fracture modes. Crack propagation occurs through three modes, as classified by Irwin (1958). Mode I, associated with traction loading, represents crack opening and is the most prevalent in typical propagation issues. Mode II, characterized by sliding due to shear in the propagation plane, is less common. Mode III, known as the tearing mode, results from shearing outside the propagation plane. Mode I is linked to traction, while modes II and III involve shearing. In this setting, mixed-mode scenarios often occur, combining these modes. In linear elastic problems, stress superposition holds, allowing additive expression of individual contributions to a given stress component (Eq. 2.28), as follows:

$$\sigma_{ij} = \sigma_{ij}^I + \sigma_{ij}^{II} + \sigma_{ij}^{III} \quad (2.28)$$

In relation to fatigue, the focus of Linear Elastic Fracture Mechanics (LEFM) is to study the calculation of crack propagation life ( $N_{f,p}$ ). It is well-known that due to repetitive stresses, cracks can initiate within an initially virgin component when subjected to cyclic or random loading. LEFM studies show that a crack can slowly grow over thousands or millions of loading cycles until it reaches a critical length and enters an unstable propagation phase, ultimately leading to component failure. The models mentioned in the previous section apply to the initiation crack phase, i.e., they examine the time required for crack nucleation or how many cycles a material can withstand under specific loading conditions before crack initiation occurs. Specifically, in classical fretting fatigue experiments, various authors have asserted that the initiation life ( $N_{f,i}$ ) is very close to the total life ( $N_{f,t}$ ) (SZOLWINSKI; FARRIS, 1998; NOWELL *et al.*, 2006). Therefore, applying these models to the calculation of the total fretting fatigue life is well-supported in the literature (ARAÚJO; NOWELL, 2002; VALLELLANO *et al.*, 2004; FERJAOUI *et al.*, 2015; INFANTE-GARCÍA *et al.*, 2022; LIU; YUAN, 2023). Equation 2.29 illustrates the relationship between these lifetimes ( $N_{f,t}$ ,  $N_{f,i}$ , and  $N_{f,p}$ ).

$$N_{f,t} = N_{f,i} + N_{f,p} \quad (2.29)$$

Another fundamental concept is the stress intensity factor,  $K$ , measuring the severity of the stress field at a crack tip. According to LEFM, Irwin (1958) investigated the distance ‘ $r_K$ ’ from the crack tip. The derived relation, expressed as Eq. 2.30 in terms of  $K$ , is applicable primarily near the crack tip, where the singularity  $1/\sqrt{r_K}$  dominates the stress field. Stresses farther from the crack tip are governed by remote boundary conditions.

$$\sigma = \frac{K}{\sqrt{2\pi r_K}} \quad (2.30)$$

Based on fracture mechanics principles, the concept of critical distance has originated from the studies conducted by Peterson (1959) and Neuber (1936) on the fatigue strength reduction factor in notched bodies. They postulated that the effective stress governing the behavior at the notched tip should be an average of the stress distribution around the stress concentration. Subsequently, Tanaka (1983) demonstrated that a similar theory could be extended to sharp cracks. In this case, the length of the line over which stresses must be averaged could be calculated to be twice the material constant ‘ $a_{K,0}$ ’, as proposed by El Haddad *et al.* (1980). This theory, further developed by Taylor (1999) using LEFM foundation, will be elucidated in subsection 2.1.4.2.

#### 2.1.4.1 Paris’s law

In his experimental design, around 1961, Paris employed two identical plates composed of the same material, each adorned with a centrally positioned crack of uniform length (PARIS; ERDOGAN, 1963). The analysis shows the correlation between crack length and the stress intensity factor,  $\Delta K$ , allowing for the association of crack growth with  $\Delta K$ . He systematically investigated several alloys, discovering that when plotting the crack growth rate against a variety of stress intensity factors, the resulting data exhibited linear relationships when presented on logarithmic scales (Fig. 2.6).

When plotting the curve of  $da_K/dN$  versus  $\Delta K$  in logarithmic form (Fig. 2.6), a graph displaying three distinct phases emerges. In Phase I, where  $\Delta K$  is below the threshold stress intensity factor,  $\Delta K_{th}$ , the crack growth rate is so slow that the crack is often assumed to

be dormant or growing at an imperceptible rate, typically defined by a growth rate of  $10^{10}$  mm/cycle. Phase II constitutes the most extensive region, ranging between growth rates of  $10^{10} \sim 10^9$  to  $10^6 \sim 10^4$  mm/cycle. During this stage, crack growth is relatively continuous along its front, evident in streaks on the crack faces observable through scanning electron microscopes. At this point, propagation is less sensitive to microstructure, medium load, environmental factors, and the thickness of the part. The impact of the stress ratio  $R_\sigma$  on the growth rate is analogous the effects observed in S-N curves for varying values of  $R_\sigma$  or mean stress. With a constant  $\Delta K$ , an increase in  $R_\sigma$  corresponds to an elevation in the growth rate, and conversely, a decrease in  $R_\sigma$  results in a deceleration of the growth rate (DOWLING, 2013).

However, when the load surpasses the fracture toughness, the growth rate becomes unstable, potentially leading to abrupt failure, as demonstrated in Phase III. This phase is notably influenced by the average load and factors impacting the material's toughness, including microstructure, environmental conditions, and component thickness. In this way, there has been several recognized empirical models which were employed to characterize crack propagation rates, utilizing parameters derived from experimental data. These models provide partial descriptions of the  $da_K/dN$  vs  $\Delta K$  curve, incorporating considerations such as  $\Delta K_{th}$ ,  $K_c$ , and the ratio between the maximum and minimum stress intensity factors. Among these models, the Paris model or Paris's law (Eq. 2.31), developed by Paris and Erdogan (1963), stands out as the most classic:

$$\frac{da_K}{dN} = C (\Delta K)^m \quad (2.31)$$

Here,  $a_K$ , represents the crack length,  $N$  is the number of load cycles,  $m$  and  $C$  are material constants, and  $\Delta K_{th}$  is the threshold stress intensity factor range. It is essential to note that this law, referred to as the Paris regime, is applicable solely in the mid-growth rate regime and does not account for the influence of loading rate, as illustrated in Fig. 2.6.

#### 2.1.4.2 The theory of critical distances

It is well-known that hot-spot approaches are not suitable for problems involving strong stress gradients as it is the case for notches, cracks and contact problems. For such cases, Taylor (1999) proposed the Theory of Critical Distances (TCD), where he assumes that the

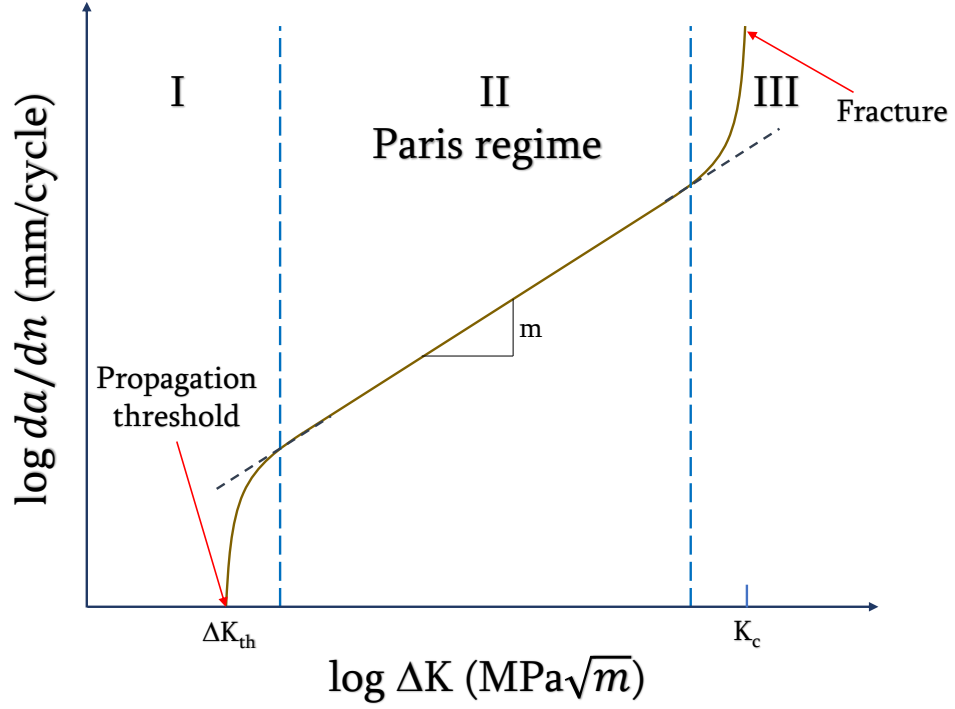


**Figure 2.6.** Scheme of the  $da/dN$  vs  $\Delta K$  in log-log diagram.

fatigue process zone is material dependent, however, it is not influenced by the geometry nor the stress state experienced by the mechanical component. In other words, the TCD relies on the determination of an effective stress near the stress raiser, which might be obtained by averaging stresses/strains over a specified volume, area or even a point. This theory has been widely applied and accepted in the literature for several cases (ARAÚJO *et al.*, 2008; CASTRO *et al.*, 2009b; FOUVRY *et al.*, 2014; FERRY *et al.*, 2017; ARAÚJO *et al.*, 2017; ZABALA *et al.*, 2020; INFANTE-GARCIA *et al.*, 2022; PINTO *et al.*, 2022b; GLODEK *et al.*, 2023; KOUANGA *et al.*, 2023; MATOS *et al.*, 2023; ALMEIDA *et al.*, 2023). In this work, one considers the TCD by means of the Point Method, where stresses/strains considered for the assessment of fatigue damage are obtained at a distance  $L/2$  from the contact trailing edge (hot-spot), where  $L$  is a material parameter given by (TAYLOR, 1999):

$$L = \frac{1}{\pi} \left( \frac{\Delta K_{th}}{\Delta \sigma_{-1}} \right)^2 \quad (2.32)$$

where  $\Delta \sigma_{-1}$  is the uniaxial fatigue limit range. Such that  $\Delta K_{th}$  and  $\Delta \sigma_{-1}$  are related to the same load ratio, in this case,  $R_\sigma = -1$ .

A notable advantage of the TCD method is its compatibility with various multiaxial fatigue

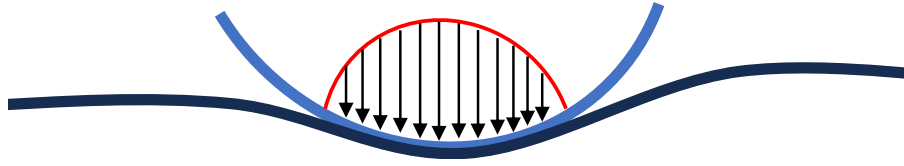


**Figure 2.7.** Example of a incomplete contact.

criteria. Susmel (2004) applied structural volume concepts combined with the modified Wöhler curve method (MWCM) to address stress concentration phenomena and the multiaxial stress field, enabling the computation of fatigue limits for both plain and notched components. Araújo *et al.* (2007) demonstrated that this combination yields more accurate predictions compared to the classical hot-spot approach using the Dang Van mesoscopic criterion (DANG-VAN *et al.*, 1982), especially when predicting fretting fatigue strength. Nevertheless, studies have introduced a novel perspective, proposing that the critical distance parameter (Eq. 2.32) may exhibit variation depending on the number of cycles ( $N_f$ ) (SUSMEL; TAYLOR, 2007; SUSMEL; TAYLOR, 2008). Some authors (CASTRO *et al.*, 2009b) have also demonstrated that the critical distance depends on the multiaxial fatigue criterion. In recent studies, the critical distance dependent on the cycles to failure has gained significance in the fretting fatigue context. This interactive approach is often integrated with some multiaxial fatigue life prediction model (ARAÚJO *et al.*, 2017; ADRIANO *et al.*, 2018; PINTO *et al.*, 2022b; RANGEL *et al.*, 2022).

### 2.1.5 Mechanics of elastic contacts

Contact mechanics constitutes a distinct branch within solid mechanics, with a primary focus on investigating the mechanical interactions and deformations between bodies engaged in physical contact. This section of the thesis will specifically explore two contact configurations: cylindrical-on-plane and spherical-on-plane contacts. These configurations are categorized as incomplete contacts due to their characteristic of continuous pressure reduction towards the contact edges (see Fig. 2.7). Examples of such contacts are commonly observed in railway wheels, rolling element bearings, gears and blade/disk joints of turbines.

In formulating the elasticity problem, it is often appropriate to consider the body as semi-infinite, a simplification that greatly aids in calculations. When the size of the contact patch is significantly smaller than the radius of curvature of the bodies' surfaces, the use of the half-

plane or half-space approximation is applicable, and these problems are termed non-conformal (HILLS *et al.*, 1993). Consequently, this section will delve into analytical formulations related to cylindrical and spherical contacts, considering these assumptions. These mathematical equations are the basis for the stress field computation under fretting fatigue.

The primary approach towards obtaining a solution for the stress distribution within the contact region is to address the contact problem itself, which involves determining the magnitude and spatial distribution of stresses on the contact surface. This can be achieved by employing two integral equations that establish the relationship between the pressure distribution,  $p(x)$ , and the normal displacement,  $h(x)$ , as well as the shear traction,  $q(x)$ , and the relative tangential displacement,  $g(x)$ . The formulation of the contact problem has been extensively explained by Hills and Nowell (1994), while the specific integral equations are provided below. For additional insights into this analysis, refer Johnson (1985). The integrals for two similarly elastic bodies, where  $A$  is considered as the composite compliance, are presented as follows:

$$\frac{1}{A} \frac{\partial h}{\partial x} = \frac{1}{\pi} \int \frac{p(\xi)}{\xi - x} d\xi \quad (2.33)$$

$$\frac{1}{A} \frac{\partial g}{\partial x} = \frac{1}{\pi} \int \frac{q(\xi)}{\xi - x} d\xi \quad (2.34)$$

### 2.1.5.1 Cylindrical-on-plane contact

The cylindrical configuration (cylinder-on-plane) stands as one of the most commonly used setups in fretting fatigue tests. Due to its axi-symmetric nature, it can be treated as a two-dimensional problem (HILLS *et al.*, 1993). Furthermore, this configuration also exhibits a plane strain state. Figure 2.8 illustrates the fretting fatigue cylindrical configuration, depicting the pads in contact with the specimen, along with their characteristic loads: bulk fatigue load ( $B$ ), shear load ( $Q$ ), and normal load ( $P$ ). The region of primary interest (contact) is highlighted. This view provides insights into the distributions of  $p(x)$  and  $q(x)$ , as well as the sizes of the contact zone (2a) and the adhesion zone (2c). This figure will serve as the basis until the final phase of this subsection. Therefore, to initiate the mathematical description of the stress fields in the cylindrical contact configuration, we shall consider that the specimen is subjected solely to pure fretting conditions, without fatigue ( $B$ ), thus involving only the loads  $Q$  and  $P$ . Notably, Hertz (1882) provided results indicating that the pressure distribution developed

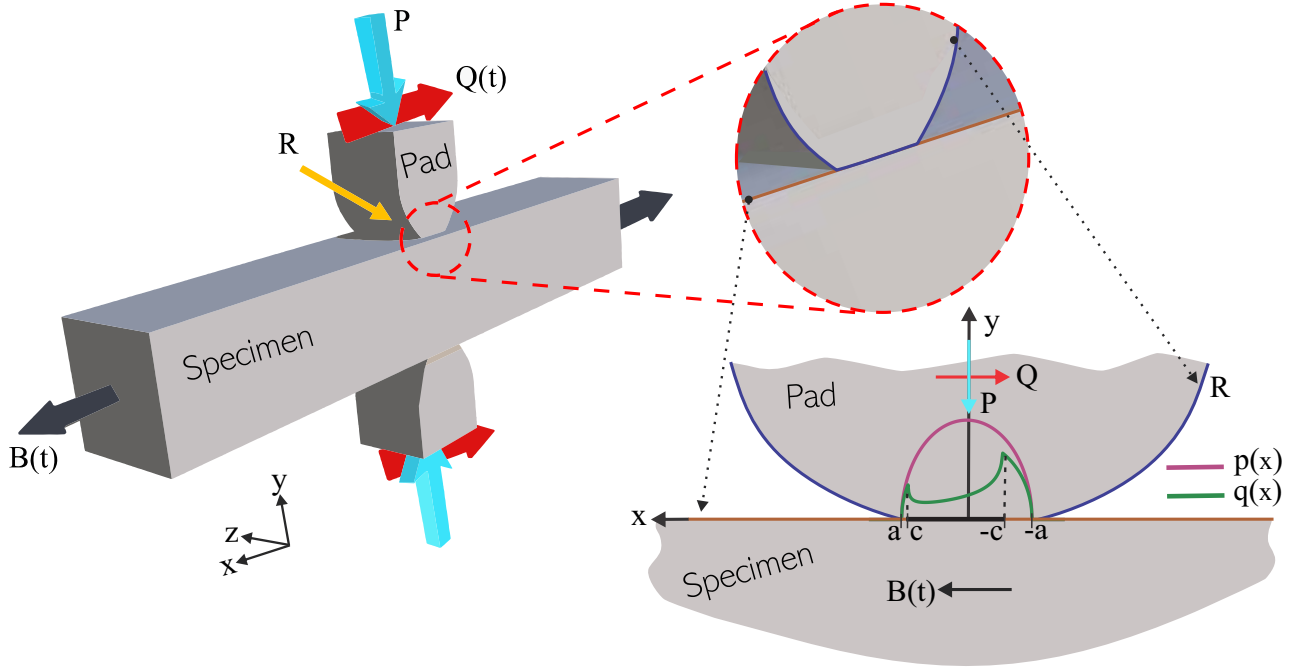


**Figure 2.8.** Representation of the cylinder-on-plane contact configuration.

between two cylindrical contact surfaces subjected to a static normal load  $P$  is given by the follow elliptical pressure profile:

$$p(x) = -p_0 \sqrt{1 - \left(\frac{x}{a}\right)^2} \quad (2.35)$$

Here,  $x/a$  represents the normalized position ( $x$ ) in relation to the contact semi-width ( $a$ ), and  $p_0$  is the peak pressure

$$p_0 = \frac{2P}{\pi a} \quad (2.36)$$

The contact semi-width,  $a$ ,

$$a = \sqrt{\frac{4PR}{\pi E^*}} \quad (2.37)$$

such that

$$R = \left( \frac{1}{R_1} + \frac{1}{R_2} \right)^{-1} \quad (2.38)$$

and

$$E^* = \left( \frac{1 - \nu_1^2}{E_1} + \frac{1 - \nu_2^2}{E_2} \right)^{-1} \quad (2.39)$$

where the subscripts 1 and 2 stand for body 1 (pad) and body 2 (specimen). In this configuration,  $R$  is simply equal to the pad radius, once  $R_2$  has a "infinity" value (Fig. 2.8).

In fretting fatigue tests, the tangential load induces a shear traction,  $q(x)$ , as initially described by Cattaneo (1938) and independently by Mindlin (1949). Due to the fact that the

applied shear load is typically smaller than the threshold for complete sliding, a partial slip regime emerges, where slip occurs within two symmetrical regions,  $c \leq |x| < a$  surrounding a central stick zone  $|x| < c$ . Consequently, it becomes advantageous to represent the shear traction as a perturbation of the solution for full sliding, as follows:

$$q(x) = fp_0 \sqrt{1 - \left(\frac{x}{a}\right)^2} + q'(x) \quad (2.40)$$

here,  $f$  is the coefficient of friction between the bounding solids. The term of perturbation  $q'(x)$  is zero in the slip zones ( $c \leq |x| < a$ ). In the stick one, the shape of  $q'(x)$  can be found acknowledging that there is no variation in the relative displacement between corresponding points ( $g(x)$ ) within this region. Hence, solving the integral equation provided by Eq. 2.34,  $q'(x)$  is computed in both contact zones, as follows:

$$q'(x) = \begin{cases} 0, & \text{if } c \leq |x| \leq a \\ -fp_0 \frac{c}{a} \sqrt{1 - \left(\frac{x}{c}\right)^2}, & \text{if } |x| < c \end{cases} \quad (2.41)$$

where  $c$  is the semi-width of the stick zone, and can be computed imposing tangential equilibrium:

$$\frac{c}{a} = \sqrt{1 - \frac{Q}{fP}} \quad (2.42)$$

It is important to note that, despite the application of a tangential load ( $Q$ ) on specimen, which is smaller than  $fP$ , in certain regions near the contact edge where the pressure decreases, local slip may occur ( $|q(x)| = -fp(x)$ ). Conversely, points near the center will remain in the adhesion regime, resulting in no slip ( $|q(x)| < fp(x)$ ). Although these displacements at the contact edge may not be macroscopically visible, they lead to small displacements in some particles, inducing the formation of micro-damages within the slip zones.

Figure 2.9 illustrates a normalized distribution of pressure and shear traction as a function of the normalized position ( $x/a$ ). The central stick zone, where the shear traction is reduced due to the perturbation in the full solution, is clearly evident, flanked by the slip zones at the edges. The tangential load exhibits variations in time under fretting conditions, as depicted in a typical  $Q$  load history in Fig. 2.10. To better understand its influence on the shear traction over time, it becomes essential to investigate the behavior at the reversal load. Consequently, it is worth emphasizing that the direction of the shear traction opposes the relative motion of the contact surfaces, yielding:

$$\text{sgn}(q(x)) = -\text{sgn}\left(\frac{\partial g(x)}{\partial t}\right) \quad (2.43)$$

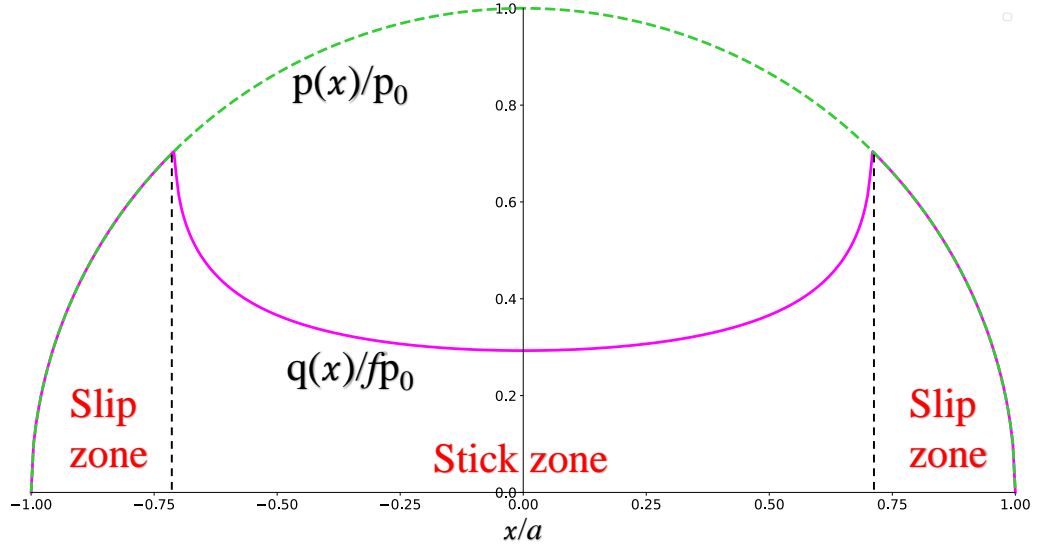


**Figure 2.9.** Pressure and shear traction profiles considering  $Q/fP = 0.5$ .

The tangential traction  $q(x)$  described earlier is valid only when the tangential load is applied monotonically, increasing from 0 to its maximum value  $Q_{\max}$  (Point A). However, the situation changes when the tangential load is infinitesimally reduced from Point A to Point B, causing the entire contact region to experience a sticking condition. This leads to a violation of the tangential traction direction, which is intended to oppose relative motion between the contact surfaces (Eq. 2.44). Subsequently reducing the load  $Q$  to Point C triggers the occurrence of reversal slip, locally reversing the relative motion between the contact surfaces. As a result, within the newly formed slip zones ( $c' < |x| \leq a$ ), the shear traction changes from  $fp(x)$  to  $-fp(x)$ . To address these effects adequately, a second corrective term  $q''$  is introduced in the construction of the shear traction, as follows:

$$q''(x,t) = 2fp_0 \frac{c'(t)}{a} \sqrt{1 - \left(\frac{x}{c'(t)}\right)^2} \quad (2.44)$$

The net shear traction can finally be written as:

$$\frac{q(x,t)}{fp_0} = \begin{cases} -\sqrt{1 - \left(\frac{x}{a}\right)^2} & \text{if } c' < |x| \leq a \\ -\sqrt{1 - \left(\frac{x}{a}\right)^2} + 2\frac{c'(t)}{a} \sqrt{1 - \left(\frac{x}{c'(t)}\right)^2} & \text{if } c < |x| \leq c' \\ -\sqrt{1 - \left(\frac{x}{a}\right)^2} + 2\frac{c'(t)}{a} \sqrt{1 - \left(\frac{x}{c'(t)}\right)^2} - \frac{c}{a} \sqrt{1 - \left(\frac{x}{c}\right)^2} & \text{if } |x| \leq c \end{cases} \quad (2.45)$$

Similar to the case of monotonic loading, the size of the new stick zone at the reversal of

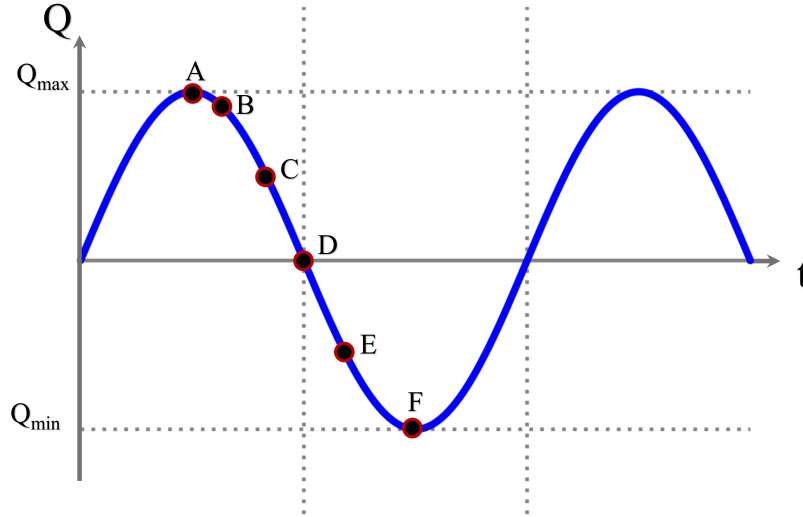


**Figure 2.10.** Shear load ( $Q$ ) over the time.

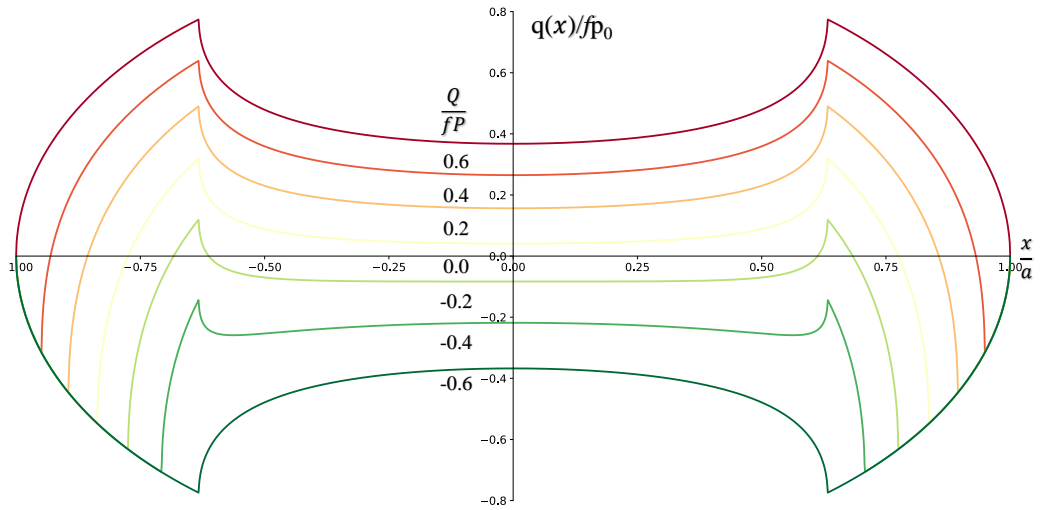


**Figure 2.11.** Shear traction distributions during a tangential cycle,  $Q_{max}/fP = 0.6$ .

load is obtained by considering the overall equilibrium of forces in the tangential direction:

$$\frac{c'(t)}{a} = \sqrt{1 - \frac{Q_{max} - sQ(t)}{2fP}} \quad (2.46)$$

In the tangential loading cycle, it is assumed that  $s = 1$  when transitioning from  $Q_{max}$  towards  $Q_{min}$ , and  $s = -1$  during the reloading phase, i.e., when moving from  $Q_{min}$  to  $Q_{max}$ , as illustrated in Fig. 2.10. As an example, Fig. 2.11 displays the distribution of shear tractions during a tangential cycle, transitioning from point  $Q_{max}$  to  $Q_{min}$ . Remarkably, even when the tangential load  $Q$  is null, the shear traction distribution along the contact surface persists, highlighting the significant influence of loading history on contact problems.

Let us go back to the complete case of Fig. 2.8 under fretting fatigue conditions. When

bulk stress is introduced into fretting, a slight modification of the classical Mindlin solution for the shear traction is necessary. The presence of bulk load on the specimen induces strain that is absent in the pads. This strain mismatch gives rise to an additional term in the tangential displacement matching equation (Eq. 2.34), leading to shear tractions that differ from those observed in the absence of bulk stress. For instance, the influence of  $B$  on the shear traction can be observed when comparing the  $q(x)$  profile in Fig. 2.9 with that in Fig. 2.8, which considers fretting fatigue. In this setting, the perturbation solutions  $q'$  and  $q''$  need to be redefined as:

$$q'(x) = -\frac{fp_0}{c} \sqrt{1 - \left(\frac{x-e}{c}\right)^2} \quad (2.47)$$

and

$$q''(x,t) = 2fp_0 \frac{c'(t)}{a} \sqrt{1 - \left(\frac{x-e'(t)}{c'(t)}\right)^2} \quad (2.48)$$

where the normalized offset terms of the stick zone,  $e/a$  and  $e'(t)/a$ , are given respectively by:

$$\frac{e}{a} = \frac{\sigma_{B,a}}{4fp_0} \quad (2.49)$$

and

$$\frac{e'(t)}{a} = \frac{\sigma_{B,a} - s\sigma_B(t)}{8fp_0} \quad (2.50)$$

such that  $\sigma_B(t)$  and  $\sigma_{B,a}$  is the bulk stress and its correspondent amplitude over a cycle.

It is important to note that these equations are applicable only for small values of bulk fatigue load ( $B$ ), and it is necessary to satisfy the following conditions:  $e+c < a$  and  $e'+c' < a$ , i.e., respecting the inequality in Eq. 2.51 (NOWELL; HILLS, 1987). For higher loads, the size and position of the adhesive zone may be numerically computed, for instance, employing quadratic programming techniques (NOWELL; DAI, 1998), these reverse slip effects may also be calculated through elaborate analytical formulations (VÁZQUEZ *et al.*, 2013).

$$\frac{\sigma_{B,a}}{fp_0} \leq 4 \left( 1 - \sqrt{1 - \left(\frac{Q}{fP}\right)^2} \right) \quad (2.51)$$

To assess the equivalent stress tensor at any subsurface point of the specimen under the loads depicted in Fig. 2.8, a superposition of the effects of contact tractions (normal and shear) and bulk stress is required. This is achieved using Muskhelishvili's potentials (MUSKHELISHVILI, 1977) for plane problems. The potential, denoted as  $\Phi$ , is a function of the complex coordinate

position,  $z = x + yi$ . Its determination involves performing a contour integral along the contact line, as follows:

$$\Phi(z) = \frac{1}{2\pi i} \int_{\text{contact}} \frac{p(\chi) - iq(\chi)}{\chi - z} d\chi \quad (2.52)$$

where  $p(\chi)$  and  $q(\chi)$  represent arbitrary contact pressure and shear stress distributions, respectively. In the case of contacts experiencing gross slip condition, the above equation can be expressed as follows:

$$\Phi(z) = \frac{1 - if}{2\pi i} \int_{\text{contact}} \frac{p(\chi)}{\chi - z} d\chi \quad (2.53)$$

Once the potential is obtained, the stress components related to the plane strain state can be expressed as:

$$\sigma_{xx} + \sigma_{yy} = 2[\Phi(z) + \bar{\Phi}(\bar{z})] \quad (2.54)$$

$$\sigma_{yy} - \sigma_{xx} + 2i\tau_{xy} = 2[(\bar{z} - z) \frac{\partial \Phi(z)}{\partial z} - \bar{\Phi}(z) - \Phi(z)] \quad (2.55)$$

Before solving this system of equations, let us express the potential in terms of our problem in study, i.e., by substituting our contact tractions, considering Eqs. 2.52 and 2.53, we obtain:

$$\Phi(z) = -\frac{(1 - if)p_0}{2\pi i} \frac{1}{a} \int_{-a}^a \frac{\sqrt{a^2 - x^2}}{x - z} dx \quad (2.56)$$

Therefore, by solving this integral, it is possible to identify the corresponding terms from Eqs. 2.54 and 2.55, involving conjugate terms ( $\bar{\Phi}(\bar{z})$  and  $\bar{\Phi}(z)$ ) and also a derivative ( $\partial \Phi(z)/\partial z$ ). In this way, one has:

$$\Phi(z) = -\frac{p_0}{2a}(i + f) \left( z - \text{sgn}(\text{Re}(z))\sqrt{z^2 - a^2} \right) \quad (2.57)$$

$$\frac{\partial \Phi(z)}{\partial z} = -\frac{p_0}{2a}(i + f) \left( 1 - \text{sgn}(\text{Re}(z)) \frac{z}{\sqrt{z^2 - a^2}} \right) \quad (2.58)$$

$$\bar{\Phi}(z) = -\frac{p_0}{2a}(-i + f) \left( z - \text{sgn}(\text{Re}(z))\sqrt{z^2 - a^2} \right) \quad (2.59)$$

$$\bar{\Phi}(\bar{z}) = -\frac{p_0}{2a}(-i + f) \left( \bar{z} - \text{sgn}(\text{Re}\bar{z})\sqrt{\bar{z}^2 - a^2} \right) \quad (2.60)$$

Manipulating the expressions from Eqs. 2.54 and 2.55, one gets the following expression:

$$\Lambda = \sigma_{yy} + i\tau_{xy} = [(\bar{z} - z) \frac{\partial \Phi(z)}{\partial z} - \bar{\Phi}(z) + \bar{\Phi}(\bar{z})] \quad (2.61)$$

With this, one can extract the stress components of interest:

$$\sigma_{xx} = 4\text{Re}(\Phi(z)) - \text{Re}(\Lambda) \quad (2.62)$$

$$\sigma_{yy} = Re(\Lambda) \quad (2.63)$$

$$\tau_{xy} = Im(\Lambda) \quad (2.64)$$

$$\sigma_{zz} = \nu(\sigma_{xx} + \sigma_{yy}) \quad (2.65)$$

It is essential to emphasize that the fretting problem is decoupled, leading to separate normal and tangential stress components. In our case, the normal stress components are computed based on the imaginary (or complex),  $\Im$ , part of equations 2.57, 2.58, 2.59, and 2.60. Conversely, the tangential stress components are derived from the real part ( $\Re$ ) of the same equations, which include the friction coefficient ( $f$ ). The corresponding stresses for the normal and tangential components will be determined using equations 2.62, 2.63, 2.64, and 2.65, while considering the aforementioned considerations. Consequently, in a matrix notation, two tensors ( $\boldsymbol{\sigma}^N$  and  $\boldsymbol{\sigma}^T$ ) result from these calculations, which are:

$$\boldsymbol{\sigma}^N = \begin{bmatrix} \sigma_{xx}^N & \tau_{xy}^N & 0 \\ \tau_{xy}^N & \sigma_{yy}^N & 0 \\ 0 & 0 & \sigma_{zz}^N \end{bmatrix} \quad (2.66)$$

$$\boldsymbol{\sigma}^T = \begin{bmatrix} \sigma_{xx}^T & \tau_{xy}^T & 0 \\ \tau_{xy}^T & \sigma_{yy}^T & 0 \\ 0 & 0 & \sigma_{zz}^T \end{bmatrix} \quad (2.67)$$

The values normalized by the semi-contact length ( $a$ ) of the components of the  $\boldsymbol{\sigma}^N$  and  $\boldsymbol{\sigma}^T$  can be readily ascertained using the tables provided by Hills and Nowell (HILLS; NOWELL, 1993). Finally, it is possible to split the final tensorial expressions into two general forms, depending on the loading conditions. It is also worth noting that all stress components are temporal and spatial functions, varying with  $x$ ,  $y$ , and  $t$ . Thus, one gets:

□ Maximum and minimum loads

$$\boldsymbol{\sigma} \left( \frac{x}{a}, \frac{y}{a}, t \right) = p_0 \left( \frac{\boldsymbol{\sigma}^N \left( \frac{x}{a}, \frac{y}{a} \right)}{p_0} \pm f \frac{\boldsymbol{\sigma}^T \left( \frac{x}{a}, \frac{y}{a} \right)}{fp_0} \mp f \frac{c}{a} \frac{\boldsymbol{\sigma}^T \left( \frac{x-e}{c}, \frac{y}{c} \right)}{fp_0} \right) + \boldsymbol{\sigma}_B(t) \quad (2.68)$$

where the signal combination  $+$  and  $-$  holds for the maximum load.

□ Unloading and reloading

$$\boldsymbol{\sigma} \left( \frac{x}{a}, \frac{y}{a}, t \right) = p_0 \left( \frac{\boldsymbol{\sigma}^N \left( \frac{x}{a}, \frac{y}{a} \right)}{p_0} \mp f \frac{\boldsymbol{\sigma}^T \left( \frac{x}{a}, \frac{y}{a} \right)}{fp_0} \right. \\ \left. \pm 2f \frac{c'(t)}{a} \frac{\boldsymbol{\sigma}^T \left( \frac{x-e'(t)}{c'(t)}, \frac{y}{c'(t)} \right)}{fp_0} \mp f \frac{c}{a} \frac{\boldsymbol{\sigma}^T \left( \frac{x-e}{c}, \frac{y}{c} \right)}{fp_0} \right) + \boldsymbol{\sigma}_B(t) \quad (2.69)$$

here the signal combination  $-$ ,  $+$  and  $-$  holds for the unloading.

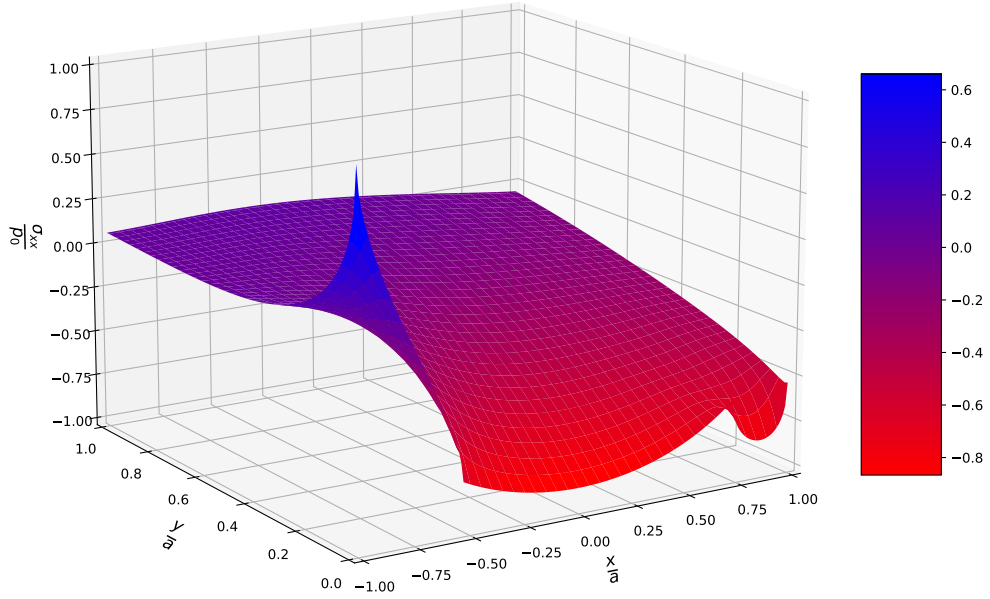


**Figure 2.12.** Subsurface distribution of the  $\sigma_{xx}/p_0$  for a cylindrical-on-plane configuration under fretting fatigue ( $Q/fP = 0.6$ ,  $\sigma_{B,a}/fp_0 = 0.4$ ,  $\nu = 0.33$ ,  $f = 0.5$ .)

In equations 2.68 and 2.69, the term  $\sigma_B(t)$  represents the stress tensor related to the bulk fatigue load, which is given by:

$$\sigma_B(t) = \begin{bmatrix} \sigma_B(t) + \sigma_{B,\text{med}} & 0 & 0 \\ 0 & 0 & 0 \\ 0 & 0 & -\nu(\sigma_B(t) + \sigma_{B,\text{med}}) \end{bmatrix} \quad (2.70)$$

where  $\sigma_{B,\text{med}}$  represents the mean bulk stress associated with the mean bulk fatigue load ( $B_{\text{med}}$ ), which remains constant over time if applied during the loading.

Figure 2.12 illustrates the profile of the surface associated with the normalized component  $\sigma_{xx}$  of the tensor in Eq. 2.68, during the maximum loading, allowing us to observe its behavior along the contact length ( $x/a$ ) as well as in the depth ( $y/a$ ).

### 2.1.5.2 Sphere-on-plane contact

Using cylindrical pads in fretting fatigue experiments presents a challenge of ensuring precise alignment with the specimen surface to avoid variations in surface tractions along the contact patch. Pressure-sensitive film and meticulous setup can help minimize alignment issues (NOWELL, 1988). Alternatively, spherical fretting pads can be used, eliminating such alignment concerns. The sphere-on-plane configuration has a three-dimensional stress state under

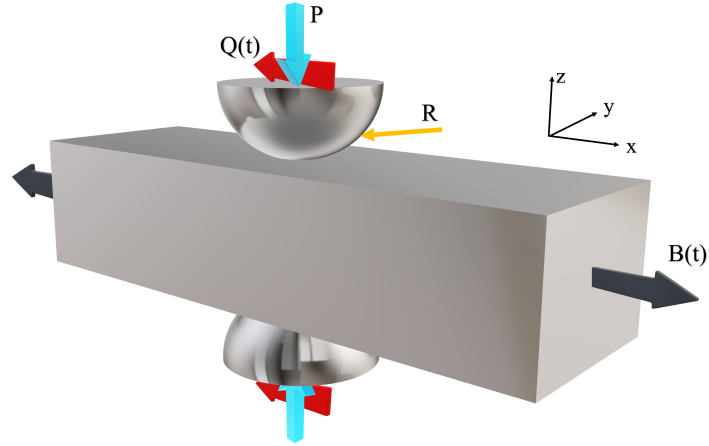


**Figure 2.13.** Sphere on-plane fretting fatigue set-up.

fretting fatigue, hence does not present axi-symmetric as the cylindric-on-plane one. However, the computation of the related stress fields is quite similar to those shown in the previous subsection (2.1.5.1). Fig 2.13 presents the fretting fatigue spherical contact set-up studied in this section, as can be seen, the axes has been changed (see Fig. 2.8) in order to facilitate the calculations in a 3D analysis. The analytical solution for this problem has been demonstrated by several authors in the literature (HILLS *et al.*, 1993; HAMILTON, 1983; HAMILTON; GOODMAN, 1966; SACKFIELD; HILLS, 1983; DOMÍNGUEZ, 1998).

In this configuration the contact patch is a circle of radius  $a$  and is calculated by the classic Hertzian expression (HAMILTON, 1983):

$$a = \left( \frac{3\pi P R_1 R_2}{4(R_1 + R_2)} \left( \frac{1 - \nu_1^2}{\pi E_1} + \frac{1 - \nu_2^2}{\pi E_2} \right) \right)^{\frac{1}{3}} \quad (2.71)$$

where  $E$ ,  $\nu$ , and  $R$  are the Young's modulus, the Poisson's coefficient, and the radius of curvature, respectively. The subscripts 1, 2 refer to the two bodies in contact, which in this case is the sphere and the plane.

The normal traction has a radial distribution, so one has:

$$p(r) = -p_0 \sqrt{1 - \left(\frac{r}{a}\right)^2} \quad (2.72)$$

where the peak pressure ( $p_0$ ) is

$$p_0 = \frac{3P}{2\pi a^2} \quad (2.73)$$

Under fretting conditions, the net shear traction acting in the x-direction is also radial and can be represented similarly to Eq. 2.133, but in terms of the radius instead of  $x$ , as is the

pressure distribution (Eq. 2.72). Considering partial slip, the semi-width of the stick zone under maximum and time-varying loading can be expressed as follows:

$$\frac{c}{a} = \sqrt[3]{1 - \frac{Q}{fP}} \quad (2.74)$$

and

$$\frac{c'(t)}{a} = \sqrt[3]{1 - \frac{Q_{max} - sQ(t)}{2fP}} \quad (2.75)$$

Equally, as with the cylindrical configuration, when the bulk fatigue load is considered, fretting fatigue arises, and the perturbation solution has to be updated to account for the offset terms of the stick zone. Therefore, the same related equations (Eqs. 2.47 and 2.48) in terms of the radius are considered ( $r$ ), and the respective offsets are now given by:

$$\frac{e}{a} = \frac{4\sigma_{B,a}}{\pi f p_0} \left( \frac{1 - \nu}{4 - 3\nu} \right) \quad (2.76)$$

$$\frac{e'(t)}{a} = \frac{2(\sigma_{B,a} - s\sigma_B(t))}{\pi f p_0} \left( \frac{1 - \nu}{4 - 3\nu} \right) \quad (2.77)$$

Subsurface's stress fields of the spherical-on-plane configuration can be achieved by the expressions proposed by Hamilton (1983) and Sackfield and Hills (1983), and adapting them for the case of fretting fatigue, as proposed by Domínguez (1998). The following equations should be applied while respecting their boundary conditions, such that the superscript  $N$  is added to denote that a particular stress component is produced by a normal load, and  $T$  to denote that it is produced by a tangential load, similar to what was considered in the cylindrical configuration (see Eqs. 2.66 and 2.67). Considering that  $r = \sqrt{x^2 + y^2}$ , the following equations should be applied on the surface inside the contact.

□ Normal stress components ( $z/a = 0$ ,  $r/a < 1$ )

$$\frac{\sigma_{xx}^N}{p_0} = \frac{1}{r^2} \left( \frac{(y^2 - x^2)(1 - 2\nu)}{3r^2} \left( (1 - r^2)^{3/2} - 1 \right) - (x^2 + 2\nu y^2) \sqrt{1 - r^2} \right) \quad (2.78)$$

$$\frac{\sigma_{yy}^N}{p_0} = \frac{1}{r^2} \left( \frac{(x^2 - y^2)(1 - 2\nu)}{3r^2} \left( (1 - r^2)^{3/2} - 1 \right) - (y^2 + 2\nu x^2) \sqrt{1 - r^2} \right) \quad (2.79)$$

$$\frac{\sigma_{zz}^N}{p_0} = -(1 - r^2)^{1/2} \quad (2.80)$$

$$\frac{\tau_{xy}^N}{p_0} = -\frac{(1 - 2\nu)xy}{r^2} \left( \sqrt{1 - r^2} + \frac{2}{3} \frac{1}{r^2} \left( (1 - r^2)^{3/2} - 1 \right) \right) \quad (2.81)$$

$$\frac{\tau_{yz}^N}{p_0} = \frac{\tau_{zx}^N}{p_0} = 0 \quad (2.82)$$

□ Tangential stress components ( $z/a = 0, r/a < 1$ )

$$\frac{\sigma_{xx}^T}{fp_0} = -\pi \left(\frac{x}{2}\right) \left(1 + \frac{\nu}{4}\right) \quad (2.83)$$

$$\frac{\sigma_{yy}^T}{fp_0} = -3\pi \frac{\nu x}{8} \quad (2.84)$$

$$\frac{\tau_{xy}^T}{fp_0} = \pi \left(\frac{y}{4}\right) \left(\frac{\nu}{2} - 1\right) \quad (2.85)$$

$$\frac{\tau_{zx}^T}{fp_0} = -(1 - r^2)^{1/2} \quad (2.86)$$

$$\frac{\sigma_{zz}^T}{fp_0} = \frac{\tau_{yz}^T}{fp_0} = 0 \quad (2.87)$$

From now on, the following equations are applied for positions outside the contact but on the surface:

□ Normal stress components ( $z/a = 0, r/a > 1$ )

$$\frac{\sigma_{xx}^N}{p_0} = \frac{(1 - 2\nu)(x^2 - y^2)}{3r^4} \quad (2.88)$$

$$\frac{\sigma_{yy}^N}{p_0} = \frac{(1 - 2\nu)(y^2 - x^2)}{3r^4} \quad (2.89)$$

$$\frac{\tau_{xy}^N}{p_0} = \frac{(1 - 2\nu)(2xy)}{3r^4} \quad (2.90)$$

$$\frac{\tau_{yz}^N}{p_0} = \frac{\tau_{zx}^N}{p_0} = \frac{\sigma_{zz}^N}{p_0} = 0 \quad (2.91)$$

□ Tangential stress components ( $z/a = 0, r/a > 1$ )

$$\frac{\sigma_{xx}^T}{fp_0} = -\frac{x}{r^4} \left( 2(r^2 + \nu y^2)F_0 + \nu(3 - 4\left(\frac{x}{r}\right)^2)H_0 \right) \quad (2.92)$$

$$\frac{\sigma_{yy}^T}{fp_0} = -\frac{\nu x}{r^4} \left( 2x^2F_0 + H_0(1 - 4\left(\frac{y}{r}\right)^2) \right) \quad (2.93)$$

$$\frac{\tau_{xy}^T}{fp_0} = -\frac{y}{r^4} \left( (r^2 - 2\nu x^2)F_0 + \nu(1 - 4\left(\frac{x}{r}\right)^2)H_0 \right) \quad (2.94)$$

$$\frac{\tau_{yz}^T}{fp_0} = \frac{\tau_{zx}^T}{fp_0} = \frac{\sigma_{zz}^T}{fp_0} = 0 \quad (2.95)$$

such that

$$\begin{aligned}
F_0 &= -\frac{1}{2}\sqrt{(r^2-1)} + \frac{1}{2}r^2 \arctan\left(\frac{1}{\sqrt{r^2-1}}\right) \\
H_0 &= \frac{1}{2}(r^2-1)^{\frac{3}{2}} - \frac{1}{4}r^4 \arctan\left(\frac{1}{\sqrt{r^2-1}}\right) - \frac{1}{4}r^2\sqrt{r^2-1}
\end{aligned} \tag{2.96}$$

Next equations considered the stress components on the  $z$  axis, on the specimen. Thus, one gets:

□ Normal stress components ( $z/a \leq 0$ ,  $r/a = 0$ )

$$\frac{\sigma_{xx}^N}{p_0} = -(1+\nu) \left(1 - z \arctan\left(\frac{1}{z}\right)\right) - \frac{1}{2(1+z^2)} \tag{2.97}$$

$$\frac{\sigma_{yy}^N}{p_0} = \frac{\sigma_{xx}^N}{p_0} \tag{2.98}$$

$$\frac{\sigma_{zz}^N}{p_0} = -\frac{1}{1+z^2} \tag{2.99}$$

$$\frac{\tau_{xy}^N}{p_0} = \frac{\tau_{zx}^N}{p_0} = \frac{\tau_{yz}^N}{p_0} = 0 \tag{2.100}$$

□ Tangential stress components ( $z/a \leq 0$ ,  $r/a = 0$ )

$$\frac{\tau_{zx}^T}{fp_0} = \frac{3}{2}z \arctan\left(\frac{1}{z}\right) - 1 - \frac{z^2}{2(1+z^2)} \tag{2.101}$$

$$\frac{\sigma_{xx}^T}{fp_0} = \frac{\sigma_{yy}^T}{fp_0} = \frac{\sigma_{zz}^T}{fp_0} = \frac{\tau_{xy}^T}{fp_0} = \frac{\sigma_{yz}^T}{fp_0} = 0 \tag{2.102}$$

The last equations considers the stress components inward the surface and out of the axis of symmetry, as follows:

□ Normal stress components ( $z/a \leq 0$ ,  $r/a > 0$ )

$$\begin{aligned}
\frac{\sigma_{xx}^N}{p_0} &= \frac{(1-2\nu)}{3(r^4)}(x^2-y^2)\left(1-\left(\frac{z}{u}\right)^3\right) \\
&+ \frac{z}{u} \left( (1+\nu)u \arctan\left(\frac{1}{u}\right) - 2\nu - \frac{(1-\nu)u^2}{1+u^2} - \frac{(1-2\nu)x^2}{r^2(1+u^2)} - \frac{x^2u^4}{(1+u^2)^2(u^4+z^2)} \right)
\end{aligned} \tag{2.103}$$

$$\begin{aligned}
\frac{\sigma_{yy}^N}{p_0} &= \frac{(1-2\nu)}{3(r^4)}(x^2-y^2) \left( \left(\frac{z}{u}\right)^3 - 1 \right) \\
&+ \frac{z}{u} \left( (1+\nu)u \arctan\left(\frac{1}{u}\right) - 2\nu - \frac{(1-\nu)u^2}{1+u^2} - \frac{(1-2\nu)y^2}{r^2(1+u^2)} - \frac{y^2u^4}{(1+u^2)^2(u^4+z^2)} \right)
\end{aligned} \tag{2.104}$$

$$\frac{\sigma_{zz}^N}{p_0} = -\frac{z^3}{u(u^4 + z^2)} \quad (2.105)$$

$$\frac{\tau_{xy}^N}{p_0} = -\frac{xyz u^3}{(1 + u^2)^2(u^4 + z^2)} + (1 - 2\nu)J \quad (2.106)$$

$$\frac{\tau_{zx}^N}{p_0} = -\frac{xz^2 u}{(1 + u^2)(u^4 + z^2)} \quad (2.107)$$

$$\frac{\tau_{yz}^N}{p_0} = -\frac{yz^2 u}{(1 + u^2)(u^4 + z^2)} \quad (2.108)$$

□ Tangential stress components ( $z/a \leq 0$ ,  $r/a > 0$ )

$$\begin{aligned} \frac{\sigma_{yy}^T}{f p_0} &= 2\nu x \left( -\frac{3}{8} \arctan\left(\frac{1}{u}\right) + \frac{u}{4(1 + u^2)} + \frac{3u}{8(1 + u^2)} - \frac{y^2 u^5}{(1 + u^2)^3(u^4 + z^2)} \right) \\ &\quad + (1 - 2\nu)z \frac{\partial J}{\partial y} \end{aligned} \quad (2.109)$$

$$\frac{\sigma_{zz}^T}{f p_0} = -\frac{xz^2 u}{(1 + u^2)(u^4 + z^2)} \quad (2.110)$$

$$\frac{\sigma_{xx}^T}{f p_0} = -(\sigma_{yy}^T + \sigma_{zz}^T) - x(1 + \nu) \left( \arctan\left(\frac{1}{u}\right) - \frac{u}{1 + u^2} \right) \quad (2.111)$$

$$\begin{aligned} \frac{\tau_{xy}^T}{f p_0} &= 2\nu y \left( \frac{1}{8} \arctan\left(\frac{1}{u}\right) - \frac{u}{8(1 + u^2)} + \frac{0.25u}{(1 + u^2)^2} - \frac{x^2 u^5}{(1 + u^2)^3(u^4 + z^2)} \right) \\ &\quad - \frac{y}{2} \left( \arctan\left(\frac{1}{u}\right) - \frac{u}{1 + u^2} \right) + (1 - 2\nu)z \frac{\partial J}{\partial x} \end{aligned} \quad (2.112)$$

$$\frac{\tau_{yz}^T}{f p_0} = -\frac{xyz u^3}{(1 + u^2)^2(u^4 + z^2)} \quad (2.113)$$

$$\frac{\tau_{zx}^T}{f p_0} = z \left( \frac{3}{2} \arctan\left(\frac{1}{u}\right) - \frac{1}{u} - \frac{u}{2(1 + u^2)} - \frac{x^2 u^3}{(1 + u^2)^2(u^4 + z^2)} \right) \quad (2.114)$$

such that

$$J = \frac{xy}{3r^4} \left( \left(\frac{z}{u}\right)^3 - 3\frac{z}{u} + 2 \right) \quad (2.115)$$

$$\frac{\partial J}{\partial x} = J \left( \frac{y^2 - 3x^2}{xr^2} \right) + \frac{ux^2 yz}{r^2(u^4 + z^2)(1 + u^2)} \quad (2.116)$$

$$\frac{\partial J}{\partial y} = J \left( \frac{x^2 - 3y^2}{yr^2} \right) + \frac{uy^2 xz}{r^2(u^4 + z^2)(1 + u^2)} \quad (2.117)$$

where  $u^2$  is the largest root that satisfies the following equation:

$$\frac{r^2}{1 + u^2} + \frac{z^2}{u^2} = 1 \quad (2.118)$$

The final tensorial equation, accounting for the effects of the three main loads ( $N$ ,  $Q$ , and  $B$ ), it is similar to the ones presented in Eqs. 2.68 and 2.69, but with the distinction that the stress tensor now varies in all three spatial directions,  $x$ ,  $y$ , and  $z$ , instead of solely  $x$  and  $y$ . Besides, the tensor is fully filled (without zero terms), as depicted in its normal and tangential components ( $\boldsymbol{\sigma}^N$  and  $\boldsymbol{\sigma}^T$ ), as follows:

$$\boldsymbol{\sigma}(x,y,z,t) = \begin{bmatrix} \sigma_{xx}(x,y,z,t) & \tau_{xy}(x,y,z,t) & \tau_{xz}(x,y,z,t) \\ \tau_{xy}(x,y,z,t) & \sigma_{yy}(x,y,z,t) & \tau_{yz}(x,y,z,t) \\ \tau_{xz}(x,y,z,t) & \tau_{yz}(x,y,z,t) & \sigma_{zz}(x,y,z,t) \end{bmatrix} \quad (2.119)$$

and

$$\boldsymbol{\sigma}^N = \begin{bmatrix} \sigma_{xx}^N & \tau_{xy}^N & \tau_{xz}^N \\ \tau_{xy}^N & \sigma_{yy}^N & \tau_{yz}^N \\ \tau_{xz}^N & \tau_{yz}^N & \sigma_{zz}^N \end{bmatrix}, \quad \boldsymbol{\sigma}^T = \begin{bmatrix} \sigma_{xx}^T & \tau_{xy}^T & \tau_{xz}^T \\ \tau_{xy}^T & \sigma_{yy}^T & \tau_{yz}^T \\ \tau_{xz}^T & \tau_{yz}^T & \sigma_{zz}^T \end{bmatrix} \quad (2.120)$$

The bulk stress tensor for the spherical-on-plane contact has only the  $x$  component, due to its 3D state of stress, i.e.:

$$\boldsymbol{\sigma}_B(t) = (\sigma_B(t) + \sigma_{B,\text{med}})(e_x \otimes e_x) \quad (2.121)$$

The Figures 2.14 and 2.15 display several plots of stress curves and surfaces associated with the investigated fretting configuration. As depicted in Fig. 2.14, normalized stress curves with respect to  $p_0$  and  $q_0$  ( $fp_0$ ) are shown for normal and shear stresses, respectively. In its sub-figures A, B, D, and E, the variation in stress distribution along the  $x$  and  $y$  directions of the contact can be observed, which is influenced by the loading directions  $Q$  and  $B$ . Additionally, panels C and F illustrate the time variation of a shear component ( $zx$ ) similar to Figure 2.11, but with respect to the  $x$  and  $y$  directions, respectively. Figure 2.15 shows some stress profiles on the  $xz$  (panels A and B),  $yz$  (panels C), and  $xy$  (panels D and E) planes, along with the stress curves from the trailing edge contact, highlighting the high-stress gradient of the  $\sigma_{xx}$  component.

### 2.1.6 Numerical methodologies in fretting fatigue

The Finite Element Method (FEM), commonly known as Finite Element Analysis (FEA), is a numerical technique widely employed in engineering and applied sciences for approximating and analyzing complex physical phenomena. It involves discretizing a continuous structure or system into smaller, finite elements, each characterized by simple geometrical shapes. The behavior of these elements is then described by mathematical models that represent the physical

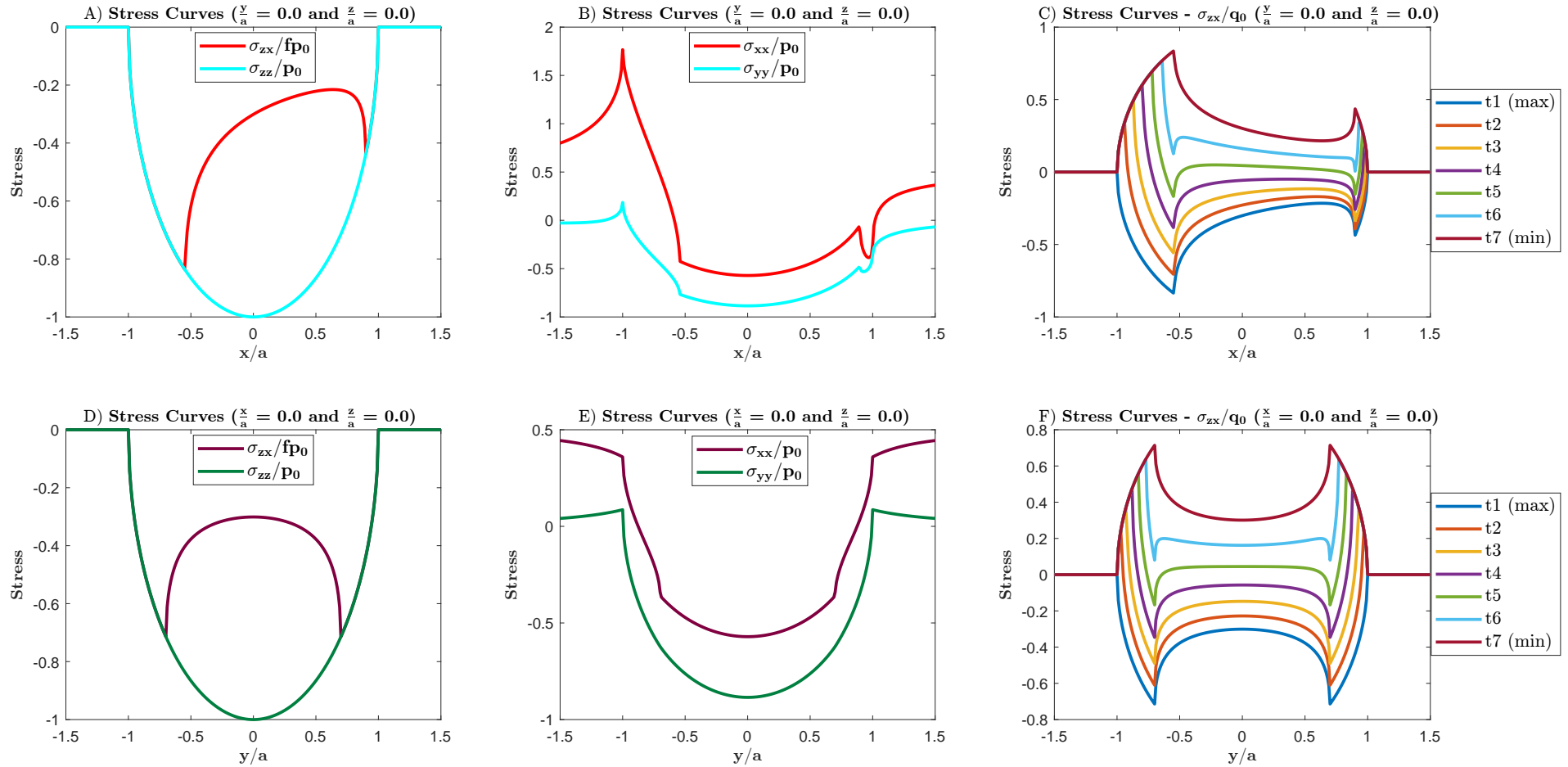


**Figure 2.14.** Sphere-on-plane configuration fretting fatigue normalized stress curves: (A), (B), and (C) under the x-contact surface and (D), (E), and (F) under the y-contact surface ( $p_0 = 200$  MPa,  $\sigma_{B,a} = 150$  MPa,  $Q/P = 0.5$ ,  $f = 0.8$ , and  $\nu = 0.33$ ).

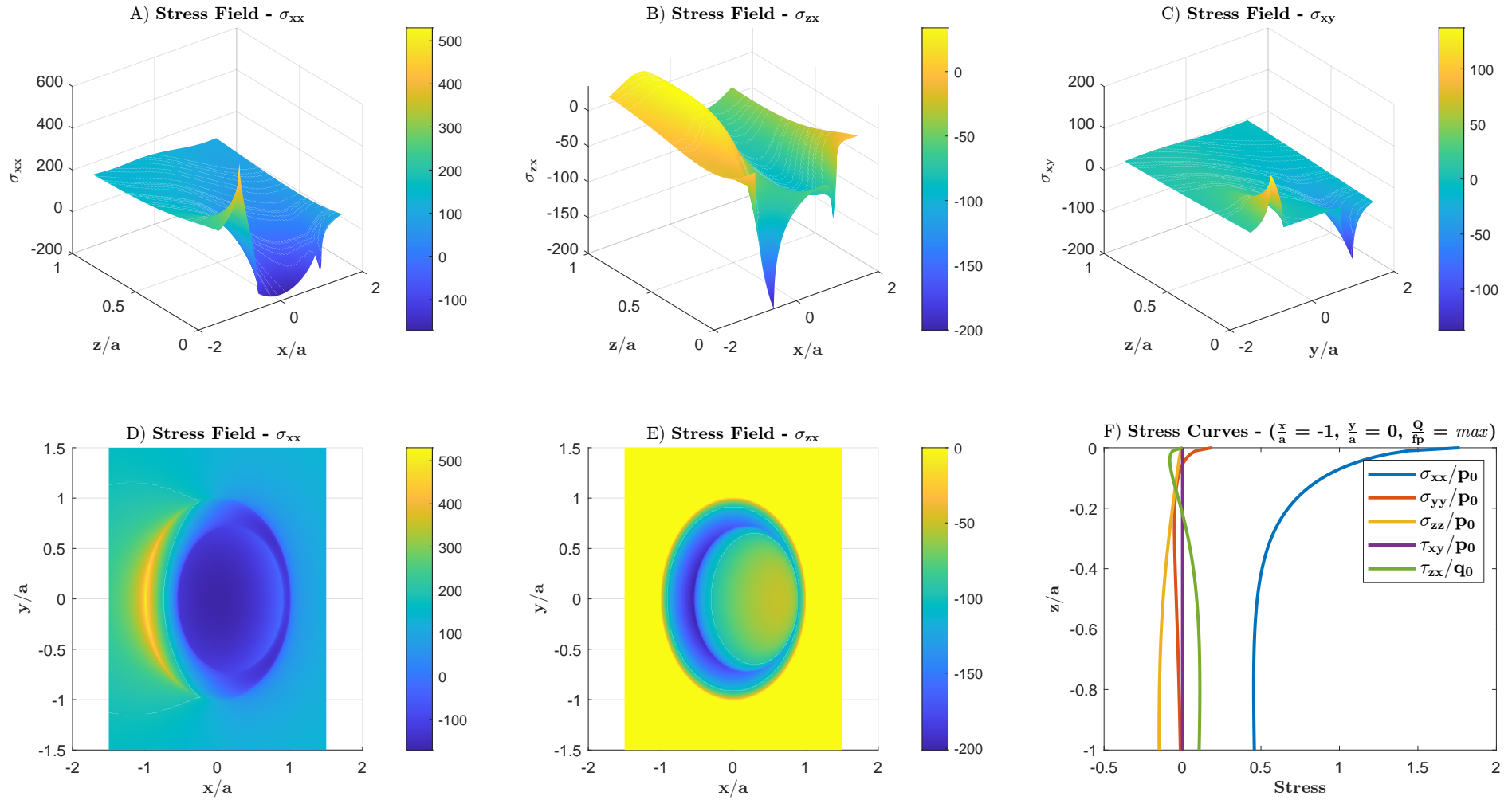


**Figure 2.15.** Sphere-on-plane configuration fretting fatigue stress fields: (A), (B) and (C) under the x-z plane and (D) and (E) under the x-y plane, both normalized. (F) shows all normalized stress components at the contact trailing edge, inward the surface ( $p_0 = 200$  MPa,  $\sigma_{B,a} = 150$  MPa,  $Q/P = 0.5$ ,  $f = 0.8$ , and  $\nu = 0.33$ ).

laws governing the system. By assembling these elements into a comprehensive system of equations, FEA facilitates the solution of complex problems, such as those involved in fretting fatigue, allowing for the prediction of the system's response to various conditions.

In the structural analysis, FEM seeks to find an approximate solution to the problem of equilibrium subject to external forces and boundary conditions. The formulation in weak form entails seeking a solution that satisfies a set of weighted integral equations over the structural domain. These equations, known as variational or residual equations, are derived from the Principle of Virtual Work. It posits that, the virtual work of all forces, both internal and external, in a system in equilibrium is equal to zero for any considered virtual displacement. By applying this principle, the FEM transforms the differential equations of the problem into a system of algebraic equations, facilitating their numerical solution through the discretization of the domain into finite elements. The judicious selection of shape functions and effective representation of boundary conditions ensure convergence to an approximate solution of the problem.

The FEM offers the opportunity to quantify parameters such as non-linearity in contact problems, as well as non-proportional and multiaxial stress states patterns resulting from externally applied loads and various boundary conditions. One of the features of the FEA method lies in its ability to provide information unachievable through analytical solutions. In the modeling of fretting fatigue, diverse approaches exist to address the problem. Some authors prefer to model the problem from a perspective closer to reality, as is the case when addressing industrial issues such as dovetail-attachment joints (MEGUID *et al.*, 2000; RAO *et al.*, 2008; GLODEK; TALEMI, 2022) or contact in overhead conductor wires (ROCHA *et al.*, 2022; MATOS *et al.*, 2023; SAID *et al.*, 2023). Another method of analyzing the problem involves standardized geometries, where an approximation of their mechanical behavior is already known through analytical solutions and well-established mechanical tests in the literature (see next section).

Therefore, one way to validate these FEA models is to compare their results with those derived from analytical solutions. In Fig. 2.16, an example of a fretting fatigue numerical simulation of sphere-on-plane contact is presented, illustrating the distribution of shear and normal tractions on the contact surface. The similarity between the results implies a way to the validation of the model. In fact, some stress values may approach reality more closely in

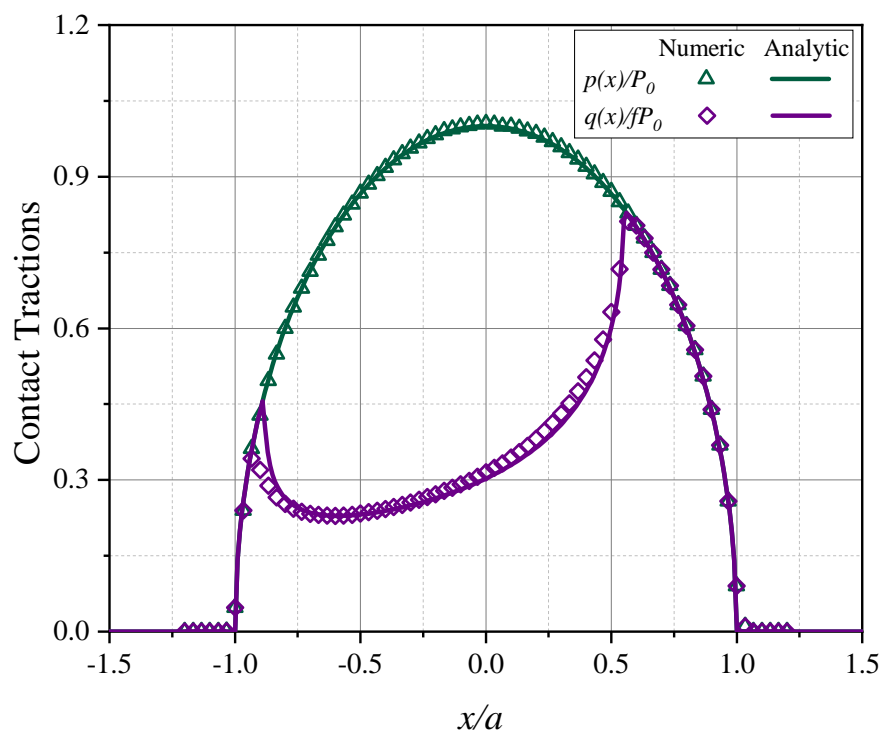


**Figure 2.16.** Comparison between the analytical and numerical solutions for the normalized normal and shear tractions, over the normalized contact position ( $P = 50$  N,  $Q = 30$  N,  $R = 25.4$  mm,  $\sigma_{B,a} = 225$  MPa).

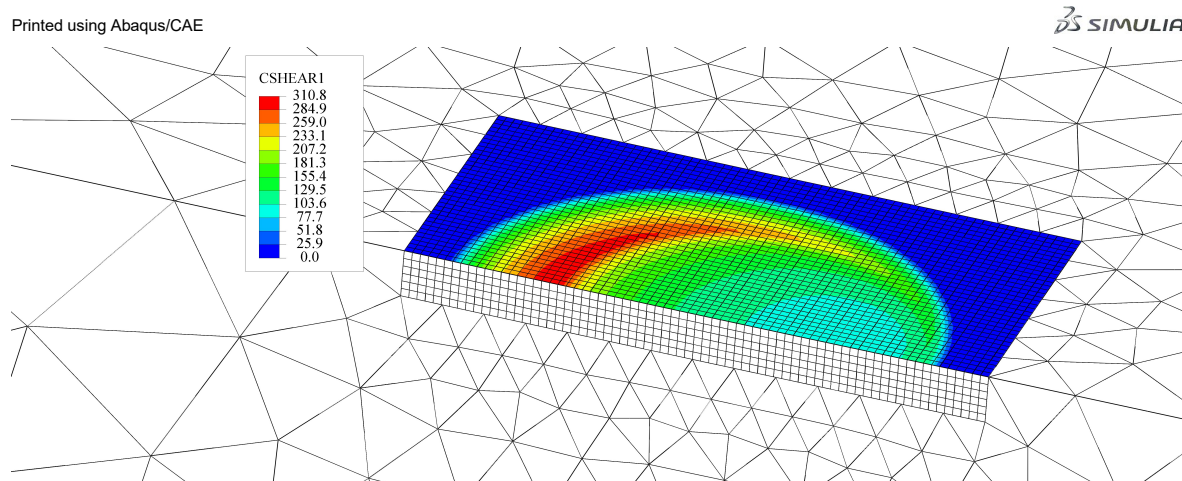


**Figure 2.17.** CSHEAR distribution example in the contact interface, for the spheric-on-plane numerical model ( $P = 50$  N,  $Q = 30$  N,  $R = 25.4$  mm,  $\sigma_{B,a} = 225$  MPa).

the numerical case than in the analytical one, given that the latter does not consider certain situations accounted for in the former, such as edge effects and thickness. In these simulations, regions of greater interest, typically exhibiting high stress gradients, are highlighted with refined meshes, as demonstrated by the example in Fig. 2.17, emphasizing the distribution of shear stress on the contact face with the test specimen. As evident, there is a distinct transition between the mesh of the contact region (colored) and the non-contact region (uncolored). This discrepancy shown one of the techniques employed to mitigate computational costs associated with surfaces in contact, referred to as 'Tie' in software Abaqus/CAE (*SIMULIA*), for instance. Additionally, other methods such as submodeling or utilizing beam elements in less critical regions are employed. We would like to emphasize that the illustrative examples shown in Figs. 2.16 and 2.17 have been reproduced using data and models that will be described in detail in Chapter 4.

As mentioned earlier, numerical and analytical solutions can vary depending on certain factors; in some cases, complex analytical solutions are necessary, as discussed in the preceding section. One way to observe this is by analyzing the ratio  $h_s/2a$ , representing the specimen height ( $h_s$ ) over the contact size ( $2a$ ). In Fig. 2.18, curves of axial stress ( $\sigma_{xx}$ ), in the fatigue bulk load direction, are depicted, featuring numerical and analytical solutions for two extreme cases with high (18.4) and low (3.4) values of  $h_s/2a$ . Literature data were employed for this analysis (NOWELL, 1988; MARTÍN *et al.*, 2020). As illustrated, the curves diverge more significantly for the case with a low  $h_s/2a$  value, reflecting the influence of this specimen thickness  $h_s$ , this behaviour were observed by other authors (FELLOWS *et al.*, 1995). In such instances, the numerical solution aligns more closely with reality than the half-plane-based solution. Figure 2.19 showcases an example of the numerical model for spherical contact solution, addressed in the preceding section, with comprehensive details about this model to be elucidated in Chapter 4.

In fretting fatigue, traditional Finite Element Method (FEM) encounters challenges in accurately modeling stationary cracks due to constraints in mesh refinement. In response, the eXtended Finite Element Method (XFEM) offers a solution by extending FEM capabilities to represent cracks without the need for mesh refinement. This advancement enables more precise simulations of crack propagation. (MOËS *et al.*, 1999).

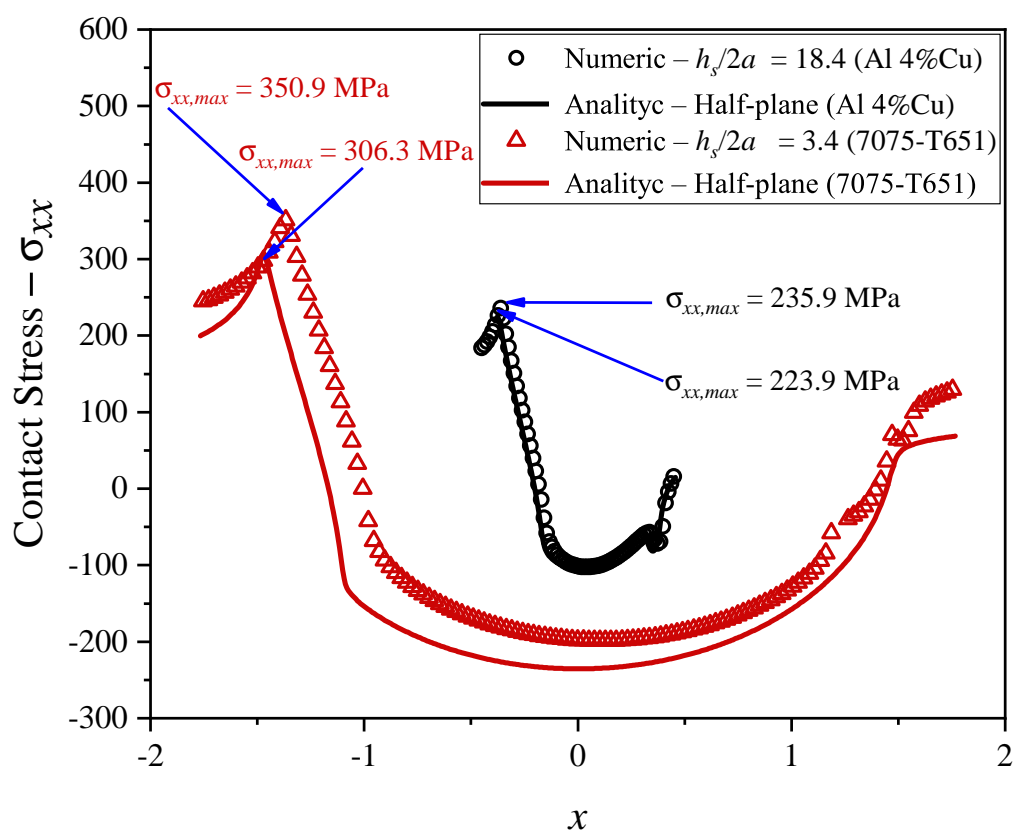


**Figure 2.18.** Comparison of numerical and analytical solutions for the aluminium alloy Al 4%Cu and 7075-T6, analysing the effect of the  $h_s/2a$  ratio.

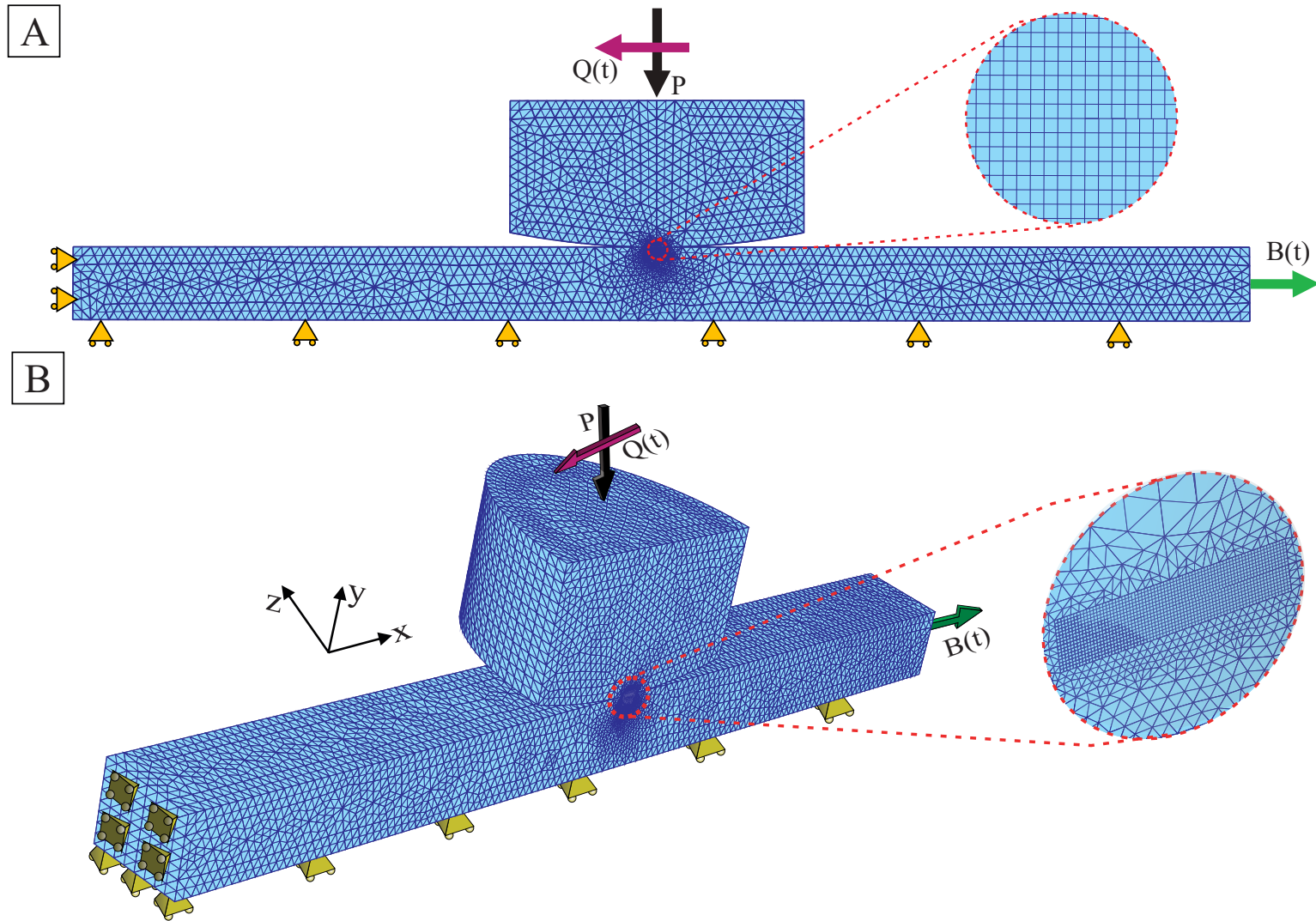


**Figure 2.19.** Example of a numerical model used for the stress solutions of the sphere-on-plane contact configuration.

### 2.1.7 Fretting fatigue experimental testing

In 1988, the ASTM E09 Committee on Fatigue instituted a Task Group on Fretting Fatigue and convened a subsequent symposium in 1990 titled "Standardization of Fretting Fatigue Test Methods and Equipment". The primary aim was to establish standards for fretting fatigue test methods and equipment (ATTIA; WATERHOUSE, 1992). The general recognized standard test method for fretting fatigue was established by the Japan Society of Mechanical Engineers (JSME) in 2002 (NEU, 2011). The standard proposes a typical test configuration, illustrated in Fig. 2.20A, called a bridge-type test. In these experiments, the measurement of the normal force is conducted using an instrumented proving ring, a small force transducer, or an instrumented bolt (ASTM, 2015). Additionally, considering that the bridge-type fretting fatigue test configuration assumes a linear elastic behavior of the fatigue specimen, the hysteresis response can be observed by plotting tangential force (or fretting pad strain) against axial force (or axial strain) in the fatigue specimen. The tangential force transmitted to the pads is commonly deduced from the displacement in the pad, typically measured using a strain gauge. Until the early 1990s, these methods remained popular for their simplicity, using standard fatigue specimens in bending or cyclic tension. However, challenges arise in characterizing contact conditions at the pad feet, particularly with bridge bending. Foot conditions may vary, leading to potential asymmetric slipping during experiments and an unknown slip regime (NOWELL *et al.*, 2006).

The ASTM Task Group E08.05.05 has been developing a fretting fatigue testing guide since 5th International Symposium on Fretting Fatigue (ISFF5) in 2007, held on Montreal, Canada. This guide aims to increase awareness and provide guidelines for designing, calibrating, and using fretting fatigue apparatuses. It does not favor specific designs but recommends means for data collection and reporting, along with defining terms used in fretting fatigue testing. The purpose of standardization is to enhance the interchange of test results among research and testing laboratories. Generic tests typically aim to isolate interacting parameters to assess their individual or collective effects (NEU, 2011).

In the standard test shown in Fig. 2.20B, based on the Standard Guide for Fretting Fatigue Testing from ASTM (ASTM, 2015), fretting fatigue occurs in the grip section as illustrated. The fretting pads are generally flat with blending radii at the edges, although alternative contact configurations could be employed. This fretting fatigue test is constrained to partial

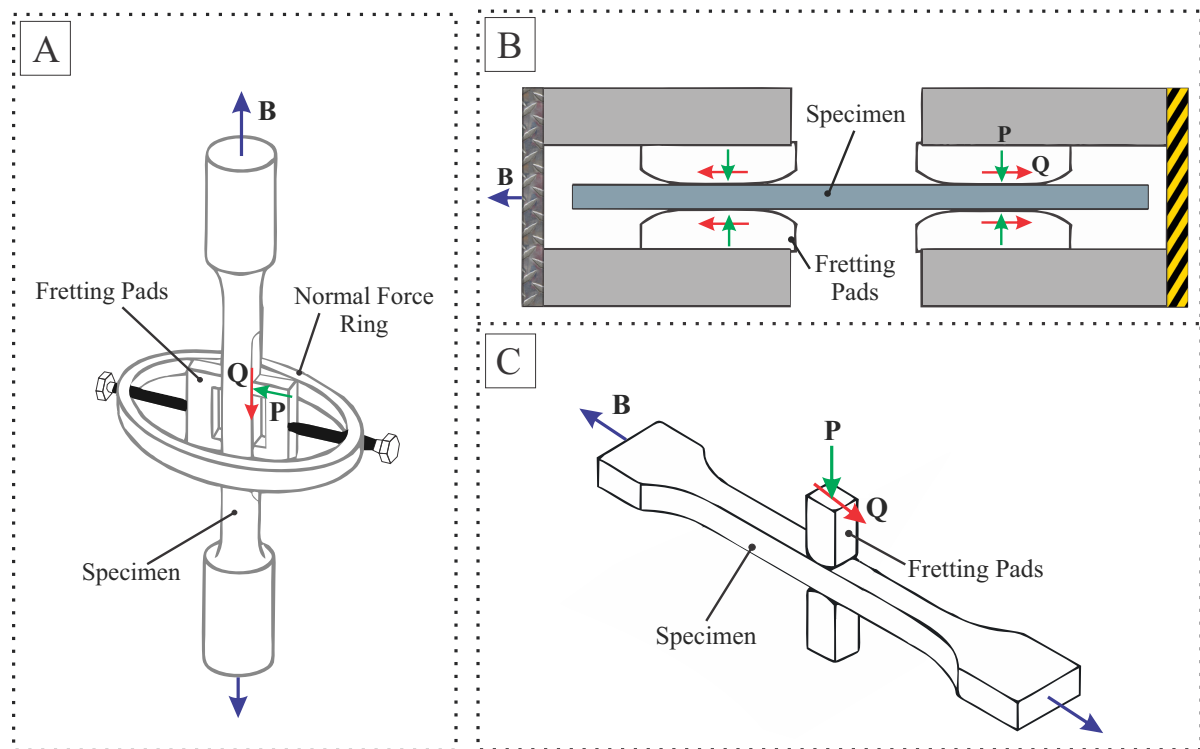


**Figure 2.20.** Commonly used types of fretting fatigue experimental testing (A) Bridge-type, (B) Grip-type and (C) Single clamp.

slip conditions, as gross slip would lead to slipping out of the grips. The tangential force at the interface is directly proportional to the axial force applied in the test system (ASTM, 2015).

In the late 1960s and early 1970s, Nishioka and Hirakawa introduced a novel experimental procedure for fretting fatigue, now known as the single clamp fretting fatigue test (Fig. 2.20C). This method involved cylindrical pads clamped against a flat specimen, offering advantages such as reduced pad alignment sensitivity and the potential for stress prediction via classical contact analysis, as explained in section 2.1.5. Key parameters for stress analysis, including normal load, tangential load, and bulk remote fatigue stress, could be easily measured and controlled (NOWELL *et al.*, 2006). The fretting loading device is attached to the test system frame, with displacement amplitude dependent on both fretting chassis and fatigue specimen compliance. Normal force application methods included springs, bolts, weights, pneumatic, or hydraulic actuators, while tangential force measurement could be achieved via strain gauges or force transducers (ASTM, 2015). Tests with spherical pads are common as well for this fretting fatigue test, as the ones conducted by Wittkowsky *et al* (2000) and Muñoz *et al* (2007).

Several researchers have directed their focus towards geometries resembling actual industrial

components (RUIZ *et al.*, 1984; RAJASEKARAN; NOWELL, 2006; SUNDE *et al.*, 2021). For instance, Ruiz *et al.*(1984) proposed an apparatus consisting of two blade specimens mounted in a central disk specimen. This setup subjected the blade specimens to tension loads to replicate centrifugal forces, while the central disk experienced tension loads simulating disc expansion under centrifugal loading. High cycle fatigue loads were induced by shakers connected to the blades. In a more recent approach, Sunde *et al.* (2021) introduced a novel fretting fatigue test rig based on the classical dovetail joint. This fixture arrangement utilized a universal joint to ensure self-alignment of the test rig when axial loads were applied, thereby providing symmetric loads to the specimens. The authors introduced a new capability for conducting fretting fatigue experiments and associated numerical analyses.

#### **2.1.7.1 Four actuators fretting fatigue machine test**

In this section, one presents the new fretting fatigue rig developed at the University of Brasilia (UnB), referred to as the UnB's four actuators fretting fatigue rig. This machine underwent several upgrades compared to its previous version, which had only two independent actuators and relied on an external device for applying the normal contact force. In this upgraded version, heating, cooling, and contact normal load application systems were implemented. The testing machine utilized is the MTS 322 Test Frame, which was modified by Almeida *et al.* (2022) to accommodate four uncoupled actuators. This modification allows for independent control of all loads involved in the fretting tests, including bulk, normal, and tangential loads. Consequently, loads can vary with time in-phase or out-of-phase and can be applied synchronously or asynchronously in their waveforms.

Equipped with both The Basic Test-Ware program and the Multipurpose Elite program, this machinery offers extensive control features, facilitating a wide range of test scenarios. Notably, the Multipurpose Elite program enhances control precision, enabling users to program the machine for executing complex tests involving variable amplitude and out-of-phase loadings. Further details will be addressed in the experiments presented in Chapter 6 of this thesis. Both programs also feature practical and effective systems for data acquisition and variable monitoring throughout the test process. Designed to operate at high temperatures (up to 750°C), this fretting fatigue apparatus is highly versatile and adaptable to various testing

conditions.

The schematic drawing in Fig. 2.21 illustrates the key components of the fretting apparatus. Notably, it includes a fixed and movable jaw (6 and 7) that securely hold the flat dog-bone tensile specimen between them. The pad holders (12), mounted on linear bearings (10), allow for precise application of normal loads or displacements to the pads. The movable jaw (7) is linked to a load cell (4) and a hydraulic actuator (3) capable of applying loads up to 250 kN, responsible for applying the fatigue load on the specimen. The fretting apparatus is further equipped with a load cell and LVDT sensor (2), along with a hydraulic actuator (1) capable of providing fretting loads up to 100 kN. Additionally, two MTS hydraulic actuators (9) apply the normal load to the fretting pads (11), with each actuator capable of applying up to 15 kN force under cyclic or static conditions. For further insights into the fretting apparatus design, refer to the work by Almeida *et al.* (2022).

### 2.1.7.2 Overhead conductors fatigue test

Another example that will be addressed in this work, specifically in Chapter 5, pertains to the effect of fretting on the fatigue response of overhead conductors. In transmission lines, overhead conductors are one of the most important components, frequently subject to fatigue failure as they are consistently exposed to random loadings with a multiaxial stress nature. This complexity makes the management of their failure a very challenging task. Failures typically manifest near or within components where the movement of the conductor is restrained, such as suspension clamps, spacer dampers, vibration dampers, and strain clamps (CARDOU *et al.*, 1992; AZEVEDO *et al.*, 2009; FADEL *et al.*, 2012; KALOMBO *et al.*, 2015). Hence, the development of a localized fatigue analysis capable of accounting for these features constitutes a more scientific approach, one that will enhance our understanding of fretting damage in wires (see Chapter 5). In this section, we will briefly discuss the overhead conductors test bench at the Laboratory of Fatigue and Structural Integrity of Overhead Conductors at the University of Brasilia. This facility is equipped with three resonance fatigue test benches, as depicted in Fig. 2.22.

Each bench spans 47 meters, divided into active (40 meters) and passive (7 meters) sections. At one end of the conductor, it is anchored in a fixed block at the passive span. The conductor is

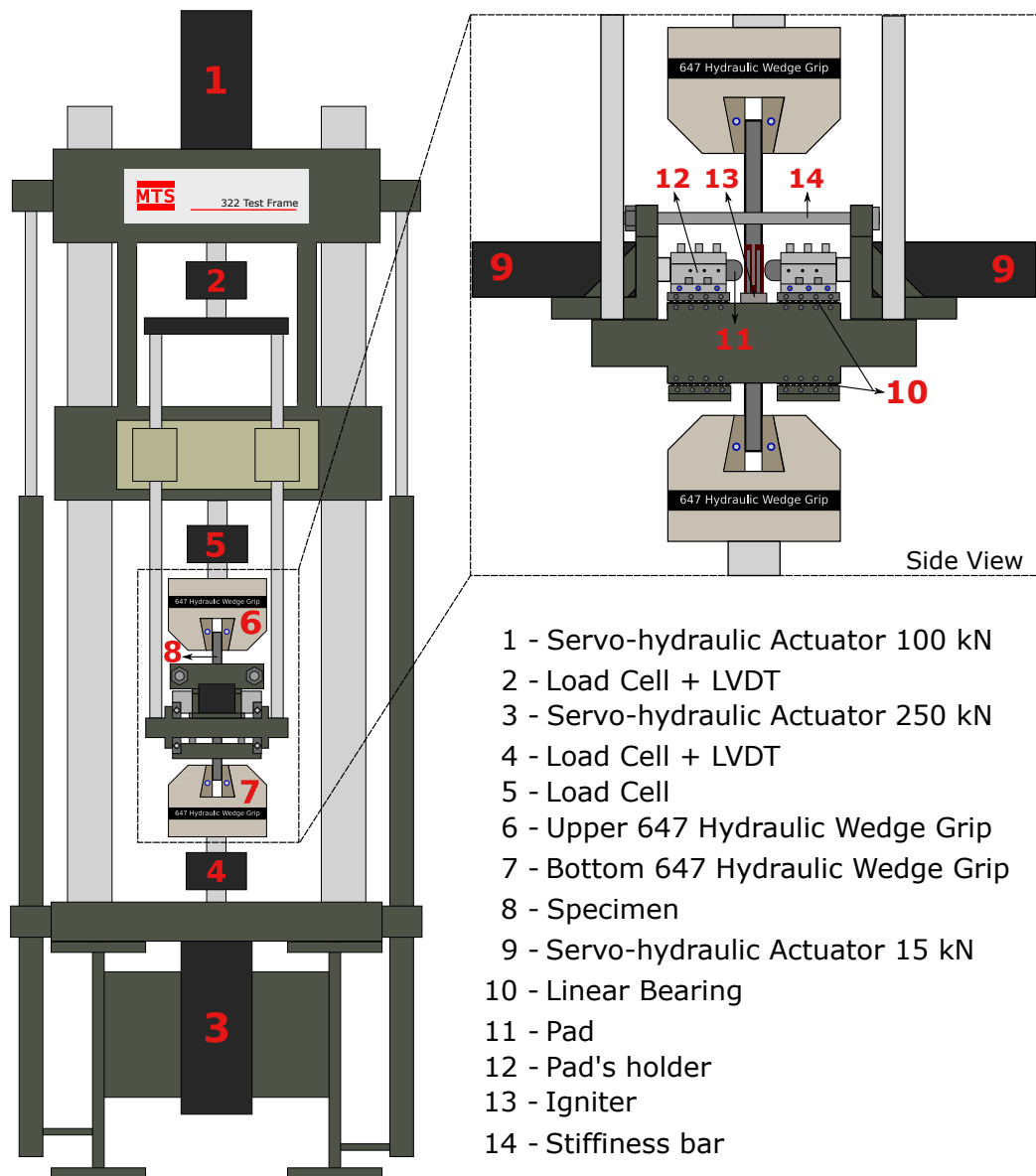


**Figure 2.21.** Schematic representation of the high-temperature fretting fatigue rig with four actuators at the University of Brasilia (ALMEIDA *et al.*, 2022).

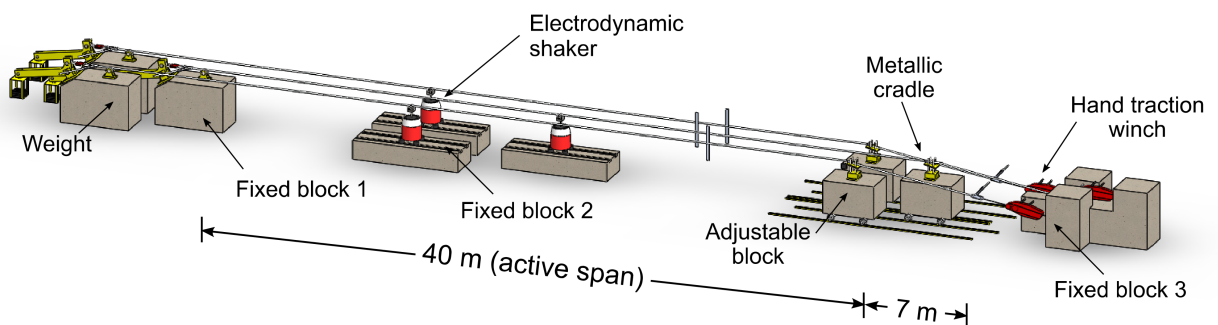


**Figure 2.22.** Schematic representation of the resonance fatigue test bench for testing overhead conductors.

then assembled into a suspension clamp attached to a metallic cradle, resting on an adjustable block. Typically, the suspension clamp is positioned at an angle of  $5^{\circ}$  to  $10^{\circ}$  to mirror the sag angle of the conductor. On the left edge of the active span, the conductor is linked to a lever arm loaded by a dead weight, generating the static tension load. To simulate aeolian vibration, an electronically controlled shaker is connected to the conductor within the active span. The fatigue test is conducted under displacement control, with the level of displacement regulated by an accelerometer installed on the conductor, 89 mm from the last point of contact between the conductor and the clamp. The accelerometer's output signal is integrated into a closed-loop control system, ensuring the shaker maintains the prescribed displacement (KALOMBO *et al.*, 2015; PESTANA *et al.*, 2018; CÂMARA *et al.*, 2021).

The excitation frequency is determined through a sweep procedure, with the test frequency selected to closely match one of the resonant frequencies. Additionally, each bench is equipped with a signal acquisition system and a wire break detection system. The acquisition system enables simultaneous data collection via the network and signal conditioners, with channels configurable for data acquisition from thermocouples, load cells, strain gauges, etc.

Wire break detection employs a rotation sensor positioned at the first node from the suspension clamp, consisting of two aluminum blades attached to the conductor by a hose clamp. Laser sensors measure displacements at each edge of the blade. When a wire breaks, the cable rotates due to a redistribution of the tangential force component among the remaining strands. Displacements in opposite directions at each edge of the blade are measured by the sensors and recorded by the acquisition system, with the number of cycles registered for each event. Given that the aluminum layers of the conductor are wrapped in opposite directions, the detection system can also identify the layer where the strand breaks. Further details regarding this test bench can be found in Badibanga (2017).

There are several factors influencing the wire fatigue behavior, and it is well known that fretting effect stands out as one of the most crucial (GARCIA *et al.*, 2020; OMRANI *et al.*, 2021; ARAÚJO *et al.*, 2020; MATOS *et al.*, 2022; MONTALVO *et al.*, 2023). The conductors itself endure simultaneous static loads, including stretching loads, the weight of spans, and contact pressure within clamps. Moreover, they are also subjected to aeolian vibrations, which give rise to intricate multiaxial stress conditions at localized regions, specifically at the wire/wire

interface (LISKIEWICZ; DINI, 2023). Consequently, these stress states possess the potential to induce premature fatigue failures. Therefore, an effective modeling of the wire behavior is fundamental for a comprehensive understanding of the overhead fretting fatigue's issue.

At the University of Brasília, there is also another specialized machine for measuring fatigue in wires of these conductors. This equipment has been thoroughly described and documented by Garcia *et al.* (2020). The MTS test frame was developed specifically to assess fretting fatigue in wires. Featuring three independent actuators, it enables tests to be conducted under controlled load or displacement. Engineered to apply normal, tangential, and bulk forces, it facilitates the examination of wear levels and surface morphology of the wires. Integrated with the universal MTS testing machine, the device can effectively control and monitor various test parameters, including tangential load, remote fatigue load, wire specimen displacement, and reactive load of the grip. Furthermore, it accommodates tests with variable angles between the wire pad and specimen, providing researchers with flexibility to explore different contact configurations for investigative purposes.

### 2.1.8 Neural networks in the fretting fatigue context

In recent decades, the integration of artificial intelligence (AI) methodologies has revolutionized the landscape of engineering disciplines. Machine learning, a subset of AI, has emerged as a powerful tool for predictive modeling and decision-making processes. Within this domain, artificial neural networks (ANNs) have garnered significant attention. ANNs draw inspiration from the human brain's neural architecture, consisting of interconnected nodes that emulate neurons. This paradigm shift towards computational models inspired by biological systems has found extensive applications in diverse fields, including mechanical engineering.

Within the mechanical engineering context, the application of neural networks has shown promise, particularly in the predictive modeling of complex phenomena such as fretting fatigue life. Fretting fatigue, as has been emphasized, is a critical concern in structural integrity, which necessitates accurate predictions for proactive maintenance and design optimization. Leveraging the capabilities of neural networks, researchers have developed models that exhibit the capacity to learn and generalize patterns from complex datasets, facilitating the prediction of fatigue life under varying conditions. As we delve into the intricacies of neural networks in

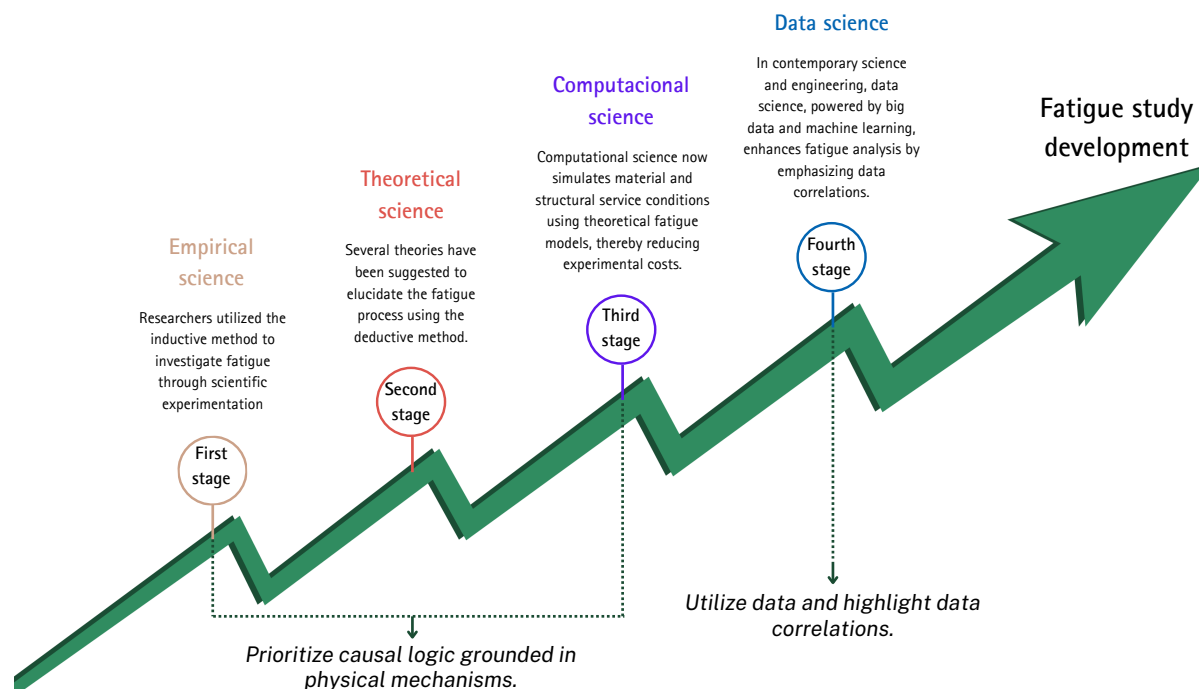


**Figure 2.23.** Stages of fatigue development, adapted from Wang *et al.* (2023b).

this work, it is essential to appreciate their roots in the broader context of machine learning and artificial intelligence.

Recent studies have delineated stages in the evolution of fatigue study, highlighting an increasing exploration of data science-based models, as depicted in Fig. 2.23 (WANG *et al.*, 2023b). This trend is primarily attributed to the potential to uncover new mathematical correlations not previously revealed by existing theoretical models. Consequently, four distinct stages have been identified in this process: empirical science, theoretical science, computational science, and data science. It is evident that each subsequent stage builds upon the preceding one, and in practice, these approaches often intertwine to enhance the robustness of the models developed.

In this doctoral thesis, the decision to adopt such approach (fourth stage in Fig. 2.23) in the context of fatigue failure analysis is motivated by several factors, in addition to its innovative nature. Traditionally, physics-based models incorporate empirical equations alongside with numerical models. However, the theoretical deductive methodology is based by numerous assumptions and idealizations, constraining its accuracy in describing real experimental phenomena. Conversely, the inductive method prioritizes the analysis of phenomena, resulting in

limited theoretical generality. Finite element simulations, while based on physical mechanisms and laws, are constrained by model reliability and often fail to fully capture variation patterns without incurring significant computational costs when feasible. These methods typically rely on idealized models and emphasize causal logic within research paradigms.

In this section, a comprehensive examination of machine learning models will be presented, focusing on their fundamental characteristics and diverse classifications. Subsequently, further details concerning the neural network employed in this study will be elucidated, alongside the adopted training algorithm, specifically the backpropagation method.

### 2.1.8.1 Machine learning models

Machine learning encompasses a spectrum of models, ranging from simpler forms like linear regression and decision trees to more intricate structures such as neural networks and support vector machines, each tailored to specific data types and tasks. The choice of model is based on factors such as problem nature, data availability, and desired outcomes. These models can be classified in various ways, specifically:

- **Learning Paradigm:** Supervised, Unsupervised, Semi-Supervised Learning, Reinforcement Learning. These paradigms delineate models based on the availability of labeled data during training. Supervised learning utilizes labeled data, unsupervised learning operates on unlabeled data, and semi-supervised learning merges both. In reinforcement learning, an agent learns to make sequential decisions to maximize cumulative rewards while interacting with a dynamic environment. The agent receives feedback in the form of rewards or penalties after each action, aiming to learn a policy that maximizes total reward over time (BISHOP; NASRABADI, 2006; HASTIE *et al.*, 2009; SUTTON; BARTO, 2018; HAYKIN, 2008).
- **Output Type:** Models can predict different outputs, such as classification (assigning inputs to categories or classes) or regression (predicting continuous values) (JAMES *et al.*, 2013). For instance, fatigue life prediction yields continuous values, typically addressed using regression analysis.
- **Complexity:** Models vary in complexity, from linear regression to intricate deep learning

architectures like convolutional neural networks (DOMINGOS, 2012).

- **Learning Approach:** Further classification is based on learning approach, such as instance-based learning (e.g., k-nearest neighbors)(ALPAYDIN, 2020), probabilistic models (e.g., naive Bayes) (BARBER, 2012), and rule-based models (e.g., decision trees) (QUINLAN, 2014).
  
- **Algorithm Family:** Models are also grouped into families based on underlying algorithms, including decision trees, support vector machines, artificial neural networks, clustering algorithms, and ensemble methods (HAYKIN, 2008; CRISTIANINI; SHAWE-TAYLOR, 2000; DIETTERICH, 2000; QUINLAN, 2014; JAIN; DUBES, 1988).

In Fig. 2.24, these machine learning models are classified based on the learning type (learning paradigm) category. Notably, supervised learning models are divided into two main categories: traditional and deep learning models. Traditional models were prevalent before the emergence of deep learning and include Support Vector Machine (SVM), Logistic Regression, K-nearest Neighbors (KNN), Decision Trees, Gaussian Process Regression (GPR) and ANNs. Deep learning models, such as Deep Neural Networks (DNN), Convolutional Neural Networks (CNN), and Recurrent Neural Networks (RNN), feature complex architectures with multiple layers of processing, capable of automatically learning intricate data representations. The distinction between traditional and deep learning models typically stands on model architecture and learning methodology. Traditional models tend to have simpler structures and were widely used before the advent of more complex deep learning architectures, characterized by their ability to learn intricate data representations automatically (BISHOP; NASRABADI, 2006; HAYKIN, 2008).

Unsupervised learning constitutes a machine learning category where algorithms are trained on data lacking predefined labels or categories. Instead, the objective is to uncover structure within the data, such as clusters or patterns, without the guidance of output labels. This makes it valuable for discovering latent information within data and exploring complex relationships between variables. It serves as a powerful tool for delving into and comprehending intricate datasets without the need for explicit label guidance. It primarily finds application in clustering and dimensionality reduction tasks, such as K-means clustering, Principal Component Analy-

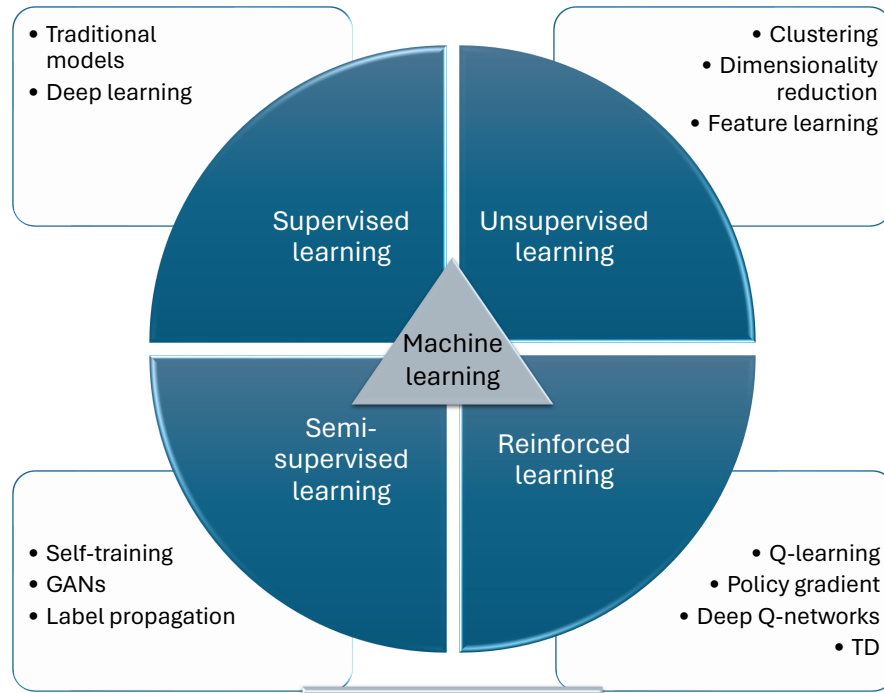


**Figure 2.24.** Classification of the machine learning models.

sis (PCA), and Self-Organizing Map (SOM). Additionally, with the widespread adoption of deep learning, unsupervised learning is also utilized for feature learning. Among deep learning models, Generative Adversarial Networks (GANs) enable the generative network to produce samples conforming to the distribution characteristics of real data through adversarial training, thereby facilitating feature enhancement (HASTIE *et al.*, 2009).

Semi-supervised learning bridges the gap between supervised and unsupervised learning paradigms, offering a pragmatic solution for scenarios where labelling vast datasets proves costly and impractical. By leveraging both labelled and unlabelled data during training, semi-supervised models enhance learning accuracy, particularly in complex processes like classification and regression tasks. The inclusion of unlabelled data enriches model iterations, providing valuable insights into data distribution and reducing human resource and time costs associated with labelling. This approach optimally balances the subjective influence of labelled data with the informative nature of unlabelled data, making semi-supervised learning a superior choice for tackling real-world machine learning challenges. Examples include self-training, GANs (also used in semi-supervised learning), and label propagation. The label propagation algorithm propagates the labels of labeled data to unlabeled data, using the similarity between examples to infer the labels of these additional data points (RASMUS, 2015).

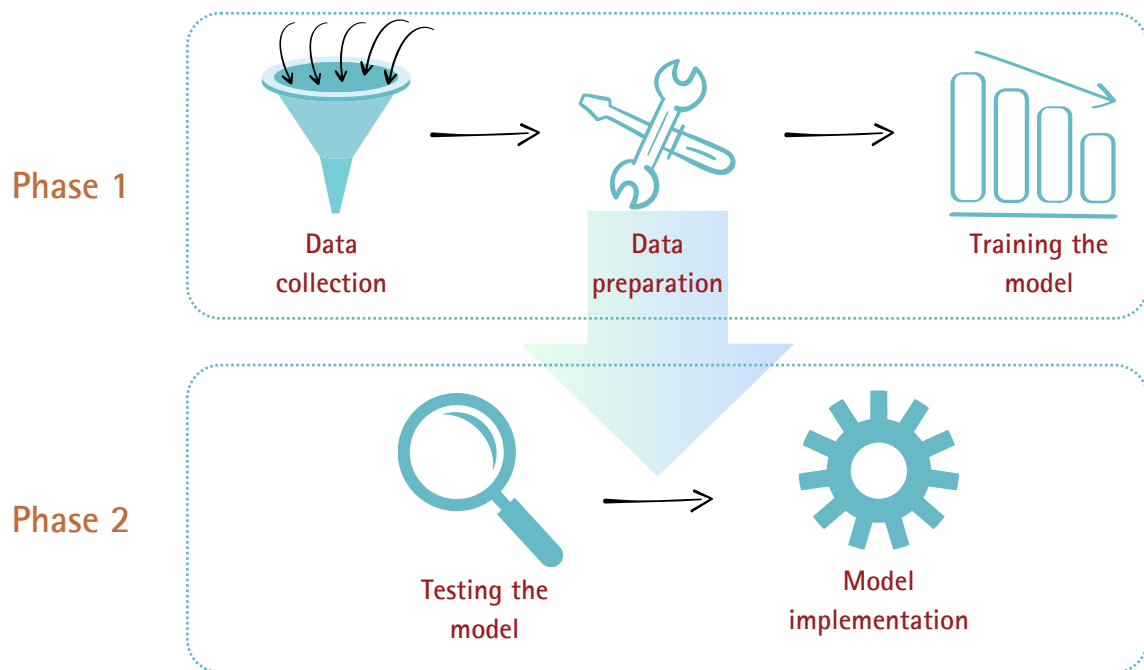


**Figure 2.25.** Development of a data-driven model based on supervised learning.

Reinforcement learning is a machine learning approach in which an agent interacts with an environment, taking actions and receiving rewards or penalties. The objective is to learn a policy of action that maximizes cumulative reward over time. The agent utilizes techniques such as Q-Learning, Policy Gradient Methods, Deep Q-Networks, and Temporal-Difference Learning (TD) to learn optimal decision-making in complex and dynamic environments. This paradigm finds wide application in sequential decision-making problems such as games, robotics, and system optimization (ARULKUMARAN *et al.*, 2017; SUTTON; BARTO, 2018).

In the process of creating a machine learning model, it is generally recommended to follow a few steps. Initially, it is essential to define the problem well, identifying the specific learning task (classification, regression, clustering, etc.), understand the requirements and constraints of the problem, and define evaluation metrics to measure the model's performance. Thus, we can divide this process into two phases, as shown in Fig. 2.25.

In Phase 1, the first step is data acquisition and exploration, obtaining the necessary data to train and test the model. This step involves data collection, cleaning, and preprocessing, removing noise, filling missing values, and transforming the data into a suitable format for the model. It is also recommended to explore this data, understanding its distribution, identifying

patterns, and relevant features. Also in Phase 1, the second step is data preparation, dividing them into training, validation, and test sets. Typically, the data is split into training and test sets to evaluate the final model's performance, and the validation set is used to adjust the model's hyperparameters.

In the final step of Phase 1, one has model selection and training, involving choosing the most suitable machine learning algorithm for the problem at hand and training it. During training, it is necessary to adjust the model's parameters to minimize the loss function, depending on the learning algorithm. Evaluation is also carried out using validation data and/or cross-validation techniques (DOMINGOS, 2012). Based on these results, the hyperparameters should be adjusted to improve the model's performance.

In the second phase, the model will be tested with other data, called test data, which were not considered during the model training stage. This phase measures the model's generalization potential against data different from the training data. Finally, there is a last step in the second phase, related to the implementation and monitoring of its performance in a real-world environment. This may include implementing an API so that the model can be accessed by other systems, continuous monitoring of the model's performance, and periodic updating of the model with new data, if necessary (JAMES *et al.*, 2013; HAYKIN, 2008).

Data-driven methodologies have garnered significant advancements across various domains and have seen widespread industrial applications. However, persistent challenges remain. Firstly, machine learning models often operate as black-box systems, lacking transparency in their prediction processes and physical interpretability. Consequently, the comprehension of fatigue damage mechanisms by these models is constrained by the inherent limitations of the datasets and model structures, leading to incomplete representations of the underlying physical processes. Secondly, while many machine learning models may yield predictions closely aligned with observed values, discrepancies arise due to inconsistencies with established physical mechanisms (WANG *et al.*, 2023b).

The comprehension of fatigue damage processes by machine learning models is constrained by the physical significance of input and output data, as well as by the model's inherent structure. Enhancing the model's understanding of underlying physics to attain interpretability remains a challenge. Physics-informed neural networks (PINN) represent an emerging research

paradigm wherein physical theories and domain constraints are integrated into data-driven models to achieve interpretability (CHEN *et al.*, 2023; ZHOU *et al.*, 2023; HALAMKA *et al.*, 2023). As another strategy, some researchers have adopted an intriguing technique, data-driven models are carried out to reduce the error between the output of a well established predefined model and the true or experimental output. In essence, these models serve to refine existing theoretical models, rendering this methodology notably robust. Such an approach is particularly well-suited for simpler models (CÂMARA; FREIRE, 2011; OLIVEIRA *et al.*, 2019; BRITO OLIVEIRA *et al.*, 2023b). Based on all these considerations, one aims to propose a novel hybrid approach, incorporating elements from all four phases of fatigue analysis (Fig. 2.23): empirical, theoretical, numerical, and data-driven. This approach will be elaborated upon in subsequent chapters. Hence, the proposed solution establishes a synergistic and coherent connection between the architecture of ANNs and the fundamental physics of the mechanical problem, mitigating the challenges associated with PINNs.

### 2.1.8.2 Artificial neural networks

The term 'developing' nervous system is indicative of a malleable brain, capable of plasticity, allowing it to adapt to its environment. Much like the essential role plasticity plays in neurons functioning as information-processing units in the human brain, it also pertains to artificial neural networks composed of artificial neurons. In this work, we refer to artificial neural networks as ANN or simply neural networks. Broadly speaking, neural networks represents a computational model designed to emulate the brain's performance in executing specific tasks or functions of interest. Typically, such networks are instantiated using electronic components or simulated within software on a digital computing platform. In this work, our focus lies on a specific category of neural networks, which achieve computational outputs through the mechanism of learning. To attain commendable performance, neural networks rely on intricate interconnections among elementary computing units termed 'neurons' or 'processing units.' In this way, the ANN can be conceptualized as an adaptive machine (HAYKIN, 2008).

According to Haykin (2008), a neural network is a massive parallel distributed processor comprised of elementary processing units, inherently inclined towards the storage and utilization of experiential knowledge. It resembles to the human brain in two fundamental aspects:

- The acquisition of knowledge by the network occurs through a learning mechanism from its environment.
- Synaptic weights, representing the strengths of interneuronal connections, serve as repositories for the assimilated knowledge.

The learning process in neural networks is facilitated by a learning algorithm, which systematically adjusts the synaptic weights to achieve specific design objectives. Nonetheless, ANN can also autonomously modify their topology, similar to the natural process observed in the human brain where neurons can perish, and new synaptic connections can emerge. Recursive neural networks (GOLLER; KUCHLER, 1996; SOCHER *et al.*, 2010), alongside self-organizing neural networks such as Kohonen’s Self-Organizing Maps (KOHONEN, 1982), exemplify a subset of neural architectures capable of dynamically modifying their own topology. These networks exhibit a remarkable capacity to adapt their structure to varying and complex input patterns, making them invaluable tools in domains requiring flexible data processing, such as natural language processing and audio analysis. By autonomously adjusting their architecture, recursive neural networks effectively tackle challenges posed by dynamic and variable data structures, thus showcasing the potential of neural networks to model and understand intricate real-world phenomena.

As said, neural networks derive their computational capabilities from two main sources: their highly parallel distributed architecture and their capacity for learning, thereby enabling generalization. Generalization denotes the neural network’s ability to generate plausible outputs for inputs absent during the training phase. These dual information-processing capabilities allow neural networks to seek effective approximate solutions for intricate and large-scale problems that would otherwise be computationally infeasible.

A main element within neural networks, neurons play a foundational role in processing information through a triad of essential components: synapses, adders, and activation functions, as shown in Fig 2.26. Synapses, characterized by individual weights, facilitate the multiplication of input signals, while adders aggregate these weighted inputs to produce a linear combination. The activation function, often termed a squashing function, imposes constraints on the output’s amplitude, confining its range to a finite value typically represented as  $[0,1]$  or  $[-1,1]$ . Notably, unlike their biological counterparts, artificial neuron synaptic weights may span negative and

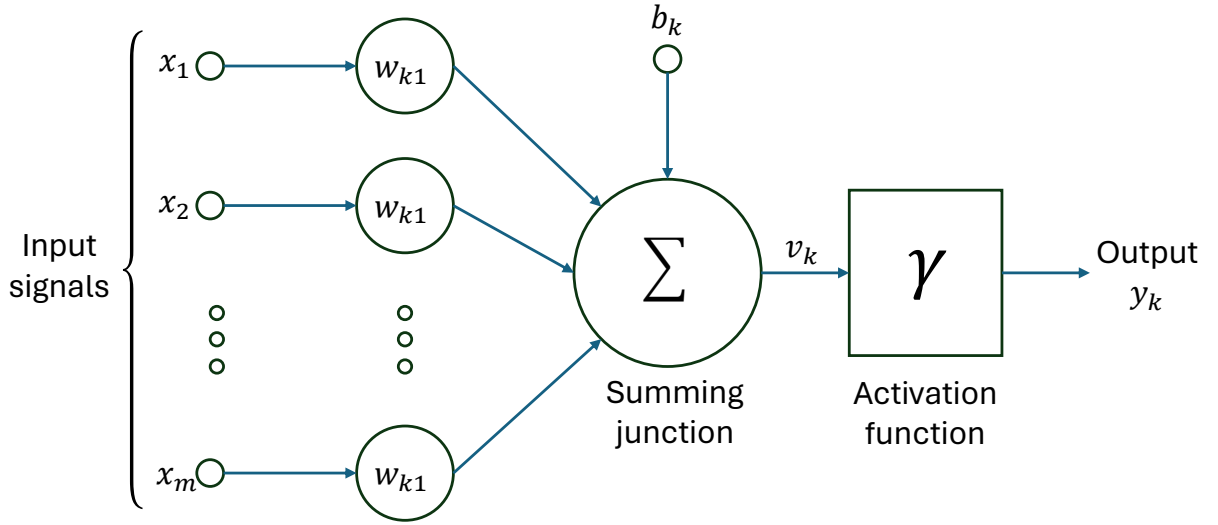


**Figure 2.26.** Example of a nonlinear model of a neuron, labeled  $k$ .

positive values, underscoring the nuanced interplay between biological inspiration and computational implementation within neural network frameworks (HAYKIN, 2008). In mathematical terms, we can describe neuron  $k$  by writing the pair of equations:

$$u_k = \sum_{j=1}^m w_{kj} x_j \quad (2.122)$$

and

$$y_k = \gamma(u_k + b_k) \quad (2.123)$$

where  $x_1, x_2, \dots, x_m$  are the input signals;  $w_{k1}, w_{k2}, \dots, w_{km}$  are the respective synaptic weights of neuron  $k$ ;  $u_k$  is the linear combiner output due to the input signals;  $b_k$  is the bias;  $\gamma(\cdot)$  is the activation function; and  $y_k$  is the output signal of the neuron. The use of bias  $b_k$  has the effect of applying an affine transformation to the output  $u_k$  of the linear combiner. They are used to regulate the input value of a given neuron.

In this study, the ANN is utilized as an approximation function, as we believe that there exists a mathematical function describing the relationship between stresses and fretting fatigue life (see details starting from Chapter 3). In Fig. 2.27, one presents a general basic example of a multi-layer perceptron network. Activation functions, denoted by  $\gamma$ , are applied from the first hidden layer up to the output layer. The arrows pointing from a previous layer to the next

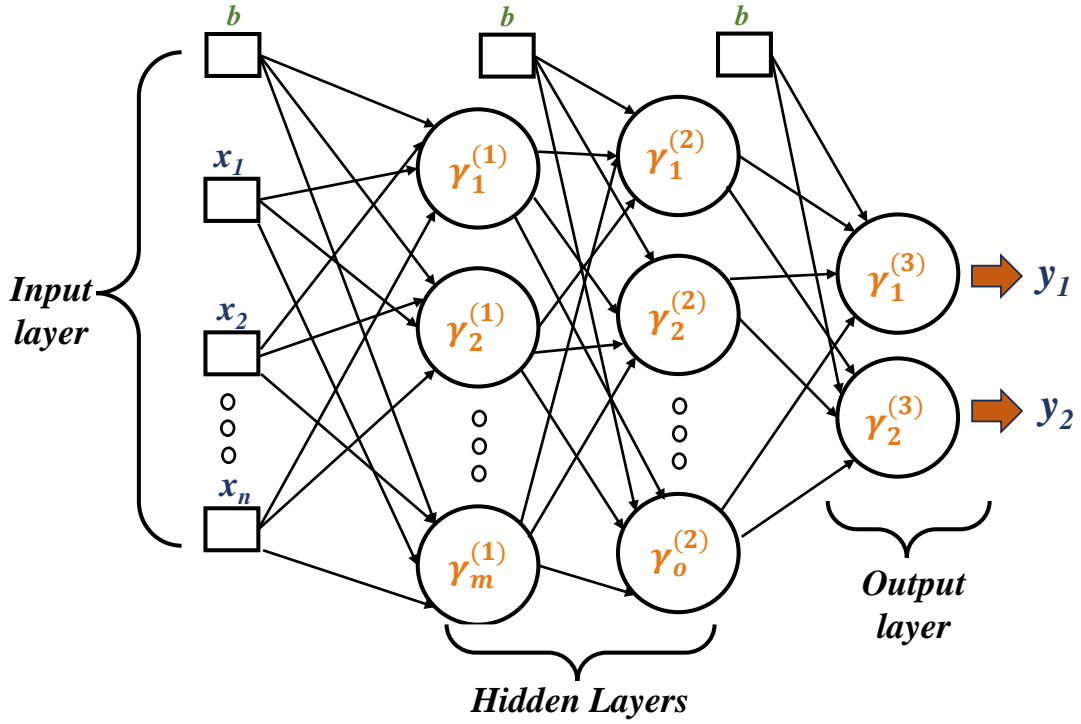


**Figure 2.27.** Example of a multi-layered ANN architecture.

one represent the weights, while  $b$  denotes the bias values, which are employed to adjust the input value of a given neuron. The output of neuron  $j$  at layer  $l$  is determined by Eq. 2.124, where the subscript  $k$  refers to the neuron index of the previous layer ( $l - 1$ ). It is noteworthy that  $\gamma^{(l-1)}$  corresponds to  $x_k$  for the first hidden layer.

$$\gamma_j^{(l)} = \gamma \left( \sum_{k=1}^n w_{jk}^{(l)} \gamma_k^{(l-1)} + b w_{j0}^{(l)} \right) \quad (2.124)$$

A fundamental theorem in the field of neural networks is the Universal Approximation Theorem. Proposed independently by George Cybenko in 1989 and further refined by Kurt Hornik in 1989, this theorem demonstrates the remarkable capability of neural networks to approximate any continuous function with arbitrary precision, provided certain conditions are met. Cybenko's original theorem asserts that a neural network with a single hidden layer and a sigmoidal activation function can approximate any continuous function on a compact input space (CYBENKO, 1989). Later, Hornik *et al.* (1989) extended this result to show that multilayer feedforward networks with only a single hidden layer are also universal approximators. These findings have profound implications for the field of machine learning, highlighting the expressive power and versatility of neural network architectures. Despite its theoretical significance,

practical applications of the Universal Approximation Theorem require careful consideration of factors such as network architecture, training algorithm, and data quality. Nonetheless, the theorem remains a cornerstone result in neural network theory, shaping the development of modern machine learning algorithms and techniques.

Based on this, as the reader will soon see, this study will consider neural network models with only one hidden layer. The input layer comprises the independent variables  $(x_1, x_2, \dots, x_n)$  believed to govern the modeled problem. Conversely, the output layer provides the predictions of the ANN model. In this research, only one output - representing the predicted fatigue life ( $y$ ) - is required from the model. The hidden layer, comprising  $m$  neurons, is responsible for establishing the complex relationships between the input and output variables of the ANN model. Thus, for an ANN with only one hidden layer, we can mathematically represent the ANN calculation process through the following expression:

$$y = \gamma^{(2)} \left( \sum_{i=1}^m w_i^{(2)} \gamma_i^{(1)} \left( \sum_{j=1}^n w_{ij}^{(1)} x_j + bw_{i0}^{(1)} \right) + bw_0^{(2)} \right) \quad (2.125)$$

In the equation,  $w_{ij}^{(1)}$  represents the weight connecting the  $i$ -th neuron of the hidden layer with the  $j$ -th entry of the input layer. The term  $bw_{i0}^{(1)}$  stands for the bias considered in the  $i$ -th neuron of the hidden layer. Similarly,  $w_i^{(2)}$  represents the weight linking the  $i$ -th neuron of the hidden layer with the output layer, and  $bw_0^{(2)}$  is the bias of the output layer. Note that some subscripts are omitted since only one neuron is considered in the output layer.

Additionally, it is worth noting that there are various types of activation functions, such as linear, sigmoid, tanh, ReLU, Leaky ReLU, and Softmax. The latter is commonly used in the output layer of neural networks for multi-class classification problems (BISHOP; NASRABADI, 2006; HAYKIN, 2008). In this work, we will primarily focus on the sigmoid and tanh functions. The following equations show the sigmoid function and its derivative, respectively:

$$\gamma(x, \zeta) = \frac{1}{1 + e^{-\zeta x}} \quad (2.126)$$

$$\frac{d\gamma}{dx}(x, \zeta) = \zeta \cdot \gamma(x, \zeta) \cdot (1 - \gamma(x, \zeta)) \quad (2.127)$$

The sigmoid and hyperbolic tangent (tanh) activation functions are pivotal components

in neural networks, each offering distinct characteristics. The sigmoid function, defined in Eq. 2.126, maps inputs to the range (0, 1), making it suitable for binary classification tasks where outputs represent probabilities. Similarly, the tanh function, expressed in Eq. 2.128, maps inputs to the range (-1, 1), maintaining a centered S-shaped curve. Both functions are differentiable across their domains, facilitating gradient-based optimization methods like backpropagation. The derivatives of these activation functions (Eqs. 2.127 and 2.129) are crucial for efficient network training, aiding in gradient propagation and weight adjustment. Despite their usefulness, the sigmoid function can suffer from vanishing gradient issues, particularly with extreme input values, while the tanh function produces more sparse outputs. Overall, these activation functions and their derivatives play fundamental roles in effective neural network training, enabling the propagation of gradients for learning meaningful data representations.

$$\gamma(x, \zeta) = \tanh(\zeta x) = \frac{e^{\zeta x} - e^{-\zeta x}}{e^{\zeta x} + e^{-\zeta x}} \quad (2.128)$$

$$\frac{d\gamma}{dx}(x, \zeta) = \zeta \cdot (1 - \tanh^2(\zeta x)) = \zeta \cdot \operatorname{sech}^2(\zeta x) \quad (2.129)$$

The parameter  $\zeta$  in the tanh and sigmoid functions (Eqs. 2.126 and 2.128) plays a pivotal role in adjusting the slope of the function's curve. As shown in Fig 2.28, increasing  $\zeta$  steepens curves, leading to a more rapid response to changes in input values. Conversely, decreasing  $\zeta$  makes the curve less steep, resulting in a smoother and more gradual response to input variations. Thus,  $\zeta$  controls the sensitivity of these activation functions to input changes, with larger values amplifying small differences and smaller values providing a more subdued response. In practical terms, adjusting  $\zeta$  during network training allows for dynamic adaptation of the activation function's behavior to suit the data characteristics and specific task requirements.

The last fundamental point to address is regarding the model training. The learning algorithm adopted in this work is backpropagation. Backpropagation stands as one of the most prevalent and widely employed training algorithms in neural networks. Its functionality lies in computing the gradient of the error function with respect to the network's weights, subsequently adjusting these weights to minimize the error. This iterative process optimizes the network's performance by updating the weights based on the calculated gradients. Gradient Descent, on the other hand, is a ubiquitous optimization algorithm frequently used with backpropagation

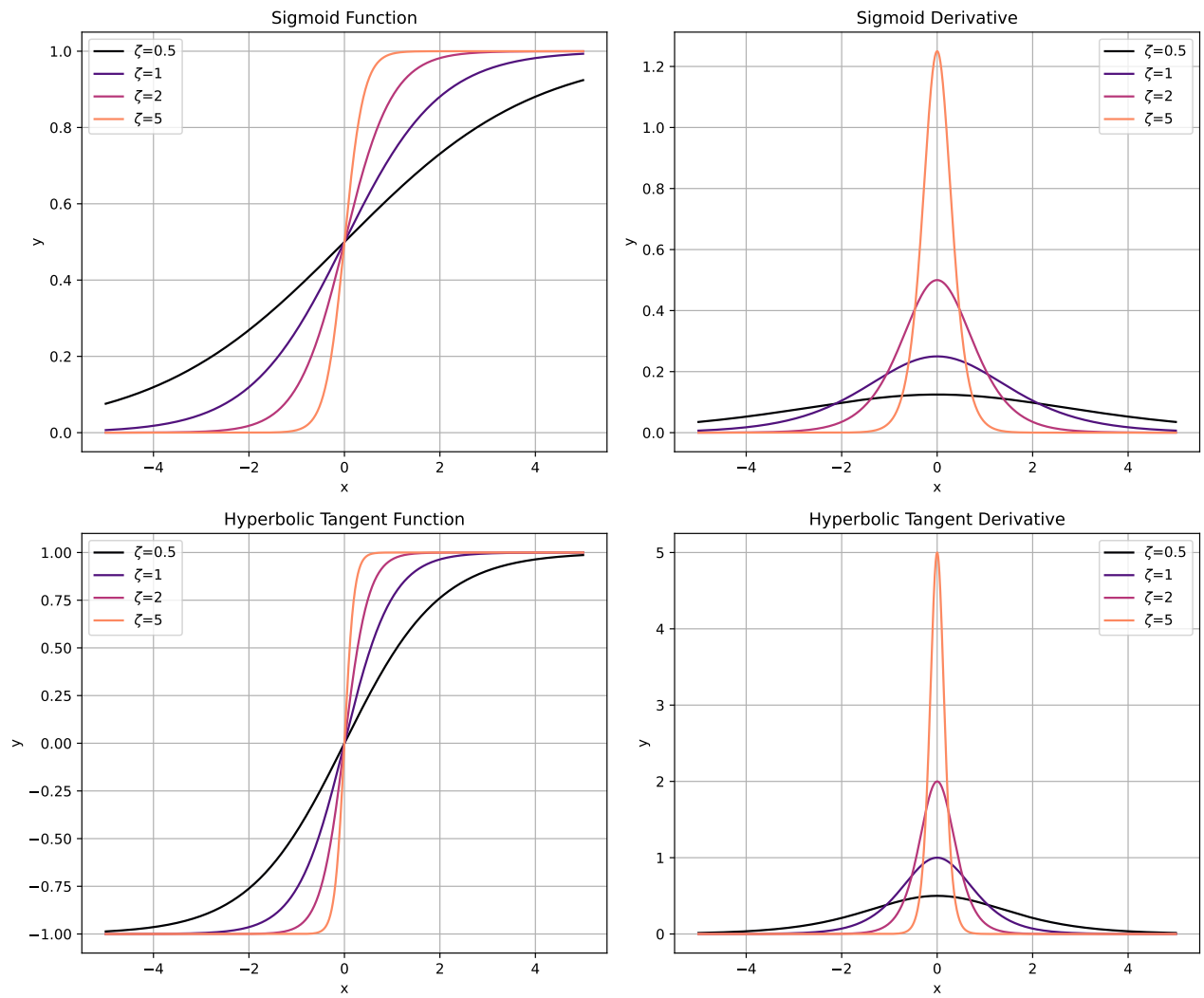


**Figure 2.28.** Examples of sigmoid and tanh functions along with their derivatives.

to fine-tune the network's weights. It involves calculating the gradient of the error function with respect to the weights and updating the weights in the opposite direction of the gradient to minimize the error. This iterative optimization process enables the network to converge gradually toward the optimal set of weights that minimize the error function, thereby enhancing its predictive capabilities. In summary, both backpropagation and gradient descent play indispensable roles in neural network training, facilitating the iterative adjustment of weights to minimize error and optimize performance.

Additionally, there are other noteworthy methods to briefly discuss. Among the most utilized are the Levenberg-Marquardt algorithm, renowned for its prowess in nonlinear regression problems, and the Newton-Raphson algorithm, which leverages the Hessian matrix to ascertain the most efficient search direction. Furthermore, Quasi-Newton methods such as BFGS and L-BFGS offer effective solutions for large-scale optimization problems, while the Conjugate Gradient algorithm is noted for its computational efficiency. Lastly, the Adam algorithm, with its dynamic adaptation of learning rates, finds extensive application in deep neural networks. From here, we will focus on creating the ANN model and subsequently on the functioning of the training algorithm.

To offer a more practical explanation of the algorithm's operation, certain considerations are necessary. Firstly, let us consider the scenario of a model featuring only one hidden layer. It is imperative to note that the explicit reasoning presented here can be readily extended to models with networks comprising multiple hidden layers. For a network with a single hidden layer, let the weight matrices ( $w_{ij}$ ) between the input layer and the hidden layer be represented as  $W$ , and those between the hidden layer and the output layer as  $V$ . Analogous to Eq. 2.125, the synaptic weights of matrix  $V$  are denoted as  $w_i^{(2)}$  and those of matrix  $W$  as  $w_{ij}^{(1)}$ . Consequently, the sole output neuron features a linear activation function, wherein its output equates to its input, corresponding to the value  $y$  specified in Eq. 2.125.

The fundamental principle of the backpropagation algorithm dictates that these weights must be updated at each iteration through a correction  $\Delta w$  to the synaptic weight  $w$ . This correction is proportionate to the partial derivative  $\partial\Gamma/\partial w$ , where  $\Gamma$  denotes the cost function used as the basis for error calculation. Notably, this function quantifies the disparity between the desired value and the calculated value. Such functions serve to evaluate the model's perfor-

mance relative to the training data and guide the process of optimizing the model's parameters during training. In our analysis, we consider the function known as the *total instantaneous error energy* (HAYKIN, 2008), which is defined as:

$$\Gamma = \frac{1}{2}e_{out}^2 \quad (2.130)$$

where  $e_{out}$  is the error signal produced at the output of neuron which is defined by:

$$e_{out} = d - y \quad (2.131)$$

where  $d$  is the desired-response value.

Thus, according to the chain rule of calculus, one can express the gradient  $\partial\Gamma/\partial w$  in terms of:

$$\frac{\partial\Gamma}{\partial w} = \frac{\partial\Gamma}{\partial e_{out}} \cdot \frac{\partial e_{out}}{\partial y} \cdot \frac{\partial y}{\partial v} \cdot \frac{\partial v}{\partial w} \quad (2.132)$$

Therefore, this gradient represents a sensitivity factor, determining the direction of search in weight space for the synaptic weight  $w$  (HAYKIN, 2008). From Eq. 2.130, we have that  $\frac{\partial\Gamma}{\partial e_{out}} = e_{out}$ , and from Eq. 2.131, we have that  $\frac{\partial e_{out}}{\partial y} = -1$ . If  $v$  represents the argument of the neuron's activation function, the corresponding linear combination of each layer, the reader may have already noticed that it will change for each of them, meaning that the gradient  $\Delta W$  and  $\Delta V$  will be different.

Thus, let us express the value of  $v$  for each case. For the neuron of the output layer, corresponding to the update of matrix  $V$ ,  $u$  will be equal to  $\left(\sum_{i=1}^m w_i^{(2)}\gamma_i^{(1)}\left(\sum_{j=1}^n w_{ij}^{(1)}x_j + bw_{i0}^{(1)}\right) + bw_0^{(2)}\right)$  and for the corresponding neurons of the hidden layer, related to the weights of matrix  $W$ , the value of  $u$  will be:  $\left(\sum_{j=1}^n w_{ij}^{(1)}x_j + bw_{i0}^{(1)}\right)$ . Similarly, the fourth term of the chain rule in equation 2.132  $dv/dw$ , for the weights related to matrix  $V$ , will be  $\left(\sum_{i=1}^m \gamma_i^{(1)}\left(\sum_{j=1}^n w_{ij}^{(1)}x_j + bw_{i0}^{(1)}\right) + b\right)$ . For the weights related to matrix  $W$ , it will be just  $\sum_{j=1}^n x_j + b$ . Thus, to simplify, one considers the following term  $\delta$ , called local gradient, which is given by  $d\Gamma/dv$ , such that:

$$\delta = \begin{cases} \frac{\partial\Gamma}{\partial e_{out}} \cdot \frac{\partial e_{out}}{\partial y} \cdot \frac{\partial y}{\partial v} = e_{out} \cdot (-1) \cdot \frac{d\gamma(v_V)}{dx} = -e_{out} & \text{if related to } \Delta V \\ \frac{\partial\Gamma}{\partial e_{out}} \cdot \frac{\partial e_{out}}{\partial y} \cdot \frac{\partial y}{\partial v} \cdot \frac{\partial v_V}{\partial v_W} = e_{out} \cdot (-1) \left(\frac{d\gamma(v_W)}{dx}\right) \cdot \sum_{i=1}^m w_i^{(2)} & \text{if related to } \Delta W \end{cases} \quad (2.133)$$

where  $v_V$  and  $v_W$  are the  $v$  values related to  $V$  and  $W$ , respectively.

Another point, not yet mentioned, is that we should also apply the learning rate parameter, denoted as  $\eta$ , to the correction terms  $\Delta W$  and  $\Delta V$ , so that:

$$\Delta W = -\eta \frac{\partial \Gamma}{\partial w_{ij}^{(1)}} \quad (2.134)$$

$$\Delta V = -\eta \frac{\partial \Gamma}{\partial w_j^{(2)}} \quad (2.135)$$

The minus sign in Eqs. 2.134 and 2.135 reflects the application of gradient descent in weight space, aiming to minimize the value of  $\Gamma$ . Thus, when employing the hyperbolic tangent as the activation function, the gradients of the weights in matrices  $W$  and  $V$  can be represented more clearly. Considering that  $W$  and  $V$  are matrices of synaptic weights created with random values at the beginning of training, it is worth noting that in this work, a weight initialization technique proposed by Xavier Glorot and Yoshua Bengio was also adopted (GLOROT; BENGIO, 2010). Therefore, the expression for the synaptic weights update ( $V_{up}$  and  $W_{up}$ ), for matrices  $W$  and  $V$ , is given by:

$$V_{up} = V + \Delta V = V + \eta e_{out} \left( \tanh \left( \sum_{j=1}^n w_{ij}^{(1)} x_j + b w_{i0}^{(1)} \right) + b \right) \quad (2.136)$$

and

$$W_{up} = W + \Delta W = W + \eta e_{out} \sum_{i=1}^m \sum_{j=1}^n x_j w_i^{(2)} \left( \operatorname{sech}^2 \left( \sum_{j=1}^n w_{ij}^{(1)} x_j + b w_{i0}^{(1)} \right) \right) \quad (2.137)$$

Note that the derivative of the output neuron is 1, since it is considered a linear activation.

During the training process, this weight update procedure is repeated tens of times. Not only after the entire training dataset has been passed through the model, updating the weights for each but also in terms of the number of epochs, which is another parameter of the network used in training. An epoch is said to occur when all training data is shown to the model; the next epoch repeats the entire process, but with the weights already updated to further decrease the error value. An example of a complete algorithm is shown in Fig. 2.29. As can be seen, first we preprocess the data, separating them into training, validation, and test datasets randomly. Then one initializes the weight matrices with random values. After that comes the

training itself. One adopts a stopping criterion, which is after a maximum number of epochs, typically around 20,000, or when the model reaches a minimum adopted error value. So, as shown in the pseudocode (Fig. 2.29), for each epoch one performs several procedures. Firstly, one shuffles all the data to reduce bias and avoid overfitting, ensuring greater generalization. The second step, considering one has been conducting stochastic training, is for each sample of the training data, one applies it to the model and applies backpropagation. After the model has seen all the training data, one passes the model through the cross-validation process, where we test the model against a validation set to see how it behaves against data not considered in its training. A condition is made from there; if the error calculated for this specific set improves, i.e., decreases, from one epoch to another, the weights related to it should be saved. Thus, the best weights, i.e., those that provide the lowest error value for the validation set, will be chosen in the end. After that, the next epoch repeats the entire process. After all epochs have occurred, one evaluates the behavior of the model against a new set, called the test set or query dataset, to see how the model performs now outside of all training, against a completely new dataset. Thus, we conclude this chapter, and in the following chapters, we will discuss the applications of such models.

```
1 # Initialization
2 Split the dataset into training, validation, and test sets
3 Randomly initialize the weights of the neural network
4
5 # Training the ANN
6 While the stopping criterion is not met:
7   # Mapping all epochs
8   For each training epoch:
9     Shuffle the training data
10    # Mapping all training data
11    For each example in the training set:
12      Perform forward propagation through the neural network
13      Compute the loss function
14      Compute the gradients of the weights using backpropagation
15      Update the weights using Gradient Descent
16
17    # Perform cross-validation
18    Evaluate the performance on the validation set
19    # Set condition to save the best weights values
20    If the performance on the validation set improves:
21      Save the weights
22    Once error falls below minimum, stop training.
23 # Test the model after the training process
24 Evaluate the final performance of the model on the test set
```

**Figure 2.29.** Pseudocode for training an ANN

## Chapter 3

# A hybrid ANN-multiaxial fatigue non-local model

*"This chapter provides a novel methodology based on neural networks and analytical equivalent stresses to estimate fretting fatigue life."*

Some parts of the text in this chapter was previously published as:

BRITO OLIVEIRA, Giorgio André; FREIRE JÚNIOR, Raimundo Carlos Silverio; VELOSO, Luís Augusto Conte Mendes; ARAÚJO, José Alexander. A hybrid ANN-multiaxial fatigue nonlocal model to estimate fretting fatigue life for aeronautical Al alloys. *International Journal of Fatigue*, v. 162, p. 107011, 2022. DOI: 10.1016/j.ijfatigue.2022.107011.

To ensure adherence to standard nomenclature, some symbols were adjusted from the original publication. Moreover, specific paragraphs were slightly modified to eliminate redundancy.

### 3.1 OVERVIEW

This chapter presents a new methodology to predict fretting fatigue life based on ANN. However, as a novelty, such a methodology considers as input parameters for the ANN equivalent stresses (as the amplitude of the shear stress on the critical plane) which are physically related to the crack initiation process. These inputs have been chosen based on several works (ARAÚJO *et al.*, 2008; TAYLOR, 1999; FINDLEY *et al.*, 1956; SUSMEL; LAZZARIN, 2002; ARAÚJO *et al.*, 2011) that demonstrate their influence on fretting fatigue problems. Thus, three datasets of aluminum alloys subjected to fretting fatigue were chosen to train the ANN and validate the analysis. The datasets consider cylindrical contacts under partial slip regime conditions. These data were pre-processed to compute the equivalent stresses usually present in multiaxial models. Later, these data are used in the ANN learning process to construct a robust ANN based model capable of foreseeing the fretting fatigue life under the influence of several variables (geometric parameters and loadings). The ANN-based model shows excellent correspondence with the experimental values, being more efficient compared to similar models. Hence, this new methodology has been shown very effective in fretting fatigue problems for dealing with different complex stress states such as those involving the nonzero mean bulk stress (BRITO OLIVEIRA *et al.*, 2022).

### 3.2 FRETTING FATIGUE ANALYSIS

This research focuses on the fretting cases involving Hertzian contact between two cylinders, as shown in Fig. 3.1, represented by contact between the pads and the specimen. In there, two cylindrical pads impose a constant compression force ( $P$ ) together with an alternated tangential force ( $Q(t)$ ) in a body which is also subject to a bulk fatigue stress ( $\sigma_B(t)$ ). To evaluate the equivalent stress tensor triggered by the loadings in Fig. 3.1, it is necessary superposing the effects of the normal pressure, shear traction, and the buck load using the potential theory by Muskhelishvili (1977). In these cases, plane strain state is assumed and one can determine all stress components. Therefore, it is possible to compute the values of the subsurface stress field of the specimen in each position ( $x/a$ ,  $y/a$ ) and in any time ( $t$ ) taking into account fretting and fatigue effects considering the Eqs. 2.68 and 2.69.

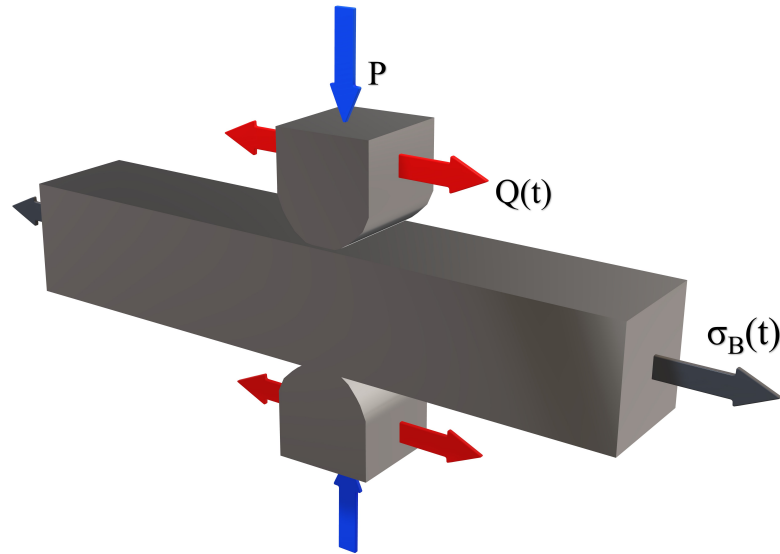


**Figure 3.1.** Fretting fatigue set-up scheme.

### 3.2.1 Computing the equivalent stresses

This methodology is focused on the critical plane approach, since the parameters used in our model are based on those usually used in this category of criteria. These parameters require the computation of equivalent stresses, such as the amplitude of the shear stress vector in a so-called critical plane. Here, this material plane is assumed as the one with the highest shear stress amplitude (SUSMEL; LAZZARIN, 2002). Further, the nature of the contact problem gives rise to stress concentration at the contact interface, however, as one moves away from this interface, the stresses will rapidly decay. Therefore, it is a common sense in the academic community working on fretting fatigue that a size effect must be either implicitly or explicitly incorporated in life predictive methodologies to take into account such size / stress gradient effect. In this setting, this chapter considers the TCD approach (subsection 2.1.4.2) to dealing with these effects.

### 3.2.2 Choosing the input parameters

Recently, Nowell and Nowell (2020) proposed the use of ANN to estimate the contact size effect and fretting fatigue life for a couple of aluminum alloys considering cylinder on plane contact configurations under partial slip condition. As input parameters they have chosen the peak pressure, the contact size, the tangential force ratio ( $Q/P$ ) and the bulk stress amplitude.

Here, one can notice that although this choice allowed the neural network to be trained and to provide good estimates of fatigue life, it lacks a physical-mechanical reasoning. The basic input parameters that are well known to control fatigue life in plain, notch or fretting fatigue are some sort of equivalent stresses. More specifically, in fretting fatigue the stress field is multiaxial, non-proportional and experiences a strong stress gradient. Superficial fretting wear also deteriorates the surface finishing and provokes premature microcracks within the slip zones. Recent works (ARAÚJO *et al.*, 2020; PINTO *et al.*, 2020) have demonstrated that it is possible to accurately estimate life for different materials under fretting fatigue by considering a theoretical approach capable of incorporating these intrinsic characteristics of the fretting problem. The main basic parameters that are believed to control fatigue life in fretting are: an equivalent or critical shear stress amplitude, the maximum normal stress, and a process zone size. Wear effects have also been considered as parameter which affects fretting life (PINTO *et al.*, 2020), but its effect is usually computed by modifications in the stress field caused by the change in the contact profile between the surfaces. Further little improvement has been observed in the accuracy of the life estimates when fretting wear is incorporated in the predictive analysis, in partial slip regime, at the expense of a significant computational effort. In this setting, this work considers three input parameters for the ANN, which were shown to be essential in the prediction of fretting fatigue life ( $N_f$ ) (ARAÚJO *et al.*, 2008; TAYLOR, 1999; FINDLEY *et al.*, 1956; SUSMEL; LAZZARIN, 2002; ARAÚJO *et al.*, 2011). The parameters are the maximum amplitude of the shear stress ( $\tau_{a,max}$ ) (based on the MRH method (ARAÚJO *et al.*, 2011)), the maximum normal stress ( $\sigma_{n,max}$ ), and the critical distance of the material ( $L/2$ ). This latter parameter ( $L/2$ ) can be seen as a value which characterizes the material in terms of the stress gradient effect severity on the trail edge contact considering fretting conditions.

### 3.3 MATERIALS AND DATASETS

To produce this work, it was necessary to gather fretting fatigue data available in the literature (ARAÚJO *et al.*, 2008; ROSSINO *et al.*, 2009; NOWELL, 1988; SZOLWINSKI; FARRIS, 1998; ARAÚJO; CASTRO, 2012; NAVARRO *et al.*, 2011). These data were generated for three aluminum alloys: Al 4%Cu, 2024-T351 and 7050-T7451. The first two datasets (Al 4%Cu and 2024-T351) are the well-known fretting fatigue tests carried out by Nowell (1988)

and by Szolwinski and Farris (1998), respectively (Tables 3.1 and 3.2). The last two datasets were based on experiments with Al 7050-T7451 and were produced by Rossino et al. (2009) and by Araújo and Castro (2012) (Table 3.3).

These experiments used cylindrical pads pressed against a flat specimen and were performed under well-controlled laboratory conditions. A constant normal load ( $P$ ) was applied to the fretting pads and retained constant, then an oscillatory shear force ( $Q(t)$ ) was applied in-phase with the bulk fatigue load ( $B(t)$ ). The latter loads varied over the time according to a sinusoidal wave. Another important feature is that all the tests were designed to run in a partial slip regime. Fig. 3.1 represents the basic scheme of the applied loading history and the test configuration. In Tables 3.1, 3.2 And 3.3 one can find all the relevant parameters to characterize these experiments, i.e.,  $a$ ,  $p_0$ ,  $\sigma_{B,a}$ ,  $Q_{max}/P$ ,  $\sigma_{B,m}$ ,  $f$  and  $N_f$ , where the subscript max represents the maximum values of the shear load and bulk fatigue stress amplitude and the subscript med stands for the mean value of the bulk stress. Hundred and three data were used. The basic mechanical properties (elasticity modulus ( $E$ ), Poisson's coefficient ( $\nu$ ) and the yield stress ( $\sigma_y$ )) and the values of the critical distance ( $L/2$ ) for each alloy, Al 4% Cu (ARAÚJO *et al.*, 2008; NOWELL, 1988), 2024-T351 (SZOLWINSKI; FARRIS, 1998; NAVARRO *et al.*, 2011), 7050-T7451 (ROSSINO *et al.*, 2009; ARAÚJO; CASTRO, 2012) tested are reported in Table 3.4.

### 3.4 ANN MODELING

After joining all dataset in Tables 3.1, 3.2 and 3.3, one created some routines to compute the equivalent stresses shown in Tables 3.5, 3.6 and 3.7. These calculations were carried out based on the modeling described in subsection 3.2. One stands out that these equivalent stresses have been computed at the critical distance point ( $x = -a$  and  $y = L/2$ ). The logarithmic experimental fretting fatigue life is also reported in Tables 3.5, 3.6 and 3.7, such that this function can be applied to improve the ANN training. Thus, the next step was to build ANN architectures to compute  $N_f$ . All calculations were conducted in routines built in MATLAB.

**Table 3.1.** Experimental data of Al4%Cu collected from Nowell (1988).

$a$ (mm)	$p_0$ (MPa)	$\sigma_{B,a}$ (MPa)	$Q_{max}/P$	$\sigma_{B,m}$ (MPa)	$f$	$N_f$
0.38	157	92.7	0.45	0	0.75	1.29E+06
0.57	157	92.7	0.45	0	0.75	6.70E+05
0.95	157	92.7	0.45	0	0.75	7.30E+05
0.76	157	92.7	0.45	0	0.75	8.50E+05
1.14	157	92.7	0.45	0	0.75	6.70E+05
0.1	157	92.7	0.45	0	0.75	1.00E+07*
0.19	157	92.7	0.45	0	0.75	1.00E+07*
0.28	157	92.7	0.45	0	0.75	1.00E+07*
1.08	143	92.7	0.24	0	0.75	1.28E+06
0.54	143	92.7	0.24	0	0.75	1.00E+07*
0.18	143	92.7	0.24	0	0.75	1.00E+07*
0.36	143	92.7	0.24	0	0.75	1.00E+07*
0.09	143	92.7	0.24	0	0.75	1.00E+07*
0.9	143	92.7	0.24	0	0.75	1.22E+06
0.72	143	92.7	0.24	0	0.75	5.06E+06
0.72	143	92.7	0.45	0	0.75	6.10E+05
0.9	143	92.7	0.45	0	0.75	1.24E+06
1.08	143	92.7	0.45	0	0.75	6.90E+05
0.36	143	92.7	0.45	0	0.75	1.50E+06
0.54	143	92.7	0.45	0	0.75	8.00E+05
0.18	143	92.7	0.45	0	0.75	1.00E+07*
0.27	143	92.7	0.45	0	0.75	4.04E+06
0.09	143	92.7	0.45	0	0.75	1.00E+07*
0.54	143	77.2	0.45	0	0.75	1.20E+06
0.36	143	77.2	0.45	0	0.75	1.00E+07*
0.9	143	77.2	0.45	0	0.75	1.02E+06
0.72	143	77.2	0.45	0	0.75	1.42E+06
0.18	143	77.2	0.45	0	0.75	1.00E+07*
0.09	143	77.2	0.45	0	0.75	1.00E+07*
0.57	120	61.8	0.45	0	0.75	1.00E+07*
0.71	120	61.8	0.45	0	0.75	1.57E+06
0.28	120	61.8	0.45	0	0.75	1.00E+07*
0.14	120	61.8	0.45	0	0.75	1.00E+07*
0.85	120	61.8	0.45	0	0.75	1.23E+06
0.21	120	61.8	0.45	0	0.75	1.00E+07*
0.42	120	61.8	0.45	0	0.75	1.00E+07*
0.21	120	61.8	0.45	0	0.75	1.00E+07*

**Table 3.2.** Experimental data of 2024-T351 collected from Szolwinski and Farris (1998).

$a$ (mm)	$p_0$ (MPa)	$\sigma_{B,a}$ (MPa)	$Q_{max}/P$	$\sigma_{B,m}$ (MPa)	$f$	$N_f$
1.54	246	110.3	0.22	0	0.65	3.10E+05
1.24	197.8	84.7	0.28	0	0.65	4.20E+05
1.31	208.4	110.3	0.31	0	0.65	2.40E+05
1.21	202.7	100.7	0.35	0	0.65	2.40E+05
1.37	230.6	110.3	0.31	0	0.65	2.20E+05
1.76	155.7	111.7	0.43	0	0.65	2.40E+05
1.75	155.3	112.9	0.37	0	0.65	2.50E+05
1.4	232	84.8	0.23	0	0.65	6.70E+05
1.66	189	100.0	0.27	0	0.65	3.40E+05
1.66	189	100.0	0.27	0	0.65	4.30E+05
1.3	207	88.4	0.35	0	0.65	5.60E+05
1.51	240	101.9	0.31	0	0.65	3.30E+05
1.53	174	85.8	0.38	0	0.65	5.80E+05
1.88	166	97.0	0.32	0	0.65	7.40E+05
1.75	200	113.1	0.34	0	0.65	4.60E+05
1.88	167	85.4	0.32	0	0.65	8.60E+05
1.28	204	115.8	0.52	0	0.65	4.70E+05
1.77	201	85.2	0.21	0	0.65	6.70E+05
2.00	177	81.8	0.24	0	0.65	7.50E+05
2.00	177	81.8	0.25	0	0.65	7.30E+05
1.4	223	109.2	0.35	0	0.65	6.20E+05
1.73	153	81.0	0.31	0	0.65	8.70E+05
1.74	154	82.9	0.26	0	0.65	7.70E+05
1.79	204	99.4	0.31	0	0.65	5.50E+05
1.99	176	109.5	0.34	0	0.65	3.20E+05
1.49	238	108.8	0.27	0	0.65	2.50E+05
1.87	166	110.8	0.33	0	0.65	4.80E+05
1.4	224	98.2	0.36	0	0.65	4.60E+05
2.01	178	97.9	0.24	0	0.65	4.60E+05
1.65	188	84.7	0.27	0	0.65	6.20E+05
1.53	174	97.4	0.36	0	0.65	4.60E+05
1.69	192	106.4	0.34	0	0.65	2.30E+05
1.53	175	110.6	0.38	0	0.65	3.30E+05
1.31	209	97.1	0.33	0	0.65	3.10E+05
1.5	239	85.4	0.27	0	0.65	3.80E+05

**Table 3.3.** Experimental data of 7050-T7451 collected from Rossino et al. (2009) and Araújo and Castro (2012).

$a$ (mm)	$p_0$ (MPa)	$\sigma_{B,a}$ (MPa)	$Q_{max}/P$	$\sigma_{B,m}$ (MPa)	$f$	$N_f$
1.19	350	92.7	0.25	15	0.54	1.65E+05
1.19	350	92.7	0.25	15	0.54	2.03E+05
1.19	350	92.7	0.25	0	0.54	1.99E+05
1.19	350	92.7	0.25	0	0.54	2.74E+05
1.19	350	92.7	0.25	-15	0.54	2.68E+05
1.19	350	92.7	0.25	-15	0.54	3.00E+05
1.19	350	92.7	0.25	-60	0.54	1.30E+06
1.19	350	92.7	0.25	-60	0.54	1.55E+06
1.19	350	92.7	0.25	-92.7	0.54	1.00E+07*
1.19	350	92.7	0.25	-145	0.54	1.00E+07*
1.19	350	50	0.13	-20	0.54	2.29E+06
1.19	350	50	0.13	-20	0.54	4.40E+06
1.19	350	50	0.13	-20	0.54	3.60E+06
1.19	350	50	0.13	0	0.54	1.86E+06
1.19	350	50	0.13	0	0.54	1.67E+06
1.19	350	50	0.13	0	0.54	1.21E+06
1.19	350	50	0.13	150	0.54	2.30E+05
1.19	350	50	0.13	150	0.54	3.50E+05
1.19	350	50	0.13	150	0.54	2.30E+05
0.59	175	35	0.37	-30	0.6	1.00E+07*
0.59	175	35	0.37	-30	0.6	1.00E+07*
0.59	175	35	0.37	0	0.6	1.00E+07*
0.59	175	35	0.37	0	0.6	4.62E+06
0.59	175	35	0.37	0	0.6	1.00E+07*
0.59	175	35	0.37	0	0.6	3.77E+06
0.59	175	35	0.37	30	0.6	1.18E+06
0.59	175	35	0.37	30	0.6	1.24E+06
0.59	175	35	0.37	30	0.6	2.24E+06
0.59	175	35	0.37	50	0.6	9.40E+05
0.59	175	35	0.37	50	0.6	1.50E+06
0.59	175	35	0.37	50	0.6	2.66E+06

**Table 3.4.** Proprieties and critical distance of the materials considered.

Material	$E$ (GPa)	$\nu$	$\sigma_y$ (MPa)	$L/2$ (mm)
Al 4%Cu	74.0	0.33	465	0.0500
2024-T351	74.1	0.33	310	0.0133
7050-T7451	73.4	0.33	453.8	0.0310

**Table 3.5.** Processed stresses ( $\tau_{a,max}$  and  $\sigma_{n,max}$ ) from MRH method for Nowell (1988) data-set. The logarithmic correspondent fatigue life is also presented.

$\tau_{a,max}$ (MPa)	$\sigma_{n,max}$ (MPa)	$N_f$	$\log_{10}(N_f)$
89.01	6.111	1.29E+06	5.785
97.61	5.826	6.70E+05	5.826
106.78	5.863	7.30E+05	5.863
103.00	5.929	8.50E+05	5.929
109.63	5.826	6.70E+05	5.826
88.15	6.107	1.28E+06	6.107
85.50	6.086	1.22E+06	6.086
82.00	6.704	5.06E+06	6.704
97.26	5.785	6.10E+05	5.785
100.81	6.093	1.24E+06	6.093
103.48	5.839	6.90E+05	5.839
84.16	6.176	1.50E+06	6.176
92.21	5.903	8.00E+05	5.903
77.83	6.606	4.04E+06	6.606
84.17	6.079	1.20E+06	6.079
92.64	6.009	1.02E+06	6.009
89.13	6.152	1.42E+06	6.152
73.05	6.196	1.57E+06	6.196
75.44	6.090	1.23E+06	6.090

### 3.4.1 ANN architecture

Initially we have proposed two models of ANN, one with two inputs and other with three inputs, both with the same output, the fretting fatigue life ( $N_f$ ). The first have only the critical shear stress amplitude ( $\tau_{a,max}$ ) and the maximum normal stress ( $\sigma_{n,max}$ ) (Fig. 3.2A) as inputs. It is nominated M2I. The other one uses the critical distance of the material ( $L/2$ ) as a third input (Fig. 3.2B). This model is denominated as M3I. Unlike the model proposed by Nowell and Nowell (2020), in which the authors considered the run-out data in the ANN training, here only the fractured dataset (finite life) is contemplated for the training, hence only a total of 79 data were considered. To facilitate the training of the ANN, avoiding the saturation of the neurons, the data was normalized with their maximum recorded values  $\tau_{a,MAX}$ ,  $\sigma_{n,MAX}$ ,  $N_{f,MAX}$  e  $L/2_{MAX}$ .

The ANN architecture uses a multiple-layer perceptron network with a hidden layer using the sigmoid function and an output layer containing the linear function. The bias is displayed in Fig. 3.2A and B. Besides, the training was operated using the backpropagation algorithm that uses the method of moments (HAYKIN, 2008). One adopted 20,000 for maximum training

**Table 3.6.** Processed stresses ( $\tau_{a,max}$  and  $\sigma_{n,max}$ ) from MRH method for Szlowinski and Farris (1998) data-set. The logarithmic correspondent fatigue life is also presented.

$\tau_{a,max}$ (MPa)	$\sigma_{n,max}$ (MPa)	$N_f$	$\log_{10}(N_f)$
141.63	5.491	3.10E+05	5.432
116.55	5.623	4.20E+05	5.623
138.56	5.380	2.40E+05	5.380
134.57	5.380	2.40E+05	5.380
147.19	5.342	2.20E+05	5.342
130.19	5.380	2.40E+05	5.380
126.46	5.398	2.50E+05	5.398
122.63	5.826	6.70E+05	5.826
123.54	5.532	3.40E+05	5.532
123.54	5.634	4.30E+05	5.634
130.13	5.748	5.60E+05	5.748
146.91	5.519	3.30E+05	5.519
119.55	5.763	5.80E+05	5.763
118.75	5.869	7.40E+05	5.869
142.44	5.663	4.60E+05	5.663
112.69	5.935	8.60E+05	5.935
159.99	5.672	4.70E+05	5.672
112.67	5.826	6.70E+05	5.826
107.15	5.875	7.50E+05	5.875
108.16	5.863	7.30E+05	5.863
148.59	5.792	6.20E+05	5.792
103.51	5.940	8.70E+05	5.940
100.93	5.887	7.70E+05	5.887
133.45	5.740	5.50E+05	5.740
131.67	5.505	3.20E+05	5.505
144.72	5.398	2.50E+05	5.398
127.14	5.681	4.80E+05	5.681
144.09	5.663	4.60E+05	5.663
116.89	5.663	4.60E+05	5.663
114.37	5.792	6.20E+05	5.792
124.16	5.663	4.60E+05	5.663
135.28	5.362	2.30E+05	5.362
133.41	5.519	3.30E+05	5.519
133.61	5.491	3.10E+05	5.491

**Table 3.7.** Processed stresses ( $\tau_{a,max}$  and  $\sigma_{n,max}$ ) from MRH method for Rossino *et al.* (2009) and Araújo and Castro (2012) data-set. The logarithmic correspondent fatigue life is also presented.

$\tau_{a,max}$ (MPa)	$\sigma_{n,max}$ (MPa)	$N_f$	$\log_{10}(N_f)$
142.74	5.217	1.65E+05	5.217
142.74	5.307	2.03E+05	5.307
142.74	5.298	1.99E+05	5.298
142.74	5.438	2.74E+05	5.438
142.74	5.429	2.68E+05	5.429
142.74	5.476	3.00E+05	5.476
142.74	6.115	1.30E+06	6.115
142.74	6.191	1.55E+06	6.191
88.90	6.360	2.29E+06	6.360
88.90	6.643	4.40E+06	6.643
88.90	6.556	3.60E+06	6.556
88.90	6.270	1.86E+06	6.270
88.90	6.223	1.67E+06	6.223
88.90	6.083	1.21E+06	6.083
88.90	5.362	2.30E+05	5.362
88.90	5.544	3.50E+05	5.544
69.18	5.362	2.30E+05	5.362
69.18	6.665	4.62E+06	6.665
69.18	6.576	3.77E+06	6.576
69.18	6.072	1.18E+06	6.072
69.18	6.093	1.24E+06	6.093
69.18	6.350	2.24E+06	6.350
69.18	5.973	9.40E+05	5.973
69.18	6.176	1.50E+06	6.176

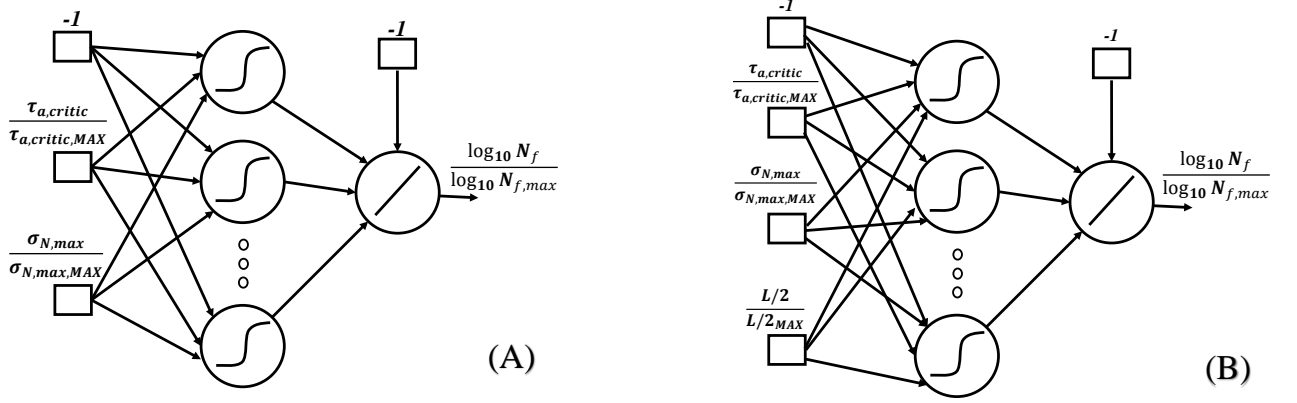


**Figure 3.2.** Representation of the ANN architecture with (A) Two inputs, and, (B) Three inputs.

epochs and the learning rate parameter was 0.1 with the momentum constant of 0.7.

Cross-validation was applied as a stopping criterion, such that the total data was divided into three sets, two for training and test with 80% and 10%, respectively, and one independent, the query data, with the last 10% to check the efficiency. We highlighted that all these values were randomly selected.

One also stands out that the empirical risk ( $ER$ ) equation (HAYKIN, 2008) was used to obtain the best results of the ANN and to make comparisons with the experimental values (see Eq. 3.1). Nevertheless, the ANN was trained by varying the number of neurons between 10 and 100, so as to decide on the best combination for each model. Fig. 3.3 shows the flowchart with all processes commented above for the ANN training.

$$ER = \frac{1}{2n} \sum (P_{exp} - P_{pred})^2 \quad (3.1)$$

In equation 3.1,  $P_{exp}$  represents the experimental value and  $P_{pred}$  the output of the ANN, both normalized. Also,  $n$  represents the number of data used in the training. In our case,  $P_{exp}$  is the normalized and logarithmized experimental fretting fatigue life and  $P_{pred}$  the ANN model output, which is the desired normalized and logarithmized fretting fatigue life.

### 3.5 RESULTS AND DISCUSSION

In this section the main results obtained by considering the M2I and M3I architectures are presented. A comparative analysis will be performed to evaluate which of these architectures

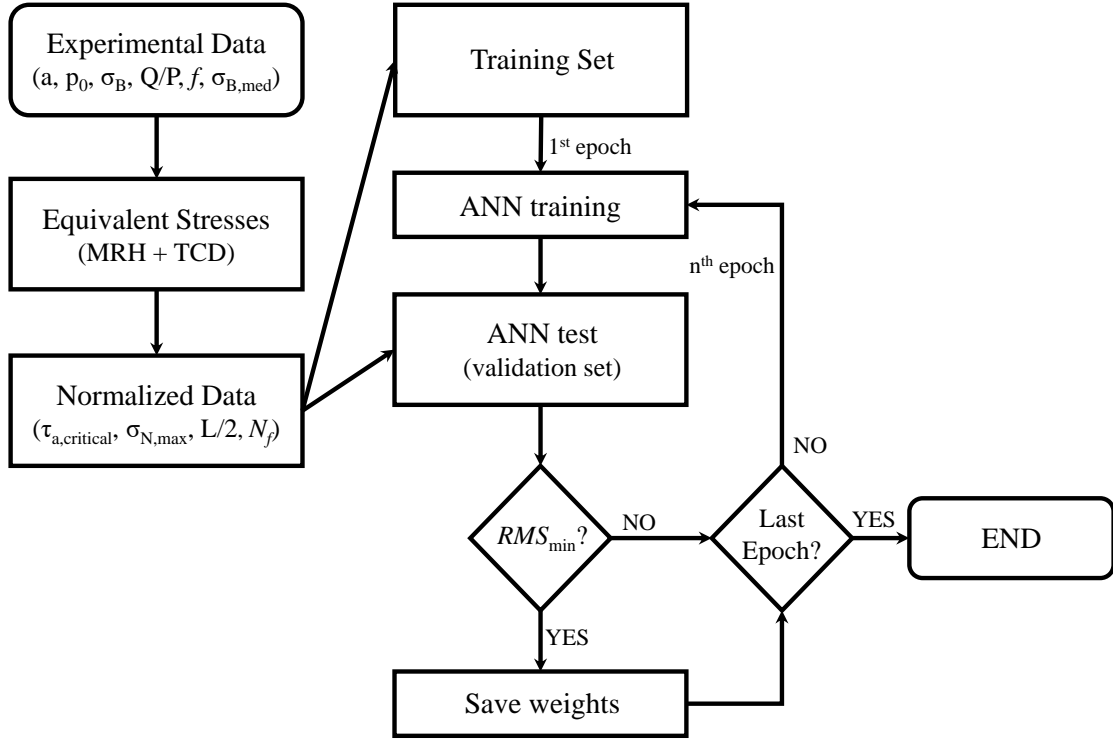


**Figure 3.3.** Flowchart demonstrating all data processing with the ANN cross validation training.

is capable of providing the best estimates of fretting fatigue life. To validate this analysis the experimental data reported in section 3.3 will be considered. Also, for a comparative purpose, the ANN model proposed by Nowell and Nowell (2020) will be reproduced.

### 3.5.1 ANN models

As previously mentioned, fractured experimental data was divided in training, test and query data, to construct the models and evaluate their accuracy. Hence, Eq. 3.1 was applied in every dataset (test, training and query) to compute the errors associated with the experimental data, which were considered for comparison. Table 3.5.1 shows the main errors associated with the two proposed models, M2I and M3I, together with the number of neurons that better fits the architectures minimizing their errors. The ER total error is a weighted average of these errors. The smaller the ER total error of the model, the better is its accuracy. Thus, one can see that the M3I architecture is the most appropriate. Therefore, the third input (the critical distance,  $L/2$ ) proves to improve the results, serving also as a parameter to differentiate the type of material, so, from then on, the M3I architecture will be chosen for all further calculations.

**Table 3.8.** ER values for M2I and M3I models with the respective hidden neuron's quantities.

Model	$ER^*$ (training)	$ER^*$ (test)	$ER^*$ (query)	$ER^*$ (total)	Hidden neurons
M2I	23.13	27.19	30.3	24.27	76
M3I	18.47	15.4	24.9	18.81	57

\* Values must be multiplied by  $10^{-5}$ .

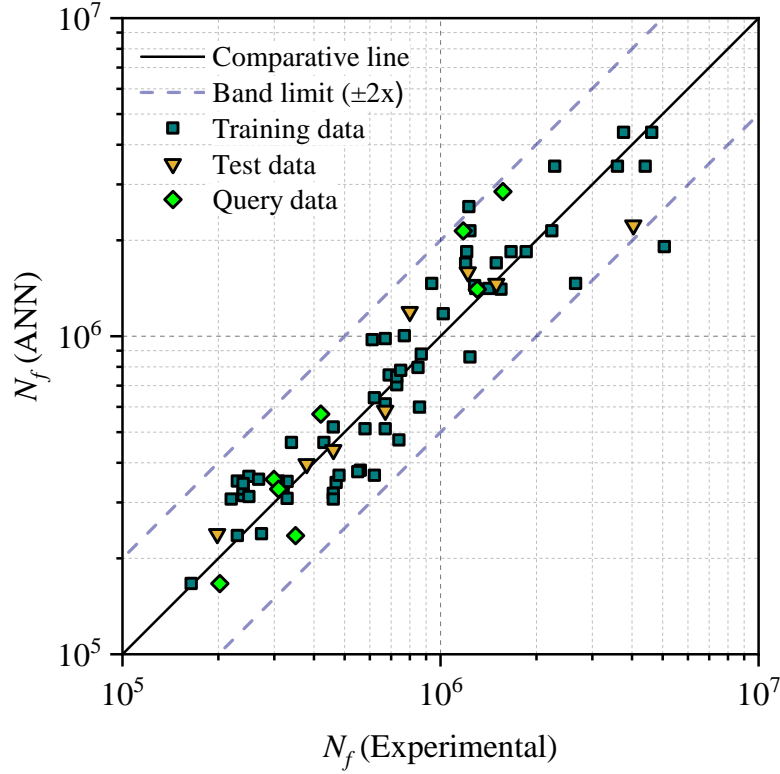
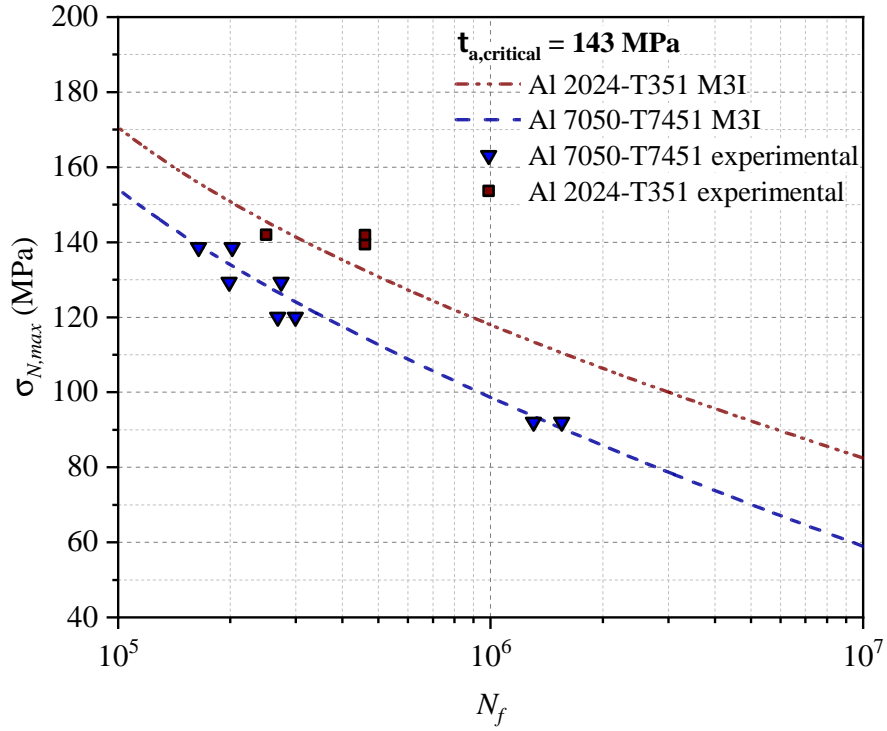
**Figure 3.4.** ANN (M3I model) estimated vs experimental fretting fatigue lives.

Fig. 3.4 shows the experimental versus the estimated life diagram obtained by the application of the M3I model. From such a figure one can see that the ANN based life methodology was capable of estimating the fretting fatigue lives within a factor of two band width. This plot presents the data considered in the ANN learning process, training (square) and test (triangle) data, together with the query (lozenge) data, which are autonomous data used to check the M3I accuracy.

Another interesting analysis is shown in the semilogarithmic graph in Fig. 3.5. Such a graph plots the estimated life by the M3I model against the maximum normal stress ( $\sigma_{n,max}$ ) for two Al alloys (2024-T351 and 7050-T7451). These data were chosen as they all presented the same value of the shear stress amplitude on the critical plane,  $\tau_{a,max} = 143$  MPa. The M3I model was trained based on data that also have nonzero mean bulk stress (more specifically the data for the



**Figure 3.5.** S-N curve for the  $\sigma_{N,max}$  vs  $N_f$  fretting fatigue life ( $N_f$ ) in function of the  $\sigma_{N,max}$  for a constant  $\tau_{a,critic}$  (143 MPa in this case), for two aluminum alloys: 2024-T351 and 7050-T7451

7050-T7451 alloy). Fig. 3.5 depicts the variation of fatigue total life in terms of the maximum normal stress. Therefore, only the maximum normal stress on the critical plane was different from one data to the other. Notice that, all data for the 7050-T7451 alloy (triangular points) have one clear loading characteristic. They have the same values of the shear and normal stress amplitudes but different values of the mean normal stress. Therefore, the variation in life from test to test is due to the effect of this different mean normal stress from one test to another. As can also be seen in Fig. 3.5, the dashed (blue) curve plotted represents the ANN estimated curve for such set of points. The behavior of the curve demonstrates that it can clearly capture such effect of the mean normal stress on the fretting lives. Additionally, the squared points in such figure represent Al 2024 T351 data whose computed shear stress amplitude was the same as those for the 7050-T7451 ones, i.e., 143 MPa, but with no mean stress. Fig. 3.5. shows that an ANN based model can create specific curves which can indicate, for a given  $\tau_{a,max}$ , which is the maximum normal stress that a material can withstand under fretting fatigue. One also points out that the results shows a fairly well trend for the Al 7050-T7451, but to obtain a more safe and accurate curve for the Al 2024-T351 data, it would be necessary more data on

this specific  $\tau_{a,critic}$ . Further it is clear that the model can correctly capture the effect of the mean normal bulk stress on the life. Here one can notice that the M3I is capable to accurately estimate the fatigue lives for data under different values of mean normal stress and having the same shear stress amplitude for two different alloys.

### 3.5.2 Comparative analysis

It has been shown that the M3I model may predict the fretting fatigue life of Al alloys with reasonable accuracy, considering only three inputs. In order to make a comparative analysis, an alternative ANN model proposed by Nowell and Nowell (2020), that also calculates the fretting fatigue life ( $N_f$ ) for aluminum data was considered. In such a model, these authors used four inputs, namely: the peak pressure ( $p_0$ ), the contact semi-length ( $a$ ), the fatigue bulk stress amplitude ( $\sigma_{B,a}$ ) and the tangential over the normal force ratio ( $Q/P$ ). Here we used the same software configuration (JUSTNN, 2015) and parameters which provided the best results in Nowell and Nowell (2020). The ANN was trained with all data considered by the authors plus one portion of Rossino *et al.* (2009) and Araújo and Castro (2012) datasets (the same considered for the M3I training). The remaining data of (ROSSINO *et al.*, 2009) and (ARAÚJO; CASTRO, 2012) served as a mean of comparison as it is illustrated in Fig. 3.6.

The 6 experimental data from Rossino *et al.* (2009) and Araújo and Castro (2012) are shown in Fig 8. It can be seen that the lives estimated by the M3I model are closer to the actual ones. Notice that the other ANN based model (NOWELL; NOWELL, 2020) computed the same fatigue life for all tests under different mechanical configurations. This dataset was chosen for the comparative analysis because of the nonzero mean bulk stress ( $\sigma_{B,m}$ ) present in the Rossino *et al.* (2009) and Araújo and Castro (2012) datasets. In other words, such ANN based model used load parameters and contact geometry as inputs, which were not capable to identify the effect of the mean bulk stress. On the other hand, the M3I model proved to be mechanically more robust and consistent. The fact that the ANN model presented in Nowell and Nowell (2020) have provided good life estimates only for the three tests with the smallest lives is associated with either the absence or the existence of small mean bulk normal stresses. As such mean bulk normal stresses become more compressive and relevant in magnitude the experimental lives increase. However, as the model proposed by Nowell and Nowell (2020)

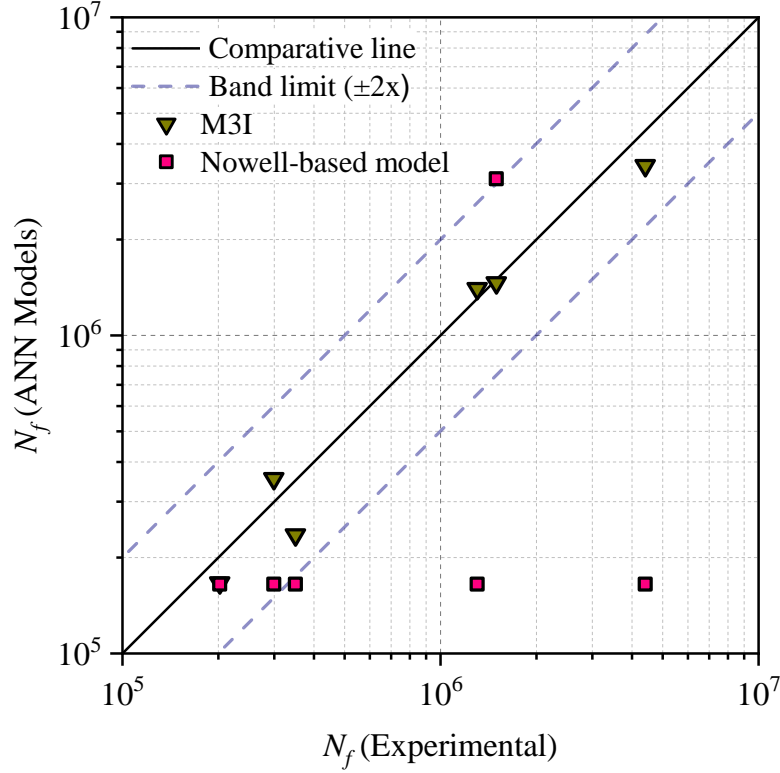


**Figure 3.6.** Comparative logarithmic fretting fatigue life diagram, for M3I model and the model constructed with (NOWELL; NOWELL, 2020) parameters, using (ROSSINO *et al.*, 2009; ARAÚJO; CASTRO, 2012) data.

cannot capture the effect of mean normal stresses on the fatigue life, it yields worse estimates than the M3I, which can clearly take such effect into account. Here one should notice that this model (M3I) was proposed and calibrated considering stress variables ( $\tau_{a,max}$  and  $\sigma_{n,max}$ ) which have been well recognized in the literature, to control the crack initiation phenomenon under complex stress states (ARAÚJO *et al.*, 2008; TAYLOR, 1999; FINDLEY *et al.*, 1956; SUSMEL; LAZZARIN, 2002; ARAÚJO *et al.*, 2011). Further, we also introduced as a third input the critical distance, to take into account not only the stress gradient effect but also the material identification. Thus, the M3I model can be considered as a hybrid model, which was developed based on an ANN with input parameters extract from a non-local multiaxial stress methodology.

### 3.6 PARTIAL CONCLUSIONS

In this chapter, a hybrid model considering the use of a three parameters artificial neural network (ANN) was proposed. These input parameters were chosen to incorporate the main variables assumed to control the crack initiation phenomenon under a rapidly varying multiaxial

stress field, i.e., the shear stress amplitude on the critical plane ( $\tau_{a,max}$ ), the correspondent maximum normal stress ( $\sigma_{n,max}$ ), and the material critical distance ( $L/2$ ). The model not only provided accurate life estimates for more than hundred tests for three different aluminum alloys, but also was able to incorporate the effects of the (i) mean normal bulk stress, (ii) stress gradient and (iii) contact size on life.

This approach is still preliminary because the M3I model here proposed may not provide accurate estimations within regions outside the range of the dataset used in the ANN training. In such regions more data are necessary to cover others states of stress as well as other materials in order to promote a greater generalization of the application of such ANN model. Future works analyzing other parameters as different phase angles, variable normal contact loads and different alloys, could be incorporated in the ANN training in order to increase its robustness and create a model capable of handling with a larger variety of fretting fatigue situations.

## Chapter 4

# A generalized ANN-multiaxial fatigue non-local numerical approach

*"This chapter refines the previously methodology, significantly enhancing the generalization capability of the ANN-based fretting fatigue models."*

Some parts of the text in this chapter was previously published in the following documents:

BRITO OLIVEIRA, Giorgio André; CARDOSO, Raphael Araújo; FREIRE JÚNIOR, Raimundo Carlos Silverio; ARAÚJO, José Alexander. A generalized ANN-multiaxial fatigue nonlocal approach to compute fretting fatigue life for aeronautical Al alloys. *Tribology International*, v. 180, n. November 2022, p. 108250, 2023a. DOI: 10.1016/j.triboint.2023.108250.

OLIVEIRA, Giorgio André Brito; CARDOSO, Raphael Araújo; FREIRE JÚNIOR, Raimundo Carlos Silverio; DOCA, Thiago; ARAÚJO, José Alexander. On the generalization capability of artificial neural networks used to estimate fretting fatigue life. *Tribology International*, v. 192, n. December 2023, p. 109222, 2024. DOI: 10.1016/j.triboint.2023.109222.

To ensure adherence to standard nomenclature, some symbols were adjusted from the original publication. Moreover, specific paragraphs were slightly modified to eliminate redundancy.

## 4.1 OVERVIEW

This chapter significantly extends the approach proposed in the previous chapter, introducing a new numerical and robust perspective along with a more profound analysis of the generalization capabilities of models for estimating fretting fatigue life based on neural networks. Invoking classical multiaxial fatigue models well-established in the literature, one conducts comparative analyses, juxtaposing our novel approach against these models and the experimental values of the corresponding data. First and foremost, one highlights a valuable contribution to the literature: the compilation of nearly all experimental fretting fatigue data available, organized into tables with their key test characteristics. This compilation greatly facilitates our data-driven analysis and future analyses within the same perspective. Another noteworthy aspect is the structure of this work. It is organized around two closely related articles, one serving as a continuation of the other. Combining them into a single chapter seemed more reasonable, considering their thematic similarities. Consequently, we shall initially present results from the first article, which conducts a simpler analysis focusing solely on aeronautical aluminum alloys but which serves as the foundation for the proposed model. Finally, one showcases the results from the second article, which encompasses fretting fatigue tests of different alloys and loading conditions, providing a more comprehensive analysis of the generalization capabilities of these new ANN-based models.

As ANN require a reasonable number of experimental data to be trained, the advantage of using it to estimate the fatigue life of a mechanical part instead of considering an analytical (usually semi-empirical) model, lies in (i) its capability to predict the lives of other parts and materials not covered in the ANN training, i.e. its generalization power, and in (ii) its accuracy when compared to such analytical models. Therefore, the main novelty of this work is to show that the ANN here considered can be accurately applied to compute the FF live of various contact configurations of different materials. To do so, a wide set of FF gathered in the literature have been used. Besides, different nonlocal stress and material parameters are considered as input of these ANN models. Nonetheless, in the results of the first part of this chapter (BRITO OLIVEIRA *et al.*, 2023a), a considerably higher amount of FF experimental data, collected from the literature (related to six different aluminum alloys) are considered. The analyses account for both cylindrical and spherical contacts under partial slip regime. Validation

of the fatigue life estimation methodology is carried out by considering FF experimental data of two Al alloys not used in the ANN training, which permits to verify the generalization of the proposed models (BRITO OLIVEIRA *et al.*, 2023a). In the second part of this chapter, important engineering materials, such as the Ti-6Al-4V and the ASTM A743 CA6NM, have been included in the analysis to test the performance of the models (OLIVEIRA *et al.*, 2024). Further, tests from the former comprise different pad geometries and nonzero mean bulk load, whereas data from the latter material include out-of-phase loading between the shear and the bulk fatigue loading. Therefore, for a total of 207 experimental FF data, the accuracy of the life estimates provided by our ANN data driven criteria has been compared with those obtained by the Smith, Watson and Topper (SWT) (SMITH, 1908), the Modified Wöhler Curve Method (MWCM) (SUSMEL; LAZZARIN, 2002) and the Crossland (CROSSLAND, 1956) multiaxial fatigue criteria.

## 4.2 NONLOCAL MULTIAXIAL STRESS METHODOLOGY

The proposed ANN methodology are considered to estimate the fretting fatigue life under medium to high cycle fatigue regime, that is, when there is no appreciable macroplasticity involved in the problem. Further clarification will be provided in subsequent subsection, but it is worthy to note that the methodology proposed in this chapter considers stress parameters employed in three well-established multiaxial fatigue criteria: SWT, MWCM, and CROSSLAND (refer to sections 2.1.3.2, 2.1.3.3, and 2.1.3.4, respectively). Additionally, as mentioned earlier, these criteria will also be employed for comparative analysis with the results obtained from our models. Besides, these stress quantities were used in order to capture the physics of the crack initiation mechanism under complex loading. The multiaxial stresses were computed at certain material critical distance (see section 2.1.4.2), so that the ANN trained would be able to capture the effects of rapidly varying stress gradients often present in FF. This proposed solution creates a synergic and consistent link between the ANN architecture (see section 2.1.8.2) and the physics of the mechanical problem without the hurdles of a Physics Informed Neural Network (HALAMKA *et al.*, 2023; CHEN *et al.*, 2023; ZHOU *et al.*, 2023).

### 4.2.1 Input parameters considered for the ANNs

As previously mentioned, this chapter draws on results from two recently published articles, each employing distinct yet somewhat analogous methodologies. To clarify for the reader, the first article delves into the application of two neural network-based models for predicting fretting fatigue. These models were trained using data from four aluminum alloys, with an additional two alloys utilized for validation purposes (details to be presented later). In contrast, the second article explores the implementation of three ANN-based models for fatigue life prediction. Notably, in their training, these models take into account the entire dataset from the preceding article, encompassing data from six aluminum alloys.

Fig. 4.1 depicts the general ANN architecture considered in this chapter, for both articles, which is basically a multilayer perceptron ANN containing only one hidden layer, as well as an input and an output layer. From the first article (BRITO OLIVEIRA *et al.*, 2023a), similar to what has been done in Chapter 3 (BRITO OLIVEIRA *et al.*, 2022), this work utilizes equivalent stresses (computed at  $L/2$  from the trailing edge) as the inputs of the ANN. Two different ANN models are here constructed. In one of them, stress parameters computed by the MWCM multiaxial fatigue model, i.e. the maximum shear stress amplitude,  $\tau_{a,max}$ , and the maximum normal stress,  $\sigma_{n,max}$ , both on the critical plane (see section 2.1.3.3) are used. Alternatively, this work also considers the stress parameters of the SWT fatigue model as inputs of the ANN, i.e. the maximum normal stress,  $\sigma_{n,max}$ , and the normal stress amplitude,  $\sigma_{n,a}$ , on the material plane that maximizes their product (see section 2.1.3.2).

In Brito Oliveira *et al.* (2022), the critical distance parameter  $L$  was adopted as one of the inputs of the ANN in an attempt to distinguish different materials. Here, on the other hand, one considers the material yield stress,  $\sigma_y$ , and ultimate stress,  $\sigma_{ult}$ , for this purpose once the  $L/2$  parameter is already considered in the calculation of the equivalent stresses. Notwithstanding, as the critical distance is assumed to be material dependent and not influenced by the geometry or by the stress state (TAYLOR, 1999; ARAÚJO *et al.*, 2007; ARAÚJO *et al.*, 2017) it is somehow a sort of implicit material dependent parameter incorporated in the other two stress inputs of the ANN. However, it is worth noticing that one keeps feeding the ANN with only three inputs since  $\sigma_{ult}$  is used only for normalizing the other stress parameters:  $(\tau_{a,max}/\sigma_{ult}, \sigma_{n,max}/\sigma_{ult}, \sigma_y/\sigma_{ult})$  or  $(\sigma_{n,max}/\sigma_{ult}, \sigma_{n,a}/\sigma_{ult}, \sigma_y/\sigma_{ult})$ .

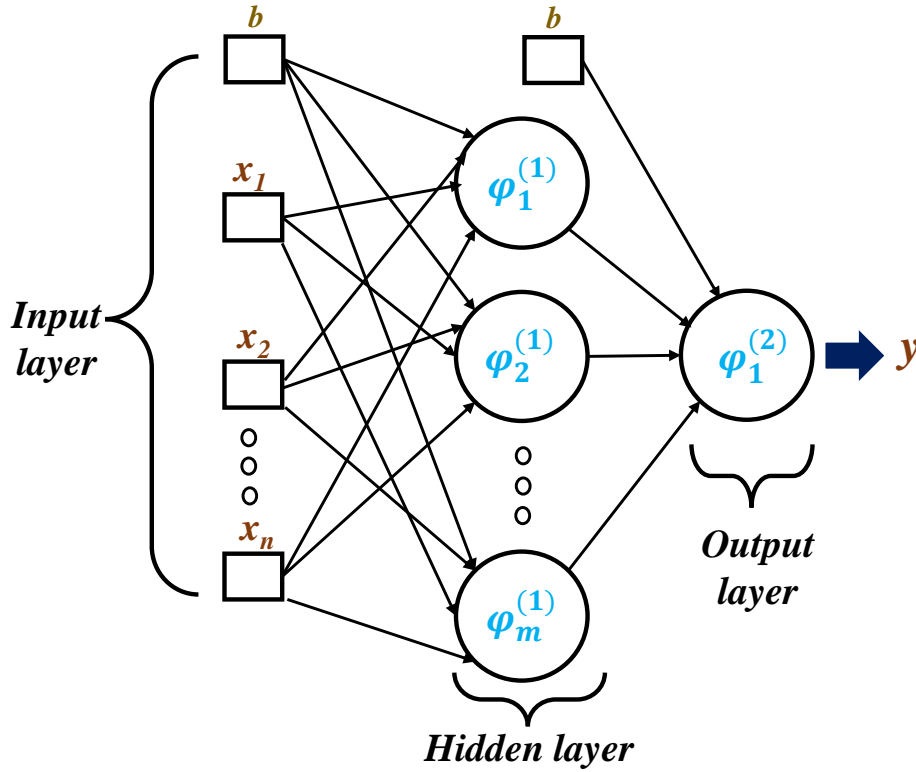


**Figure 4.1.** Example of a simple-layered ANN architecture.

Concerning the stress parameters considered in the aforementioned ANN models, it is worth noticing that the computation of  $\sigma_{n,max}$  and  $\sigma_{n,a}$  is straightforward. However, the determination of  $\tau_{a,max}$  is more challenging for non-proportional loads as it is the case for FF. In this setting, due to its simplicity and ability to handle non-proportional stress paths, the Maximum Rectangular Hull (MRH) method (see Fig. 2.4 and Eq. 2.15) is considered for the definition of  $\tau_a$ . It is also worth to remember that in the definition of the critical plane in the MWCM model, it corresponds to for the material plane which maximizes  $\tau_a$ . In this case, if more than one plane present values close to maximum  $\tau_a$  (i.e., 1% tolerance), the critical plane is defined as the one which yields the maximum normal stress  $\sigma_{n,max}$  (ARAÚJO *et al.*, 2011).

The second article (OLIVEIRA *et al.*, 2024) proposes the implementation of three ANN fatigue models also utilizing stress quantities as inputs. The stress quantities in each model were also computed at a critical distance ( $L/2$ ) from the contact trailing edge, where fretting crack initiation has usually been reported. The material yield stress,  $\sigma_y$ , and the ultimate tensile stress,  $\sigma_{ult}$ , are also considered in the ANN inputs as a way to distinguish different materials.

More specifically, the ANN models based on the MWCM and SWT stress parameters have the same inputs of the ANN models from the first article, i.e.:  $\tau_{a,max}/\sigma_{ult}$ ,  $\sigma_{n,max}/\sigma_{ult}$ ,  $\sigma_y/\sigma_{ult}$ ) or  $(\sigma_{n,max}/\sigma_{ult}$ ,  $\sigma_{n,a}/\sigma_{ult}$ ,  $\sigma_y/\sigma_{ult}$ ), which are related to each multiaxial fatigue model, respectively. The ANN model based on Crossland equivalent stress parameters has the following inputs:  $S_a/\sigma_{ult}$ ,  $\sigma_{H,max}/\sigma_{ult}$ ,  $\sigma_y/\sigma_{ult}$ . Note that all the input parameters of the proposed models have been normalized also by  $\sigma_{ult}$ . Such a strategy, in addition to helping to distinguish different materials, also bounds the magnitude of the ANN input parameters, which in turn facilitates the training process. Moreover, it also allows us to feed each model with four different pieces of information, whereas retaining the number of inputs as three. It is also worth noticing that the stress invariant approach provided by Crossland affords a computational advantage by eliminating the requirement to search for stress parameters among numerous material planes. However, one should always keep in mind that, the hydrostatic stress in such a model, may provide non-conservative fatigue strength estimates for certain stress states!

### 4.3 MATERIALS AND DATASETS

In this chapter, several fretting fatigue datasets as well as axial and torsional fatigue datasets have been considered in both works (BRITO OLIVEIRA *et al.*, 2023a; OLIVEIRA *et al.*, 2024). Six types of aeronautical aluminum alloys: 2024-T351 (SZOLWINSKI; FARRIS, 1998; NAVARRO *et al.*, 2011), Al4%Cu (NOWELL, 1988), 7050-T7451 (ROSSINO *et al.*, 2009; ARAÚJO; CASTRO, 2012), 7075-T6 (WITTKOWSKY *et al.*, 2000; KIRKPATRICK, 1999), 7075-T651 (MARTÍN *et al.*, 2020; MUÑOZ *et al.*, 2007; NAVARRO *et al.*, 2011), and 2024-T3 (PINTO *et al.*, 2022b; HOJJATI-TALEMI *et al.*, 2014) Al alloys are considered. The mechanical properties (Young’s modulus,  $E$ , Poisson’s coefficient,  $\nu$ , yield stress,  $\sigma_y$ , and the ultimate stress,  $\sigma_{ult}$ ) for each alloy are reported in Table 4.1. Moreover, one also collected uniaxial fatigue data for the 2024-T3 and 7075-T6 Al alloys. Such data are used for the calibration of the SWT and MWCM multiaxial fatigue models, which are utilized to estimate fatigue life for a further comparison with the ANN model results. This analysis are presented in (BRITO OLIVEIRA *et al.*, 2023a).

The study from the second article (OLIVEIRA *et al.*, 2024) considers the application of ANN models for two completely different materials: Ti-6Al-4V (BELLECAVE, 2015; FERRY,

**Table 4.1.** Proprieties of the aluminum alloys considered.

Material	$E$ (GPa)	$\nu$	$\sigma_y$ (MPa)	$\sigma_{ult}$ (MPa)
Al 4%Cu	74.0	0.33	465	500
2024-T351	74.1	0.33	310	470
7050-T7451	73.4	0.33	453.8	513
7075-T651	71	0.33	503	572
7075-T6	72	0.33	531	572
2024-T3	72.1	0.33	383.5	506

2017; ARAUJO, 2000; VENKATESH *et al.*, 2001; KIRKPATRICK, 1999) and ASTM A743 CA6NM (GAILLIEGUE, 2018; LOBATO DA SILVA *et al.*, 2010). Also, some FF data for Al 7050-T7451 is used, but under an out-of-phase loading condition, which was not included in the ANN training (which considers only Al alloys). In this way, fatigue data (axial and torsional loadings) related to these materials (Ti-6Al-4V, ASTM A743 CA6NM and Al 7050-T451) have been also considered, once these data are used to calibrate the multiaxial fatigue models (MWCM, SWT and Crossland). Table 4.2 reports the mechanical properties (Young's modulus,  $E$ , Poisson's coefficient,  $\nu$ , yield stress,  $\sigma_y$ , and the ultimate stress,  $\sigma_{ult}$ ) of such alloys.

**Table 4.2.** Proprieties of the titanium and steel alloys considered.

Material	$E$ (GPa)	$\nu$	$\sigma_y$ (MPa)	$\sigma_{ult}$ (MPa)
Ti-6Al-4V	120	0.29 – 0.34	910 – 974	1000
A743 CA6NM	204	0.30	550	755

### 4.3.1 Axial and torsional fatigue data

In the first article (BRITO OLIVEIRA *et al.*, 2023a), plain fatigue data available in the literature (NEWMAN *et al.*, 1999; LINDSTRÖM, 2020) for the 2024-T3 and the 7075-T6 Al alloys are utilized to perform the calibration of the SWT and MWCM multiaxial fatigue models. Such data are reported in Fig. 4.2a and 4.2b for the 2024-T3 and the 7075-T6 Al alloys, respectively, where  $\sigma_a$  is the stress amplitude and  $N_f$  is the fatigue life to failure. It can be noted that, for both the materials,  $S - N$  curves are available for two different load ratios, i.e.,  $R_\sigma = -1$  and  $R_\sigma = 0$ . Note that the calibration of MWCM, for instance, requires the use of fatigue data related to different load conditions.

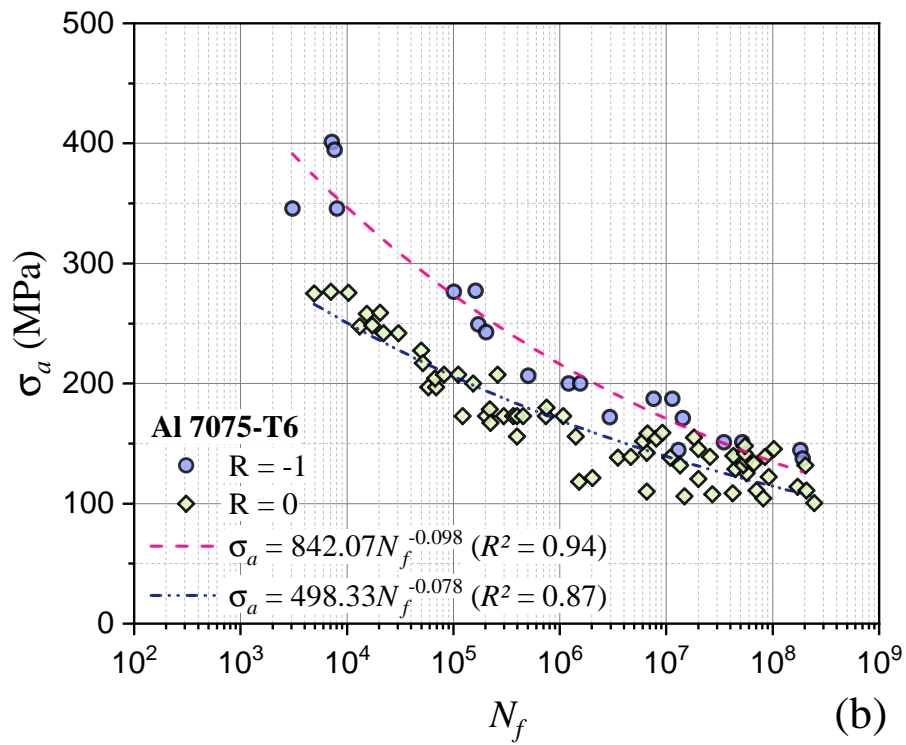
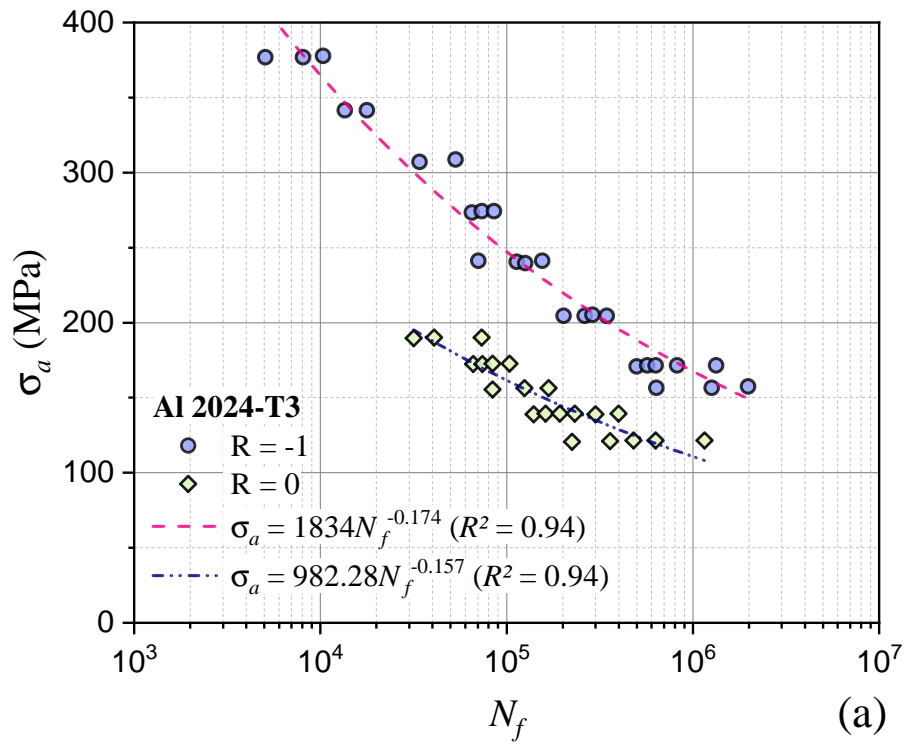


**Figure 4.2.** Uniaxial fatigue data for the 2024-T3 Al alloy (a), and for the 7075-T6 Al alloy (b).

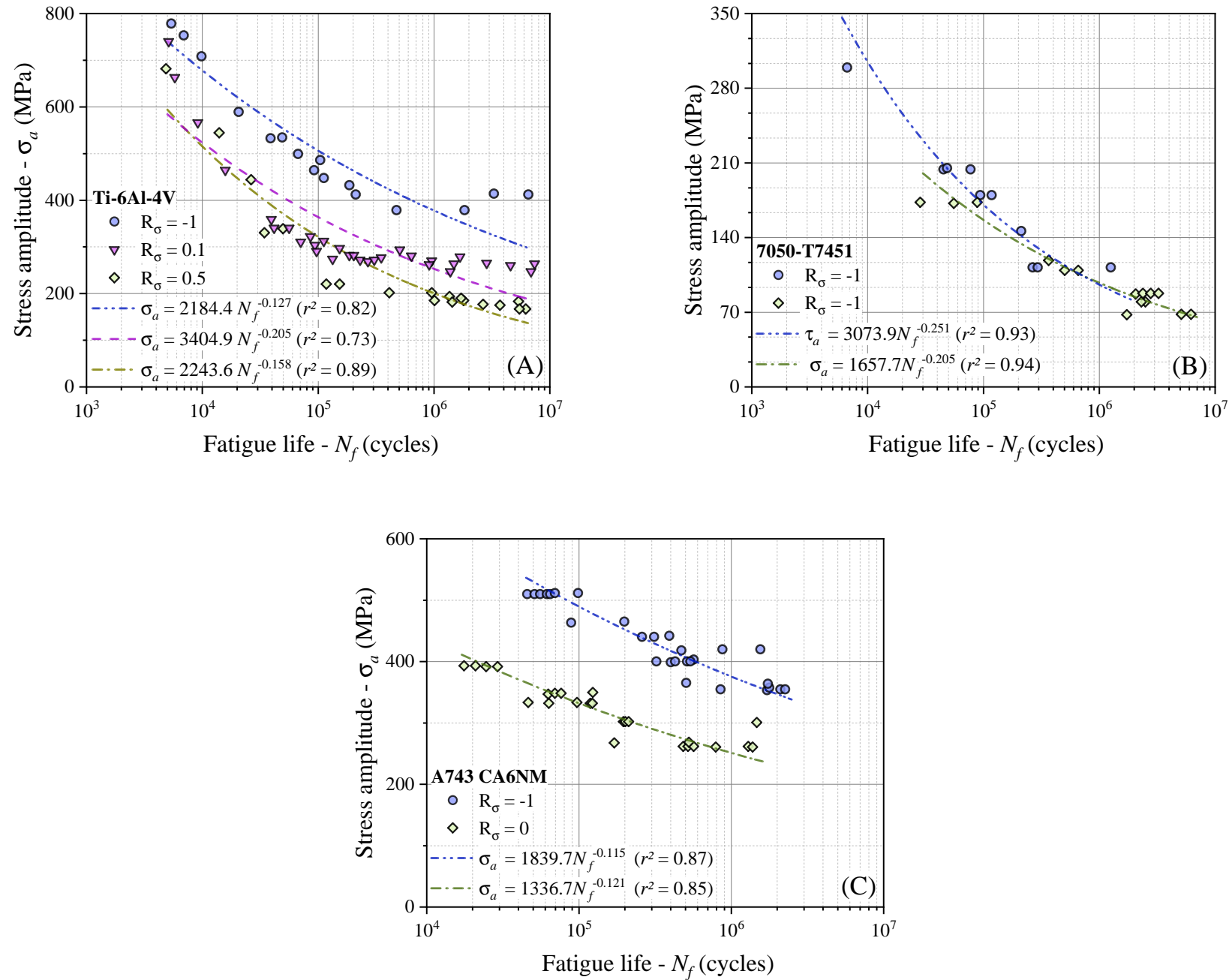


**Figure 4.3.** Axial and torsional fatigue data for the Ti-6Al-4V alloy (A), Al 7050-T7451 alloy (B), and ASTM A743 CA6NM alloy.

For the second approach (OLIVEIRA *et al.*, 2024), fatigue data from the literature (GAILLIEGUE, 2018; KALLMEYER *et al.*, 2002; LOBATO DA SILVA *et al.*, 2010) for Ti-6Al-4V, ASTM A743 CA6NM, and Al 7050-T451 are reported in Fig. 4.3a, Fig. 4.3b, and Fig. 4.3c, respectively, where  $\sigma_a$  and  $\tau_a$  are the axial and torsional stress amplitudes, respectively, and  $N_f$  is the fatigue life to failure. As can be seen, the Wöhler curves are available for at least two curves once the calibration process of MWCM and Crossland models demands fatigue data with different load conditions.

### 4.3.2 Fretting fatigue data

For the training and assessment of the ANN models, several fretting fatigue experimental data available in the literature are considered. For the first article, which considers only aluminum alloys, such data (NOWELL, 1988; SZOLWINSKI; FARRIS, 1998; ROSSINO *et al.*, 2009; ARAÚJO; CASTRO, 2012; HOJJATI-TALEMI *et al.*, 2014; MARTÍN *et al.*, 2020; WITTKOWSKY *et al.*, 2000; MUÑOZ *et al.*, 2007; KIRKPATRICK, 1999) were divided into six groups, one for each material, as shown in Tables 4.3–4.8. Experimental data from ref. (NOWELL, 1988; SZOLWINSKI; FARRIS, 1998; ROSSINO *et al.*, 2009; ARAÚJO; CASTRO, 2012; HOJJATI-TALEMI *et al.*, 2014; MARTÍN *et al.*, 2020) (see Tables 4.3–4.6 and 4.8) were obtained by performing tests with the cylinder-on-flat contact configuration (Fig. 4.5a), whereas in references (WITTKOWSKY *et al.*, 2000; MUÑOZ *et al.*, 2007; KIRKPATRICK, 1999) (see Tables 4.7 and 4.8) the tests were performed by using the sphere-on-flat contact configuration (Fig. 4.5b). Note that in Table 4.8 there are results for both cylindrical (Numbers: 90–112) and spherical contacts (Numbers: 113–132). In Fig. 4.4 the experimental fatigue life range for each Al alloy considered is plotted.

In (OLIVEIRA *et al.*, 2024), to analyze the behavior of the ANN functions in the presence of different materials and loadings conditions, more experimental FF data (BELLECAVE, 2015; FERRY, 2017; ARAUJO, 2000; VENKATESH *et al.*, 2001; KIRKPATRICK, 1999; GAILLIEGUE, 2018; LOBATO DA SILVA *et al.*, 2010) have been gathered in the literature. The FF data were divided into four groups, most of them are from titanium alloys as shown in Tables 4.9–4.12. The first two groups (Tables 4.9 and 4.10, respectively) are FF tests performed with Ti-6Al-4V, being the data reported in Table 4.9 generated with cylindrical pads while the ones

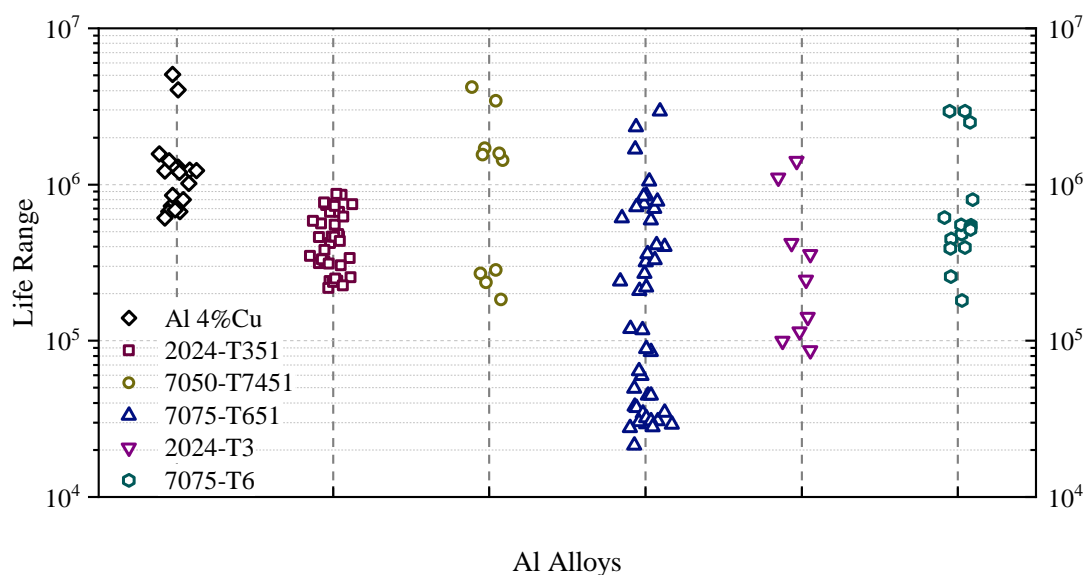


**Figure 4.4.** Experimental fretting fatigue life range for all aluminum alloys considered.

**Table 4.3.** Experimental data of Al 4%Cu collected from (NOWELL, 1988) (cylindrical contact).

Number	R(mm)	$P(N)$	$Q_{max}$ (N)	$\sigma_{B,a}$	$\sigma_{B,m}$	$f$	$N_f$
1	50	1177.26	529.77	92.7	0.0	0.75	1.29E+06
2	75	1765.89	794.65	92.7	0.0	0.75	6.70E+05
3	125	2943.15	1324.42	92.7	0.0	0.75	7.30E+05
4	100	2354.52	1059.53	92.7	0.0	0.75	8.50E+05
5	150	3531.78	1589.30	92.7	0.0	0.75	6.70E+05
6	150	3169.80	760.75	92.7	0.0	0.75	1.28E+06
7	125	2641.50	633.96	92.7	0.0	0.75	1.22E+06
8	100	2113.20	507.17	92.7	0.0	0.75	5.06E+06
9	100	2113.20	950.94	92.7	0.0	0.75	6.10E+05
10	125	2641.50	1188.67	92.7	0.0	0.75	1.24E+06
11	150	3169.80	1426.41	92.7	0.0	0.75	6.90E+05
12	75	1584.90	713.20	92.7	0.0	0.75	8.00E+05
13	37.5	792.45	356.60	92.7	0.0	0.75	4.04E+06
14	75	1584.90	713.20	77.2	0.0	0.75	1.20E+06
15	125	2641.50	1188.67	77.2	0.0	0.75	1.02E+06
16	100	2113.20	950.94	77.2	0.0	0.75	1.42E+06
17	125	1643.92	739.77	61.8	0.0	0.75	1.57E+06
18	150	1963.46	883.56	61.8	0.0	0.75	1.23E+06

**Table 4.4.** Experimental data of 2024-T351 collected from (SZOLWINSKI; FARRIS, 1998) (cylindrical contact).

Number	R(mm)	$P$ (N)	$Q_{max}$ (N)	$\sigma_{B,a}$	$\sigma_{B,m}$	$f$	$N_f$
19	127	7562.0	1663.64	110.3	0.0	0.65	3.14E+05
20	127	4893.0	1370.04	84.7	0.0	0.65	4.22E+05
21	127	5427.0	1682.37	110.3	0.0	0.65	2.41E+05
22	121	4880.0	1708.00	100.7	0.0	0.65	2.41E+05
23	121	6316.0	1957.96	110.3	0.0	0.65	2.17E+05
24	229	5454.0	2345.22	111.7	0.0	0.65	2.38E+05
25	229	5427.0	2007.99	112.9	0.0	0.65	2.50E+05
26	127	6228.0	1432.44	84.8	0.0	0.65	6.68E+05
27	178	6268.0	1692.36	100.0	0.0	0.65	3.50E+05
28	178	6263.0	1691.01	100.0	0.0	0.65	4.34E+05
29	127	5370.0	1879.50	88.4	0.0	0.65	5.64E+05
30	127	7226.0	2240.06	101.9	0.0	0.65	5.45E+05
31	127	7226.0	2240.06	101.9	0.0	0.65	3.38E+05
32	178	5310.0	2017.80	85.8	0.0	0.65	5.83E+05
33	229	6223.0	1991.36	97.0	0.0	0.65	7.39E+05
34	178	6994.0	2377.96	113.1	0.0	0.65	4.56E+05
35	229	6268.0	2005.76	85.4	0.0	0.65	8.57E+05
36	127	5201.0	2704.52	115.8	0.0	0.65	4.65E+05
37	178	7085.0	1487.85	85.2	0.0	0.65	6.65E+05
38	178	7085.0	1487.85	85.2	0.0	0.65	7.49E+05
39	229	7072.0	1697.28	81.8	0.0	0.65	7.47E+05
40	229	7073.0	1768.25	81.8	0.0	0.65	7.30E+05
41	127	6215.0	2175.25	109.2	0.0	0.65	3.03E+05
42	229	5293.0	1640.83	81.0	0.0	0.65	8.67E+05
43	229	5325.0	1384.50	82.9	0.0	0.65	7.68E+05
44	178	7251.0	2247.81	99.4	0.0	0.65	5.52E+05
45	229	7002.0	2380.68	109.5	0.0	0.65	3.21E+05
46	127	7070.0	1908.90	108.8	0.0	0.65	2.54E+05
47	229	6187.0	2041.71	110.8	0.0	0.65	4.80E+05
48	127	6275.0	2259.00	98.2	0.0	0.65	4.64E+05
49	229	7153.0	1716.72	97.9	0.0	0.65	4.63E+05
50	178	6176.0	1667.52	84.7	0.0	0.65	6.21E+05
51	178	5319.0	1914.84	97.4	0.0	0.65	4.60E+05
52	178	6460.0	2196.40	106.4	0.0	0.65	2.26E+05
53	178	5351.0	2033.38	110.6	0.0	0.65	3.31E+05
54	127	5462.0	1802.46	97.1	0.0	0.65	3.12E+05
55	127	7118.0	1921.86	85.4	0.0	0.65	3.82E+05

**Table 4.5.** Experimental data of 2024-T3 collected from (HOJJATI-TALEMI *et al.*, 2014) (cylindrical contact).

Number	R(mm)	$P(N)$	$Q_{max}$ (N)	$\sigma_{B,a}$	$\sigma_{B,m}$	$f$	$N_f$
56	50	543.00	155.17	45.0	55.0	0.65	1.41E+06
57	50	543.00	186.25	51.8	63.3	0.65	1.11E+06
58	50	543.00	223.70	60.8	74.3	0.65	3.58E+05
59	50	543.00	195.55	60.8	74.3	0.65	4.20E+05
60	50	543.00	193.70	72.0	88.0	0.65	2.46E+05
61	50	543.00	330.15	85.5	104.5	0.65	1.42E+05
62	50	543.00	322.10	92.3	112.8	0.65	1.15E+05
63	50	543.00	267.15	99.0	121.0	0.65	9.96E+04
64	50	543.00	317.85	99.0	121.0	0.65	8.66E+04

**Table 4.6.** Experimental data of 7050-T7451 collected from (ROSSINO *et al.*, 2009; ARAÚJO; CASTRO, 2012) (cylindrical contact).

Number	R(mm)	$P(N)$	$Q_{max}$ (N)	$\sigma_{B,a}$	$\sigma_{B,m}$	$f$	$N_f$
65	70	8500.00	2125.00	92.7	15	0.54	1.84E+05
66	70	8500.00	2125.00	92.7	0	0.54	2.36E+05
67	70	8500.00	2125.00	92.7	-15	0.54	2.84E+05
68	70	8500.00	2125.00	92.7	-60	0.54	1.43E+06
69	70	8506.85	1105.89	50	-20	0.54	3.43E+06
70	70	8506.85	1105.89	50	0	0.54	1.58E+06
71	70	8506.85	1105.89	50	150	0.54	2.70E+05
72	70	2091.12	773.71	35	0	0.6	4.20E+06
73	70	2091.12	773.71	35	30	0.6	1.55E+06
74	70	2091.12	773.71	35	50	0.6	1.70E+06

**Table 4.7.** Experimental data of 7075-T6 collected from (WITTKOWSKY *et al.*, 2000; KIRKPATRICK, 1999) (spherical contact).

Number	R(mm)	$P(N)$	$Q_{max}$ (N)	$\sigma_{B,a}$	$\sigma_{B,m}$	$f$	$N_f$
75	25.4	20.00	15.00	84.2	0.0	1.2	5.49E+05
76	25.4	10.30	7.50	83.6	0.0	1.2	2.94E+06
77	25.4	30.00	15.00	85.0	0.0	1.2	4.80E+05
78	25.4	20.80	15.00	83.0	0.0	1.2	4.49E+05
79	25.4	15.60	15.00	85.0	0.0	1.2	3.95E+05
80	25.4	18.50	13.60	77.0	0.0	1.2	5.51E+05
81	25.4	16.00	11.70	83.0	0.0	1.2	5.30E+05
82	25.4	13.90	10.00	83.0	0.0	1.2	8.03E+05
83	25.4	20.00	15.00	70.0	0.0	1.2	5.16E+05
84	25.4	20.00	15.00	100.0	0.0	1.2	3.90E+05
85	25.4	20.00	15.00	125.0	0.0	1.2	2.58E+05
86	25.4	20.00	15.00	150.0	0.0	1.2	1.81E+05
87	25.4	20.00	15.00	74.0	0.0	1.2	2.50E+06
88	25.4	8.33	8.00	83.0	0.0	1.2	6.16E+05
89	25.4	10.30	7.50	83.0	0.0	1.2	2.94E+06

**Table 4.8.** Experimental data of 7075-T651 collected from (MARTÍN *et al.*, 2020) (cylindrical contact, 90 to 112) and (MUÑOZ *et al.*, 2007) (spherical contact, 113 to 132).

Number	R(mm)	$P$ (N)	$Q_{max}$ (N)	$\sigma_{B,a}$	$\sigma_{B,m}$	$f$	$N_f$
90	100	6629.00	971.00	70.0	0.0	0.75	2.41E+05
91	100	5429.00	971.00	110.0	0.0	0.75	1.19E+05
92	100	5429.00	1257.00	110.0	0.0	0.75	1.17E+05
93	100	4217.00	1543.00	110.0	0.0	0.75	8.88E+04
94	100	5429.00	1543.00	110.0	0.0	0.75	8.50E+04
95	100	3006.00	971.00	150.0	0.0	0.75	5.96E+04
96	100	4217.00	971.00	150.0	0.0	0.75	6.40E+04
97	100	5429.00	971.00	150.0	0.0	0.75	4.97E+04
98	100	3006.00	1543.00	150.0	0.0	0.75	2.93E+04
99	100	4217.00	1543.00	150.0	0.0	0.75	4.47E+04
100	100	5429.00	1543.00	150.0	0.0	0.75	4.47E+04
101	100	3006.00	2113.00	150.0	0.0	0.75	3.80E+04
102	100	4217.00	2113.00	150.0	0.0	0.75	3.74E+04
103	100	5429.00	2113.00	150.0	0.0	0.75	3.44E+04
104	100	3006.00	971.00	175.0	0.0	0.75	2.92E+04
105	100	4217.00	971.00	175.0	0.0	0.75	3.03E+04
106	100	5429.00	971.00	175.0	0.0	0.75	3.21E+04
107	100	3006.00	1543.00	175.0	0.0	0.75	3.07E+04
108	100	4217.00	1543.00	175.0	0.0	0.75	3.48E+04
109	100	5429.00	1543.00	175.0	0.0	0.75	3.07E+04
110	100	3006.00	2113.00	175.0	0.0	0.75	2.14E+04
111	100	4217.00	2113.00	175.0	0.0	0.75	2.78E+04
112	100	5429.00	2113.00	175.0	0.0	0.75	2.81E+04
113	100	210.00	210.00	45.0	0.0	1.27	1.68E+06
114	100	210.00	210.00	47.0	0.0	1.27	2.34E+06
115	100	210.00	210.00	50.0	0.0	1.27	8.50E+05
116	100	210.00	210.00	60.0	0.0	1.27	7.50E+05
117	100	210.00	210.00	68.0	0.0	1.27	5.90E+05
118	100	210.00	210.00	82.0	0.0	1.27	4.00E+05
119	100	210.00	210.00	95.0	0.0	1.27	2.70E+05
120	100	120.00	120.00	60.0	0.0	1.27	8.40E+05
121	100	120.00	120.00	68.0	0.0	1.27	6.10E+05
122	100	120.00	120.00	82.0	0.0	1.27	4.10E+05
123	100	120.00	120.00	95.0	0.0	1.27	3.20E+05
124	100	120.00	120.00	112.0	0.0	1.27	2.10E+05
125	100	60.00	60.00	68.0	0.0	1.27	1.05E+06
126	100	60.00	60.00	82.0	0.0	1.27	7.20E+05
127	100	60.00	60.00	112.0	0.0	1.27	2.20E+05
128	100	30.00	30.00	82.0	0.0	1.27	2.95E+06
129	100	30.00	30.00	95.0	0.0	1.27	3.60E+05
130	100	30.00	30.00	112.0	0.0	1.27	3.30E+05
131	100	170.00	170.00	60.0	0.0	1.27	7.00E+05
132	100	140.00	140.00	60.0	0.0	1.27	7.80E+05

**Table 4.9.** Experimental data of the Ti-6Al-4V collected from ref. (BELLECAVE, 2015; ARAUJO, 2000; FERRY, 2017) (cylindrical contact).

Number	R(mm)	$P$ (N)	$Q_{max}$ (N)	$\sigma_{B,a}$	$\sigma_{B,m}$	$f$	$N_f$
133	70	14500	2320	139.6	140.5	0.55	1.73E+05
134	60	12430	1988.8	139.6	140.5	0.55	1.96E+05
135	50	10360	1657.6	139.6	140.5	0.55	3.74E+05
136	37.5	7770	1243.2	139.6	140.5	0.55	5.21E+05
137	20	6110	1729	99.4	99.4	0.5	3.59E+05
138	20	6110	1537	89.6	89.6	0.5	5.94E+05
139	20	6110	1637	89.6	89.6	0.5	5.10E+05
140	20	6110	1616	89.6	89.6	0.5	7.75E+05
141	20	6110	1689	95.2	95.2	0.5	6.46E+05
142	20	3117	717	170	170	0.5	2.26E+05
143	20	3117	779	190	190	0.5	1.64E+05
144	20	3117	717	160	160	0.5	4.79E+05
145	20	3117	717	160	160	0.5	4.89E+05
146	20	3117	717	155	155	0.5	7.23E+05
147	70	10910	2493	150	150	0.5	1.68E+05
148	70	10910	2537	140	140	0.5	2.49E+05
149	70	10910	2537	120	120	0.5	3.80E+05
150	70	10910	2182	100	100	0.5	3.98E+05
151	70	10910	2291	100	100	0.5	5.80E+05
152	70	10910	2755	95	95	0.5	5.84E+05
153	70	10910	2498	110	110	0.5	6.35E+05
154	70	10910	2455	105	105	0.5	6.97E+05
155	70	10910	2509	95	95	0.5	7.07E+05
156	70	10910	2564	90	90	0.5	9.72E+05
157	50	7793	1831	150	150	0.5	1.65E+05
158	50	7793	1987	150	150	0.5	1.68E+05
159	50	7793	2143	150	150	0.5	1.89E+05
160	50	7793	2104	150	150	0.5	2.04E+05
161	50	7793	1714	100	100	0.5	5.41E+05
162	70	10910	2509	150	150	0.5	1.66E+05
163	70	10910	2400	115	115	0.5	4.74E+05
164	70	10910	2291	100	100	0.5	4.95E+05
165	70	6714	2283	112.5	112.5	0.5	1.53E+05
166	70	6714	2182	75	75	0.5	6.72E+05
167	70	6714	1544	150	150	0.5	2.07E+05
168	70	6714	1410	100	100	0.5	5.29E+05

**Table 4.10.** Experimental data of the Ti-6Al-4V collected from ref. (VENKATESH *et al.*, 2001; KIRKPATRICK, 1999) (spherical contact).

Number	R(mm)	$P$ (N)	$Q_{max}$ (N)	$\sigma_{B,a}$	$\sigma_{B,m}$	$f$	$N_f$
169	25.4	50	23.5	400	0	0.5	1.10E+05
170	25.4	50	14.5	394	0	0.5	1.08E+05
171	25.4	50	12.3	298	0	0.51	3.04E+05
172	25.4	50	14.5	300	0	0.5	4.75E+05
173	25.4	50	23	327	0	0.48	1.44E+05
174	12.7	50	14.5	394	0	0.34	1.08E+05
175	12.7	50	15	341	0	0.34	2.66E+05
176	12.7	50	14.5	300	0	0.34	4.75E+05
177	25.4	50	15	341	0	0.34	1.92E+05
178	25.4	50	15	325	0	0.34	8.73E+05
179	12.7	50	30	315	0	0.34	1.17E+05
180	12.7	50	30	300	0	0.34	1.43E+05
181	12.7	50	30	250	0	0.34	2.78E+05
182	12.7	50	33	225	0	0.34	6.92E+05
183	25.4	50	30	375	0	0.34	8.60E+04
184	25.4	50	30	320	0	0.34	2.12E+05
185	25.4	50	30	265	0	0.34	2.46E+05
186	25.4	50	30	260	0	0.34	2.54E+05
187	12.7	50	30	300	0	0.34	1.43E+05
188	12.7	50	23	300	0	0.34	3.08E+05
189	12.7	50	14.5	300	0	0.34	4.75E+05
190	25.4	50	32	300	0	0.34	2.07E+05
191	25.4	50	21	300	0	0.34	5.98E+05
192	12.7	50	14.5	300	0	0.34	4.75E+05
193	12.7	40	16	300	0	0.34	4.01E+05
194	12.7	30	16	300	0	0.34	4.99E+05
195	12.7	50	37.5	300	0	0.34	1.83E+05
196	12.7	50	23	300	0	0.34	2.28E+05
197	12.7	50	21	300	0	0.34	3.17E+05
198	12.7	50	20	300	0	0.34	2.61E+05
199	12.7	50	18	300	0	0.34	4.33E+05
200	12.7	50	17	300	0	0.34	6.05E+05
201	12.7	50	14	300	0	0.34	7.45E+05
202	25.4	50	20.5	300	0	0.34	2.44E+05

**Table 4.11.** Experimental data of the 7050-T7451 collected from ref. (GAILLIEGUE, 2018) (cylindrical contact).

Number	R(mm)	$P$ (N)	$Q_{max}$ (N)	$\sigma_{B,a}$	$\sigma_{B,m}$	$f$	$N_f$	$\varpi(^{\circ})$
203	70	5800	2300	113.6	0	0.6	9.40E+04	0
204	70	5800	2300	113.6	0	0.6	1.57E+05	45
205	70	5800	2300	113.6	0	0.6	2.09E+05	90
206	70	5800	2300	113.6	0	0.6	7.95E+04	135

**Table 4.12.** Experimental data of the A743 CA6NM collected from ref. (GAILLIEGUE, 2018) (cylindrical contact).

Number	R(mm)	$P$ (N)	$Q_{max}$ (N)	$\sigma_{B,a}$	$\sigma_{B,m}$	$f$	$N_f$	$\varpi(^{\circ})$
207	70	15990	5499	295.8	0	0.7	1.69E+05	45
208	70	15990	5499	295.8	0	0.7	1.57E+05	135

in Table 4.10, with sphere-on-flat contact configuration. The third group (Table 4.11) is related to the FF tests performed with Al 7050-T451 (cylinder on flat configuration). The last group (Table 4.12) is related to FF tests carried out with ASTM A743 CA6NM, also using cylindrical pads. It should be noted that the out-of-phase loading effect is present in the FF experiments in Tables 4.11 and 4.12.

Fig. 4.5c also illustrates loading configurations present in the tests. In this case, firstly, the pads are pressed against the flat specimen due the application of the normal load  $P$ . Secondly, the bulk fatigue load,  $B(t)$ , is applied on the specimen in conjunction with the tangential load,  $Q(t)$ . For the fretting data reported in (BRITO OLIVEIRA *et al.*, 2023a), they utilized fretting fatigue rigs with only one fatigue actuator. In this setting, the tangential load arises as a reaction force due to the presence of the bulk fatigue load, which means that both loads are coupled and in phase. Some tests (Tables 4.5 and 4.6) were conducted under the presence of mean bulk load. For the former, the mean bulk load was prescribed after the normal contact load  $P$ , and prior to the  $P$  for the later one. In reference to the data of (OLIVEIRA *et al.*, 2024), for those with the out-of-phase shear loading effect, the correspondent phase angle ( $\varpi$ ) is also indicated (Tables 4.11 and 4.12). All tests reported were set under a partial slip regime. By summarizing, Tables 4.3–4.12 report the following main parameters for each test considered in this chapter: pad radius,  $R$ , normal load,  $P$ , tangential load,  $Q$ , bulk stress amplitude,  $\sigma_{B,a}$ , mean bulk stress,  $\sigma_{B,m}$ , friction coefficient,  $f$ , and the observed fatigue life  $N_f$

Table 4.13 contains the relevant specimen dimensions, i.e. its height,  $h_s$ , and thickness,  $thk$  (see Fig. 4.5) for Al 4%Cu (ARAÚJO *et al.*, 2008; NOWELL, 1988), 2024-T351 (SZOLWINSKI; FARRIS, 1998; NAVARRO *et al.*, 2011), 7050-T7451 (ROSSINO *et al.*, 2009; ARAÚJO; CASTRO, 2012), 7075-T651 (MARTÍN *et al.*, 2020; MUÑOZ *et al.*, 2007; GAILLIEGUE, 2018), 7075-T6 (WITTKOWSKY *et al.*, 2000; KIRKPATRICK, 1999; VALLELLANO *et al.*, 2004), 2024-T3 (HOJJATI-TALEMI *et al.*, 2014; PINTO *et al.*, 2022a), Ti-6Al-4V (BELLECAVE, 2015; ARAUJO, 2000; FERRY, 2017; VENKATESH *et al.*, 2001; KIRKPATRICK, 1999;

**Table 4.13.** Geometrical and critical distance parameters for all the materials studied.

Material	$h_s$ (mm)	$thk$ (mm)	$L/2$ (mm)
Al 4% Cu	14	12.5	0.050
2024-T351	12.7	12.7	0.013
7050-T7451	13	13	0.031
7075-T651	10	8 and 5	0.026
7075-T6	5	5	0.021
2024-T3	10	4	0.023
Ti-6Al-4V	5 – 13	5 – 13	0.028
A743 CA6NM	13	13	0.030

CARDOSO *et al.*, 2020), A743 CA6NM (GAILLIEGUE, 2018). The material critical distances collected from the literature are also reported in Table 4.13, we assume values based on the  $N_f \times L$  curves for  $10^6$  cycles reported in (KOUANGA *et al.*, 2018) and (GAILLIEGUE, 2018), for the titanium and steel alloys, respectively, once the properties related to compute  $L$  based on Eq. 2.32 has not been found.

To provide clarity to the reader, it is important to note that all aluminum data (excluding out-of-phase data) is encompassed within the scope of the first article (BRITO OLIVEIRA *et al.*, 2023a), while all data referenced thus far is contained within the second article (OLIVEIRA *et al.*, 2024). The next section discusses the details regarding all numerical simulations (finite element and ANN training) performed to create the ANN models.

## 4.4 SIMULATION DEVELOPMENTS

### 4.4.1 Finite element models

In order to obtain the stress solutions for the test conditions addressed in the previous section, the commercial finite element (FE) software ABAQUS is used (see section 2.1.6). A numerical approach has been chosen over the use of closed-form analytical solutions since the specimen's finite dimension might play an important role in the fretting fatigue stress distribution. Fellows *et al.* (1995), for instance, pointed out that the axial stress component,  $\sigma_{xx}$  (being  $x$  the axial direction, see Fig. 4.5a and 4.5b), induced by the normal contact load might considerably diverge from the half-plane analytical solution even for specimens with heights,  $h_s$ , as large as ten times the size of the contact zone,  $2a$ . Some of the data here investigated, as test Number 90, for example, exhibits a ratio  $h_s/2a$  near three, which makes

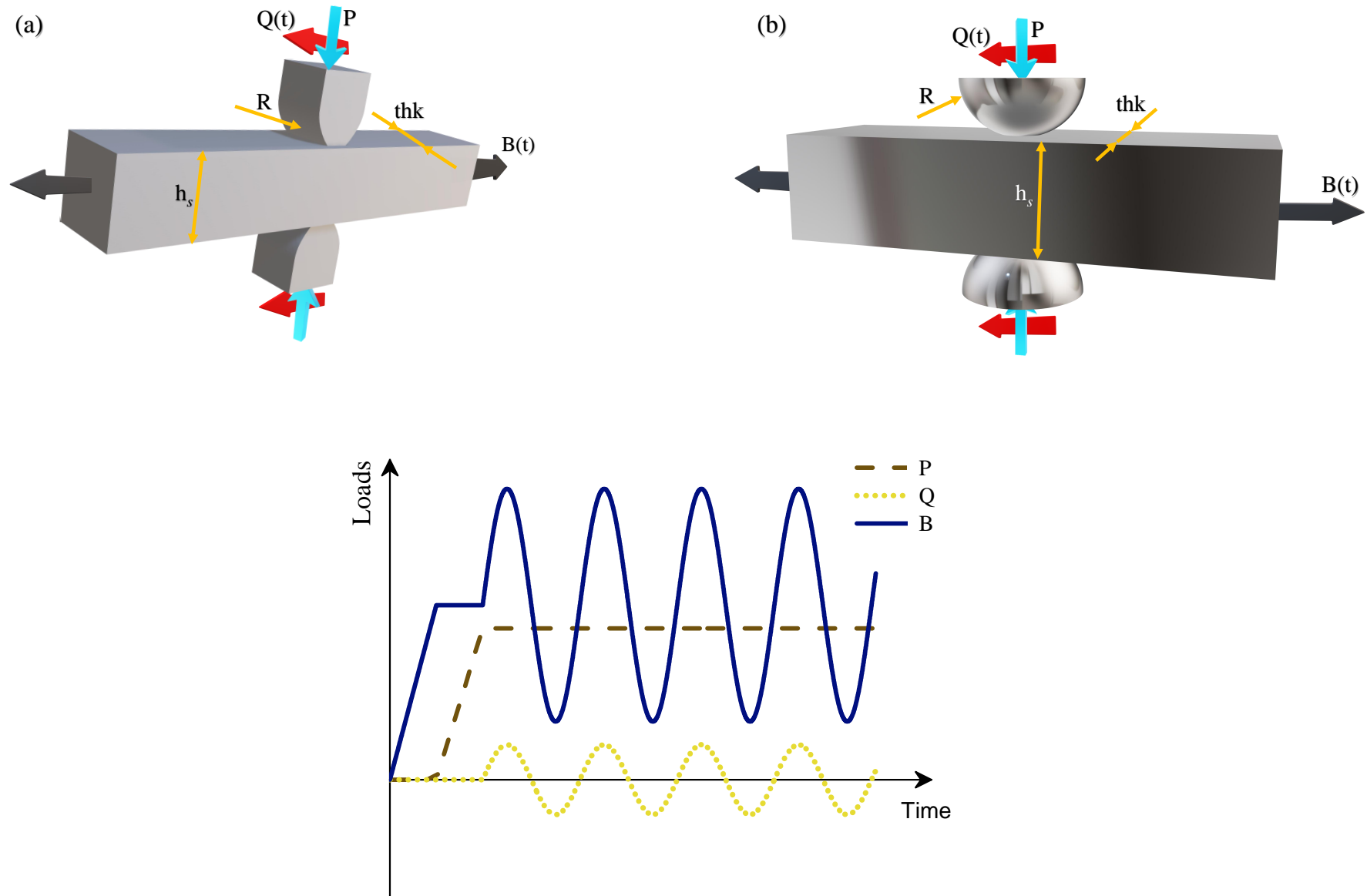


**Figure 4.5.** Cylinder on-plane fretting fatigue experimental set-up scheme (a), sphere on-plane fretting fatigue experimental set-up scheme (b), and a schematic of loading history (c).

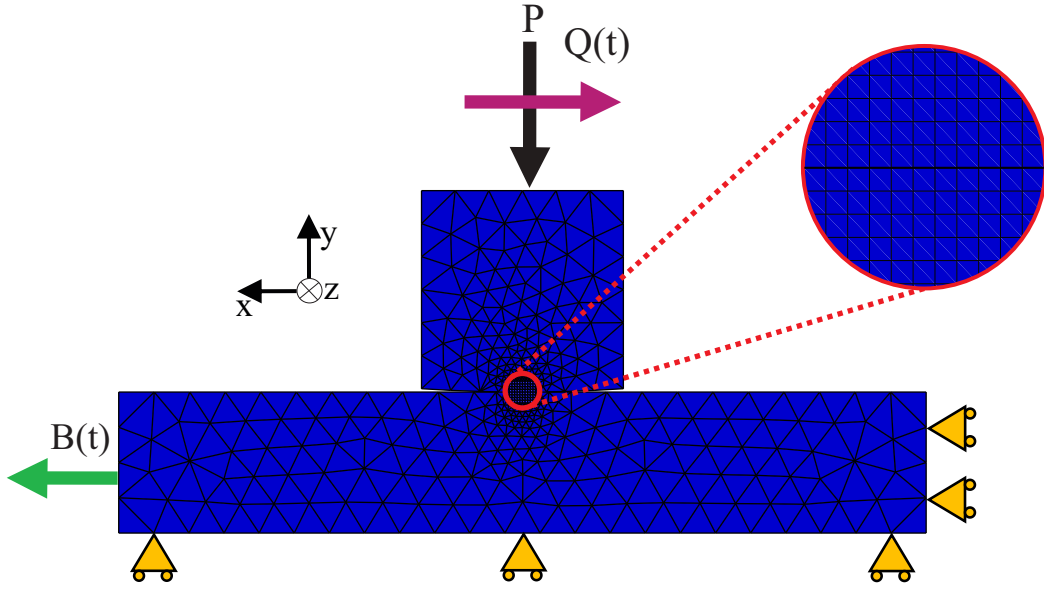


**Figure 4.6.** Finite element model used to simulate the cylinder on-plane fretting fatigue experiments.

the use of the half-plane closed-form solution not adequate. Besides, some fretting fatigue data experienced reverse slip (presence of large bulk loads), which requires elaborate analytical formulations (VÁZQUEZ *et al.*, 2013) or numerical solutions.

Figures 4.6 and 4.7 illustrate the numerical models developed for the assessment of cylindrical (2D) and spherical (3D) fretting contacts, respectively. In accordance with the experiments, firstly, the mean bulk load is prescribed on the left surface of the specimen (see Figs. 4.6 and 4.7), which generates the mean bulk stress,  $\sigma_{B,m}$ . Secondly, the cylindrical or spherical pad is pressed against the flat specimen due the application of the normal load  $P$ . Finally, the alternate bulk load is prescribed on the specimen in phase with the tangential load,  $Q$ , which is applied on the pad. Notice that the alternate bulk load generates the bulk stress amplitude,  $\sigma_{B,a}$ .

Due to symmetry, only half of the specimen height ( $h_s/2$ ) is considered for both contact configurations. For the spherical set-up, we take advantage of the problem's symmetry along the  $xy$  plane passing through the center of contacting bodies, and only half of the specimen thickness is considered in the analyses (Fig. 4.7). A similar approach was previously adopted in Tur *et al.* 2003. In addition, for both contact conditions, multi-point constraints are set on

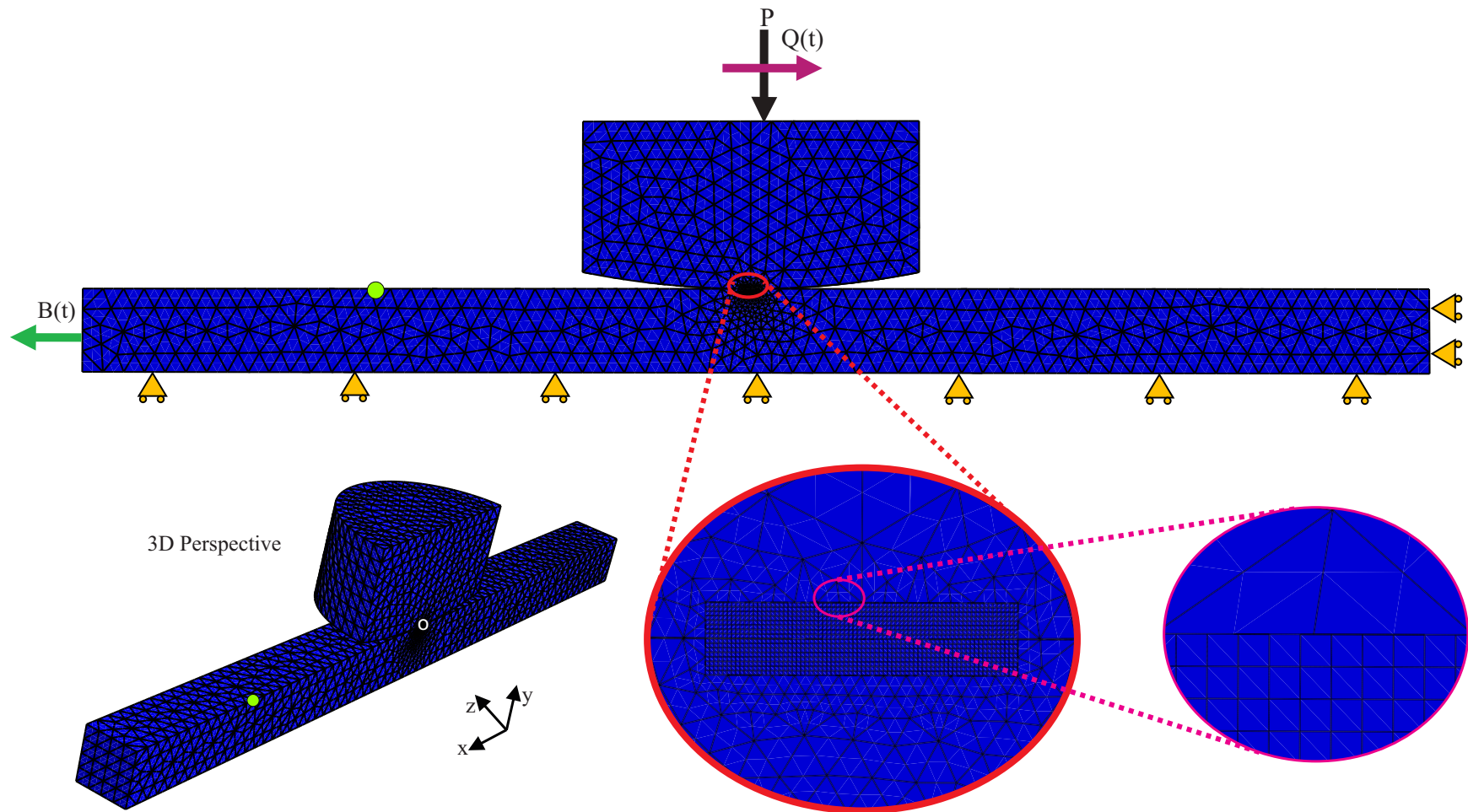


Figure 4.7. Finite element model used to simulate the sphere on-plane fretting fatigue experiments.

the pad's upper surface so that rotation is avoided.

Concerning the discretization of the models, a region with a fine mesh is established near the contacting surfaces for both cylindrical and spherical setups, as can be noted in Figs. 4.6 and 4.7. In the former, the refinement region is formed by quadrangular elements, whereas in the 3D spherical model, cubic elements are adopted. Far from the contact region, the coarser mesh is composed of triangular and tetrahedral elements for the cylindrical and spherical configurations, respectively. In the cylindrical model, 2D plane strain elements are considered. Besides, linear elements are adopted in all the analyses. Friction contact constraints are established by using the penalty formulation, where the slave and master nodes were defined in the mesh refinement region, the former set on the pad's contact surface and the latter on the specimen.

As it can be noted in Fig. 4.7, for the spherical 3D model, non-matching meshes are used in the transition between the fine and the coarse mesh regions. Such a strategy, implemented via ABAQUS tie constraint, is considered for reducing computational costs. In this work, after a convergence study, it was observed that, on the mesh transition boundaries, a relation of four elements in the fine region for one element in the coarse one yields a good compromise between stress solution accuracy and computational cost.

Since various fretting fatigue data with different geometries and materials are investigated here, it is necessary standardize the mesh refinement in the models. In this case, after a convergence analysis, the size of the element in refinement zone was defined based on minimum value between the material critical distance,  $L/2$ , and the semi-width of the contact zone over thirty,  $a/30$ .

Figure 4.8 shows a comparison between the surface stress components obtained numerically and analytically (half-plane assumption), when the test condition Number 1 in Table 4.3 (cylinder-on-plane) is considered.

It can be observed that, the numerical and the analytical solutions present a good accordance, which validates the accuracy of the cylindrical 2D FE model. To validate the spherical model, the fretting fatigue analytical solution for sphere-on-plane contacts proposed by Domínguez (1998), which is based on the explicit stress expressions by Hamilton (1983) and Sackfield and Hills (1983), have been reproduced here (see section 2.1.5.2). Figures 4.9a and 4.9b show

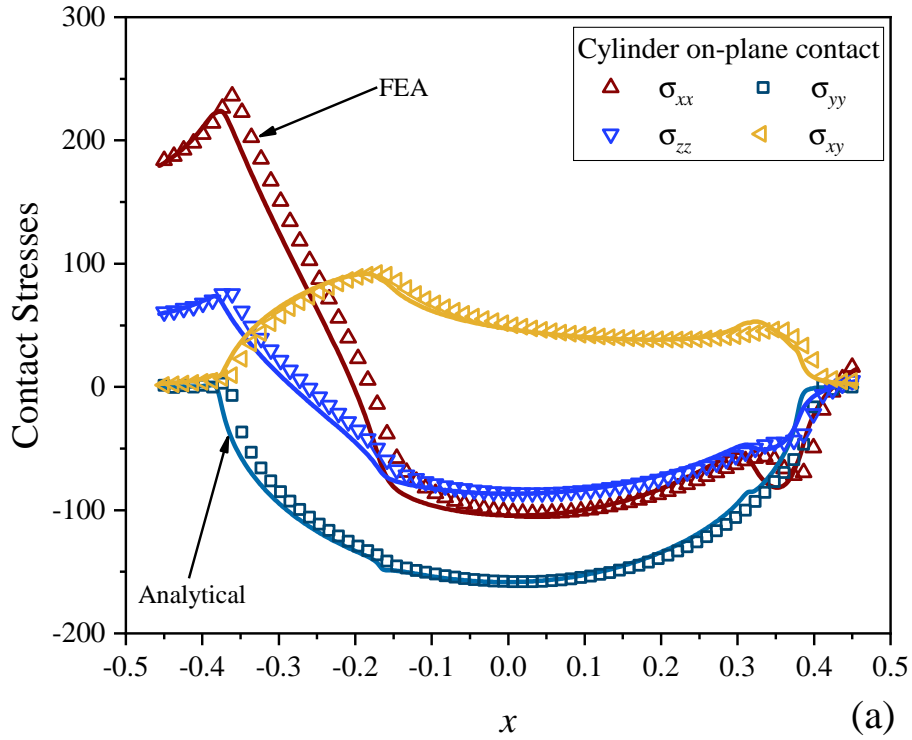


**Figure 4.8.** Comparison between the analytical and the numerical contact surface stresses for the cylinder-on-plane model.

a comparison between the numerical and the analytical solutions. In the former, one has the stress distribution over the contact surface on the line of symmetry,  $y/a = z/a = 0$ , whereas in the latter, one has the stress distribution inward the contact, i.e.,  $x/a = -1$  and  $z/a = 0$ . As it can be observed, a good accuracy is also observed in the 3D numerical FE model.

Concerning the second article (OLIVEIRA *et al.*, 2024), it is important to highlight the utilization of the models previously described which is related to previous works (BRITO OLIVEIRA *et al.*, 2023a), for cylindrical (2D) and spherical (3D) fretting contacts, solely changing the type of material and the new loading conditions. For the cases with the presence of the out-of-phase loading effect, the  $Q$  loading is set according to the correspondent phase angle ( $\varpi$ ) of each test (Tables 4.11 and 4.12).

#### 4.4.2 Neural networks based models

Based on the results of the FE numerical simulations, one could compute the equivalent stresses required by the ANN models. Once again, it is emphasized that this chapter is grounded

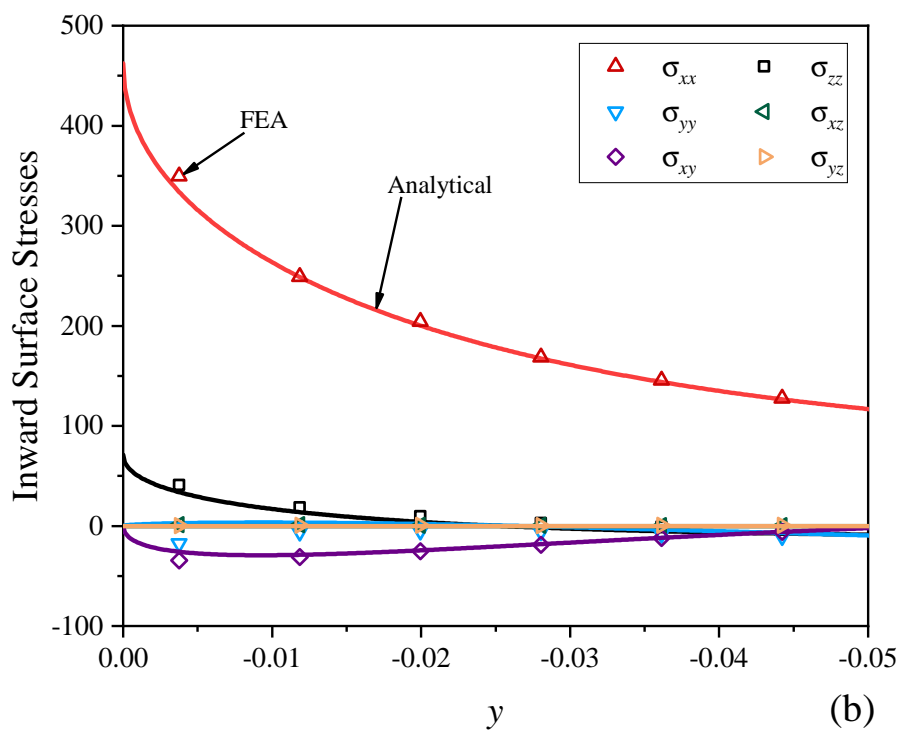
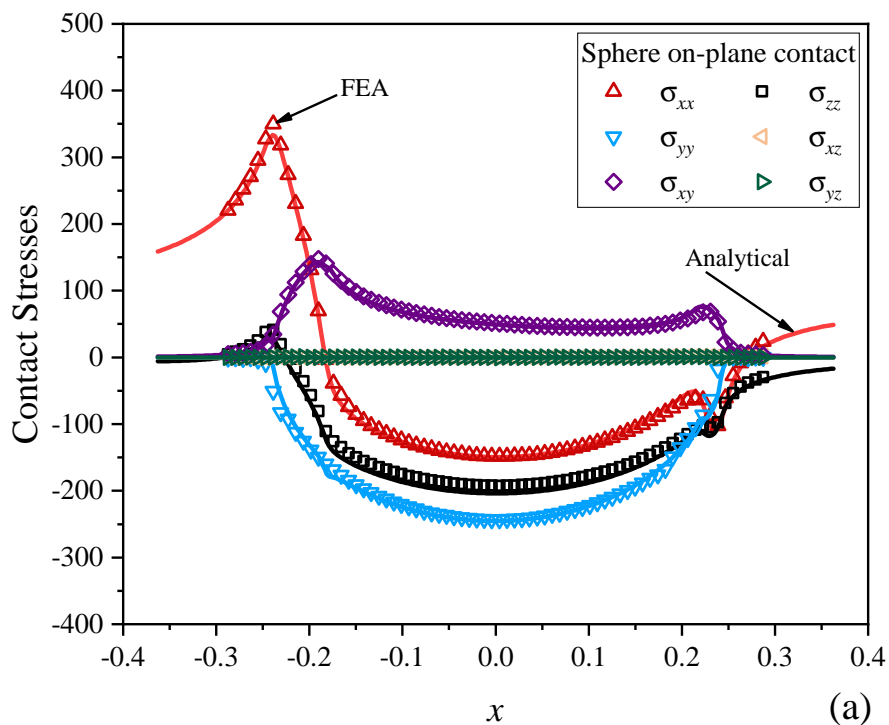


**Figure 4.9.** Comparison between the analytical and the numerical stress field for the sphere on-plane model: (a) on the contact surface and (b) inward the contact surface (trailing edge).

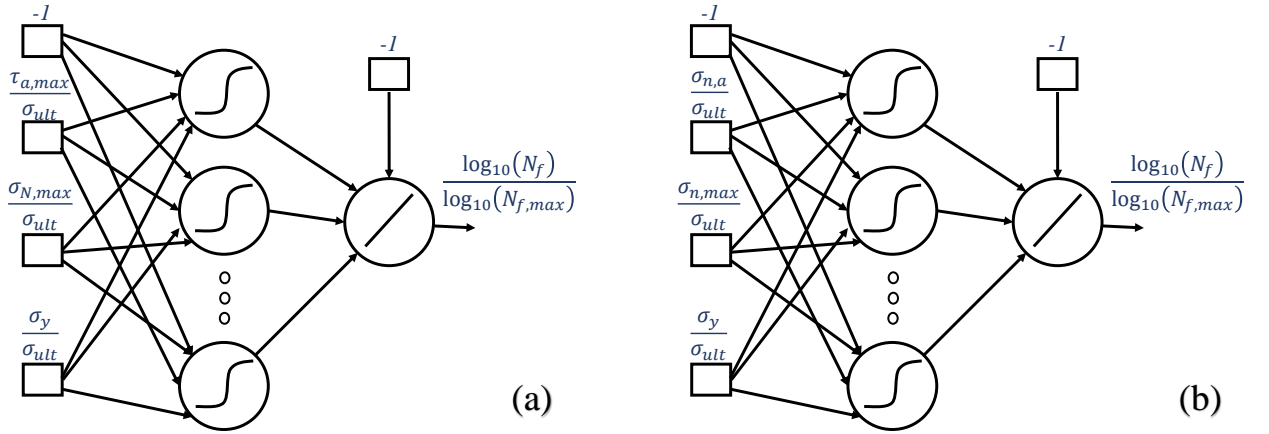


**Figure 4.10.** ANN architecture based on the parameters of the MWCM model (a) and on the parameters of the SWT model (b), based on (BRITO OLIVEIRA *et al.*, 2023a).

in the models proposed by two articles. Consequently, one will delineate five models in this section — two associated with the first article (BRITO OLIVEIRA *et al.*, 2023a) and three linked to the second (OLIVEIRA *et al.*, 2024). From the first one, the data from four aluminum alloys (Al 4%Cu, 7075-T651, 7050-T7451, and 2024-T351 Al alloys) are chosen for training and testing the ANN models. Fretting fatigue data from the 2024-T3 and 7075-T6 alloys, on the other hand, are selected as the query data, i.e., a set of independent data used for analyzing the potential of generalization and robustness of the ANN-based models. In this case, besides considering fretting fatigue data conducted on Al alloys not used in the construction of the ANN models, the query data also contemplate different contact configurations (spherical and cylindrical), presence of mean bulk load and a fair range of observed fatigue lives (see Fig. 4.4). Both ANNs have three inputs and, to avoid neurons saturation, all of them are normalized with respect to the material ultimate tensile strength,  $\sigma_{ult}$ . The shear based ANN model is here named as ANN\_SHEAR, where its inputs data are the normalized maximum shear stress amplitude ( $\tau_a/\sigma_{ult}$ ), the normalized maximum normal stress ( $\sigma_{N,max}/\sigma_{ult}$ ) and the normalized yield stress ( $\sigma_y/\sigma_{ult}$ ). Fig. 4.10a shows the ANN architecture for this model. The other ANN model proposed in this work, named ANN\_NORMAL, is based on the SWT stress parameters. The input data are the normalized normal stress amplitude ( $\sigma_{n,a}/\sigma_{ult}$ ), the normalized maximum normal stress ( $\sigma_{n,max}/\sigma_{ult}$ ) and the normalized yield stress ( $\sigma_y/\sigma_{ult}$ ), as shown in Fig. 4.10b. In summary, to train the ANN models, 99 experimental data were randomly chosen for training and 9 for testing. The query data have a total of 24 experiments.

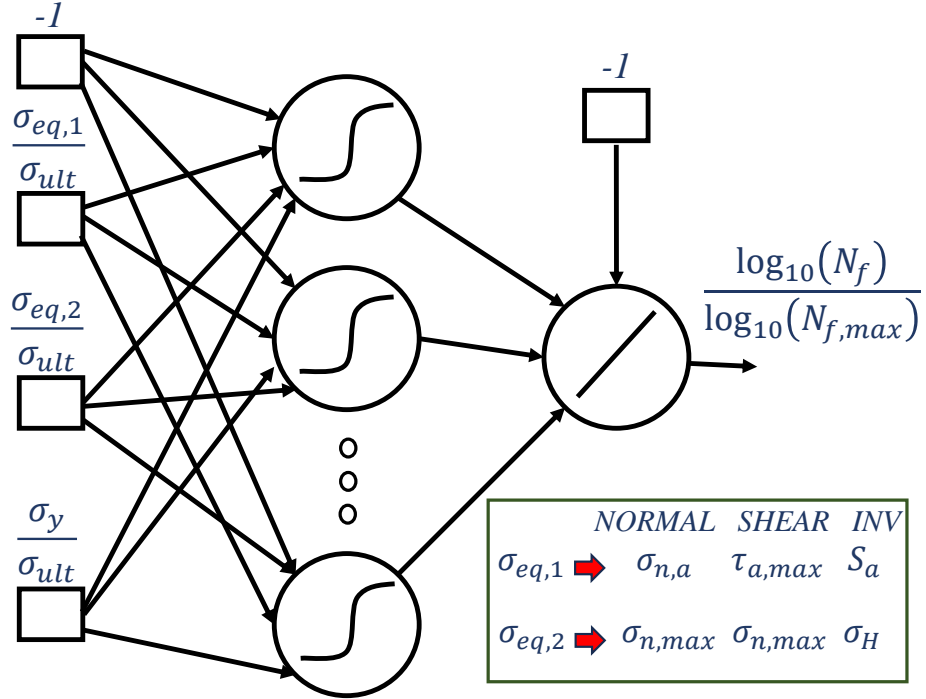


**Figure 4.11.** General ANN architecture for all ANN models considered in (OLIVEIRA *et al.*, 2024).

The ANN models considered in the second article (OLIVEIRA *et al.*, 2024) were trained and validated using a total of 132 FF experiments with Al alloys under in phase loading (all data from (BRITO OLIVEIRA *et al.*, 2023a)). In order to evaluate the performance of the ANN models to generalize and sustain robustness, independent FF data sets, never seen before by such models, have now been considered. The ANN models have been named as: SHEAR, NORMAL, and INV. The first two are inspired by stress parameters present in two critical plane models (MWCM and SWT) and the last one by stresses from an invariant multiaxial fatigue model (Crossland). Fig 4.11 shows the general ANN architecture, for the three models considered in the second article. The equivalent stresses  $\sigma_{eq,1}$  and  $\sigma_{eq,2}$  represent the set of equivalent stresses for each model, i.e.:  $(\tau_{a,max}, \sigma_{n,max})$ ,  $(\sigma_{n,a}, \sigma_{n,max})$  and  $(S_a, \sigma_{H,max})$ . The Al experimental data are randomly chosen for training (119 experiments) and test (13 experiments) datasets. The collection of query data has a total of 75 experiments, 69 for Ti-6Al-4V, 2 for A743 CA6NM and 4 for 7050-T7451.

For all five models cited here, The output is the normalized fatigue life in the logarithmic scale  $(\frac{\log_{10}(N_f)}{\log_{10}(N_{f,max})})$ , such that  $N_{f,max}$  has been assumed as  $10^8$ , which is a maximum value we elect that no FF experiment will reach.

The ANN architecture adopted both articles uses a multiple-layer perceptron network with

a single hidden layer. Neurons in the hidden layer are activated by the tangent hyperbolic function, while the output layer uses a linear function. The use of biases is also displayed in Fig. 4.10 and 4.11. For the weight's initialization in the ANN training, the Xavier initialization method (GLOROT; BENGIO, 2010) is implemented in order to guarantee the stabilization of the gradient descent during the training and ensure greater generalization. The training algorithm adopted is the backpropagation one together with the method of moments (HAYKIN, 2008). The maximum training epoch considered is 20,000, with a learning rate of 0.1 and a moment constant of 0.7. Besides, cross-validation is employed during 20,000 epochs considering the empirical risk error (ER) (Eq. 3.1). After that, the weights which yields the lowest testing error are chosen to define the final trained ANN model.

We point out that various hyperparameters of the ANN were analyzed during this study, including training with stochastic or minibatch gradient descent methods, weight initialization effects, varying the number of neurons in the hidden layer from 10 to 100 to find the optimal value for each architecture, and testing different activation functions (ReLU, tanh, sigmoid) in the hidden layer.

#### 4.4.2.1 Development of the models

To better understand the development of the models, Fig. 4.12 shows a flowchart where all the followed steps are divided into three phases. Phase I represents the pre-processing of the data, with the experimental data collection, the equivalent stresses computation, normalization of the results and selection of the three main datasets (training, test, and query data). Phase II is the ANN training phase, here the training and the test data are applied in the ANN and the training algorithm is used to minimize the empirical error through cross-validation, finally capturing the best values for the weights. In Phase III, these obtained weights are used to create a function capable of estimating the fretting fatigue life. Note that the variables  $x_1$ ,  $x_2$  and  $x_3$  (see Figs. 4.10 and 4.11) represent the inputs of the function considered.

Fig. 4.13 summarizes the modeling process considered to test the ANN models with the query data. As can be seen, experimental parameters (outlined in Tables 4.5, 4.7 and 4.9-4.12) guide the numerical modeling. Subsequently, the correspondent stress tensor is extracted at the material critical distance. Finally, equivalent stresses are then calculated and utilized as

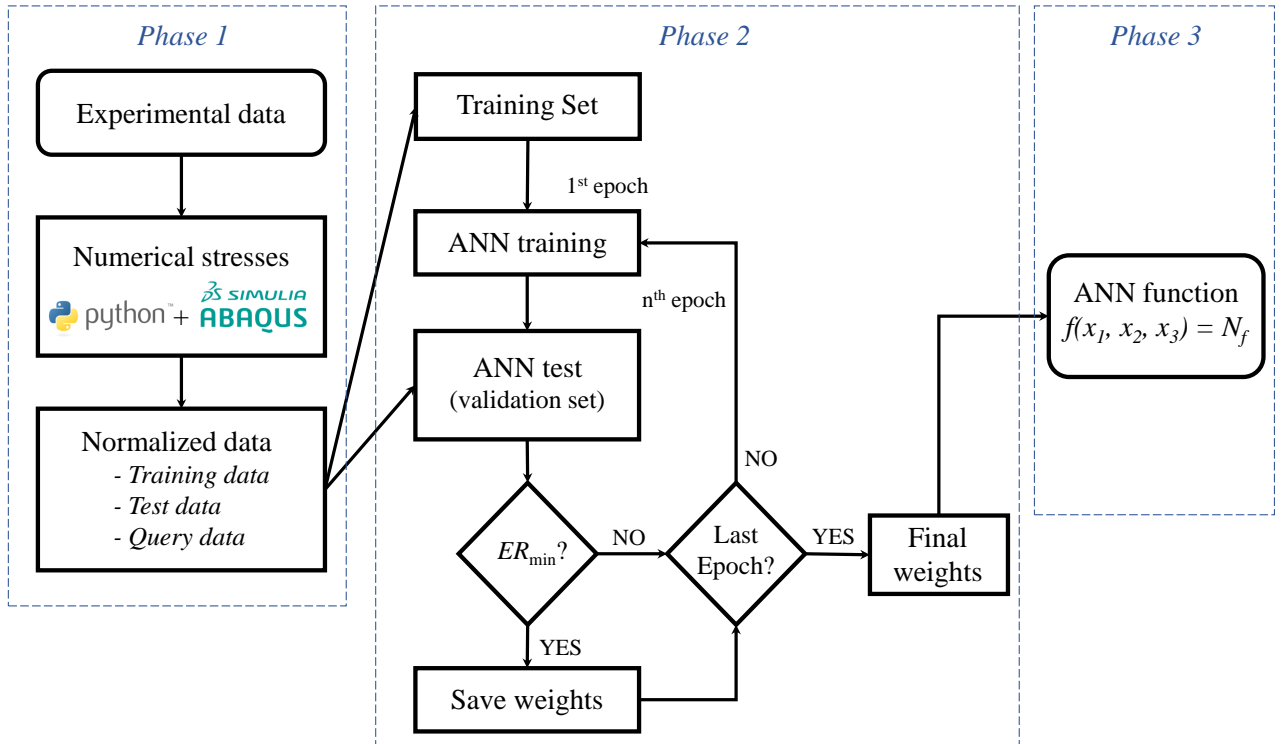


Figure 4.12. Flowchart illustrating all the process to construct the ANN models

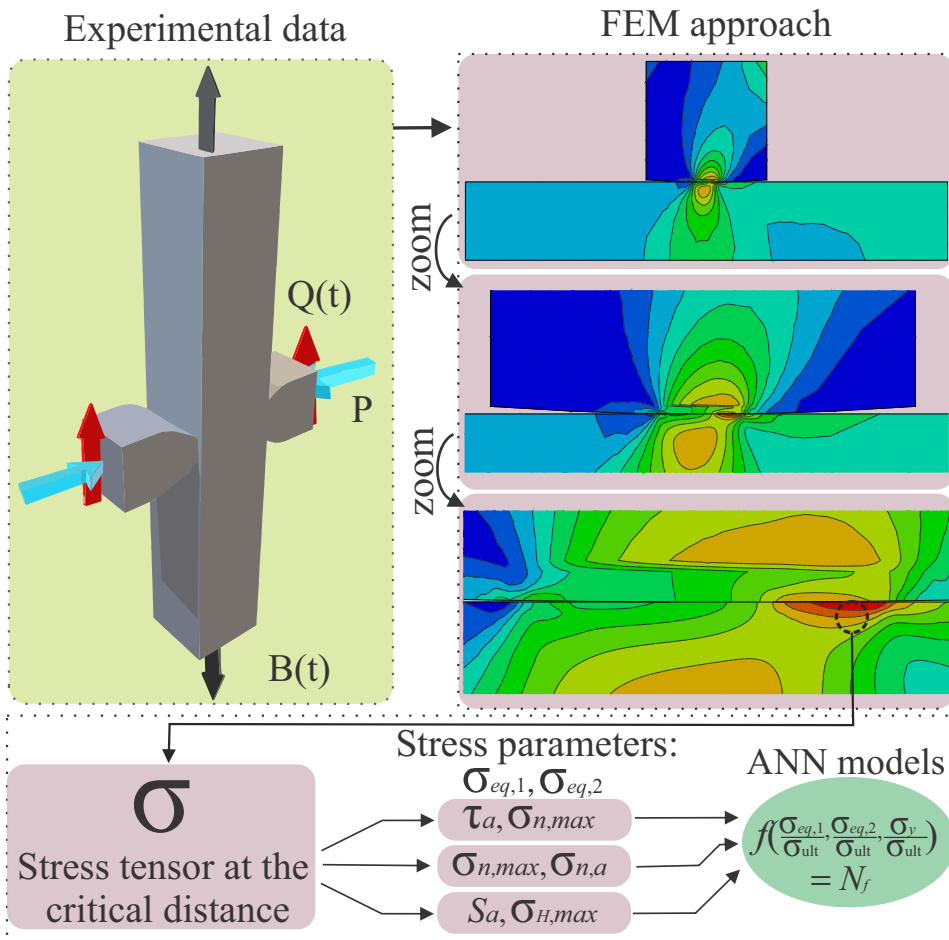


Figure 4.13. Summary of the considered modeling

inputs of the ANN models.

## 4.5 RESULTS AND DISCUSSIONS

This section are divided into two parts: the first presenting results from the first article (BRITO OLIVEIRA *et al.*, 2023a), and the second focusing on outcomes from the second article (OLIVEIRA *et al.*, 2024). These parts are designated as Part 1 - Aluminium Article and Part 2 - Titanium Article, named after the most significant alloys discussed in each respective article.

### 4.5.1 Part 1 - Aluminium Article

#### 4.5.1.1 Calibration of the multiaxial models

Experimental uniaxial fatigue data for the 2024-T3 and 7075-T6 Al alloys were used to calibrate the SWT and MWCM multiaxial fatigue models. Expressions relating the SWT parameter with the number of cycles to failure are given in Figs. 4.14a and 4.14b for the 2024-T3 and 7075-T6 Al alloys, respectively. For the MWCM, Fig. 4.14c and 4.14d show the  $\tau_a$  vs.  $N_f$  curves for the two aforementioned alloys. Thus, expressions to estimate fatigue life based on the MWCM are given in Eqs. 4.1 and 4.2 for the 2024-T3 and 7075-T6 Al alloys, respectively. In Section 4.5.1.3, fatigue life estimates by considering these multiaxial fatigue models are compared with the ones obtained through the ANN models.

$$N_f = 10^7 \left[ \frac{-16.408\rho + 70.919}{\tau_a} \right]^{0.622\rho + 5.125} \quad (4.1)$$

$$N_f = 10^7 \left[ \frac{-15.883\rho + 102.642}{\tau_a} \right]^{2.616\rho + 7.588} \quad (4.2)$$

#### 4.5.1.2 ANN results

Table 4.14 reports the empirical risk error (Eq. 3.1) associated with the training and testing datasets for both models here proposed in (BRITO OLIVEIRA *et al.*, 2023a). Such errors are obtained by considering the optimum number of neurons in the hidden layer, i.e., 27 and 25 neurons for the ANN\_SHEAR and ANN\_NORMAL models, respectively. The total error

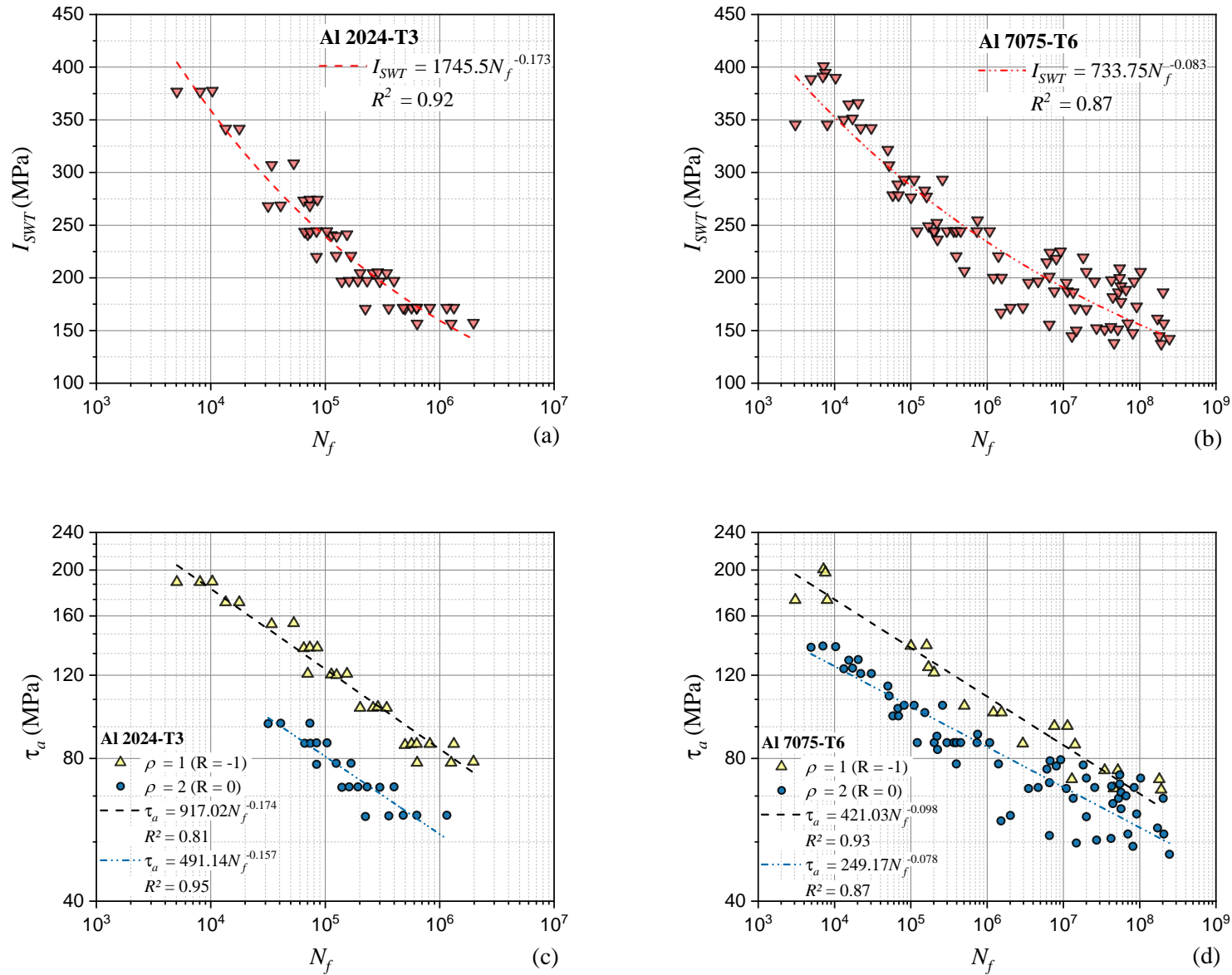


**Figure 4.14.** SWT parameter versus fatigue life for the 2024-T3 (a) and the 7075-T6 (b) Al alloys. Modified Wohler “ curve for the 2024-T3 (c) and the 7075-T6 (d) Al alloys.

**Table 4.14.** Empirical risk (ER) error for the ANN\_SHEAR and the ANN\_NORMAL models by considering their respective optimum number of neurons in the hidden layer.

Model	ER* (training)	ER* (test)	ER* (total)	Hidden neurons
ANN_SHEAR	46.533	9.049	43.409	27
ANN_NORMAL	43.096	14.509	40.714	25

\* Values must be multiplied by  $10^{-5}$ .

in Table 4.14 is defined as the weighted average of the training and testing errors. Overall speaking, both models presented similar performance.

Experimental vs. estimated fatigue life plots for the ANN\_SHEAR and ANN\_NORMAL models are showed in Fig. 4.15a and 4.15b, respectively. The solid black lines represent the exact estimates and the dashed ones the factor of two error boundaries. The blue squares, the red triangles and the green diamonds represent, respectively, the training, test and query data. As can be observed, both models proved themselves promising by providing most of the life estimates for the query data within the error factor of two. Such results confirm the proposed methodologies capability of accurately handling material, geometry and loading conditions other than those used in the ANN training.

### 4.5.1.3 Comparative analysis

For the sake of comparison, fatigue life can be also estimated by utilizing the SWT and MWCM multiaxial fatigue models for the fretting fatigue tests conducted on the 2024-T3 and 7075-T6 Al alloys (query data). Results for the 2024-T3 alloy are presented in Fig. 4.16a. In this case, blue up triangles and yellow down triangles represent, respectively, life estimate results by considering the MWCM and the SWT models. The circle and hexagon markers are used for the life estimates obtained with the ANN\_SHEAR and ANN\_NORMAL models. Concerning the multiaxial fatigue models, both provide conservative results, especially the shear stress based one (MWCM). The ANN models, on the other hand, provide non-conservative life estimates, however, with most of the results within the error factor of two. However, it is worth noticing that, even though the ANN predictions are more optimistic, results presented less dispersion when compared to the investigated multiaxial fatigue models. Note that both the ANN and the multiaxial fatigue model based on normal stresses provide better life estimates than their shear stress based counterparts, which suggests the crack initiation mechanisms take

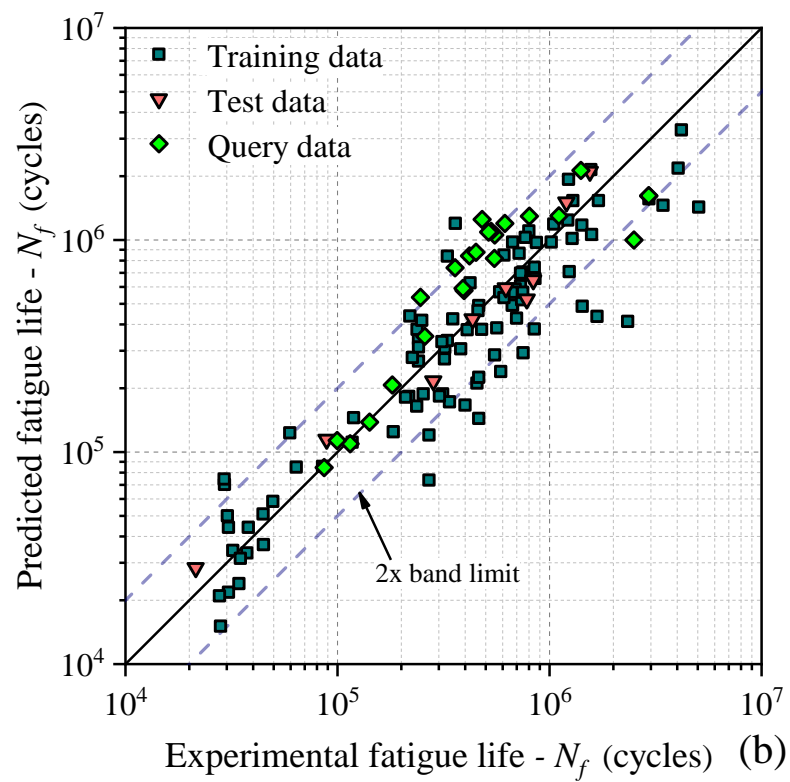
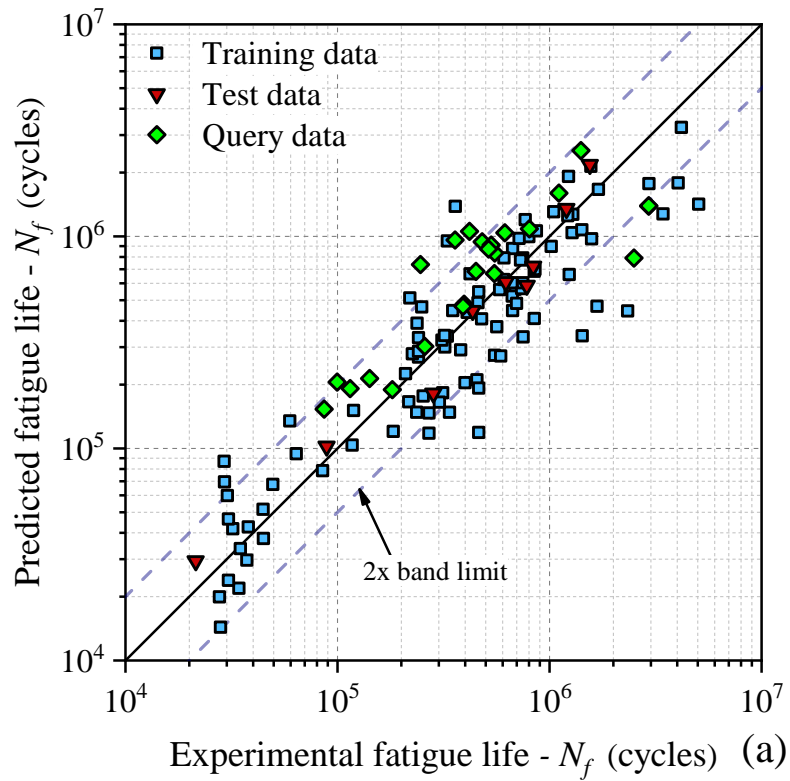


**Figure 4.15.** Estimated fatigue life by the ANN\_SHEAR model vs. the experimental one (a). Estimated fatigue life by the ANN\_NORMAL model vs. the experimental one (b).

**Table 4.15.** Empirical risk (ER) error for the query data by considering all models.

Alloy	Model	$ER^*$
2024-T3	ANN_SHEAR	78.54
	ANN_NORMAL	30.06
	SWT	165.99
	MWCM	463.87
7075-T6	ANN_SHEAR	42.47
	ANN_NORMAL	55.90
	SWT	375.52
	MWCM	149.42

\* Values must be multiplied by  $10^{-5}$ .

place under mode I (CARDOSO *et al.*, 2019; SMITH, 1908) for this material.

Similarly, Fig. 4.16b shows fatigue life estimates for the 7075-T6 Al alloy when the multi-axial fatigue and ANN models are employed. As can be noted, the ANN models performed considerably better than the standard multi-axial fatigue ones. In this case, both the shear and normal based ANN models presented similar accuracy, where most of the estimates are within the factor of two lines. The same cannot be said about the standard MWCM and SWT models, where the former yields very conservative results in some cases and the latter predicts too optimistic results for most of the investigated data. Again, the ANN-based models provide the best life estimates with almost all data inside the two-band width limit. The investigated multi-axial fatigue models, on the other hand, performed poorly producing life estimates, in many cases, quite far from the factor of two lines.

To quantify and compare the performance of all the fatigue life estimate approaches considered in this work, the empirical risk error (ER) was used. Table 4.15 reports the values of ER for all the models when considering the query data tests, i.e., fretting fatigue tests conducted on the 2024-T3 and 7075-T6 alloys. Overall speaking, normal stress based models perform better for the 2024-T3 alloy, while shear stress based models result in more precise life estimates for the 7075-T6 alloy. Moreover, the ANN results are considerably more accurate than the standard multi-axial fatigue models. For the 2024-T3 dataset, for instance, the ANN model based on normal stress (ANN\_NORMAL) yields an error (ER) 81.9% smaller than that obtained by using the SWT parameter. For the 7075-T6 Al alloy, the shear stress based ANN model (ANN\_SHEAR) produces an error 71.6% smaller than the one found with the MWCM.

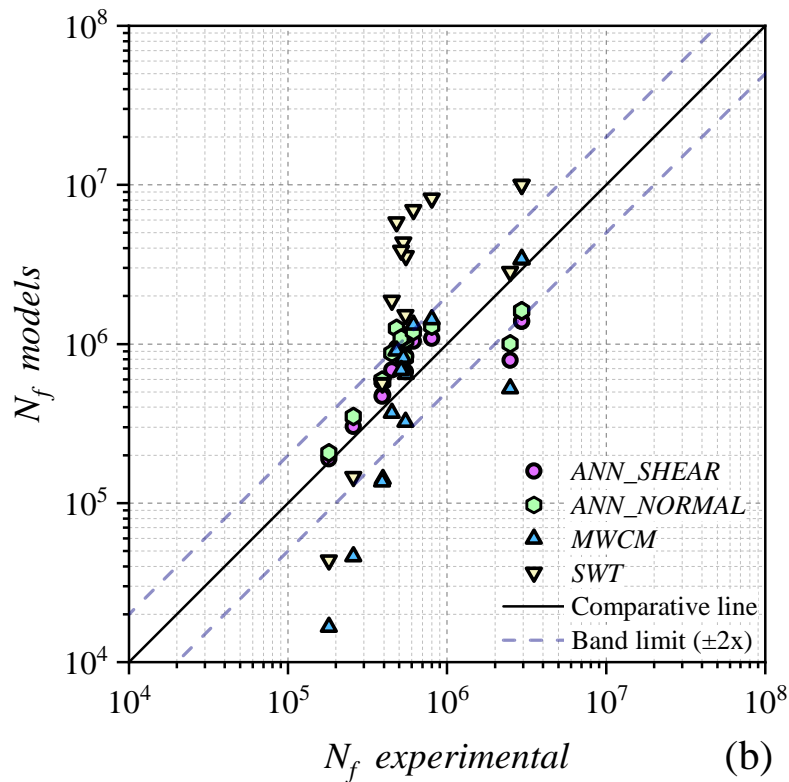
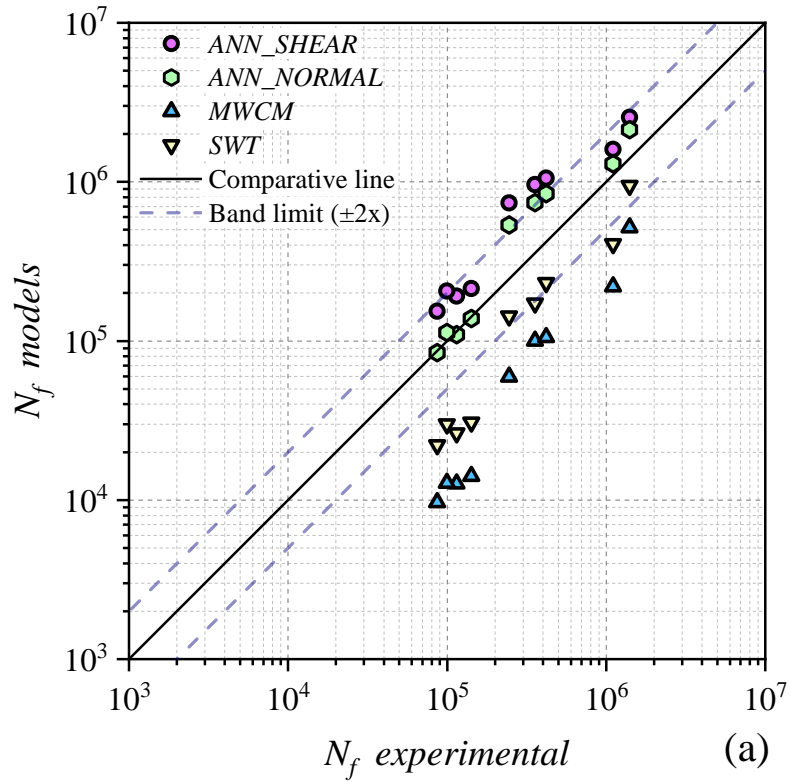


**Figure 4.16.** Estimated fatigue life considering all the models vs. experimental one for the 2024-T3 (a) and the 7075-T6 (b) Al alloys

#### 4.5.1.4 Discussions

In this work (BRITO OLIVEIRA *et al.*, 2023a), several experimental fretting fatigue datasets (99 tests) were used to train the ANN models. The training process, in its turn, ensures the obtaining of approximation functions able to efficiently describe complex behaviours of the problem investigated. Standard multiaxial fatigue models, on the other hand, rely on the use of simple expressions relating the fretting fatigue life with the stress/strain parameters believed to govern the fatigue damage mechanisms. In the present study, it has been shown that both the shear and normal stress based ANN models performed considerably better than the multiaxial fatigue ones. However, it is worth mentioning that such a better performance comes at a cost, once the training process requires the use of several fretting fatigue data obtained, preferably, for different materials, loading and geometrical configurations. However, as long as such data are available, which was the case here, it is possible to build such powerful fatigue life assessment tools. In this work, the inputs of the ANN models are the equivalent stresses obtained at the material critical distance ( $(\tau_{a,max}, \sigma_{n,max})$  or  $(\sigma_{n,a}, \sigma_{n,max})$ ), as well as the material yield stress  $\sigma_y$ , all of them normalized with respect to the material ultimate tensile strength,  $\sigma_{ult}$ . The relatively easy determination of those parameters makes the ANN models attractive for practical applications. It is also worth noting that the ANN models proposed here could accurately estimate the fatigue life for tests conducted on Al alloys never seen in the training phase, which shows up an advantage in relation to the use of standard multiaxial fatigue models since in the former there is no need for the calibration of material parameters.

For a more general view of the results provided by the ANN models, Fig. 4.17 and 4.18b show, respectively, the life surface for the Al 7075-T651 alloy, which has the largest amount of data (see Fig. 4.4), in terms of the stress parameters considered in the shear and in the normal stress based models. Dots represent the experimental data. In addition to a verification of the accuracy of the proposed models, these figures also permit evaluate how each stress parameter affects the fretting fatigue behavior of the Al 7075-T651. As can be seen in Fig. 4.17, life is decreased with the increase of both the shear stress amplitude,  $\tau_a$ , and the maximum normal stress,  $\sigma_{n,max}$ . Besides, it is possible to see that the former ( $\tau_a$ ) has a greater impact on the fatigue life, which is in accordance with fatigue observations, where cyclic stresses govern the fatigue damage mechanisms. It is also possible to see that for a given  $\tau_a$ , life decreases with the

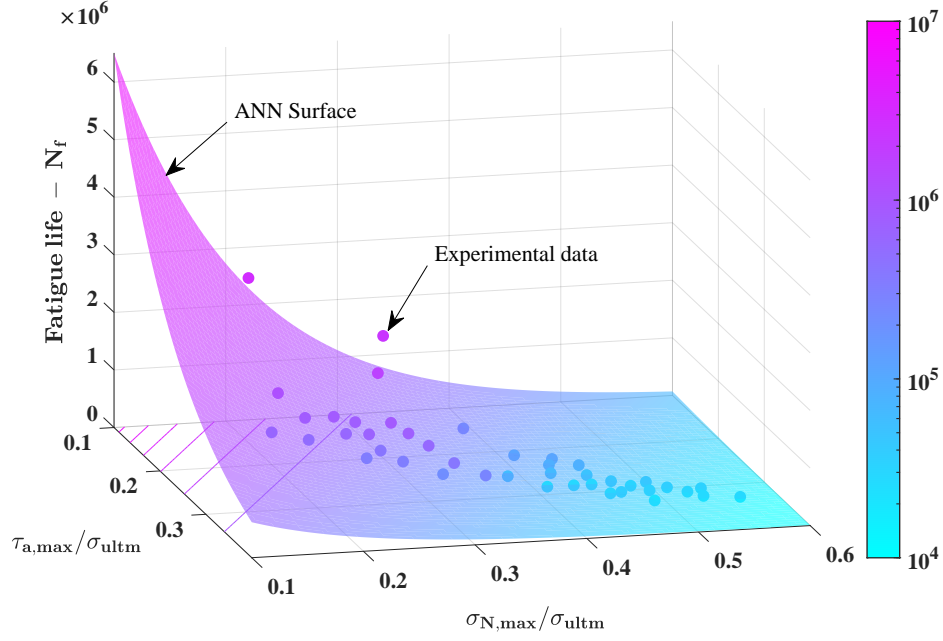


**Figure 4.17.** Fatigue life surface for the 7075-T651 Al alloy by using the ANN\_SHEAR model. The experimental data provided in (MARTÍN *et al.*, 2020; MUÑOZ *et al.*, 2007) are also reported.

increase of  $\sigma_{n,max}$ , which makes sense from a mechanical viewpoint once mean normal stresses contribute to crack opening. Similarly, for the normal stress ANN model, fatigue life reduces with the increase of both the normal stress amplitude,  $\sigma_{n,a}$ , and the maximum normal stress,  $\sigma_{n,max}$ . As expected, one can also notice that  $\sigma_{n,a}$  has a greater impact than  $\sigma_{n,max}$  on the fatigue life. Such results also help to confirm the good generalization of the proposed models and their alignment with well established fatigue theories.

#### 4.5.2 Part 2 - Titanium Article

In this section, one evaluates the accuracy of the life estimates for each model investigated in (OLIVEIRA *et al.*, 2024) by means of the band mean error factor (BMEF), which is defined according to the following relations:

$$\text{BMEF} = \frac{1}{n} \sum_{i=1}^n \psi^{(i)} \quad (4.3)$$

$$\psi^{(i)} = \begin{cases} \frac{N_{f,\text{pred}}^{(i)}}{N_{f,\text{exp}}^{(i)}}, & \text{se } N_{f,\text{pred}}^{(i)} \geq N_{f,\text{exp}}^{(i)} \\ \frac{N_{f,\text{exp}}^{(i)}}{N_{f,\text{pred}}^{(i)}}, & \text{se } N_{f,\text{pred}}^{(i)} < N_{f,\text{exp}}^{(i)} \end{cases} \quad (4.4)$$

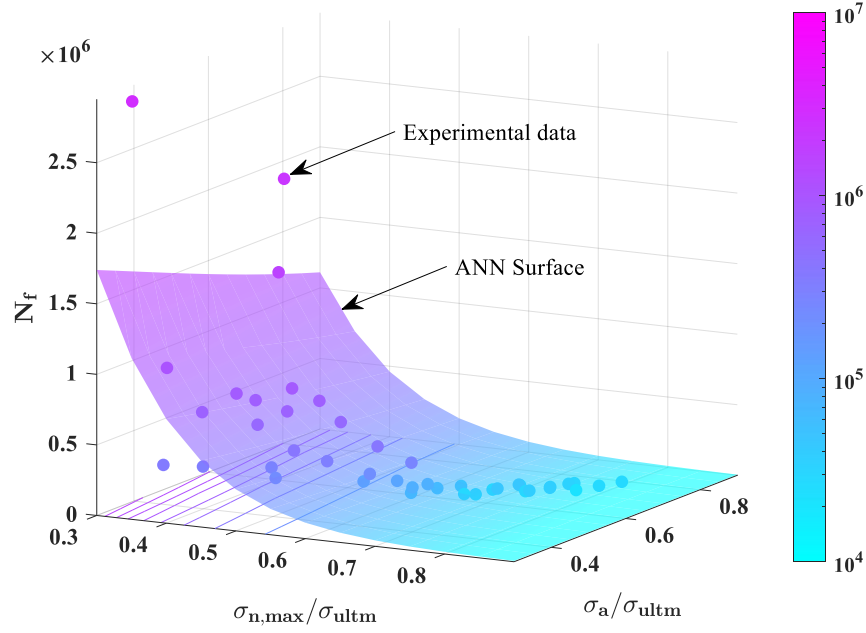


**Figure 4.18.** Fatigue life surface for the 7075-T651 Al alloy by using the ANN\_NORMAL model. The experimental data provided in (MARTÍN *et al.*, 2020; MUÑOZ *et al.*, 2007) are also reported.

where  $N_{f,\text{pred}}^{(i)}$  and  $N_{f,\text{exp}}^{(i)}$  hold for the  $i_{th}$  predicted and  $i_{th}$  experimental fretting fatigue life for a dataset of size  $n$ .

Note that the BMFE is a straightforward way to evaluate the mean scatter of the fatigue life estimates, however, it does not distinguish between conservative and optimistic results. The main results and discussions of this section have been divided into the following three subsections: 4.5.2.1 focuses on the main results related to the errors of the training models, 4.5.2.2 presents the main results concerning the titanium FF data, 4.5.2.3 details the results related to data with the out-of-phase loading effect FF data, and 4.5.2.4 provides a more in depth analysis of the behavior of the ANN models.

#### 4.5.2.1 ANN training results

We proposed three ANN-based models (SHEAR, NORMAL, and INV) for fretting fatigue life prediction (Fig. 4.11). Table 4.16 shows the ER error (Eq. 3.1) for each model considering the training and test data (Al data Tables 3.1-4.8), with the total error representing the weighted average error. The SHEAR and INV models outperformed the NORMAL model, exhibiting lower total errors and higher accuracy. However, each model's performance may vary for other materials (e.g., titanium and steel). In summary, the SHEAR, NORMAL, and INV models

**Table 4.16.** Empirical risk (ER) error for the query data by considering all models.

Model	$ER^*(\text{training})$	$ER^*(\text{test})$	$ER^*(\text{total})$
SHEAR	43.26	15.54	40.53
NORMAL	90.78	14.97	83.31
INV	44.82	16.75	42.06

\* Values must be multiplied by  $10^{-5}$ .

showed similar performance, with SHEAR and INV being slightly more accurate.

#### 4.5.2.2 Ti-6Al-4V results

□ Classical multiaxial fatigue models (Ti-6Al-4V)

Based on the experimental fatigue data reported in Section 4.3, the SWT, MWCM, and Crossland multiaxial fatigue models have been calibrated for the Ti-6Al-4V alloy. Hence, Eqs. 4.5, 4.6, and 4.7 represent, respectively, the SWT, MWCM and Crossland expressions, all in terms of the fatigue life. In Eq. 4.7,  $A_1$ ,  $A_2$ ,  $b_1$ , and  $b_2$  hold for the fatigue coefficients showed in Fig. 4.5a for  $R_\sigma = -1$  and  $0.1$  ( $A_1 = 2184.4$ ,  $A_2 = 3404.9$ ,  $b_1 = -0.127$ , and  $b_2 = -0.205$ ). These curves are also considered for the MWCM calibration. One considers a double power law (Eq. 4.5) to calibrate the SWT model, since it better fits the three experimental curves considered (Fig. 4.5a).

$$\sqrt{\sigma_{n,\max}\sigma_{n,a}} = 209.73N_f^{0.0317056} + 55689.5N_f^{-0.5} \quad (4.5)$$

$$N_f = 10^7 \left[ \frac{-26.165\rho + 167.191}{\tau_{a,\max}} \right]^{-0.999\rho + 8.873} \quad (4.6)$$

$$\frac{S_a}{\sqrt{2}} + \frac{\sqrt{3}(A_1N_f^{b_1} - A_2N_f^{b_2})}{4A_2N_f^{b_2} - A_1N_f^{b_1}} \sigma_{H,\max} = A_1N_f^{b_1} A_2N_f^{b_2} \frac{\sqrt{3}}{4A_2N_f^{b_2} - A_1N_f^{b_1}} \quad (4.7)$$

Fig. 4.19 illustrates a comparison between the experimental vs. estimated fatigue life for the multiaxial fatigue models considered here. The estimated values can be divided into two groups, one for the spherical and the other for the cylindrical fretting contacts, which are represented by circles and diamonds, respectively. As can be seen, the SWT results (filled geometries in magenta) indicate a conservative behavior with most of the data

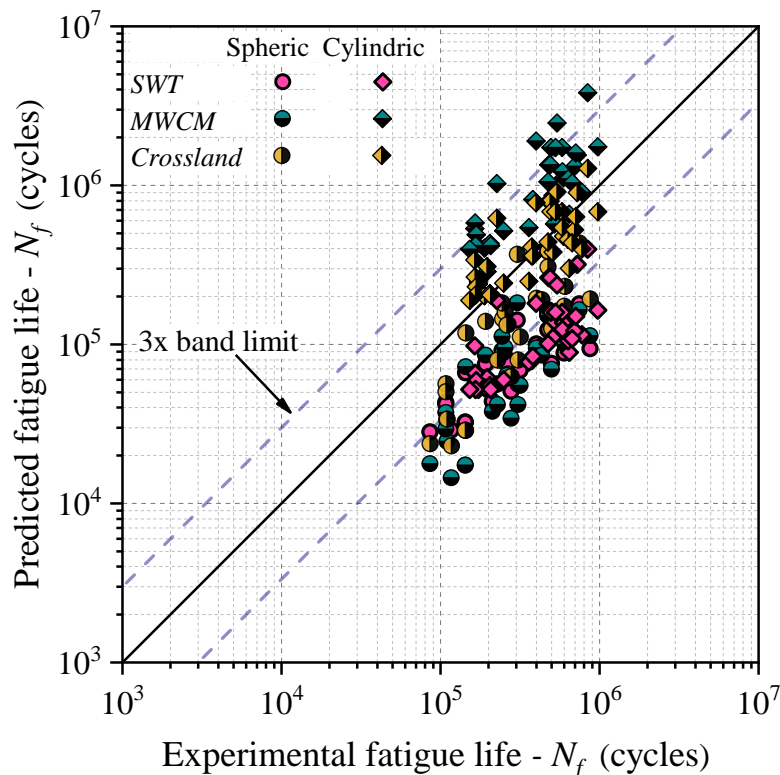


**Figure 4.19.** Estimated fatigue life considering all the multiaxial fatigue models vs. experimental one for the Ti-6Al-4V alloy.

(70%) out of the three-band width. Conversely, the MWCM results (top filled geometries in dark cyan) show a high sensitivity to pad geometry, with non-conservative values for cylindrical contact data and conservative behavior for spherical contact data, with a large part of data (47%) outside the three-band limit. Finally, the Crossland fatigue model yields the best estimates (left half-filled geometries in gold), with most of the data (84%) falling within the three band limit. Notably, this model shows little sensitivity to the pad geometry, similar to the SWT model.

#### □ ANN models result (Ti-6Al-4V)

The ANN results associated to the Ti-6Al-4V alloy (Tables 4.9 and 4.10) are shown in Fig. 4.20. Such figure depicts the experimental versus the estimated life diagram for the three ANN models under consideration. As for the analytical criteria, the results here have also been divided into two groups, one for spherical (circles) and the other for cylindrical (triangles) contacts. Fig. 4.20a depicts the results from the SHEAR model with most of the data (81%) lying within the two-band width. This model presents good estimations for both contact geometries, with low scatter. Similarly, the INV model (Fig. 4.20c)

**Table 4.17.** Band Mean Error Factor (BMEF) for the Ti-6Al-4V data by considering all models.

Alloy	Model	BMEF
Ti-6Al-4V	SHEAR	1.56
	NORMAL	1.91
	INV	1.57
	MWCM	3.48
	SWT	3.89
	CROSSLAND	1.97

provides comparable outcomes to the SHEAR one, with 84% of the total data falling inside the two bands limit, and its best predictions are for the spherical data (90% inside the two-band limit). The NORMAL model (Fig. 4.20b) also presents good estimates for the spherical contact data (same percentage error as INV). However, for the cylindrical fretting contact ones, it presents conservative values with more than 68% of the data out of the two-error boundary.

It is observed that the ANN models based either on the shear stress amplitude or on the deviatoric stress amplitude ( $\tau_{a,max}$  and  $S_a$ ) performed better than the one based on normal stresses. Table 4.18 reports the BMEF values associated to each model in study. These values can be utilized to quick determine the most suitable models for this alloy, in terms of the band width admitted. As expected from Figs. 4.19 and 4.20, the ANN models have the smallest mean errors for these query data. A comparative analysis reveals that the best life estimates for all contact configurations have been obtained by the SHEAR model. Additionally, all ANN models exhibit a mean band error magnitude bellow the two-band width. The Crossland model, which showed the best performance among the multiaxial fatigue models for the Ti-6Al-4V, presented life estimates quite as good as the ANN ones. It is interesting that both SWT and NORMAL models, which are based on normal equivalent stresses ( $\sigma_{n,max}$ ,  $\sigma_{n,a}$ ), produce conservatives results nonetheless the NORMAL presents a lower dispersion than SWT (see Fig. 4.19 and Fig. 4.20b). Comparing the SHEAR and the MWCM models, one can see that the former has a low dispersion of the data with respect to the other one. The latter dataset includes 100% cylindrical data with optimistic estimates and 100% spherical data with conservative predictions, whereas the former dataset has a majority of cylindrical data (62%) with optimistic values and a majority of spherical data (83%) with conservative values. To conclude, it has been

observed that, among the ANN models, the INV and the SHEAR were the ones with the lowest dispersion, while among the analytical criteria, the Crossland was the best in terms of accuracy.

### 4.5.2.3 Out-of-phase loading results

#### □ Classical multiaxial fatigue models (Out-of-phase)

The same analysis performed in subsection 4.5.2.2 has been reproduced here for the Al 7050-T7451 and the ASTM A743 CA6NM. Therefore, Eqs. 4.8 and 4.9 show the calibrated SWT expressions for each material, aluminum and steel, respectively. As can be seen, for both materials a simple power law is required for the experimental data considered (Fig. 4.5b and 4.5c).

$$\sqrt{\sigma_{n,\max}\sigma_{n,a}} = 2381.63N_f^{-0.231} \quad (4.8)$$

$$\sqrt{\sigma_{n,\max}\sigma_{n,a}} = 2437.14N_f^{-0.142} \quad (4.9)$$

The calibrated MWCM expressions are shown in Eqs. 4.10 and 4.11 for aluminum and steel, respectively.

$$N_f = 10^7 \left[ \frac{-23.562\rho + 53.607}{\tau_{a,\max}} \right]^{-0.870\rho + 3.984} \quad (4.10)$$

$$N_f = 10^7 \left[ \frac{-48.427\rho + 192.219}{\tau_{a,\max}} \right]^{-0.431\rho + 9.127} \quad (4.11)$$

Equations 4.12 and 4.13 show the calibrated Crossland fatigue life expressions, such that  $A_3$ ,  $A_4$ ,  $b_3$ , and  $b_4$  are the fatigue coefficients for 7050-T7451 ( $A_3 = 3073.9$ ,  $A_4 = 1657.7$ ,  $b_3 = -0.251$ , and  $b_4 = -0.205$ ) and  $A_5$ ,  $A_6$ ,  $b_5$ , and  $b_6$  are the fatigue coefficients for A743 CA6NM ( $A_5 = 1839.7$ ,  $A_6 = 1336.71$ ,  $b_5 = -0.115$ , and  $b_6 = -0.121$ ) as shown in Fig. 4.5b and 4.5c.

$$\frac{S_a}{\sqrt{2}} + \frac{\sqrt{3}(A_4N_f^{b_4})}{A_3N_f^{b_3} - \sqrt{3}}\sigma_{H,\max} = A_4N_f^{b_4} \quad (4.12)$$

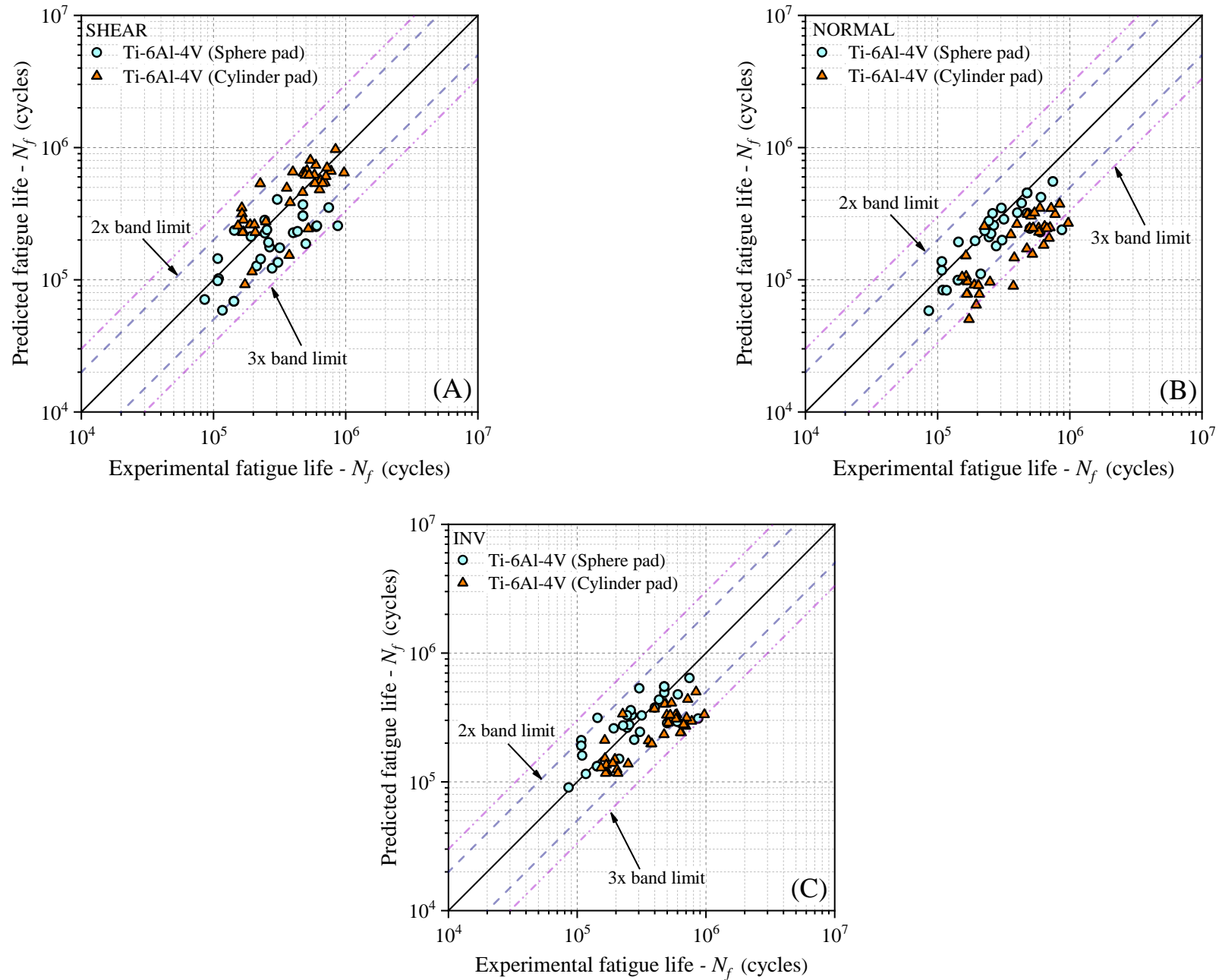


**Figure 4.20.** Estimated fatigue life vs. experimental one for the SHEAR (A), NORMAL (B) and INV (C) models for the Ti-6Al-4V alloy

$$\frac{S_a}{\sqrt{2}} + \frac{\sqrt{3} (A_5 N_f^{b_5} - A_6 N_f^{b_6})}{2A_6 N_f^{b_6} - A_5 N_f^{b_5}} \sigma_{H,\max} = A_5 N_f^{b_5} A_6 N_f^{b_6} \frac{\sqrt{3}}{2A_6 N_f^{b_6} - A_5 N_f^{b_5}} \quad (4.13)$$

As previously commented, the data related to these materials has the presence of an out-of-phase loading effect, more specifically with phase angles of  $0^\circ$ ,  $135^\circ$ ,  $45^\circ$ , and  $90^\circ$  for the aluminum and  $135^\circ$  and  $45^\circ$  for the steel. Fig. 4.21a depicts the predicted versus experimental life diagram for the three multiaxial fatigue models in the study: SWT (left half-filled geometries in blue), MWCM (bottom filled geometries in salmon), and Crossland (filled geometries in green). It is evident that only two data points,  $0^\circ$  and  $45^\circ$  (represented by the circle and diamond), fall within the specified three-band width for the Crossland model, whereas the other two models produce non-conservative values. SWT and MWCM models have very conservative life values, mostly the MWCM. All models indicated the highest fatigue life for the experiment with  $135^\circ$  (triangles) of phase angle, while experiments showed that the highest life was observed for the  $45^\circ$  phase angle.

In the analysis of the CA6NM we conducted, at first, standard simulations assuming a linear elastic behavior for the material. However, upon discovering that the resulting stresses exceeded the material's yield strength, we decided to incorporate a perfect plasticity model into the analysis for greater accuracy and reliability. Plastic flow took only near the contact surface in both experiments (Table 4.12), but with more severity for the one with  $135^\circ$  of phase angle. Thus, we consider an elastic-perfectly plastic behavior in our simulations for this data. The results of the CA6NM are shown in Fig. 4.21b and, overall speaking, all the estimates remain conservative. SWT (right half-filled geometries in blue) and Crossland (filled geometries in dark cyan) present similar results for the  $135^\circ$  (star) phase angle experiment. The SWT produces the best results for this material and the MWCM (bottom filled geometries in salmon) the worst ones.

#### □ ANN functions results (Out-of-phase)

Before presenting the results relating to the ANN models, a few considerations are addressed regarding the preceding results and the selection of input parameters for the ANN-based models. As previously discussed, these input parameters were chosen based on the parameters employed in the previously demonstrated models (SWT, MWCM, and

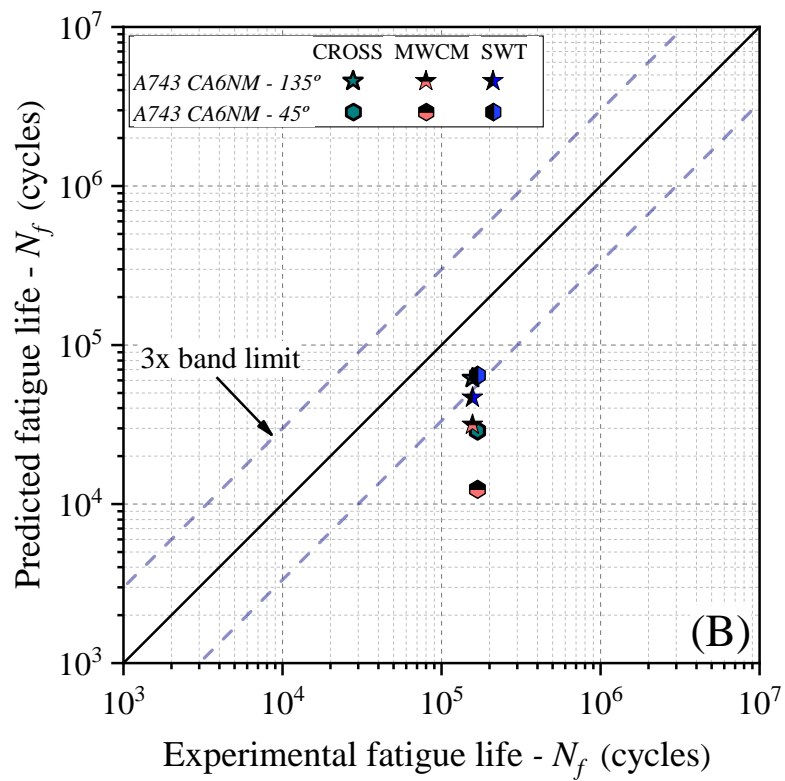
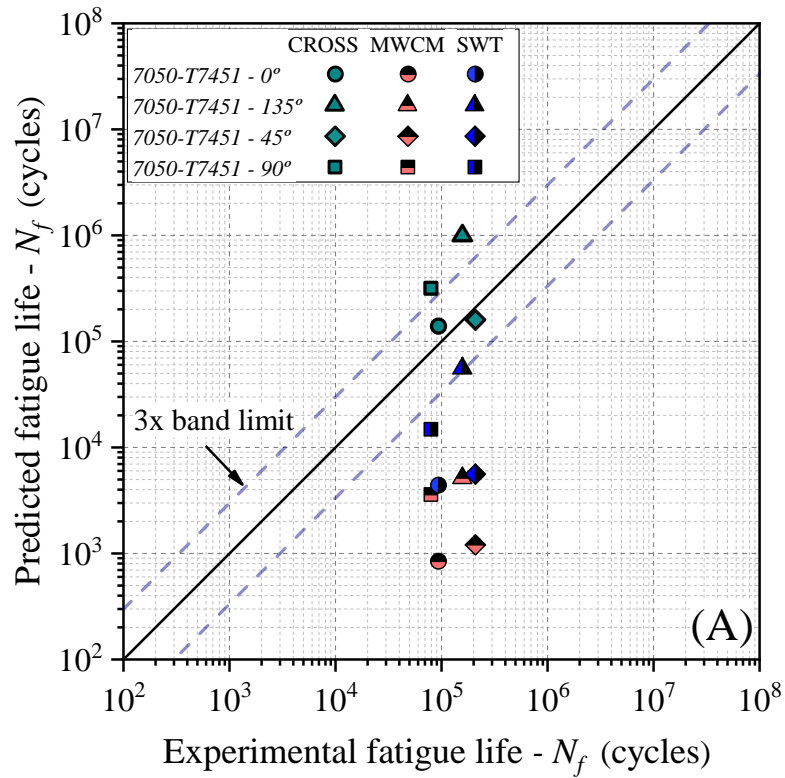


**Figure 4.21.** Estimated fatigue life considering all the multiaxial fatigue models vs. experimental one for the Al 7050-T7451 alloy (A), and ASTM A743 CA6NM alloy (B).

Crossland). Despite the prior observations suggesting that these classical criteria might fall short in predicting fretting fatigue life, particularly in scenarios with out-of-phase loading effects, our approach solely incorporates their parameters as inputs. Nonetheless, one maps new mathematical pathways within the data-driven methodology to establish connections with fatigue life. In this section, one shall examine whether this strategy improves the identified results or not.

The ANN results (INV, SHEAR and NORMAL models) for both materials are illustrated in Fig. 4.22. As can be seen from Fig. 4.22a, all ANN models present highly similar results for the aluminum out-of-phase data. In the case of the experiments conducted with  $0^\circ$  (circles) and  $45^\circ$  (diamonds) all the ANN yielded predictions that fell within the band limits (3x). However, as the Crossland model the ANN models showed a tendency to overestimate the life for data corresponding to the  $135^\circ$  (triangles), with optimistic results. Fig. 4.22b shows the results for the CA6NM. As can be observed, the models based on shear and deviatoric stress amplitude (SHEAR and INV) provided the most accurate predictions, falling within the three-band width admitted. Overall, for the CA6NM data, the SHEAR (left half-filled geometries in orange) model represented the most effective ANN model.

In order to perform a comparative analysis, Table 4.18 reports the BMEF (Eqs. 4.3 and 4.4) for all models considered in this study for both materials (Al 7050-T7451 and the ASTM A743 CA6NM). Overall, the models based on invariant stress approaches (INV and Crossland) demonstrated the best estimates for the aluminum alloy. For this material, the Crossland criterion produced predictions comparable to those of the ANN models. Conversely, for the steel alloy, the ANN models consistently demonstrated the highest level of accuracy, often yielding predictions accurate to the second decimal place. The sole exception was the SWT model, which outperformed the normal model in this specific scenario. Summarizing, the ANN models demonstrated better performance for both materials.

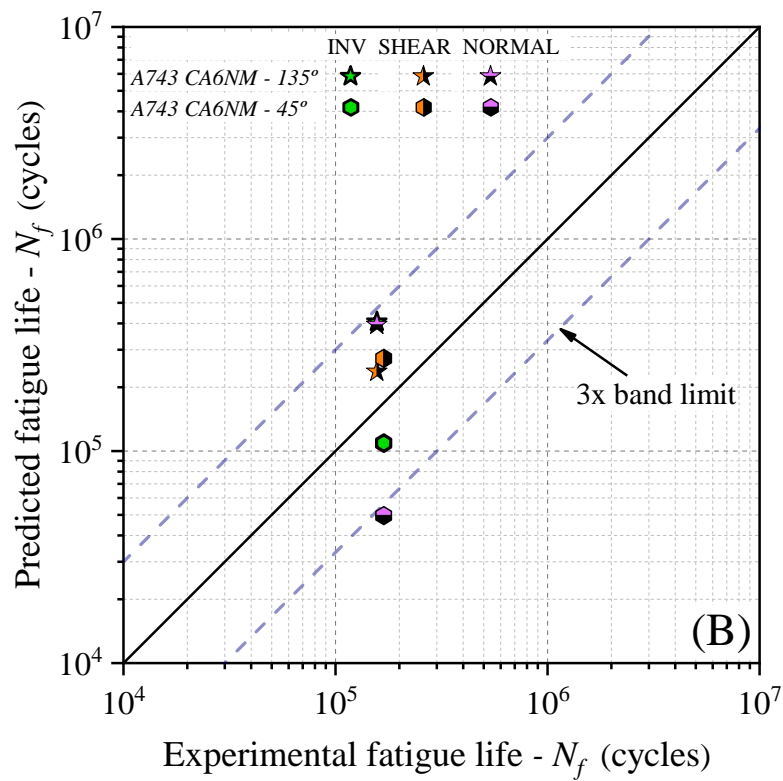
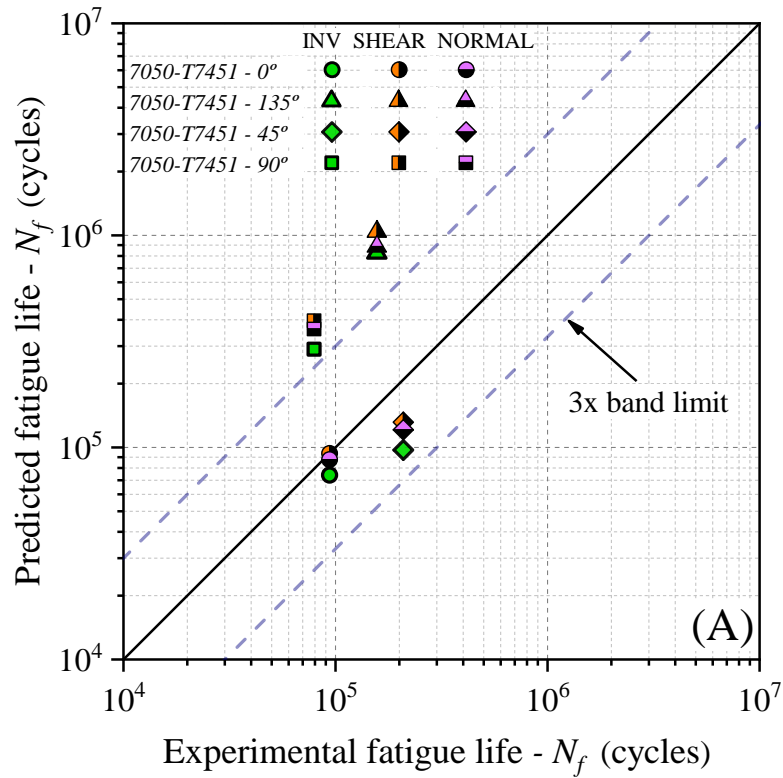


**Figure 4.22.** Estimated fatigue life considering all the ANN models vs. experimental one for the Al 7050-T7451 alloy (A), and ASTM A743 CA6NM alloy (B).

**Table 4.18.** Band Mean Error Factor (BMEF) for the out-of-phase data by considering all models.

Alloy	Model	BMEF
7050-T7451	SHEAR	3.55
	NORMAL	3.25
	INV	3.08
	MWCM	84.18
	SWT	12.65
	CROSSLAND	3.27
A743 CA6NM	SHEAR	1.56
	NORMAL	2.95
	INV	2.07
	MWCM	9.30
	SWT	2.27
	CROSSLAND	4.21

#### 4.5.2.4 Further discussions

The ANN models in (OLIVEIRA *et al.*, 2024) were trained using 132 aeronautical aluminum fretting fatigue data points and proved to be more efficient than the standard multiaxial fatigue ones even in front of different types of materials and loadings. As shown in earlier sections, the INV, SHEAR, and NORMAL models provided better estimates than their corresponding multiaxial fatigue models in the study (Crossland, MWCM, and SWT). An important advantage of these ANN models is that they do not require prior calibration for each material, unlike classical multiaxial fatigue criteria. These models often rely on simple expressions linking fretting fatigue life to stress/strain parameters believed to govern fatigue damage mechanisms, and probably more complex functions should be considered in these analyses. This study suggests then that, once trained, the aforementioned ANN can be applied to any material, i.e., they showed an excellent generalization capability. The ANN models' attractiveness for practical applications is enhanced by the relatively straightforward determination of their input parameters.

To enhance the comparative analysis respective to the multiaxial fatigue models, Fig. 4.23 presents three different comparisons that examine how each input parameter affects the assessment of fretting fatigue, considering a specific fatigue life range. Such a figure depicts constant life curves for  $10^5$  (top curves in maroon) and  $5 \times 10^5$  (lower curves in green) cycles for Ti-6Al-4V data. In this life range, this material has the largest amount of data with different loading conditions and pad geometries/sizes. The dots represent the titanium FF data within

this life range, the continuous lines represent the multiaxial fatigue criteria, and the dashed lines represent the ANN model's constant life curves. The objective is to illustrate that the model's accuracy increases with the amount of data contained within the model's respective curves. Figures 4.23a, 4.23b and 4.23c include the six models in the study, which were distributed according to the main related stress parameters. The shaded area represents the region between the two multiaxial fatigue model constant life curves.

Fig. 4.23a contains a graph of the shear stress amplitude versus the maximum normal stress ( $\tau_a$  vs  $\sigma_{n,max}$ ). One can see from such a figure that, the majority of the data falls within the SHEAR model curves, with only a small portion falling within the MWCM region (hatched area). The SHEAR model demonstrates a nearly linear relation between the stress parameters ( $\tau_a$ ,  $\sigma_{n,max}$ ), indicating that the increase in shear stress amplitude is inversely proportional to the increase in maximum normal stress to maintain a given constant life, but in a steeper form than that proposed by the MWCM model. Fig. 4.23b depicts the normal stress amplitude vs. the maximum normal stress when considering the SWT and NORMAL criteria. As can be seen, most of the data falls between the curves of the NORMAL model, indicating that the mathematical relationship proposed in SWT does not adequately follow the distribution of the experimental data. Perhaps, somewhat counter intuitive, for constant fatigue life, the ANN (NORMAL) model shows almost constant  $\sigma_{n,a}$  curves, suggesting a pattern quite different from the one proposed by the SWT criterion. Fig. 4.23c illustrates the plot of deviatoric stress amplitude versus the maximum hydrostatic stress using the INV and the Crossland models. As can be observed, a similar pattern is repeated and most of the data lies within the INV constant life curves. In contrast to the Crossland model, the INV model reveals smoother curves that align well with the titanium experimental data. These mathematical relationships can be the key for the development of new multiaxial fatigue models with better correspondence with the mechanical behaviour of materials, under a rapidly varying multiaxial stress field such as those encountered in fretting fatigue.

## 4.6 PARTIAL CONCLUSIONS

This work assessed the generalization capability of five different ANN-based models fed with material parameters and stress quantities that have also been considered in classical multiaxial

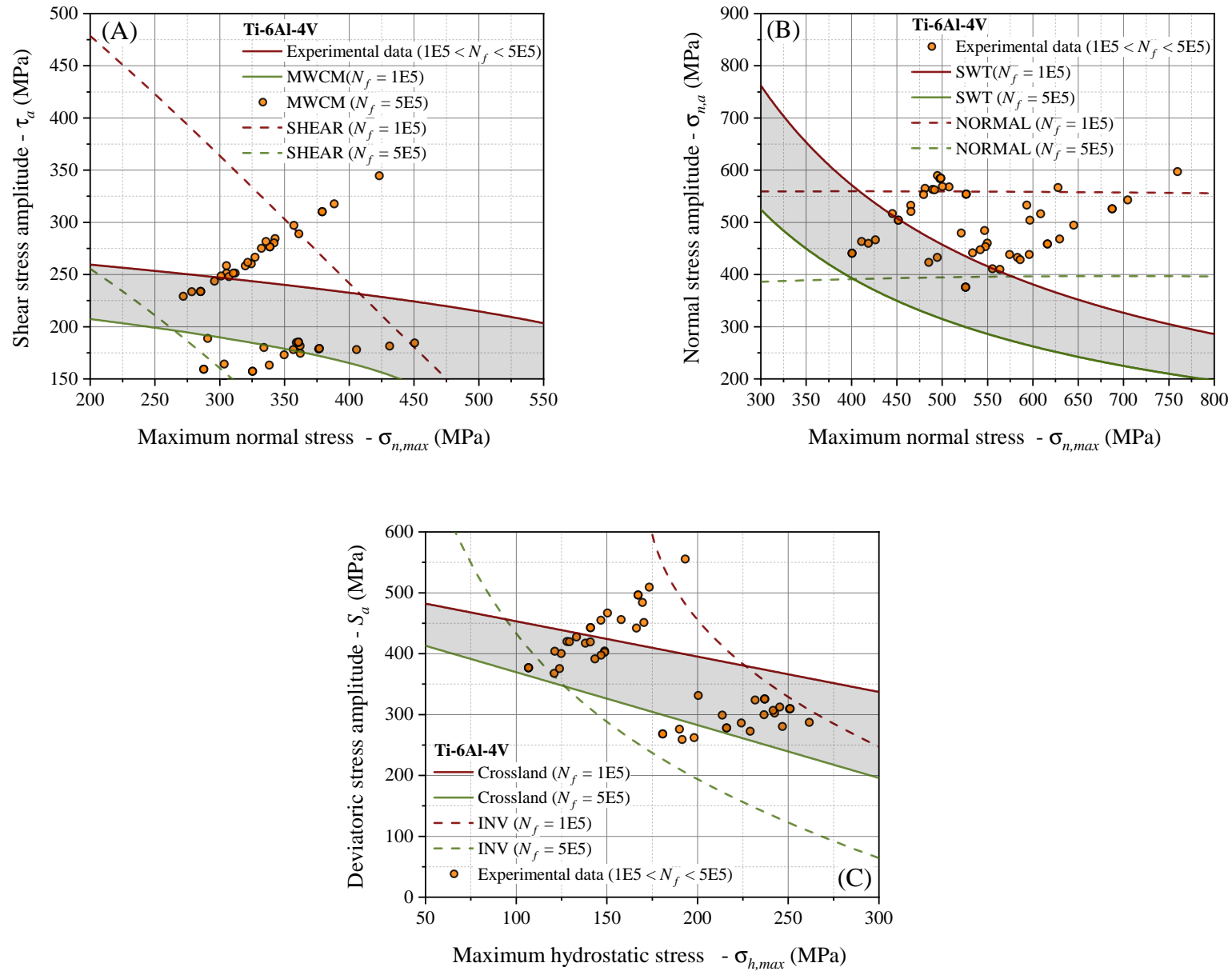


**Figure 4.23.** Constant life curves for the Ti-6Al-4V alloy by using the SHEAR and MWCM models (A), NORMAL and SWT models (B), and INV and Crossland models (C). The experimental data are also reported.

fatigue criteria (MWCM, SWT, Crossland) and presented in (BRITO OLIVEIRA *et al.*, 2023a) and (OLIVEIRA *et al.*, 2024). The results demonstrated that such models are quite robust and can predict fretting fatigue lives accurately, even for materials, loading conditions and contact geometries never “seen” by the ANN in the training phase. Moreover, the ANN-based models have performed considerably better than the multiaxial fatigue ones that inspired them. Therefore, even though the initial construction of such ANN models requires a considerable amount of FF data, once they are trained, there is no need for further calibration when considering new materials.

## Chapter 5

# Applications and insights of ANN models

*"This chapter explores the application of ANN models in three distinct cases of fretting fatigue, including the one in overhead conductors."*

Some parts of the text in this chapter was previously published and submitted in the following documents:

BRITO OLIVEIRA, Giorgio André; CARDOSO, Raphael Araújo; FREIRE JÚNIOR, Raimundo Carlos Silverio; ARAÚJO, José Alexander. A Hybrid ANN Multi-axial Fatigue Model for the Assessment of Fretting Fatigue under Variable Amplitude Shear Loading. *Procedia Structural Integrity*, v. 57, 2024, p. 228-235, 2024b. DOI: [10.1016/j.prostr.2024.03.025](https://doi.org/10.1016/j.prostr.2024.03.025)

OLIVEIRA, Giorgio André Brito; MATOS, Ian de Medeiros; ROCHA, Pedro Henrique Correa; CASTRO, Fábio Comes; FREIRE JÚNIOR, Raimundo Carlos Silverio; ARAÚJO, José Alexander. On the life estimation of wires using non-local ANN methodology. **In process of submission.**

OLIVEIRA, Giorgio André Brito; ROCHA, Pedro Henrique Correa; MATOS, Ian de Medeiros; CASTRO, Fábio Comes; LANGLOIS, Sébastien; FREIRE JÚNIOR, Raimundo Carlos Silverio; ARAÚJO, José Alexander. On the fatigue life prediction of overhead conductors using neural networks. **In process of submission.**

To ensure adherence to standard nomenclature, some symbols were adjusted from the original publication. Moreover, specific paragraphs were slightly modified to eliminate redundancy.

## 5.1 OVERVIEW

This chapter addresses the application of neural network models in three mechanical situations involving fretting fatigue. Consequently, this chapter is divided into three parts. Each one corresponds to a specific article that details each situation. In the first two sections, one discusses the application of models covered in Chapter 4, focusing on specific scenarios involving variable shear amplitude loading and fatigue in conductor wires. The third section introduces a new ANN model specifically developed for predicting the fretting fatigue life of overhead conductors.

## 5.2 PART I – FRETTING FATIGUE UNDER VARIABLE SHEAR AMPLITUDE

Due to the complexities involved in experimental setups, fretting fatigue problems have mostly been tested in laboratories using constant amplitude loading. However, this condition does not reproduce what truly occurs in practical applications, where variable amplitude loading predominates. Recently, some studies have focused on addressing this issue by attempting to replicate experiments with variable amplitude loading (KOUANGA *et al.*, 2023; MATOS *et al.*, 2023; PINTO *et al.*, 2023; ROUSSEAU *et al.*, 2019). Additionally, a recent trend in the field of FF is the utilization of Machine Learning techniques (BRITO OLIVEIRA *et al.*, 2023a; OLIVEIRA *et al.*, 2024; HAN *et al.*, 2023a; LIU; YUAN, 2023), which has gained popularity due to its excellent results and generalization capabilities. In this setting, this part of this chapter aims to test some damage model, inspired in Miner’s cumulative damage mode, combined with a consolidated ANN-based model to predict the fretting fatigue life under varying shear loading amplitude.

### 5.2.1 Fretting fatigue under variable amplitude data

In this study, one considers the experimental FF data from Pinto *et al.* (2023). The material is the Al 7075-T651, which has an elastic modulus ( $E$ ) of 68 GPa, a Poisson’s ratio ( $\nu$ ) of 0.33, a yield stress ( $\sigma_y$ ) of 506 MPa, and an ultimate tensile stress ( $\sigma_{ult}$ ) of 570 MPa, and a friction coefficient ( $f$ ) of 0.85. The specimens have a cross-section of 13 mm  $\times$  13 mm. The tests were performed under load control. Tables 5.1 and 5.2 present the key experimental values that will

**Table 5.1.** Fretting fatigue tests under H-L and L-H loading sequence.

H-L (High-Low)				L-H (Low-High)			
$d_1$	$n_1$ (cycles)	$n_2$ (cycles)	$N_f$ (cycles)	$d_1$	$n_1$ (cycles)	$n_2$ (cycles)	$N_f$ (cycles)
0.75	1.07E+05	2.26E+04	1.30E+05	0.75	2.61E+05	5.79E+04	3.19E+05
0.75	1.07E+05	4.48E+04	1.52E+05	0.75	2.61E+05	6.29E+04	3.24E+05
0.5	7.16E+04	9.64E+04	1.68E+05	0.50	1.74E+05	8.70E+04	2.61E+05
0.5	7.16E+04	1.25E+05	1.97E+05	0.5	1.74E+05	7.90E+04	2.53E+05
0.5	7.16E+04	1.34E+05	2.06E+05	0.5	1.74E+05	6.71E+04	2.41E+05
0.4	5.73E+04	2.01E+05	2.59E+05	0.35	1.22E+05	9.22E+04	2.14E+05
0.3	4.30E+04	2.55E+05	2.98E+05	0.25	8.70E+04	9.80E+04	1.85E+05
0.25	3.58E+04	3.33E+05	3.68E+05	0.25	8.70E+04	1.76E+05	2.63E+05
0.25	3.58E+04	3.04E+05	3.40E+05	0.25	8.70E+04	1.69E+05	2.56E+05
0.25	3.58E+04	3.09E+05	3.45E+05	0.25	8.70E+04	1.50E+05	2.37E+05
-	-	-	-	0.15	5.22E+04	1.45E+05	1.97E+05

**Table 5.2.** Fretting Fatigue loading configuration of each configuration.

Model	$Q$ (N/mm)	$P$ (N/mm)	$Q/P$	$\sigma_{B,a}$	$N_f$ (cycles)
High	210	300	0.7	70	122,037
					146,178
					168,048
Low	120	300	0.4	70	345,313
					350,891

be employed in this work.

In Table 5.2, the main loads are reported, named High and Low due to the shear load ( $Q$ ) amplitude. In the conducted tests, only the tangential load amplitude,  $Q$ , varies, while the amplitude of the bulk fatigue load,  $\sigma_B$ , remains constant, and the normal load,  $P$ , remains unchanged. Fig. 5.1a illustrates a High-Low (H-L) loading sequence, where the tangential load amplitudes analyzed are  $Q_1$  and  $Q_2$ , corresponding to a given number of cycles,  $n_1$  and  $n_2$ , respectively, with  $Q_1 > Q_2$ . Conversely, Fig. 5.1b represents a Low-High (L-H) loading sequence, where the first tangential load of amplitude  $Q_1$  is applied, followed by the one of amplitude  $Q_2$  ( $Q_1 < Q_2$ ). Table 1 shows the variable shear loading FF data, under H-L and L-H loading configurations, such that  $n_1$  represents the predefined number of cycles for the first load block (High or Low), which produces a damage  $d_1$  according to Miner's rule. In this setting,  $n_2$  is the remaining number cycles experienced by the second load block until failure is observed. Therefore,  $N_f$  is the total FF life ( $n_1 + n_2$ ) in the tests. Table 5.2 presents the

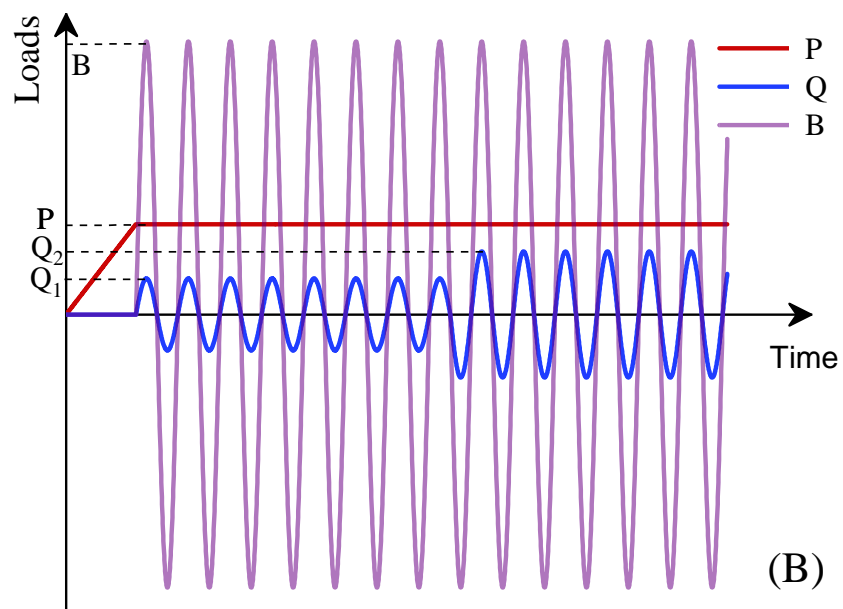
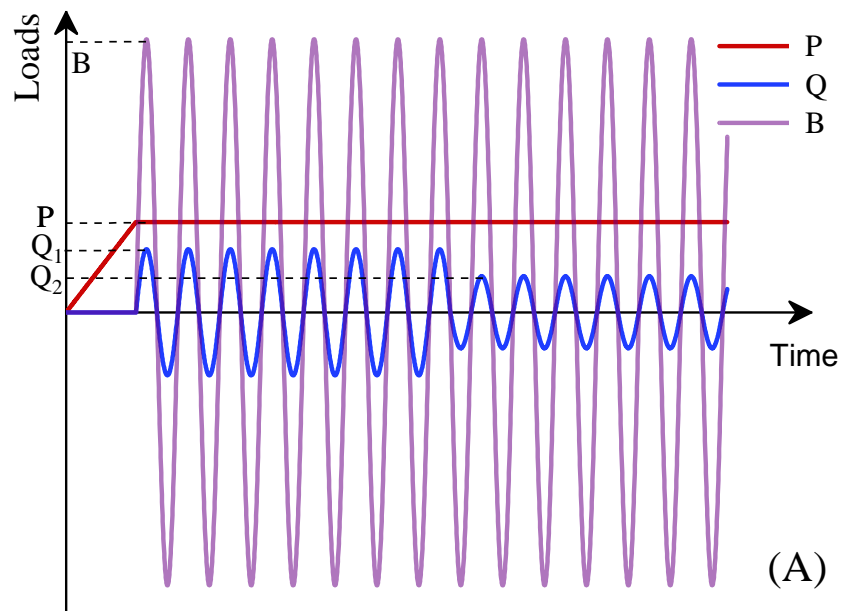


Figure 5.1. Representation of the loads in (A) H-L configuration; (B) L-H configuration.

experimental FF lives of tests conducted considering one single loading block for each case, High or Low.

## 5.2.2 Modelling framework

All numerical models to compute the stress field related to the tests in study have been implemented using the ABAQUS commercial finite element (FE) software in conjunction with Python scripts. For details concerning the FE modelling, see Chapter 4 (section 4.4.1). Thus, initially the cylindrical pad is pressed against the flat specimen by applying a normal load,  $P$ , then the alternate bulk load,  $B$ , is imposed on the specimen concurrently with the tangential load,  $Q$ , which is applied to the pad. Hence, two numerical simulations have been performed, for each high and low block so that later some damage models can be evaluated.

Similar to the methodology presented in Chapter 4, based on the results obtained from FE numerical simulations, the equivalent stresses required by the ANN models can be calculated. This work considers the model named SHEAR, as described in Chapter 4 (section 4.4.2).

### 5.2.2.1 Damage rule model

To compute the total damage ( $D_t$ ) based on the experimental data, Miner's damage rule (Eq. 5.1) serves as the foundation for all damage models considered in this study. Miner's rule establishes that the damage produced by each block ( $d_j$ ) is permanent and cumulative. According to Eq. 5.1, failure occurs when the cumulative damage reaches a critical value ( $D_t$ ), typically set at 1. This assumption can be interpreted as a summation of damage percentages until the material reaches 100% damage.

Additionally, three more models, represented by Eqs. 5.2, 5.3, and 5.4, are examined in this research. The model presented in Eq. 5.2 is referred to as LSM-Miner. It is essentially an adaptation of Miner's damage rule for two blocks, where each block's damage ( $d_1$  or  $d_2$ ) is multiplied by a constant ( $v_1$  or  $v_2$ ). This linear combination is designed to yield a unity value. The constants are determined using the Least Squares Method (LSM), which involves computing the block damages associated with H-L or L-H loading using the data presented in Table 5.1 and Table 5.2. The constants are then adjusted to best fit this dataset with Eq. 5.2.

The model described in Eq. 5.3 introduces a function developed using an ANN, named ANN-damage, with two inputs: the damage from block 1 ( $d_1$ ) and the fretting ratio of this block ( $Q_1/fP$ ). The output represents the remaining life cycles ( $n_2$ ) to failure (experimental observation). This function was devised to establish an ANN-based model capable of capturing variations in the total life based on the initial fretting loading block, as observed in the research conducted by Pinto et al. (2023). Data presented in Table 5.1 and 5.2 have been used in the training process.

The final damage model, see Eq. 5.4, is the one presented in Pinto et al. (2023), whose formulation closely resembles Miner's damage rule, differing only by the exponent  $\beta$  appearing in the first term of the left-hand side of Eq. 5.4. Such an additional parameter has been incorporated to capture the effect of the loading sequence (L-H or H-L).

$$D_t = \sum d_i = \sum \frac{\Delta N_j}{N_{f,j}} \quad (5.1)$$

$$v_1 d_1 + v_2 d_2 = 1 \quad (5.2)$$

$$\epsilon(d_1, \frac{Q_1}{\mu P}) = n_2 \quad (5.3)$$

$$D_t = \left(\frac{n_1}{N_1}\right)^\beta + \left(\frac{n_2}{N_2}\right), \quad \beta = \left(\frac{N_H}{N_L}\right)^{(2.5 \frac{n_1}{N_1} - 1)} \quad (5.4)$$

### 5.2.3 Results and discussions (Part I)

The main findings are divided into the following four subsections, each one into a distinct approach for computing fretting fatigue life under varying shear loading amplitudes. As the results solely based on Miner's model have already been presented in Pinto et al. (2023), we will refrain from showcasing them again.

Results here presented considered the experimental values of Table 5.1 for the calibration of the damage models introduced in the previous section. Total life estimates for the FF tests with variable amplitude tangential load were carried out based on the life estimates provided by

the SHEAR ANN model in association with the calibrated damage models. Finally, we provide a comparative analysis of the errors associated with the outcomes of the approaches presented in the last subsection.

#### 5.2.4 SHEAR model + LSM-Miner rule approach results

This modelling consists of applying Eq. 5.2 considering the SHEAR model estimates for the High and Low load configurations. For the High loading, the estimated life is 101,920 cycles, and for the Low one is 327,200 cycles. These estimates fall within the 1.5 band-width limit, when compared to the experimental ones, which is considered a satisfactory outcome in the context of fatigue analysis. Hence, in order to calibrate the  $v_1$  and  $v_2$  parameters in Eq. 5.2, the LSM is employed in three modes. The first mode solely considers the H-L data presented in Table 5.2. The second mode considers only the L-H data. Finally, the third mode takes into account all data listed in Table 5.1, encompassing both H-L and L-H configurations. The corresponding parameters are presented in Table 5.2.4.

**Table 5.3.** Values of coefficients  $v_1$  and  $v_2$  for each approach considered (Model 1, 2 and 3).

	Mode 1	Mode 2	Mode 3
$v_1$	1.170	0.993	1.091
$v_2$	0.882	0.789	0.812

Figure 5.2a illustrates the fretting fatigue life versus block 1 damage ( $d_1$ ) diagram for both load configurations (H-L and L-H). This plot represents the experimental values for the H-L (orange circles) and L-H (green diamonds) load configurations. The Mode 1 estimates for the H-L configuration are represented by the orange dashed line, while the Mode 2 estimates for the L-H configuration are depicted by the green dashed line. The Mode 3 estimates, which take into account both load configurations, are shown as solid lines in both green and orange. From such a figure, it is evident that there is no significant advantage in utilizing separate models for each case, as the Model 3 estimates adequately capture the behavior in both configurations. This observation is further supported by the coefficients presented in Table 5.2.4, which demonstrates close values for the different models. The average error of all data are reported in Table 5.2.4.3, for each model.

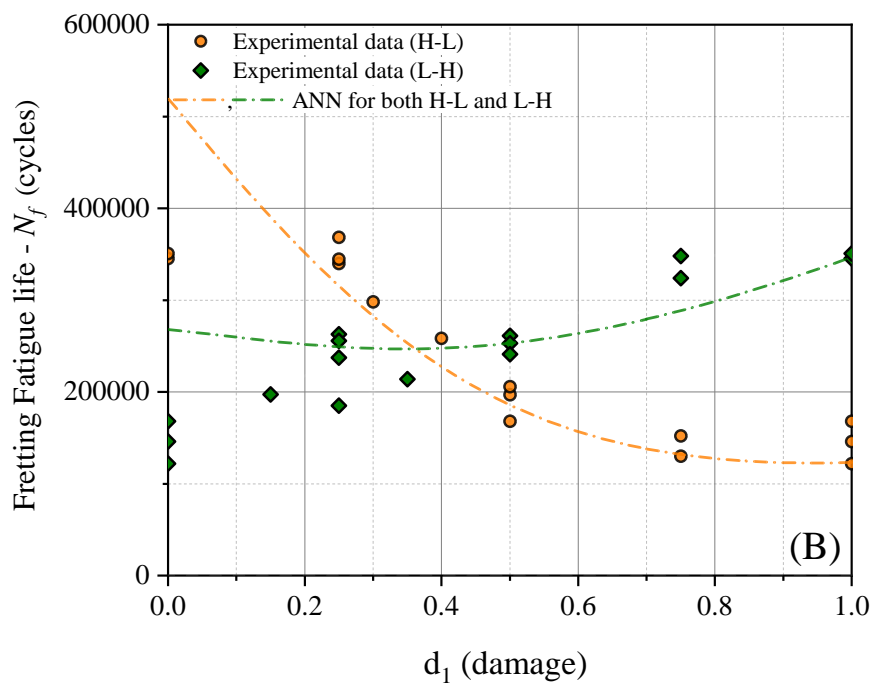
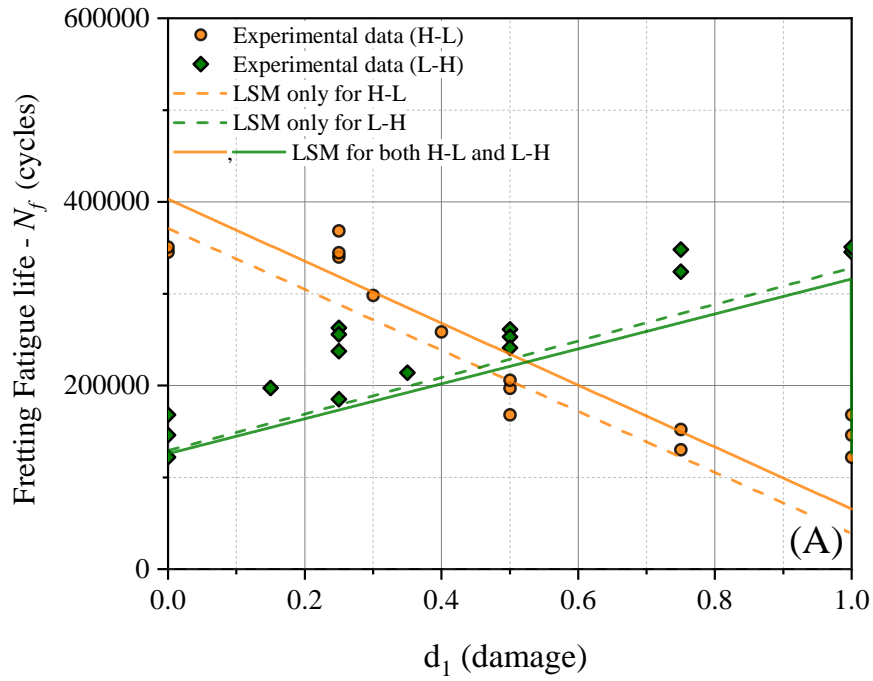


**Figure 5.2.** Fretting fatigue life vs. damage of first block ( $d_1$ ) showing the experimental data and (A) analytical models based on LSM and (B) ANN damage model.

### 5.2.4.1 SHEAR model + ANN-damage rule approach results

The approach considered here involves the utilization of an ANN trained using -data from Tables 5.1 and 5.2. In this setting, the ANN works as a representation of the equation presented in Eq. 5.2. The results are depicted in Fig 5.2b. Notably, the ANN curves demonstrate a higher level of consistency with the experimental values, despite not considering the values at the extreme ends ( $d_1 = 0.0$  or  $1.0$ ) during the training process. This observation is further supported by the values presented in Table 5.2.4.3, where this approach utilizing two neural networks proves to be the most effective, yielding the lowest error values.

Note that the models investigated in this work performed worse for very low and very high values of fatigue damage ( $d_1$ ) in the first loading block (Fig. 5.2). However, even in those cases, estimates are with the error band of 3, which can be regarded satisfactory in the view of the complexity and dispersion found in fretting fatigue problems.

### 5.2.4.2 SHEAR model + Pinto-damage rule approach results

This approach employs Eq. 5.4 in order to estimate the FF life under varying shear loading amplitudes. Thus, the results from the SHEAR model are utilized to determine the N1 and N2 values in Eq. 5.4 for the High and Low load configurations. These results are presented in Fig. 5.3 (orange triangles), which illustrates the comparison between experimental and estimated fatigue life. It is evident that the majority of the data falls within the 1.5 band limit, exhibiting similar behavior as reported in Pinto et al. (2023).

### 5.2.4.3 SHEAR model + Miner rule approach results

This last approach combines the ANN model (SHEAR) results with the Miner cumulative damage model (Eq. 5.1). Hence, this model is regarded as the simplest model and as expected, it exhibits lower accuracy compared to Miner's model (Table 5.2.4.3). Miner's model considers the experimental results of NH and NL lives, whereas the discussed model solely relies on estimates derived from SHEAR. Nevertheless, these estimates fall within the specified two band limit, as shown in Fig ??.

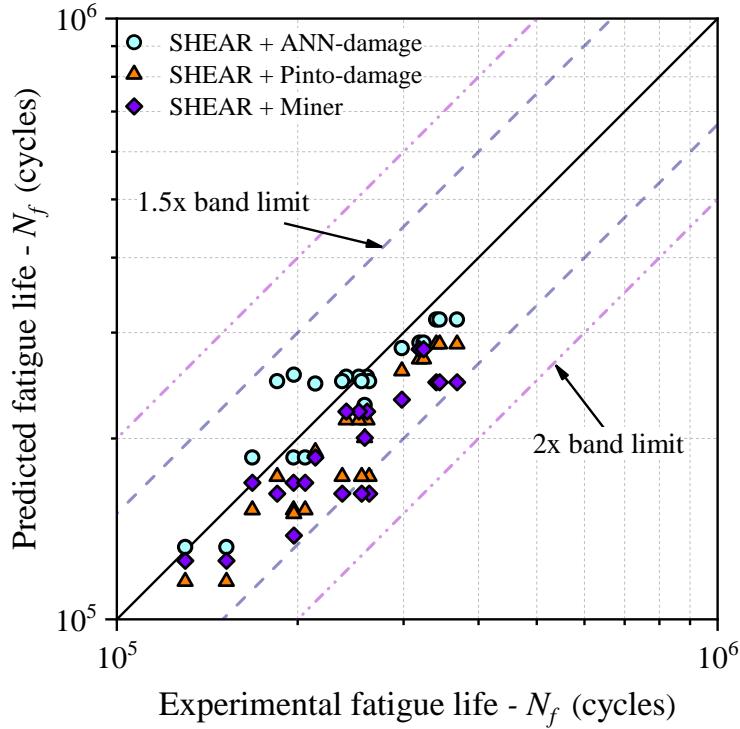


**Figure 5.3.** Estimated fatigue life considering all the three models vs. experimental one for varying amplitude FF data.

**Table 5.4.** Mean percentage error of all models considered.

Model	Miner	SHEAR <sub>LSM</sub> (%)	SHEAR <sub>ANN-d</sub> (%)	SHEAR <sub>Pinto-d</sub> (%)	SHEAR <sub>Miner</sub> (%)
ME (%)	17.37	19.63	5.24	24.21	25.10

### 5.3 PART II – ON THE LIFE ESTIMATION OF WIRES USING NON-LOCAL ANN METHODOLOGY

The fatigue analysis of overhead conductors involves a complex process, as these components are difficult to test and have intricate geometries (KALOMBO *et al.*, 2015; FADEL *et al.*, 2012; LÉVESQUE *et al.*, 2010; AZEVEDO; CESCO, 2002). Apart from specialized companies with their own laboratories, there are very few university laboratories worldwide capable of conducting such fatigue analyses, this results in limited data and analyses in the literature (AZEVEDO *et al.*, 2009; KALOMBO *et al.*, 2017; LALONDE *et al.*, 2017). To overcome these challenges, some authors have proposed analyzing the fatigue behavior of the wires in these conductors in separation. More specifically, fretting fatigue is considered, as it occurs in practice where contact with other wires, combined with the random and continuous loading caused by wind forces, leads to the failure of these overhead conductors. This approach allows for faster fatigue testing of these wires, generating more data and enabling a deeper understanding of

the phenomenon. Consequently, fretting fatigue analyses under constant amplitude (ARAÚJO *et al.*, 2020; MATOS *et al.*, 2022; GARCIA *et al.*, 2020) and variable (MATOS *et al.*, 2023), high temperatures (GARCIA *et al.*, 2024), notches (ROCHA *et al.*, 2019; MATOS *et al.*, 2020; ADRIANO *et al.*, 2018), hardening effects (JURKIEWICZ; SMYRAK, 2024; BARTOSZ *et al.*, 2019), with defects (GOMES *et al.*, 2023), as well as specific studies on the effect of the conductor/clamp connection (LALONDE *et al.*, 2018), have also been conducted. Additionally, numerical analyses incorporating the Theory of Critical Distances (TCD) (TAYLOR, 1999) along with the application of multiaxial fatigue models are also being explored to address this issue (ROCHA *et al.*, 2023; MATOS *et al.*, 2023; ARAÚJO *et al.*, 2020). Therefore, understanding the fatigue behavior of these wires is of fundamental importance for comprehending the fatigue characteristics of overhead conductor as a whole.

Recently, data-driven models have seen significant growth in their application to the field of fretting fatigue (BRITO OLIVEIRA *et al.*, 2022; WANG *et al.*, 2022b; NOWELL; NOWELL, 2020; LIU; YUAN, 2023; CARDOSO *et al.*, 2024). In Chapter 4 it has been demonstrated that such models exhibit a high generalization capability, enabling the application of a model trained with a limited dataset to various cases involving different loading conditions, geometries, and materials, even those significantly different from the training set. This success is attributed not only to the adoption of machine learning approaches but also to the careful selection of input and output parameters. In this study, one aims to extend the generalization potential of these models by evaluating their applicability to fretting fatigue cases involving wires against wires under both constant and variable amplitude bulk fatigue loading, using recent data from tests collected from the literature (MATOS *et al.*, 2022; MATOS *et al.*, 2023; VIEIRA, 2020). Other methodologies are also to be reproduced for comparative analysis purposes. This type of analysis is of ultimate importance to support the feasibility of applying these methodologies to more realistic scenarios but also contributes to understanding even more the generalization capabilities of such models in front of new scenarios.

### 5.3.1 Methodology (Part II)

This study aims to utilize an ANN non-local stress-based model previously developed and tested to estimate fretting fatigue lives (OLIVEIRA *et al.*, 2024; BRITO OLIVEIRA *et al.*,

2023a). The model provided accurate in predicting fretting life estimates for various contact geometries under partial slip regime and considering a range of different Al and Ti alloys under cyclic and more complex loading histories. It uses three stresses as input parameters and yields the corresponding fretting fatigue life as the output. To assess the model's performance under fretting fatigue wire conditions, a comprehensive dataset has been collected from relevant literature sources (MATOS *et al.*, 2022; MATOS *et al.*, 2023; VIEIRA, 2020) and numerically replicated using the finite element method. In this section, the details of the proposed methodology are presented.

### 5.3.1.1 The ANN\_NORMAL model

This ANN model uses as inputs non-local stress parameters physically linked to the crack initiation process, along with relevant material mechanical properties. As shown in Chapter 4, the ANN\_NORMAL has three inputs:  $\sigma_{n,max}/\sigma_{ult}$ ,  $\sigma_{n,a}/\sigma_{ult}$ ,  $\sigma_y/\sigma_{ult}$ . The model's output corresponds to the fretting fatigue life of the material.

To incorporate in the life analysis the impact of a rapidly varying stress field invariably present in fretting fatigue problems, the Theory of Critical Distances is considered (MATOS *et al.*, 2023; TAYLOR, 1999; OLIVEIRA *et al.*, 2024). Such a theory assumes that fatigue initiation under severe stress gradient conditions is better characterized by the average state of stress within a characteristic volume of material (a semi-sphere with radius  $L$ ).

Figure 5.4 illustrates the sequential steps to apply this model to estimate lives in fretting fatigue contact wires. Finite Element Analysis is considered to compute the time varying stress field, either for constant or for variable amplitude loadings. Following this, the stress tensor is extracted and averaged within the critical volume, as described by Eq. 5.5.

$$\sigma = \frac{1}{V} \int_V \hat{\sigma} dV \quad (5.5)$$

where  $\hat{\sigma}$  is the stress tensor at a point within the damage zone, with the flat side of the hemisphere positioned at the hot spot. The hot spot is the site at the contact surface where the formation of a fatigue crack occurs. Subsequently, equivalent stresses are calculated and employed as inputs for the ANN. The Miner's damage rule is considered for the computation of

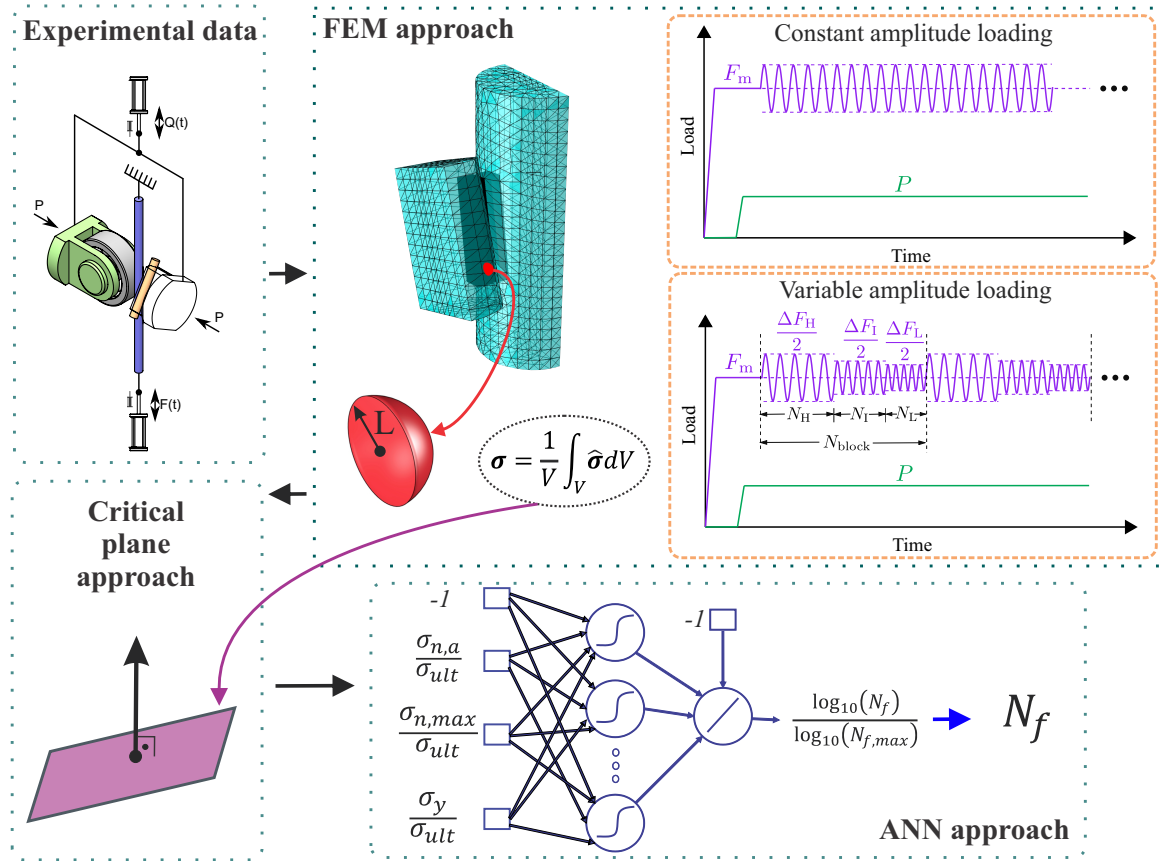


Figure 5.4. Flowchart illustrating all the modelling conducted in Part I of this work

the fatigue live over the variable amplitude loading data. It must be point out that the model, referred to as ANN\_NORMAL, is a relatively simple ANN model featuring only a single hidden layer and is based on normal stress parameters. All its details, related to the training process and the choice of the hyperparameters, can be found Chapter 4.

It is important to emphasize at this stage that such hybrid data driven model that captures the stress quantities related to the crack initiation mechanism has been trained and tested against classical fretting fatigue data (cylinder/sphere on plane) for another type of Aluminium alloys (series 7000, 2000). The challenge and new aspect to be explored in this work concerns the capability of such a model to be generalized! Thus, we seek to understand whether it will be able to accurately estimate fatigue life in a completely different fretting problem (wire against wire contact geometry), whose length scales are much smaller and using Al alloys and loading histories that the model has never seen before!

### 5.3.2 Experimental data and FE analysis

The ANN model is evaluated considering the test data of fretting wires subjected to constant and variable amplitude loading. The fretting test device (see schematic illustration in Fig. 5.4) contains two hydraulic actuators: one used to control the cyclic force applied to the specimen (vertical wire),  $F(t)$ , while the other controls the tangential force,  $Q(t)$ , or the vertical displacement of the pad (tilted wire). Additionally, the normal static force,  $P$ , is applied to the wire pad by a pair of pneumatic actuators.

The loading histories applied in the fretting fatigue tests are also represented in Fig. 5.4. In the first type of loading, the specimen is subjected to a mean bulk force  $F_m$ . Then, a compressive force  $P$  is applied to press the pad against the specimen and is kept constant during the test. Finally, the specimen is subjected to a cyclic bulk force until its rupture (MATOS *et al.*, 2022; VIEIRA, 2020). A variable amplitude fretting test program was also considered (MATOS *et al.*, 2023), Fig. 5.4. Block loadings,  $N_{block}$ , were applied up to final rupture of the wire. Each block was composed by three sub-blocks with distinct amplitudes, organized in a decreasing way. The subscripts H (high), I (intermediate), and L (low), are applied according to their force amplitudes and number of cycles.

The constant bulk amplitude dataset comprises wires fabricated from AA1120, extracted from an AAAC 823 MCM conductor. The variable amplitude dataset comprises AA6201 wires from an AAAC 900 MCM conductor. The mechanical properties (Young's modulus ( $E$ ), Vickers hardness ( $HV$ ), yield stress ( $\sigma_y$ ) and ultimate tensile stress ( $\sigma_{uts}$ )), the wire diameter ( $d$ ) and the critical distance ( $L$ ) associated with each material, i.e., AA1120 (MATOS *et al.*, 2020) and AA6201 (MATOS *et al.*, 2020; MATOS *et al.*, 2023) are provided in Table 5.5. The critical distance values have been obtained from (MATOS *et al.*, 2022; MATOS *et al.*, 2023) considering a  $10^6$  cycles for the critical distance versus life curve. Notably, each type of wire exhibits a corresponding crossing angle ( $\alpha$ ), which represents the typical angle between the outermost layers of the conductor from which the wires were extracted and is accounted for in our FE simulations. For instance, the AA6201 wires exhibit a crossing angle of  $20^\circ$ . In the case of AA1120, crossing angles of  $20^\circ$  (Numbers: 1–6) and  $29^\circ$  (Numbers: 7–13) are considered. The contact compressive force ( $P$ ) is set at 500 N for all AA1120 and AA6201 data.

Tables 5.6 reports the corresponding amplitude and mean nominal stresses ( $S_{B,a}$  and  $S_{B,m}$ )

**Table 5.5.** Properties, dimensions and critical distance of the materials considered.

Aluminum alloy	$E$ (GPa)	$HV$	$\sigma_y$ (MPa)	$\sigma_{ult}$ (MPa)	$d_w$ (mm)	$L$ ( $\mu\text{m}$ )
1120	71	57	245	249	3.79	64
6201	70	83	306	311	3.96	198

**Table 5.6.** Nominal stresses, numerical critical plane stresses (at the critical distance), and the fatigue life of the AA1120 (MATOS *et al.*, 2022; VIEIRA, 2020).

Number	$S_{B,a}$ (MPa)	$S_{B,m}$ (MPa)	$\sigma_{n,a}$ (MPa)	$\sigma_{n,max}$ (MPa)	$N_f$ (cycles)
1	31	176.0	143.5	82.2	1.87E+06
2	28	159.0	135.6	62.8	1.92E+06
3	32	181.0	147.1	82.0	1.15E+06
4	29	164.0	140.4	62.9	2.04E+06
5	29	164.0	140.4	62.9	2.17E+06
6	32	181.0	147.1	82.0	1.00E+06
7	90	110.0	219.8	93.3	2.08E+05
8	70	85.6	213.8	73.5	3.58E+05
9	70	85.6	213.8	73.5	5.30E+05
10	70	85.6	213.8	73.5	4.75E+05
11	62	75.8	206.2	67.5	6.39E+05
12	62	75.8	206.2	67.5	1.06E+06
13	62	75.8	206.2	67.5	9.10E+05

for the AA1120. The equivalent stresses,  $\sigma_{n,a}$  and  $\sigma_{n,max}$ , computed at the critical distance, are also reported in these tables. The last column reports the wire fatigue life ( $N_f$ ).

Table 5.7 presents data for AA6201 subjected to variable amplitude loading. In addition to the set ( $S_{B,a}$ ,  $S_{B,m}$ ,  $\sigma_{n,a}$ ,  $\sigma_{n,max}$ ,  $N_f$ ), this table also provides information regarding the loading type (i.e., high, intermediate, and low) and cycles ( $N$ ) executed within each sub-block of these tests.

A 3D Finite Element analysis has been considered to compute the stress parameters from

**Table 5.7.** Nominal stresses, numerical critical plane stresses (at the critical distance), and the fatigue life of the AA6201 (MATOS *et al.*, 2023).

Loading	$S_{B,a}$ (MPa)	$S_{B,m}$ (MPa)	$\sigma_{n,a}$ (MPa)	$\sigma_{n,max}$ (MPa)	$N$ (cycles)	$N_f$ (cycles)
H	40	243	233.3	107.7	2500	
I	24	243	181.5	69.5	7500	5.70E+06
L	16	243	117.7	15.3	40,000	7.45E+06
H	36	243	218.4	112.7	2500	5.65E+06
I	24	243	177.4	79.7	7500	9.50E+06
L	16	243	117.4	29.2	40,000	
H	32	243	211.4	94.3	2500	
I	24	243	180.7	67.0	7500	5.70E+06
L	16	243	116.7	14.5	40,000	7.45E+06

the critical distance. Details from this modeling are available elsewhere (MATOS *et al.*, 2022; MATOS *et al.*, 2023; ROCHA *et al.*, 2019; OMRANI *et al.*, 2021). Here just a succinct explanation is provided. The specimen and pad are represented as half-cylinders in contact. Partitioning is employed in the contact regions, facilitating a refined mesh in the contact zone and a coarser mesh for the bulk of the wires. The simulations initiate with the application of a mean bulk load to the specimen, followed by a compressive normal force to engage the pad with the specimen. Subsequently, the specimen undergoes a variable amplitude loading considering three stresses within each block, as depicted in Fig. 5.4.

### 5.3.3 Results and discussions (Part II)

One assesses the accuracy of life estimates for each investigated model using the band mean error factor (BMEF). The BMEF is defined as follows:

$$BMEF = \frac{1}{n} \sum_{i=1}^n (\psi^{(i)}) \quad (5.6)$$

$$\psi^{(i)} = \begin{cases} \frac{N_{f,pred}^{(i)}}{N_{f,exp}^{(i)}}, & \text{if } N_{f,pred}^{(i)} \geq N_{f,exp}^{(i)} \\ \frac{N_{f,exp}^{(i)}}{N_{f,pred}^{(i)}}, & \text{if } N_{f,pred}^{(i)} < N_{f,exp}^{(i)} \end{cases} \quad (5.7)$$

where  $N_{f,pred}^{(i)}$  and  $N_{f,exp}^{(i)}$  represent the  $i$ -th predicted and  $i$ -th experimental fretting fatigue life values within a dataset of size  $n$ , respectively. It is worth noting that the BMEF provides a straightforward means to assess the average dispersion of fatigue life predictions. However, it does not distinguish between conservative and optimistic outcomes (OLIVEIRA *et al.*, 2024).

#### 5.3.3.1 Wires under constant amplitude loading

To predict the fretting fatigue life of wire against wire, one adopts two approaches to perform a comparative analysis. First, one considers the ANN\_NORMAL model, which has been already referenced. Second, it is proposed the methodology by Matos *et al.* 2022, which incorporates the critical plane approach and the TCD theory. This method is more complex, taking into account the concept of variable critical distance. The results associated to the AA1120 data (Tables 5.6) are shown in Fig. 5.5. Such figure portrays the experimental versus

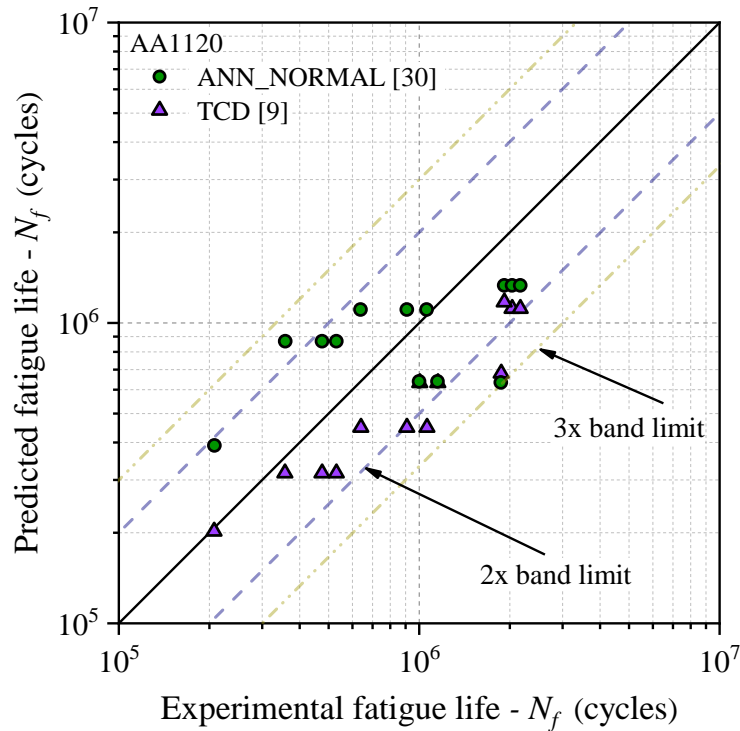


**Figure 5.5.** Estimated life vs. experimental life for fretting fatigue tests on AA1120 and AA1350 wires, subjected to constant amplitude loading.

**Table 5.8.** Comparative analysis of BMEF for the AA1120 and AA6201.

Alloy	Amplitude	Model	BMEF
AA1120	Constant	ANN_NORMAL	1.74
		TCD	1.75
AA6201	Variable	ANN_NORMAL	2.03
		TCD	1.63
		Master Curve	2.54

the estimated life diagram for both models.

As can be seen, it is evident that all data points fall within a factor of three, with the majority of them falling within a factor of two of the expected values. For this material, the models exhibit a scattering behavior analogous to that observed experimentally. The BMEF values associated with both models' estimates are reported in Table 5.8. Both models provided similar estimations, with the ANN\_NORMAL model indicating more optimistic forecasts compared to the TCD model, which exhibited entirely conservative behavior. In terms of BMEF, the results were nearly identical, with a band average error value around 1.7.

It is important to note that the model proposed by Matos was specifically designed to address fatigue in wires, being calibrated with similar data and the same material under analysis here, while also incorporating the variable critical distance consideration, which tends to improve es-

timates, as highlighted by the author (MATOS *et al.*, 2022). Conversely, the ANN\_NORMAL model featured in this study was developed based on different materials, different geometries, and different loading conditions, distinct from AA1120 (BRITO OLIVEIRA *et al.*, 2023a). Despite these differences, the model performed well under constant amplitude conditions, providing estimates on par with the TCD model. This demonstrates the versatility of such data-driven models, which exhibit a high degree of generalization capability.

### 5.3.3.2 Variable amplitude loading

For the AA6201 dataset with variable bulk load amplitude, the life predictions obtained in this work using the ANN\_NORMAL model are compared to those previously obtained in (MATOS *et al.*, 2023) using two methodologies: one based on the combination of a critical plane criterion with the TCD, and the other based on the use of a master fatigue curve. The latter was introduced by Rocha *et al.* (2022) and is based on the similitude between the fatigue damage of conductor’s wires and of fretting fatigue tests. The underlying assumption of this methodology is that, if the nominal stress history in a wire of the conductor and in a specimen’s wire used in a fretting fatigue test are the same, both will have the same fatigue life. The Master Curve model’s effectiveness lies in its ability to account for the influence of stress concentration and stress gradients, as the curve is established using data from fretting fatigue tests in wires (MATOS *et al.*, 2023; ROCHA *et al.*, 2022).

Figure 5.6 displays the results of the experimental vs. estimated life for all models under consideration. It is evident that the ANN\_NORMAL model and TCD model exhibit similar outcomes, with data predominantly within the three-band boundaries. However, the ANN\_NORMAL model tends to provide more conservative estimates. In this case, the Master Curve model presented less favorable results, marked by more conservative predictions, although still offering satisfactory results within the context of wire fatigue, which often exhibits significant experimental dispersion (ARAÚJO *et al.*, 2020). Table 5.8 reports the BMEF values for all models under examination. The results indicate that, on average, the estimates from both TCD and ANN\_NORMAL models fall within the 2-band width.

One reiterates here that, the interesting aspect of the ANN model is that it has been developed/trained considering only aeronautical aluminum alloys and contact geometries, which

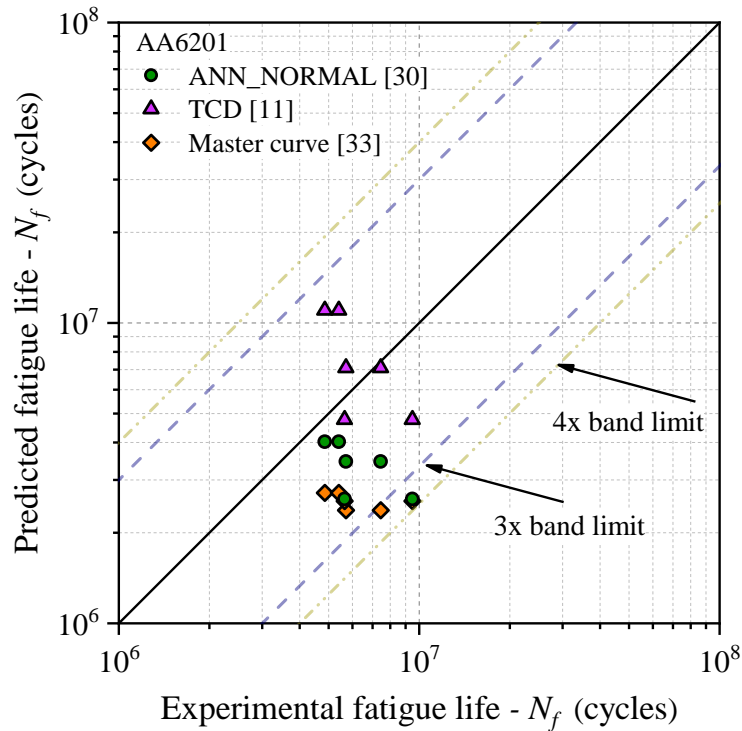


**Figure 5.6.** Estimated life vs. experimental life for fretting fatigue tests on AA6201 wires, subjected to variable amplitude loading.

are substantially different from the ones analyzed here (BRITO OLIVEIRA *et al.*, 2023a; OLIVEIRA *et al.*, 2024). Nevertheless, the model yielded very similar life estimates of other models with a higher level of complexity and which were specifically calibrated for the material in question.

#### 5.4 PART III – NOMINAL STRESS -ANN APPROACH FOR LIFE ESTIMATION OF OVERHEAD CONDUCTORS

The ANN models presented so far employs a non-local approach to address stress gradient effects. Despite its promising capabilities in fatigue life prediction, a significant drawback arises from the need for precise stress computation at the critical distance point. This often limits the size of the finite element model due to the substantial computational cost required for accurate stress calculations at this level of precision. Consequently, employing this method to compute the fatigue life of overhead conductors, with their numerous strands, numerous contact zones (common sites for fatigue failures), and intricate non-linear effects (such as localized plasticity, wear, and friction), becomes impractical. To address the challenge of making life predictions for overhead conductors, this section proposes an adaptation of the ANN model approach.

This adaptation involves modifying the ANN model to utilize stress information provided by more cost-effective finite element models, ensuring they still capture crucial details about the mechanisms governing damage accumulation in the conductor cable.

Beam element-based FE modeling of overhead conductors has proved to be a promising approach to accurately compute stress along strands of conductors while maintaining a favorable balance with computational cost (LALONDE *et al.*, 2018; ROCHA *et al.*, 2022; ROCHA *et al.*, 2023). Leveraging the slender nature of conductors, this method takes advantage of beam elements to represent its strands, specifically suited for representing slender structural members. It is a notable advantage over solid element-based approaches (SAID *et al.*, 2020; NAWROCKI; LABROSSE, 2000; SCHILLAI, 2019). This significantly reduces the number of model degrees of freedom, while maintaining a comparable level of accuracy when compared to solid element-based methodologies (LALONDE *et al.*, 2017). Based on this, Rocha et al. 2022 proposed a new methodology to assess the fatigue life of overhead conductors, which is based on the similitude concept of the S-N method.

Within this context, this last section part proposes a new hybrid model based on data-driven approach to predict the fretting fatigue lives of overhead conductors. It uses a nominal stress-based machine learning methodology in conjunction with finite element simulations to predict the fatigue life of two types of overhead conductors, an AAAC 900 MCM and an ACSR Tern. The accuracy of these machine learning models will be investigated and compared with other available criteria in the literature. The proposed methodology is also able to estimate the fretting crack initiation site in the conductor wire, identifying its layer and distance from the keeper edge! Experimental data will be used to assess the model capacity to determine crack initiation site in such complex problem.

#### 5.4.1 The machine learning-based modeling approach

As introduced, the proposed approach specifically aims to use stress parameters computed from overhead conductors' fatigue numerical simulations as input to a machine learning model to predict the fatigue life of such conductors. Preceding the demonstration the application of this model for this specified purpose, this subsection details the ML model development process.

### 5.4.1.1 A brief theoretical background

There are numerous machine learning (ML) models available and each one containing different hyperparameters. The aim of this work is not to exhaustively explore all types of ML or to try to optimize their hyperparameters, but to choose few models that have been consistently used to study fatigue of materials and assess which one has the best performance in terms of accuracy and generalization!

In this study, four types of machine learning-based regression models were considered within the scope of mechanical engineering: Random Forest (RF), Gaussian' Process Regression (GPR), XGBoost, and Artificial Neural Network (ANN). These models were chosen due to their established acceptance within the scientific community (SONG *et al.*, 2023; LIU *et al.*, 2022; YANG *et al.*, 2022; HORŇAS *et al.*, 2023; GAN *et al.*, 2022; ZHAN; LI, 2021; HU *et al.*, 2020; HENG *et al.*, 2022) and their suitability for situations with limited data, as is the case in our study (BREIMAN, 2001; CHEN; GUESTRIN, 2016; SEEGER, 2004; HAYKIN, 2008).

The Random Forest (RF) model, when used for regression, is an ensemble learning technique that amalgamates multiple decision trees to enhance prediction accuracy while mitigating overfitting. It leverages bootstrapped samples and random feature selection to construct diverse trees, with the final predictions derived through a weighted aggregation of individual tree outputs (YANG *et al.*, 2022; HORŇAS *et al.*, 2023; GAN *et al.*, 2022; ZHAN; LI, 2021; BREIMAN, 2001)

XGBoost is another machine learning algorithm, based on tree structures, that enhances performance through bagging and boosting of weak trees, making it effective for classification and regression problems, even when dealing with imbalanced datasets. The XGBoost model is more complex due to embedded optimizations and regularization, when compared to RF. However, it is more sensitive to the fine-tuning of its hyperparameters, making it better suited for scenarios with larger datasets and greater complexity (SONG *et al.*, 2023; LIU *et al.*, 2022; CHEN; GUESTRIN, 2016).

Another machine learning model under consideration is Gaussian Process Regression (GPR), which is a machine learning method based on Gaussian processes to model relationships between variables. It is particularly valuable for modeling nonlinear relationships and uncertainties in

data, rendering it suitable for regression predictions. This model characterizes the relationship between variables as a probability distribution over functions. GPR is a robust choice when aiming to model complex relationships and estimate uncertainties (HU *et al.*, 2020; HENG *et al.*, 2022; SEEGER, 2004).

The final model in question is the Artificial Neural Network (ANN) with a single hidden layer. The model is also considered as a universal function approximator (HAYKIN, 2008). Neural networks with a single hidden layer are more adaptable to nonlinear relationships, although they may require more fine-tuning and can be sensitive to weight initialization and learning rates. This model finds widespread application in classification and regression tasks (BRITO OLIVEIRA *et al.*, 2023a; HAYKIN, 2008).

Various methodologies can be employed to perform comparative analyses of these types of models. In this study, one focuses on two specific formulas that are applied to compute the error between estimated and experimental values. The first is the same as that used classically in cross-validation analyses, the Empirical Risk (Eq. 3.1) error. One also assesses the accuracy of life estimates for each investigated model using the band mean error factor (BMEF).(Eq. 4.3).

#### 5.4.1.2 The choice of the input parameters

In the development of a machine learning model, the first crucial step is the selection of the inputs and output parameters. The choice of physical parameters, which are known to be inherently related to the mechanical aspects of the problem, greatly facilitates the model creation process.

The subsequent step involves data collection, a process that may require a significant amount of time, depending on the complexity of the predefined input parameters and their availability. Additionally, the quantity of data in the training set directly impacts the robustness of the final model, particularly when the dataset exhibits considerable variability, thereby preparing the model to handle diverse scenarios and enhancing its generalization capabilities. Furthermore, the issue of dimensionality, i.e., the number of input features, may also affect the model's ultimate performance. A preference for a reduced number of inputs is advisable to reduce the demand for extensive training data. The collected data should be partitioned into training

and test sets to evaluate the model's performance on unseen data. The penultimate step encompasses the model selection. In our context, we are primarily interested in regression-based models. Consequently, it is prudent to explore a variety of models to determine the one that best aligns with the specific problem, it typically follows a tentative empirical approach, as there is no definitive method for this choice. It is noteworthy that hyperparameter tuning is also recommended during this phase to optimize the chosen model's performance. Lastly, the model should undergo testing across diverse scenarios to assess its generalization potential, and, of course, being a model that is straightforward to implement.

Based on this, three parameters were chosen as inputs for our models. Fatigue life was selected as the output, using the normalization technique, which considers the logarithmic scale. Such life is then normalized by a maximum fatigue life, which we assumed to be  $10^8$  ( $\log_{10}(N_f)/\log_{10}(10^8)$ ). The input parameters were inspired by the works of Rocha *et al.* (ROCHA *et al.*, 2022; ROCHA *et al.*, 2023), which utilized the Master Curve model. It is a model that integrates finite element stress analyses of the conductor-clamp system with the utilization of master fatigue curves. These curves are derived from (i) tests involving both plain and fretting fatigue tests of wires and (ii) the use of the SWT parameter (computed in terms of the nominal stress amplitude ( $S_{B,a}$ ) and the nominal mean stress ( $S_{B,m}$ )).

The present ML model also will consider  $S_{B,a}$  and  $S_{B,m}$  as driving/input parameters to its training process! These stresses are normalized by the ultimate tensile strength of the material ( $\sigma_{uts}$ ), in order to optimize the training and to introduce the first material parameter to the model. The third input chosen for this model is the Vickers material's hardness ( $HV$ ). Somehow, hardness provides a measure to the wire's resistance against fretting wear, thus it may well constitute an important information to the model's training. Not only it does assist the model in distinguishing between different materials, but it also introduces a material parameter that may influence the fretting fatigue life of the conductors. This last input has been normalized by a maximum Vickers hardness ( $HV_{max}$ ) assumed to be 150 (MATOS *et al.*, 2022). This choice ensures that this parameter will never exceed unity for aluminum alloys.

In this study, four types of machine learning models are tested, as detailed in section 2.1. These models are trained using two datasets from two different materials (AA1120 and AA1350). A third material (AA6201) will be employed to assess the model's generalization

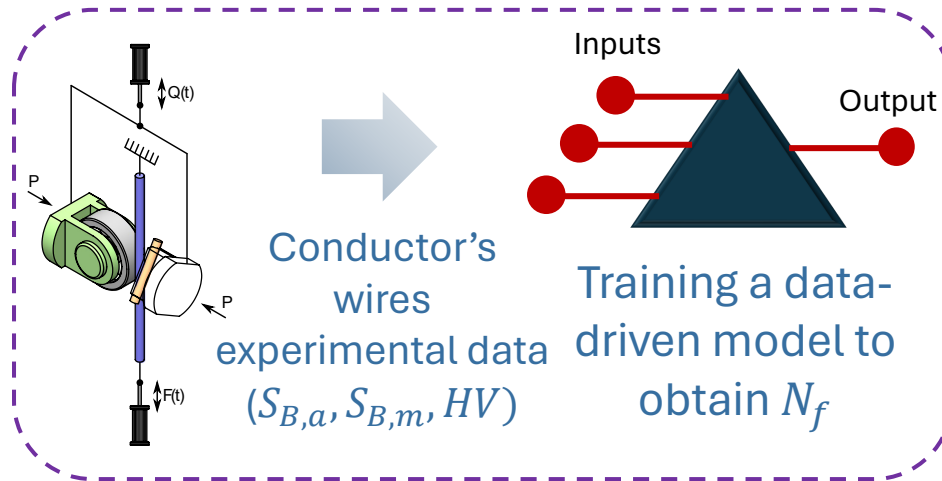


**Figure 5.7.** Schematic of the machine learning model using wire fatigue data for training.

capability. The model that exhibits the lowest error on the test set, involving the unknown alloy, will be selected for the final testing on overhead conductors' data. Figure 5.7 presents a schematic summary of this approach.

## 5.4.2 Training and test of the machine learning models

### 5.4.2.1 Fatigue data on wire against wire

Before detailing the model training process, this section describes the experimental data used for training and test datasets. A larger fretting fatigue wire/wire dataset has been collected from the literature (MATOS *et al.*, 2020; GARCIA *et al.*, 2020; VIEIRA, 2020; MATOS *et al.*, 2022; VIEIRA, 2020; MATOS *et al.*, 2023). These data are depicted in Fig. 2 in terms of the SWT parameter computed by means of nominal stresses. Here on it will be denominated  $SWT_{\text{nom}}$  (i.e.:  $SWT_{\text{nom}} = \sqrt{S_{B,\alpha} \langle S_{B,\text{max}} \rangle}$ ). The respective curve fitting for each material dataset is also shown in Fig. 5.8. In these tests, there is a longer wire under the action of a bulk fatigue load  $F(t)$ , which is pressed by a short “wire pad”, generating the static normal load,  $P$ . Due to friction and the deformation of the longer wire, a tangential force will arise at the contact interface.

Table 5.9 reports the mechanical properties (Young's modulus ( $E$ ), Vickers hardness (HV), yield stress ( $\sigma_y$ ) and ultimate tensile stress ( $\sigma_{uts}$ ) associated with each material. Table 5.10 provides the experimental parameters (fatigue ratio ( $R_\sigma$ ), wire crossing angle ( $\alpha$ ), contact

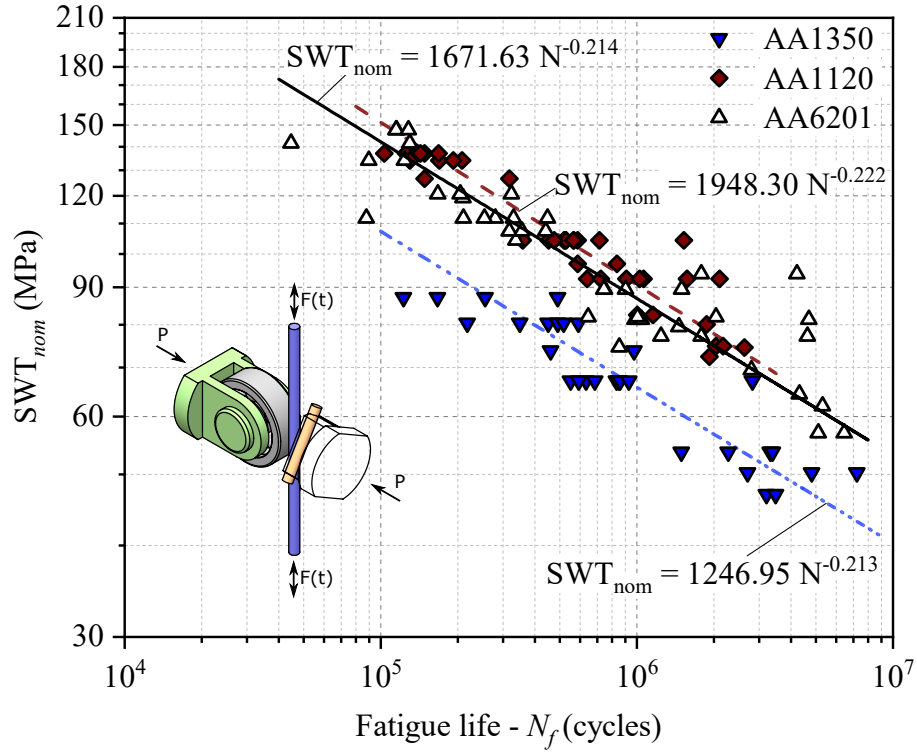


**Figure 5.8.** Correlation of the SWT parameter, calculated using the bulk nominal stress, with lives of fretting fatigue tests of wires made of AA6201, AA1120 and AA1350.

**Table 5.9.** Mechanical properties of the materials considered.

Aluminum Alloy	E(GPa)	HV	$\sigma_y$ (MPa)	$\sigma_{ult}$ (MPa)
1120	71	57	245	249
1350	69	41	166	186
6201	70	83	306	311

normal force ( $P$ ) and the nominal stress amplitude ( $S_{B,a}$ ) of the wires tested and from the conductors of which they were extracted.

#### 5.4.2.2 Training and testing the models

Given that the majority of the data comprises same loading conditions with different fatigue lives, one decided to incorporate only data points with average lifespans into the model. This choice has been made because providing identical input data (stress values) with different outputs (fatigue life) would not contribute to the training of our model. After the data pre-processing, 18 data points were used in the training phase. These values were collected from two types of aluminum alloys: 1120 and 1350. Despite the limited quantity of data points, these alloys were selected due to their significant variability in stress states ( $S_{B,a}$  and  $S_{B,m}$ ), covering a range of lives from  $10^5$  and  $10^7$  cycles. Furthermore, this approach aimed to push the

**Table 5.10.** Fretting fatigue test parameters of wires on AA6201, AA1120 and AA1350 for Part II.

Alloy	Conductor	$\alpha$ (°)	$P$ (N)	$R_\sigma$	$S_{B,a}$ (MPa)
AA6201	AAAC 900 MCM	20	250	0.1	63–99
	AAAC 1055 MCM		500, 750, 1000	0.1	55–95
	AAAC 900 MCM		500, 750	0.79–0.83	24
	AAAC 900 MCM		500	0.81–0.85	15–24
AA1120	AAAC 823 MCM	20	500	0.7	29–32
	AAAC 823 MCM	29	250, 500, 1000	0.1	50–92
AA1350	ACSR Ibis 397.5 MCM	29	250, 500	0.1	32–59

boundaries of artificial intelligence-based models by evaluating their performance with minimal training data. Subsequently, 20 data points related to the AA6201 are employed for test purposes. These data encompass fatigue life across the entire spectrum considered in the training data and include some points that fall outside of this fatigue life range, further challenging the model in terms of generalization capabilities.

The ML models have been developed using MATLAB and Python libraries, such as scikit-learn and XGBoost. During their creation, various hyperparameters have been systematically tested for each model. In general, 14 data points were randomly selected for training, with an additional 4 data points reserved for validation purposes. Regarding the RF model, the optimal hyperparameters were found to be 100 decision trees with a depth of 2. On the other hand, the XGBoost model exhibited improved performance with 74 decision trees, a depth of 3, a learning rate of 0.0517, a gamma value of 0.000015, and a 'min\_child\_weight' parameter of 2. The latter indicates that the model requires at least 2 samples in a leaf node to allow for division.

For the GPR model, the search for optimal hyperparameters yielded a very low alpha value of  $10^{-5}$  and an RBF kernel with a length scale of 1. This low regularization parameter alpha indicates that the model is highly flexible, with relatively minimal penalization, given the limited training data available. The ANN model achieved its best results with only 12 neurons in the hidden layer, employing the hyperbolic tangent function in the hidden layer, and a learning rate of 0.1, using the backpropagation training algorithm. Cross-validation was implemented during the model training, and to assess their predictions against the 20 validation data points, we employed the ER error.

Figure 5.9 presents a comparative analysis of all models, displaying estimated life versus

**Table 5.11.** Comparative error analysis (ER and BMEF) for the learning and query dataset by considering the machine learning models.

Data	Model	ER*	BMEF
Learning	ANN	9.45	1.25
	RF	3.50	1.13
	XGBoost	6.71	1.13
	GPR	2.70	1.13
Validation	ANN	92.05	2.15
	RF	152.81	2.76
	XGBoost	142.55	2.58
	GPR	149.70	2.70

\* Values must be multiplied by  $10^{-5}$ .

experimental life in separate graphs for each model and each dataset under study, encompassing both the training and test (query) datasets. As observed, the model exhibiting the least data dispersion in the query dataset was the ANN-based model. This observation is further substantiated by the values presented in Table 5.11, which provide insights into the ER and BMEF for each model. Notably, the ANN-based model achieved the lowest ER and BMEF values for the validation dataset. By examining these results, it becomes evident that the RF model displayed limited generalization capabilities, yielding reasonable results for the training data but underperforming when applied to distinct data (i.e., different materials) not encountered during training. The XGBoost model achieved the lowest BMEF value for the materials in the training dataset and ranked second in terms of ER and BMEF for the analysis of the query data, i.e., when applied to distinct data (i.e., different materials and loadings) not encountered during training. Its robustness would make it the best candidate for selection; however, the focus of this work lies in practical simplicity. Therefore, opting for a simpler model with greater generalization capability becomes more appealing. Conversely, the ANN-based model exhibited the weakest performance when applied to the training dataset. However, it is worth noting that this outcome remains highly satisfactory, considering its BMEF value of 1.25. Consequently, despite the ANN model providing less accurate estimates for the training data, its superior generalization, which aligns with the primary objective of our model, deems it the most suitable candidate in meeting our requirements. Consequently, this model which we named as "ANN\_Cable", will be employed for predicting the fatigue lives of overhead conductor in the subsequent section.

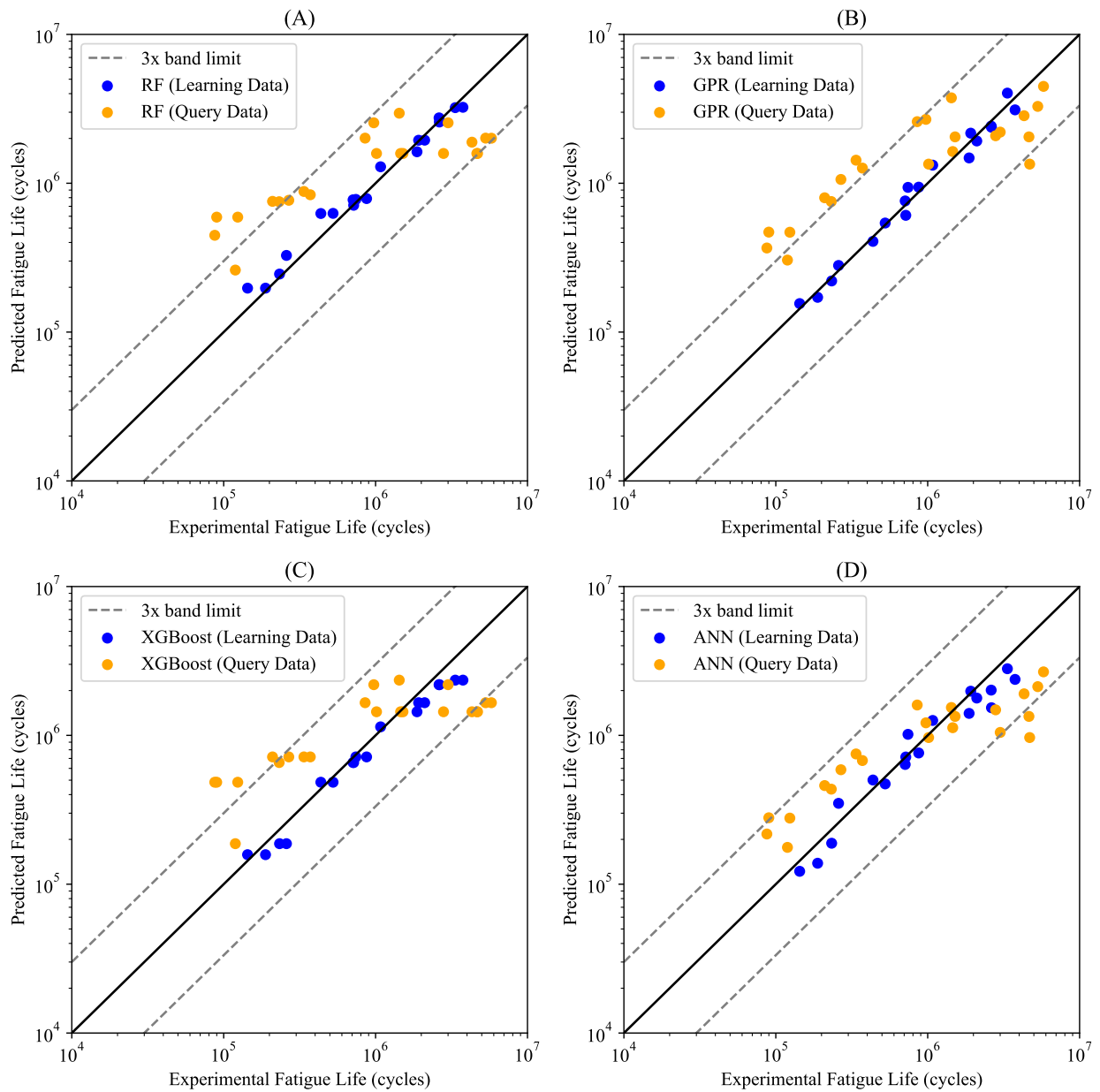


**Figure 5.9.** Estimated life vs. experimental life for fretting fatigue tests on learning data (AA1120 and AA1350) and validation data (AA6200). Prediction made using all the ML models (A) RF, (B) GPR, (C) XGBoost and (D) ANN.

### 5.4.2.3 Determining the weights matrices of the ANN model

As mentioned earlier, the ANN model consists of only one hidden layer with a linear function in the output layer. One can also represent the ANN formulation in a matrix notation, such that the input vector can be represent as follows:

$$\mathbf{x} = \left[ \frac{\sigma_{B,m}}{\sigma_{uts}}, \frac{\sigma_{B,a}}{\sigma_{uts}}, \frac{HV}{HV_{max}} \right]^T \quad (5.8)$$

Please note that the model has been trained using nominal stress representations, denoted as  $S_{(B,a)}$  and  $S_{(B,m)}$ . However, following the concept of similitude as discussed by Rocha *et al.* (2022), local stresses at the wire contacts will be computed in the conductor's analysis. Therefore, for practical purposes, we have chosen to refer to these variables as  $\sigma_{(B,a)}$  and  $\sigma_{(B,m)}$ . As a result, the final equation representing the model's output is given by:

$$y = \mathbf{V}^T \cdot [-1 \parallel \tanh(\mathbf{W} \cdot [-1 \parallel \mathbf{x}])] \quad (5.9)$$

where  $\parallel$  is used to denote concatenation such that the term  $[-1 \parallel x]$  is the extended input vector with the bias  $(-1)$ . This bias is presented from the input layer to the hidden layer and also from the hidden layer to the output layer (Fig. 5.10). The weight matrices  $W$  and  $V$  are obtained through training, and they are the main parameters of the network. After training, the model can be used for query with other data. The matrix  $W$  represents the weights between the input layer and the hidden layer, while the matrix  $V$  represents the weights between the hidden layer and the output layer. In this case, matrix  $W$  is a  $12 \times 4$  matrix, and matrix  $V$  is a column matrix with dimensions  $13 \times 1$  both  $V$  and  $W$  are provided as follows:

Finally, to calculate the fatigue life, it is necessary to perform the inverse normalization and logarithm process, as follows:

$$N_f = 10^{8y} \quad (5.10)$$

where  $y$  is given by Eq. 5.9.

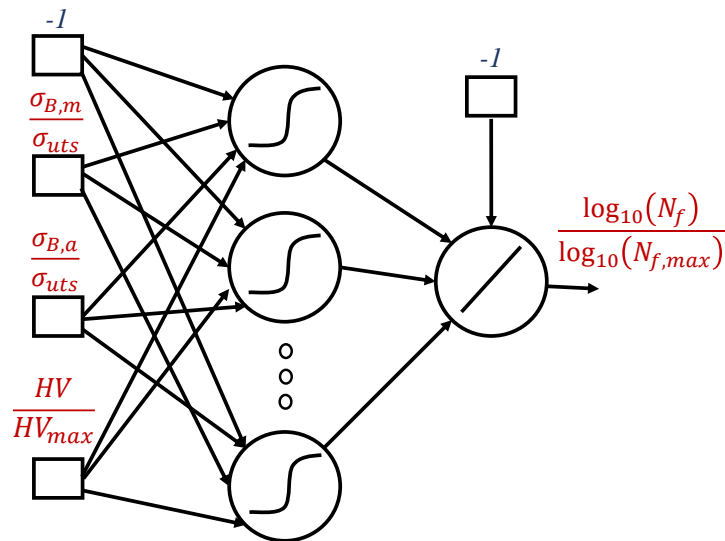
In the following section, the complete procedure for applying the model to estimate the fatigue life of overhead conductors will be discussed.

**Table 5.12.**  $W$  matrice.

$W$			
-0.592125884302411	0.581200864629651	0.499923766186536	0.104182349666597
-0.521331498453038	0.627614788351375	-0.031584664829717	0.549536240247139
-0.309239886000316	-0.103917737857773	-0.066580698868630	-0.088074606106932
0.155044315204933	-0.192340983643266	0.099544282372236	0.530480792013319
-0.026217255240082	-0.348720310649509	0.116960863471809	-0.668082183224774
0.367089008809558	0.364193341614766	0.617359252543475	0.229967087224138
0.252802831794848	0.496502611716215	0.182129242512519	-0.143964675864882
0.500002469317718	0.378926208778418	0.394127843499098	-0.106400461388168
-0.006194695091329	0.575527655691166	0.148913578798355	0.604028167527775
0.124828127298321	-0.569924484417509	0.561946913512864	-0.152643580631925
0.229058604261740	0.551573830174446	0.162093355818329	0.268482376089732
0.712533201894417	0.428731136955001	0.206365440671165	0.313546873898215

**Table 5.13.**  $V$  matrice.

$V$
-0.312701861098058
0.254329741853432
-0.412807778884357
-0.181515622509871
-0.356090715374834
-0.603725358699780
-0.659228928416747
0.025878211851523
-0.019012399237646
0.288729671875138
-0.252405150314290
-0.263123486684421
-0.601609365369458

**Figure 5.10.** ANN architecture for the ANN\_Cable model.

### 5.4.3 Application of the ML model to estimate overhead conductors' fatigue life

This section provides a description of the procedure for applying the ANN\_Cable model to fatigue life estimation in overhead conductors. Initially, the experimental data are described, as these are utilized both in constructing the numerical model and for comparative purposes in the life estimation process. This is followed by a detailed explanation of the numerical modeling. Drawing on the concept of similitude proposed by Rocha *et al.* (2022, 2023), stresses computed at the contact regions between the wires of a conductor are applied to the model, which is trained with experimental wire/wire fatigue data.

#### 5.4.3.1 Overhead conductors' experimental data

Fatigue data for the overhead conductors were obtained from resonant test benches with a 40-meter active span and 7-meter passive spans (BADIBANGA, 2017), as depicted in Fig. 5.11a. An electrodynamic shaker is attached to simulate Aeolian vibration in the conductor. The primary controlled parameters for these tests are the tension load applied to the conductor ( $T$ ) and the bending displacement amplitude ( $Y_b$ ). Figure 5.11a shows a scheme of the test configuration in the fatigue test bench.

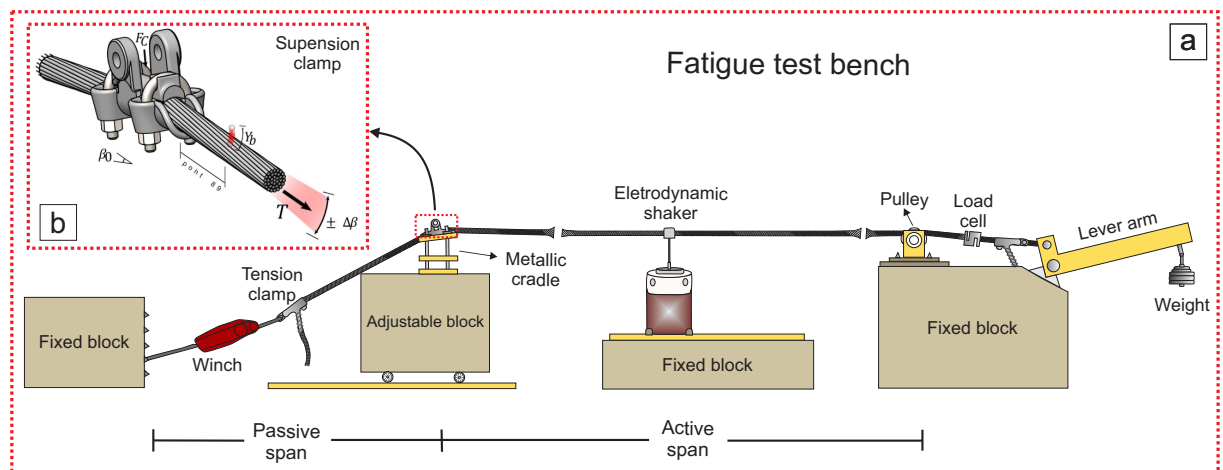


**Figure 5.11.** Schematic of the overhead conductor fatigue test bench. Adapted from (BADIBANGA, 2017)

The bending displacement amplitude is controlled by an accelerometer at a specific point—89 mm from the last point of contact between the conductor and the clamp (Fig. 5.11b). The experimental data for the overhead conductors are presented in Tables 5.14 e 5.15. Two overhead

**Table 5.14.** Experimental data from AAAC 900 MCM overhead conductor.

Tension (kN)	$Y_b$ (mm)	1 <sup>st</sup> break	2 <sup>nd</sup> break	3 <sup>rd</sup> break	4 <sup>th</sup> break
26.3	0.68	1.03E+06	1.12E+06	1.18E+06	1.50E+06
26.3	0.68	8.87E+05	1.06E+06	1.06E+06	1.40E+06
26.3	0.68	6.88E+05	7.78E+05	1.11E+06	1.29E+06
26.3	0.81	5.46E+05	6.82E+05	1.06E+06	1.04E+06
26.3	0.81	4.00E+05	4.40E+05	6.00E+05	9.21E+05
26.3	0.81	5.40E+05	6.35E+05	7.30E+05	8.57E+05
26.3	0.9	4.34E+05	4.63E+05	6.93E+05	7.44E+05
26.3	0.9	2.93E+05	5.68E+05	6.45E+05	7.63E+05
26.3	0.9	5.47E+05	5.77E+05	6.00E+05	6.08E+05
22.4	0.71	7.60E+05	9.98E+05	1.32E+06	1.79E+06
22.4	0.71	9.68E+05	1.18E+06	1.29E+06	1.68E+06
22.4	0.71	8.62E+05	9.75E+05	1.28E+06	1.51E+06
22.4	0.85	6.74E+05	8.97E+05	8.97E+05	1.45E+06
22.4	0.85	6.35E+05	7.47E+05	7.47E+05	1.01E+06
22.4	0.85	5.27E+05	6.78E+05	9.04E+05	1.32E+06
22.4	0.94	4.24E+05	6.90E+05	8.42E+05	9.55E+05
22.4	0.94	3.41E+05	7.20E+05	7.20E+05	9.33E+05
22.4	0.94	3.02E+05	4.44E+05	4.85E+05	8.93E+05
33.4	0.63	5.47E+05	7.30E+05	8.03E+05	9.85E+05
33.4	0.63	4.64E+05	7.41E+05	1.11E+06	1.16E+06
33.4	0.76	5.48E+05	6.21E+05	6.58E+05	7.67E+05
33.4	0.76	5.87E+05	6.97E+05	9.30E+05	9.30E+05
33.4	0.84	3.29E+05	3.66E+05	4.39E+05	5.12E+05
33.4	0.84	5.14E+05	5.60E+05	6.07E+05	6.53E+05

conductors are used: one is a ACSR Tern, with a diameter of 27.03 mm, composed of a 7-wire steel core and 45 aluminum wires (AA1350) distributed across 3 layers. The other one is the AAAC 900 MCM, in which all wires are made of the AA6201 alloy. This conductor has a diameter of 27.74 mm and consists of 37 wires distributed across 3 layers. Tables 5.14 and 5.15 also presents, for each conductor, the tensile load during stretching (*Tension*), the range of various bending amplitude displacements tested ( $Y_b$ ), and the lifetime until the break failures related to each wire break from the conductors. Further details regarding these data can be found in (ROCHA *et al.*, 2023; BADIBANGA, 2017).

#### 5.4.3.2 Finite element modelling

Figure 5.12 shows a general view of the numerical model for the ACSR Tern, one of the conductor types studied. The model employs three-dimensional quadratic beam elements, each measuring 10 mm in length, to discretize the conductor wires. To compute the effects of inelastic

deformation in wires during the initial loading of the conductor, elastic-perfectly plastic material behavior has been assigned to the beam elements of the model. For the clamp body and keeper, quadratic rigid surface elements with a length of 2.5 mm are used to represent their geometry.

To emulate the loading sequence used in the fatigue tests of the conductor-clamp assembly, multiple steps-loading are adopted on the simulation. To impose boundary conditions on the conductor, the nodes of each end of the conductor are coupled to the central wire node forming a rigid link among them. The displacement/force constraints related to the conductor are applied directly to these central wire nodes.

**Table 5.15.** Experimental data from AAAC 900 MCM overhead conductor.

Tension (kN)	$Y_b$ (mm)	1 <sup>st</sup> break	2 <sup>nd</sup> break	3 <sup>rd</sup> break	4 <sup>th</sup> break	5 <sup>th</sup> break
28.2	0.8	2.54E+06	2.54E+06	2.90E+06	2.90E+06	3.09E+06
28.2	0.8	1.38E+06	1.38E+06	1.38E+06	2.07E+06	2.96E+06
28.2	0.8	1.12E+06	1.12E+06	2.21E+06	2.77E+06	3.43E+06
28.2	0.84	1.64E+06	1.64E+06	2.00E+06	2.94E+06	3.04E+06
28.2	0.84	9.88E+05	1.35E+06	2.10E+06	2.53E+06	2.89E+06
28.2	0.84	1.45E+06	1.67E+06	1.67E+06	3.11E+06	3.14E+06
28.2	0.93	1.36E+06	1.36E+06	1.36E+06	1.36E+06	1.65E+06
28.2	0.93	1.30E+06	1.33E+06	1.33E+06	1.33E+06	1.49E+06
28.2	0.93	1.10E+06	1.10E+06	1.99E+06	1.99E+06	1.99E+06

The loads are imposed in a quasi-static manner, divided into several stages, as illustrated in Fig. 5.12b. Throughout the simulation, the pilot node of the suspension clamp body remains fixed in all degrees of freedom (DOF), while the y-direction DOF of the keeper's pilot node is controlled either by displacement or force along the simulation. During load step 1, an initial tensile load,  $T_0$ , is applied to the passive end of the conductor in a direction to generate the static deflection angle,  $\beta_P$ , while the other end of the conductor is kept restrained. In load step 2, the passive end of the conductor is restrained while the active end has its constraint replaced by a force condition. The tension load,  $T_0$ , is then applied to the active end so that the static sag angle,  $\beta_0$ , is achieved. During load steps 3 and 4, the tension load  $T_0$  is raised to the fatigue testing load  $T$ . On load step 5, the clamping force,  $F_C$ , is applied to the pilot node of the keeper. Along load steps 6 to 10, the vibration of the conductor is emulated by varying the direction of  $T$  by  $\pm\Delta\beta$  with respect to  $\beta_0$ . The value of  $\Delta\beta$  is determined such that the bending displacement  $Y_b$  is equal to the prescribed displacement applied to the conductor during the fatigue test.

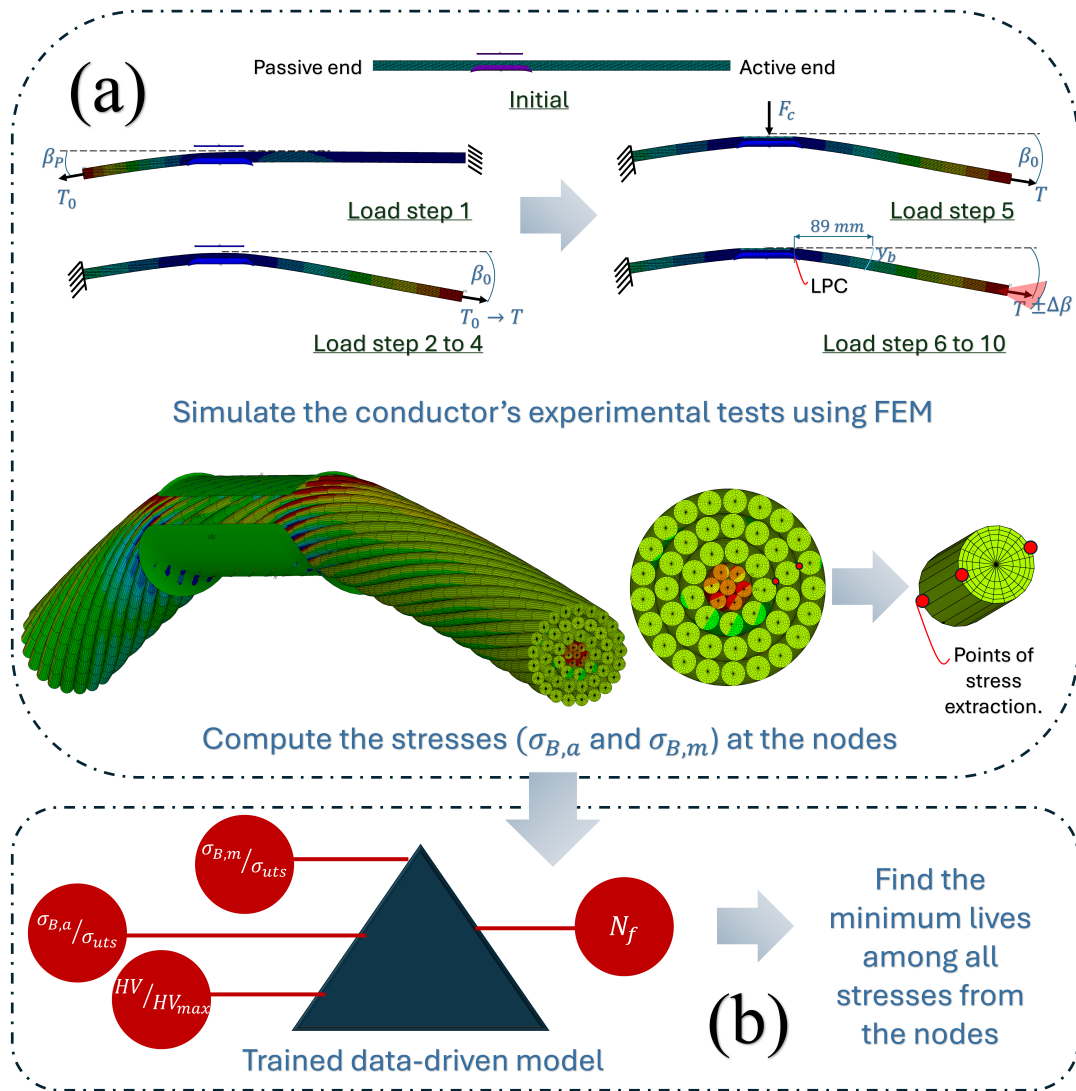


Figure 5.12. Flowchart illustrating all the modelling procedure.

After this procedure, a post-processing step is performed to gather the resultant stresses at the nodes, enabling their application in our model. For further details regarding this numerical modeling, refer to (LALONDE *et al.*, 2017; ROCHA *et al.*, 2022; ROCHA *et al.*, 2023). Considering the ANN\_Cable model, Eqs. 5.8, 5.9, and 5.10 have been employed to determine the fatigue lives at all critical wire contact points susceptible to fretting fatigue. These points were located within the penultimate and final layers of the numerical model representing each conductor. The predictions of the most critical lives (those with the fewest life cycles) are interpreted as the first, second, and so on, wire break life cycle as discussed in the next section.

## 5.4.4 Results and Discussions (Part III)

### 5.4.4.1 Overhead conductors' life estimation

The leading outcomes are presented in Fig. 5.13, which illustrates the results of the experimental versus estimated life predictions produced by the ANN model. The experimental data outlined in Tables 4 and 5 have been depicted in this figure. The ANN-based model successfully generalized its estimation capabilities to overhead conductors, including the AAAC 900 MCM made of AA6201, despite not being trained on data specifically involving this material and loading conditions, most of these data (94%) fall within the specified two-band width (87% for the ACSR TERN). This generalizability is similar to the observations made in the previous section for wire fatigue data. Notably, the model effectively incorporated hardness as an input parameter, enabling it to identify the material type with high accuracy even beyond the training dataset. Furthermore, the robust similitude approach which has been observed between the wire-based assessments and the numerical simulations involving the conductors made from these wires underscores the model's generalizability.

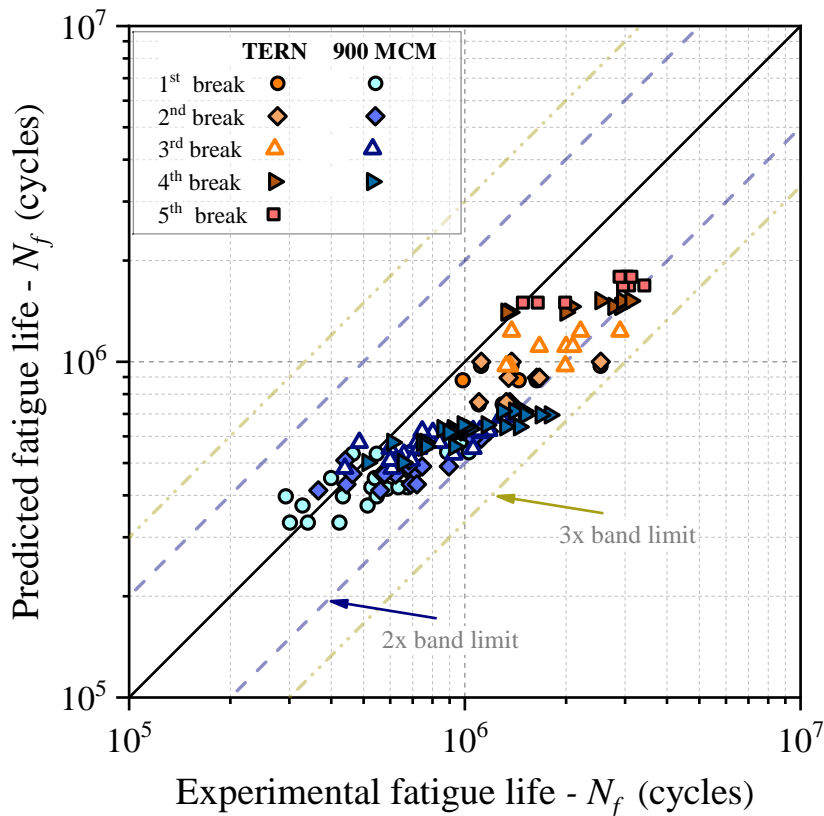


**Figure 5.13.** Estimated life vs. experimental one for overhead conductors' fatigue tests (AAAC900 and TERN), for all wire breaks considered. Estimates made using the ANN-Cable model.

**Table 5.16.** BMEF for the 1<sup>st</sup>, 2<sup>nd</sup> and 3<sup>rd</sup> break of both overhead conductors by considering the ANN\_Cable

Conductor	Break	BMEF
AAAC 900 MCM	1st	1.33
	2nd	1.43
	3rd	1.49
	4th	1.68
ACSR Tern	1st	1.65
	2nd	1.69
	3rd	1.70
	4th	1.61
	5th	1.57

As can be seen, the estimates are related to the number of wire breaks, specifically the fourth break for the AAAC 900 MCM and the fifth break for the ACSR TERN, as established in the literature for these specific overhead conductors. Overall, the model exhibited a conservative behavior for all wire breaks in both conductors. Table 6 provides a compilation of the BMEF values for all wire breaks number of cycles. The fatigue life error values are presented in ascending order, starting with the shortest and ending with the longest durations, encompassing the breaks determined by the model for each wire contact point. From a purely mechanical perspective, it is worth noting that following an initial wire failure, updated simulations incorporating the post-failure stress redistribution would be ideal for a more accurate numerical representation. However, it is important to emphasize that even without such refinements, the model produced satisfactory results for all failure scenarios across both materials, yielding BMEF values below the 2.0 band mean value. The presented results yielded fatigue life estimates closely aligned with those obtained by Rocha *et al.* (2022, 2023) using the Master Curve approach. However, it is noteworthy that the results of Rocha *et al.* exhibited a more non-conservative behavior for the AAAC 900 MCM conductor. It is also important to highlight that the models proposed authors were specifically designed to each material, whereas our study employs a single model for all materials.

It is interesting to note that the observed and predicted fatigue lives of the AA6201 conductor are notably shorter than those of the AA1350 conductor, despite the model being trained solely with AA1350 data. This observation aligns with the explanation presented by Rocha *et al.* (2022, 2023).

The surface plot in Fig. 5.14 illustrates that this model can expand and suggest safe

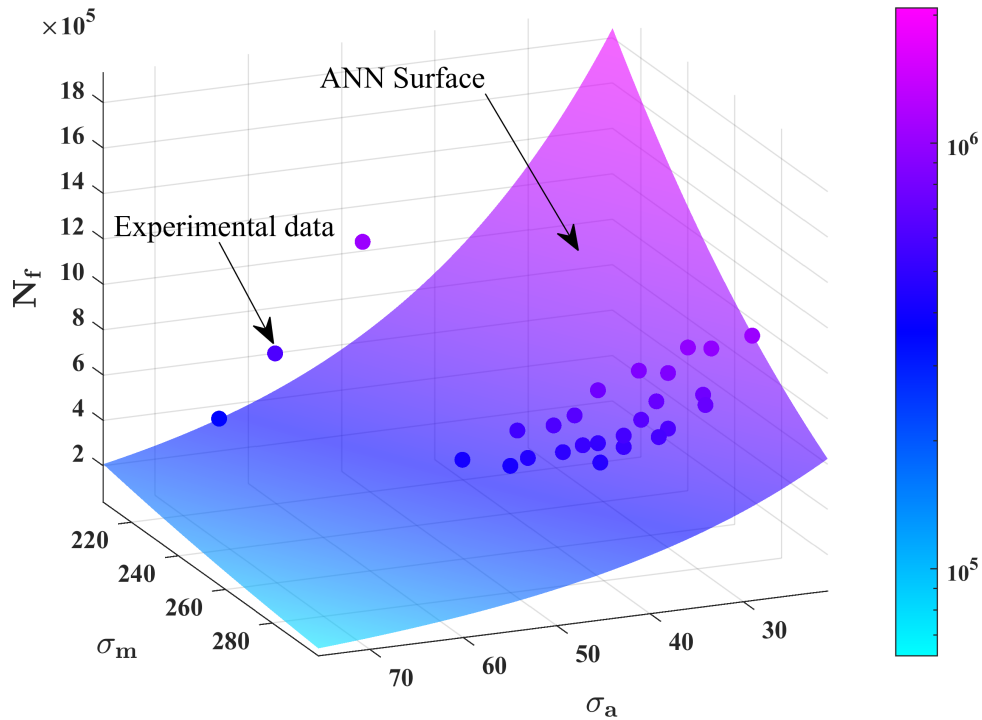


**Figure 5.14.** Fatigue life surface for the conductors with AA6201 alloy by using the ANN\_Cable. The experimental data provided in ref (BADIBANGA, 2017) for the AAAC 900 MCM conductor are also reported.

regions, depending on the desired fatigue life, based on the stress levels depicted in the model surface. As shown, this plot was generated for the AAAC 900 conductor, as it has the largest amount of experimental data, making it easier to visualize the dispersion relative to the model's predictions. The horizontal axes represent the values of  $\sigma_{B,m}$  and  $\sigma_{B,a}$ , while the vertical axis represents the material's fatigue life ( $N_f$ ). The model delineates the stress region with experimental data and also highlights other stress levels that can either increase or decrease the fatigue life.

#### 5.4.4.2 Location fracture prediction

This model is also capable to estimate the wires fatigue failure position. Figure 5.15 shows this an AAAC 900 MCM, including its three main layers. The crack initiation position is determined by using a damage life index, which is a parameter defined as the ratio of the logarithms of the minimum fatigue life for a certain load condition, to the fatigue life computed for each beam finite element. Higher values of such an index (the reddest points), which can vary from zero to one, correspond to the most likely position for failure. The blue zone in Fig. 5.15 depicts the observed failure positions according to the experimental data. It can be

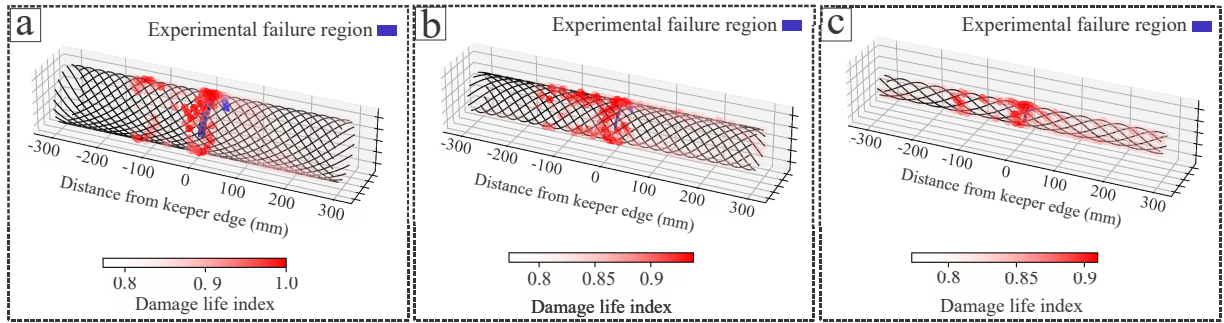


**Figure 5.15.** Segment of the cable with the most critical values of the Damage Life Index, highlighting the three layers from the outermost to the innermost in (a), (b), and (c), respectively. Data from the tests with Tension = 33.4 kN and  $Y_b = 0.84$ . The experimental failure regions are taken from Badibanga’s work (2017).

notice that the outer layers experience higher index values, while the inner ones show the lowest indexes. Thus, fatigue failure is expected to start at the outer layers.

To construct this figure, some considerations have been made. As shown in Fig. 5.12a, each beam element has two contact points where the model’s input parameters were calculated, representing the inner and outer stress points. For geometric visualization (based on the centroid locations of these elements) of these critical points relative to the fatigue lives, the most critical value between these two extraction points have been considered to be plotted.

## 5.5 PARTIAL CONCLUSIONS

This work highlights the potential of data-driven models in predicting the fatigue life of critical components, such as the case of overhead conductors, with implications for enhanced design and maintenance strategies in engineering applications. The partial conclusions are divided according to each specific Part and are presented below:

- (Part I) Even when exposed to loadings not encountered during training, such as variable shear loading amplitude, the ANN model was able to estimate fatigue lives within the 2-band range, even when applied in conjunction with all damage models, including Miner’s rule.
- (Part II) The ANN model approach has been successful in estimating the fretting fatigue life of wires, despite being trained with data entirely different from those tested in this study. This result further demonstrates the model’s potential for generalization across various loading conditions and materials. Additionally, it effectively handled the geo-

metric variations introduced by 3D wire geometries featuring elliptical contacts, which differ significantly from the training dataset. Furthermore, the utilization of the volume method in the critical distance approach for these wires did not adversely affect the model's performance, even though it was trained using the point method

- (Part III) This work demonstrates the effectiveness of a data-driven model trained with a limited dataset, but enriched with relevant mechanical parameters, to predict fretting fatigue life in overhead conductors. While the generalization potential of such models is well-established (see Chapter 4), this study is a pioneering effort in exploring this capability for overhead conductors. The key strengths of our model lie in its ability to handle diverse materials, loading conditions, geometries, and predict not only fatigue life but also critical failure locations.
  
- (Part III) The ANN demonstrated strong estimates capabilities for fretting fatigue life of wires, even for those made of different materials. This performance raised expectations for its ability to predict the fatigue life of the AAAC 900 MCM (made from the same materials the ANN model was tested). However, a more conservative prediction pattern was observed, which could be attributed to limitations of the finite element model in capturing the overall system behavior or the influence of unaccounted-for phenomena such as creep-induced stress relaxation in the conductor. Creep, which was not considered in the model, could potentially lower cable stress levels and consequently lead to longer fatigue lives.

## Chapter 6

# Extended load conditions - Experimental design

*"This chapter introduces novel non-conventional fretting fatigue tests inspired by the loading conditions experienced by an aircraft fuselage."*

Some parts of the text in this chapter was previously submitted in the following documents:

BRITO OLIVEIRA, Giorgio André; ALMEIDA, Gabriel Magalhães Juvenal; CARDOSO, Raphael Araújo; GARCIA, Miguel Angel; FREIRE JÚNIOR, Raimundo Carlos Silverio; ARAÚJO, José Alexander. Complex fretting fatigue tests and analysis with Al 7075-T651. **In process of submission.**

To ensure adherence to standard nomenclature, some symbols were adjusted from the original publication. Moreover, specific paragraphs were slightly modified to eliminate redundancy.

## 6.1 OVERVIEW

This final chapter of the thesis introduces another aspect that has yet to be fully explored: the experimental aspect. As demonstrated up to the preceding chapters, it was shown that data-driven models were capable of effectively handling a range of fretting fatigue cases without significant issues, showcasing the considerable generalization potential of our models across different loading scenarios, materials, and geometries. However, the complexities encountered in this stage exposed the weaknesses of our ANN-based approach, highlighting the need for combined modeling with other methodologies and even upgrades to the current approach.

As our analysis will reveal, even for materials well-known to the neural network, the loading conditions themselves can significantly increase the complexity of the analysis. Furthermore, the innovative aspect of the work compelled us to conduct a more in-depth analysis of the material's mechanical behavior under these conditions. Therefore, we will focus extensively on describing material failure, aiming to enhance readers' comprehension of an unconventional fretting fatigue test, although it is a highly representative when compared to real-world situations.

In this way, this chapter investigates novel fretting fatigue experiments inspired by the type of loading experienced by aircraft aluminum fuselages during flight. The tests were conducted under complex high and low cycle fatigue loadings with different waveforms and frequencies for the following loads: normal load ( $P$ ), tangential load ( $Q$ ), and bulk fatigue load. Failure analyses of the tests revealed consistent crack propagation behavior. Inclined cracks initiated near both contact edges. Their propagation towards the center of contact eventually led to the formation of a detached triangular-shaped body. Prior to failure, a mode I dominant crack perpendicular to the contact surface was observed in the tests. This last propagation stage was marked by extended time periods. Fatigue life predictions were carried out by combining finite element modeling with the use of theoretical (SWT and MWC) and Artificial Neural Network (ANN) models based on critical plane multiaxial fatigue approaches. The ANN and the MWCM models provided accurate life estimates considering the complexities involved in the problem investigated.

## 6.2 TEST DESIGN

### 6.2.1 Test specimens and machine apparatus

The contact configuration utilized in this study corresponds to the commonly referred to "cylindrical contact", wherein a cylindrical contact pad is pressed against a flat surface. As illustrated in Fig. 6.1, the specimens employed in the fretting fatigue tests adopt the flat dog-bone configuration. Both the specimens and the pads were fabricated using the same material: Al 7075-T651. Relevant mechanical and material properties of such alloy are outlined in Table 6.1 (PINTO, 2022; BRITO OLIVEIRA *et al.*, 2023a). Each specimen possesses a cross-section measuring  $13\text{ mm} \times 13\text{ mm}$ , while the pads have a radius of  $R = 70\text{ mm}$  (Fig. 6.1).

**Table 6.1.** Material and mechanical proprieties of the Al 7075-T651.

Properties	Value
Young's Modulus ( $E$ )	68 GPa
Poisson coefficient ( $\nu$ )	0.33
Yield stress ( $\sigma_y$ )	503 MPa
Ultimate tensile stress ( $\sigma_{ult}$ )	572 MPa
Friction coefficient ( $f$ )	0.85
Torsional fatigue limit ( $\tau_{-1}$ )	168 MPa
Axial fatigue limit ( $\sigma_{-1}$ )	204 MPa
Material critical distance ( $L/2$ )	$26\ \mu\text{m}$

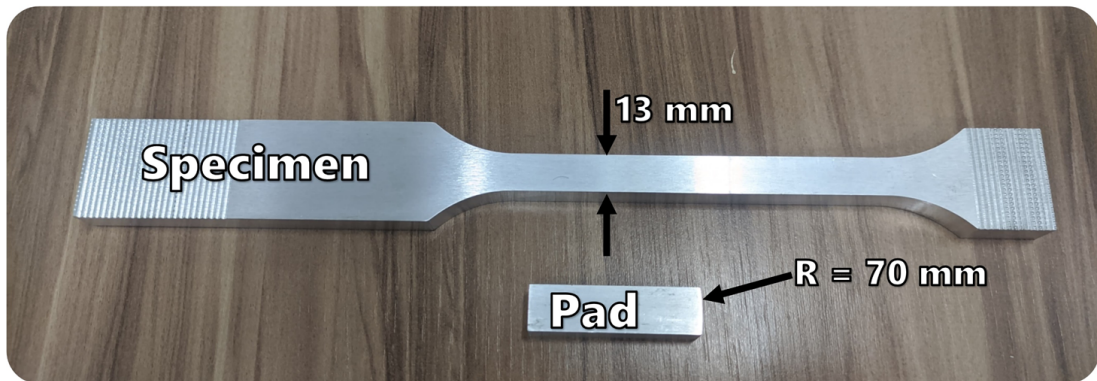


**Figure 6.1.** Specimen and pad for the fretting fatigue tests.

The experimental rig utilized in this study was the MTS 322 Test Frame located within the mechanical engineering laboratory at the University of Brasília (UnB). This fretting fatigue rig was recently customized to incorporate four uncoupled actuators and a heating system, allowing for independent control of all loads involved in the fretting tests (bulk, normal, and fretting loads) and to reach testing temperatures up to  $750^\circ\text{C}$  (ALMEIDA *et al.*, 2023). This

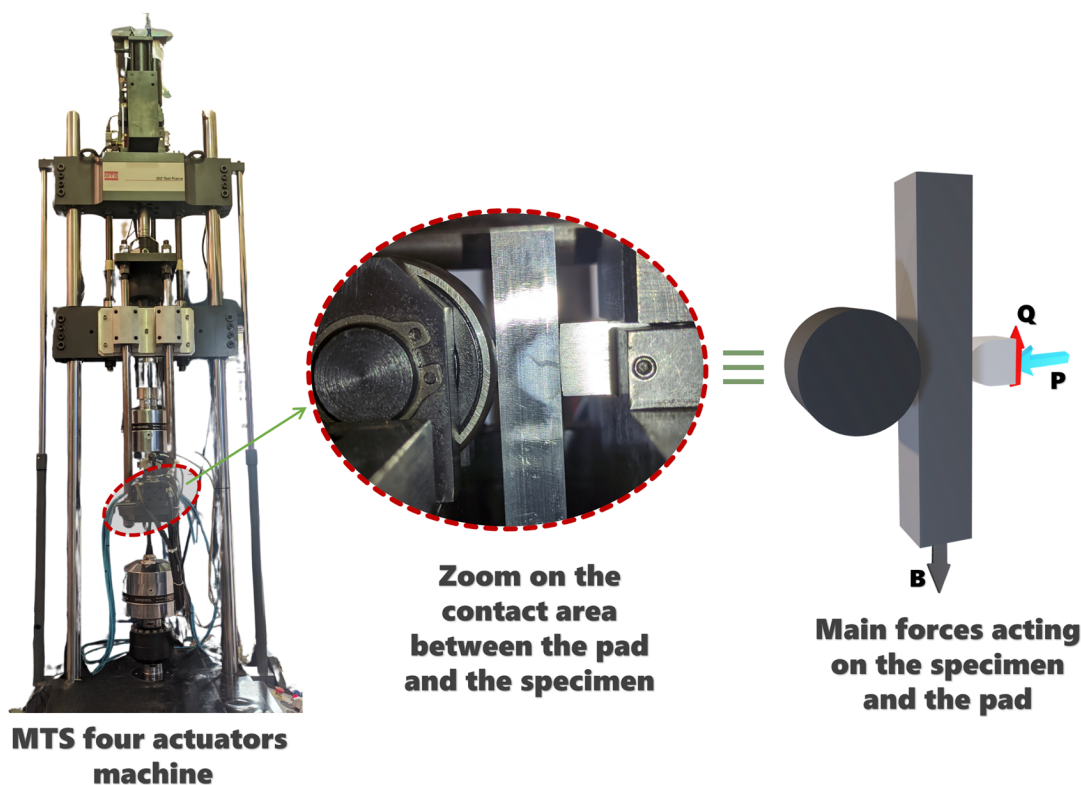


**Figure 6.2.** UnB's fretting fatigue rig test, zoomed view of contact region, and illustration of main forces acting on the test.

configuration enables load variations over time, whether in-phase or out-of-phase and facilitates synchronous or asynchronous application of load waveforms. Control of the tests was conducted by using the Basic Test-Ware and Multipurpose Elite software, both from MTS. Figure 6.2 depicts the UnB's fretting fatigue rig, shows the contact configuration and illustrates the main forces acting on the test. In this schematic representation, one can see at the bottom, a hydraulic actuator capable of applying loads up to 250 kN related to the bulk fatigue load ( $B$ ). The fretting apparatus is connected to another hydraulic actuator positioned at the upper section of the machinery, capable of applying fretting loads up to 100 kN. Additionally, the last two MTS hydraulic actuators are responsible for applying the normal load to the fretting pads. It is worth noticing that each actuator has its own LVTD, and force transducer. These actuators enable the exertion of contact pressure; in our setup, the pad is positioned on the right-side actuator and a bearing on the left-side actuator, as depicted in the zoomed-in portion of Fig. 6.2. The figure also highlights the three primary forces involved in these tests: the normal load ( $P$ ), the fretting load ( $Q$ ), and the bulk fatigue load ( $B$ ).

Prior to starting the fretting fatigue tests, it is important to note that the contact surfaces undergo cleaning with ethyl alcohol. Subsequently, the specimen is securely positioned within

the jaws of the testing machine. Furthermore, precise positioning of the pad is essential to align its sides with those of the specimen, while ensuring perpendicularity to establish a uniform pressure field. To verify the uniform distribution of load across the width of the specimen, Fujifilm pressure-sensitive paper was employed. Improper positioning may result in anomalous and accelerated crack initiation attributed to the edge effect phenomenon. Consequently, cracks may propagate from the contact edge (corner crack) towards the opposite and lateral sides of the specimen, following a diagonal path. Hence, utmost precautionary measures were undertaken to adhere to these procedures carefully.

### 6.2.2 Flight fretting fatigue tests

The experimental campaign conducted in this work deviate from conventional fretting fatigue tests, as our aim was to come closer to real-flight conditions. Consequently, the test configurations were set under variable amplitude loadings and encompassing both high-cycle (HCF) and low-cycle (LCF) fatigue regimes, simulating the condition experienced by aircrafts during service. In aircraft junction regions, two types of fretting damage occur in response to loading conditions during distinct flight phases (take-off, cruise, landing): one associated with changes in rotational speed during take-off and landing, inducing hoop stress and relative motion, and the other arising from high-frequency vibrational loads generated by aerodynamic forces during cruise, resulting in minor relative displacements at the contact interface of their components. Consequently, a loading scheme was conceived to replicate such conditions. A similar series of fretting fatigue test was proposed over 10 years ago by Araújo and Nowell 2009 to evaluate the behavior of Ti-6Al-4V, a titanium alloy commonly used in aeronautical applications, such as fan blades and discs of aircrafts. However, to date, no other author has ventured into analyzing such types of loading due mainly to the great complexity involved, as one will demonstrate later on. Another interesting finding in work (ARAÚJO; NOWELL, 2009) is that the authors discovered the primary effect on fatigue response in this loading conditions to be related to the intensity of the fretting load ( $Q$ ), while the normal ( $P$ ) and bulk fatigue ( $B$ ) loads have minimal influence. This information, along with some preliminary experiments, served as the basis for focusing on the effect of load  $Q$  in the present study.

### 6.2.3 Test configuration

The proposed fretting fatigue loading setup, inspired by the loading experienced by the aircraft fuselage during flight, is depicted in Fig. 6.3. Essentially, the loading pattern can be divided into three stages corresponding to take-off, cruise, and landing. During the aircraft ascent,  $P$  and  $B$  loadings were both simultaneously increased until they reach their respective maximum values, which is then maintained constant along the cruising altitude. Subsequently, the fretting load comes into effect, representing the aircraft vibrational forces experienced when cruising. Following 8000 fretting cycles, the landing phase starts, in which the fretting loading is set to zero, and  $P$  and  $B$  loadings gradually decrease. To prevent complete loss of the contact, the compressive force  $P$  (hence negative load values in Fig. 6.3) is maintained only up to a certain threshold, preserving contact between the pad and the specimen. This entire process is considered as one loading block. In order to apply such complex loading conditions, specific programming of the UnB four actuators fretting rig is necessary by using the MTS Multipurpose Elite program software. At the conclusion of the test, the number of blocks the specimen endured and the respective fatigue life in terms of fretting loading cycles ( $N_{f,Q}$ ) is determined. As the reader may discern, a mixture of LCF and HCF regimes is observed in the testing configuration investigated.

### 6.2.4 Fretting machine programming

In order to apply these loading conditions, specific programming of the MTS machine is necessary using the Multipurpose Elite program software. Thus, it is configured for the left lateral actuator to be in displacement control = 0 (initially, we tested using force control, but this caused a considerable bending effect, which led us to switch to displacement control), where the bearing is positioned (see Fig. 6.2). The right lateral actuator, on the other hand, is set to force control, starting at -1 kN and ramping up over 10 seconds to the maximum value. This occurs simultaneously with the increase in the bulk fatigue force,  $B$ , which ramps up to 33.8 kN, equivalent to a stress of 200 MPa in the specimen; this actuator also remains in force control. For experiments with  $P = -10$  kN, the actuator applying compressive loading remains in force control at -10 kN for 800 seconds during the fretting cycle, considering a frequency  $\omega = 10$  Hz. Throughout the fretting cycle, the actuator responsible for the shear

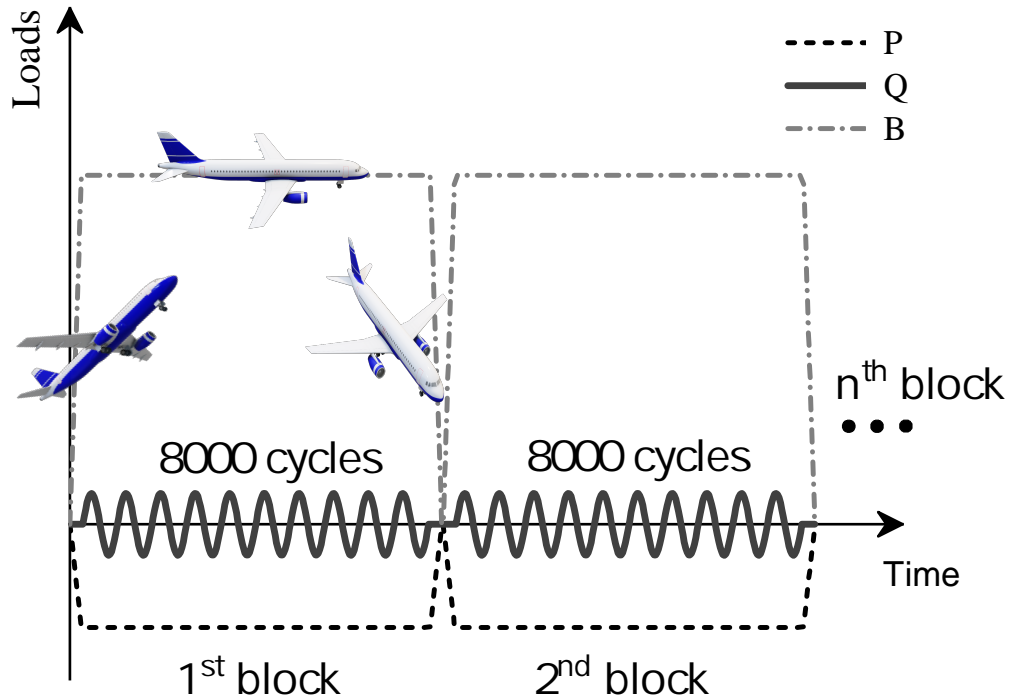


**Figure 6.3.** Schematic of the load history investigated

load remains in force control, such that when the cycles conclude, the fretting actuator is set at 0 kN. Subsequently, the right lateral actuator discharges to -1 kN, while simultaneously, the bulk fatigue load actuator also gradually decreases its intensity, both under force control throughout. This simultaneously occurs over a ramp period of 10 seconds.

Figure 6.4 depicts a schematic of the programming established using block language via the Multipurpose Elite program. Initially, the four channels responsible for controlling the four actuators are activated. Subsequently, a loop condition is established, ensuring that cycles are continuously repeated as long as the condition is met. Within the loop process, the first command frame (Apply bulk fatigue and normal loads) is configured to control three actuators: the left and right lateral actuators, and the bulk fatigue load actuator. The left actuator is set to displacement control, already positioned in contact with the specimen. The right actuator is programmed to execute a ramp waveform over 10 seconds, increasing its force from 1 kN to the established maximum value (5 or 10 kN). Subsequently, the waveform is set to "hold" to maintain this maximum force for the specified time, 800 seconds ( $\approx 13$  minutes) for  $\omega = 10$  Hz and 500 seconds ( $\approx 8$  minutes) for  $\omega = 16$  Hz. For the right lateral actuator, the next step is to reset the waveform to ramp mode to decrease its force to 1 kN. A similar process is prescribed for the bulk fatigue load actuator, with the distinction that it applies a fatigue tensile load

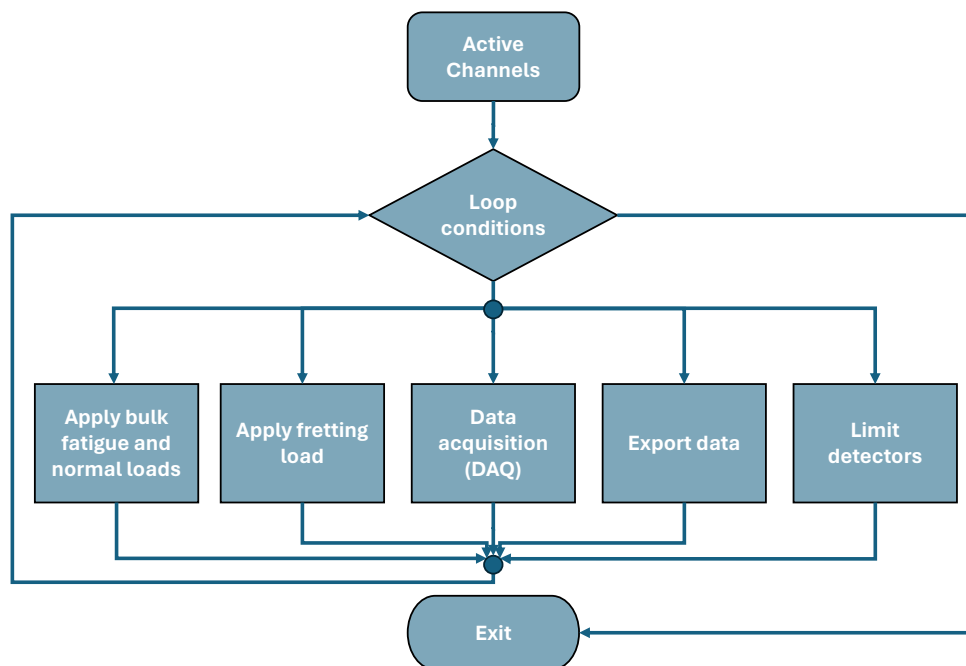


**Figure 6.4.** Schematic of the programming established using block language via the Multipurpose Elite program.

ranging from 0 kN to 33.8 kN.

For the second command frame (Applying fretting load), the actuator responsible for applying the fretting load is configured. Initially, it is set to maintain force control for the first 10 seconds. Subsequently, we activate the desired frequency at which the loading will be imposed (10 Hz or 16 Hz), specify the number of cycles (8000 cycles), and set the Absolute end levels, i.e., the maximum and minimum values to be applied in the shear load. Following this, it remains in force control for an additional 20 seconds, corresponding to the descent and re-rise of the  $P$  and  $B$  force levels, initiating a new loading block.

The third frame is responsible for data acquisition, where we set all the values we want to be saved. These include the displacements and forces applied to all actuators, cycle counters, and test time. The fourth frame is related to saving this data, i.e., exporting it to DAT files. Each time the loop is performed, a new file is saved. The last frame is related to detectors, used to identify when the specimen has fractured or if the test has failed, such as due to slippage. Limits for force and displacement are set to ensure safe operation, and all necessary data acquisition is fulfilled. Once the detectors are triggered and the specimen fractures, the loop is terminated, and the test process is concluded.

## 6.3 EXPERIMENTAL RESULTS AND INVESTIGATION

### 6.3.1 Experimental campaign

The present experimental campaign consists in eleven tests carried out under the aforementioned conditions. In Table 6.2 below, the primary experimental values of the applied loads in the test (loads  $Q$ ,  $P$ , and  $B$ ), along with the corresponding lives under LCF ( $N_{f,B}$ ) and HCF ( $N_{f,Q}$ ), and the frequency ( $\omega$ ) adopted for each test, are presented. Test frequencies were either 10 Hz or 16 Hz. It has been noted that even slight variations in  $Q$  were capable of significantly altering the life of the specimens, hence, the majority of experiments focused on examining the influence of the load  $Q$  on fretting fatigue life under the investigated loading setup.

**Table 6.2.** Experimental loading parameters and fatigue lives.

TEST ID	$Q$ (kN)	$P$ (kN)	$Q/P$	$B$ (kN)	$N_{f,B}$ (cycles)	$N_{f,Q}$ (cycles)	$\omega$ (Hz)
T01	3	10	0.3	33.8	85	6.80E+05	10
T02	3	10	0.3	33.8	69	5.52E+05	10
T03	2.25	10	0.225	33.8	166	1.33E+06	16
T04	2.25	10	0.225	33.8	340	2.72E+06	16
T05	2.25	10	0.225	33.8	393	3.14E+06	16
T06	1.875	10	0.1875	33.8	536	4.29E+06	10
T07	1.875	10	0.1875	33.8	539	4.31E+06	16
T08	1.5	10	0.15	33.8	1031	8.25E+06	10
T09	2.25	5	0.45	33.8	183	1.46E+06	10
T10	2.25	5	0.45	33.8	415	3.32E+06	10
T11	1.875	5	0.375	33.8	1250	1.00E+07	10

For the loading configuration with  $P = 10$  kN, the maximum analytically obtained values for the contact semi-width and peak pressure were 1.34 mm and 365 MPa, and for the condition with  $P = 5$  kN, 0.94 mm and 258 MPa, respectively. It is noteworthy that the use of different frequencies during the test had no impact on the fatigue life (T06 and T07). Figure 6.5 illustrates the fatigue life ( $N_{f,Q}$ ) variation with the fretting/shear load amplitude for both,  $P = 10$  kN and  $P = 5$  kN. As depicted, a strong correlation is evident in the data for  $P = 10$  kN, indicating that the increase in fatigue life is related to the reduction in shear loading ( $Q$ ). Consequently, minimal scattering was observed under these loading conditions. To perform a comparative analysis, we reproduced some of the tests from Table 4.8, conducted on the same material in classic fretting fatigue experiments. As observed, even with much less severe loading, the fatigue life in these tests was significantly shorter, indicating that the influence of this

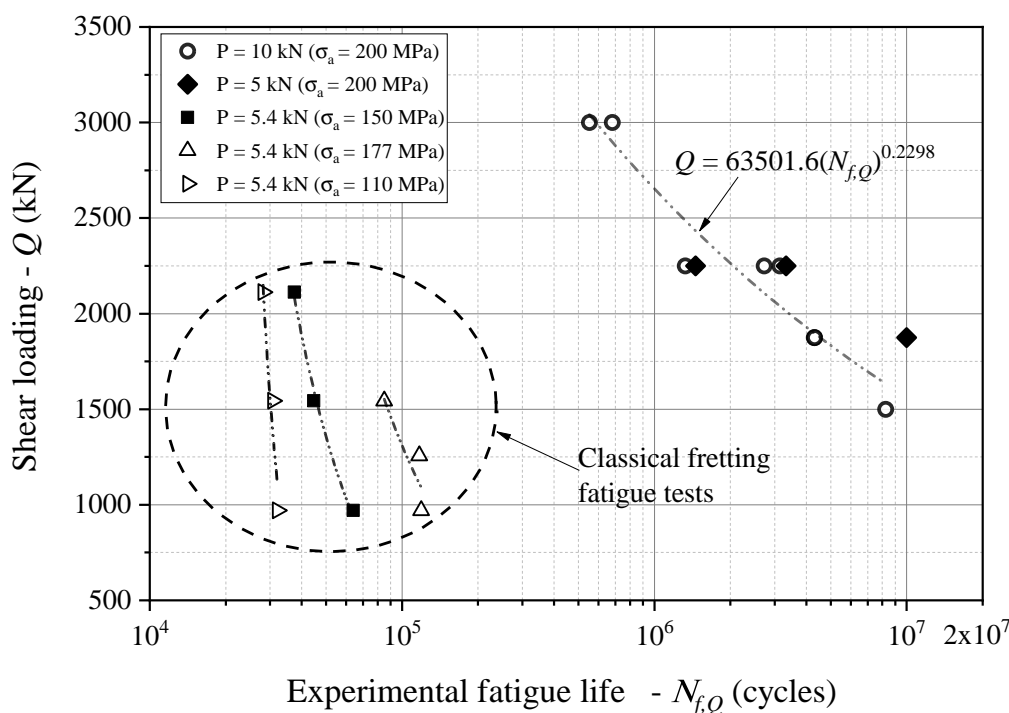


**Figure 6.5.** Shear loading amplitude for  $P = 10$  kN and  $P = 5$  kN vs. experimental fatigue life for the 7075-T651 specimens.

new loading condition contributed to longer fatigue life.

### 6.3.2 Cracks during tests

Figures 6.6, 6.7, and 6.8 depict photographs captured during the execution of these experiments. Figure 6.6 highlights crack propagation on both specimen laterals, where inclined cracks emerge around the contact edges and grow to meet near to the contact center line on the specimen. In Fig. 6.7, a temporal evolution is shown to observe crack behavior over time. Initially, on the second day of testing, we observe prominent cracks emerging from the trailing edge contact and another in the early stage emerging from the leading edge. A day later, a photograph taken in the same location revealed that the smaller crack had grown sufficiently to merge with the first one nucleated at the trailing edge, creating a triangular crack pattern that detached part of the specimen beneath the contact and gave rise to a triangular body in the experiment itself. It is noteworthy that such behaviors were not unique but rather observed in the majority of the conducted tests.

Figure 6.8 showcases photographs of several specimens exhibiting this triangular crack pat-

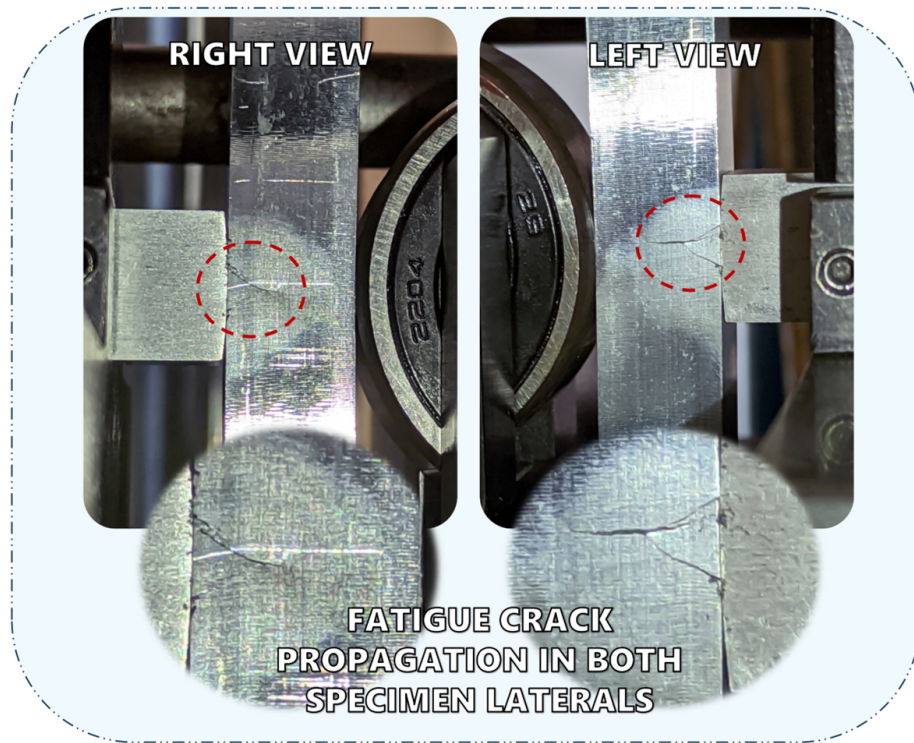


**Figure 6.6.** Crack propagation highlighted on both specimen side views revealing a distinctive triangular pattern on test T08.

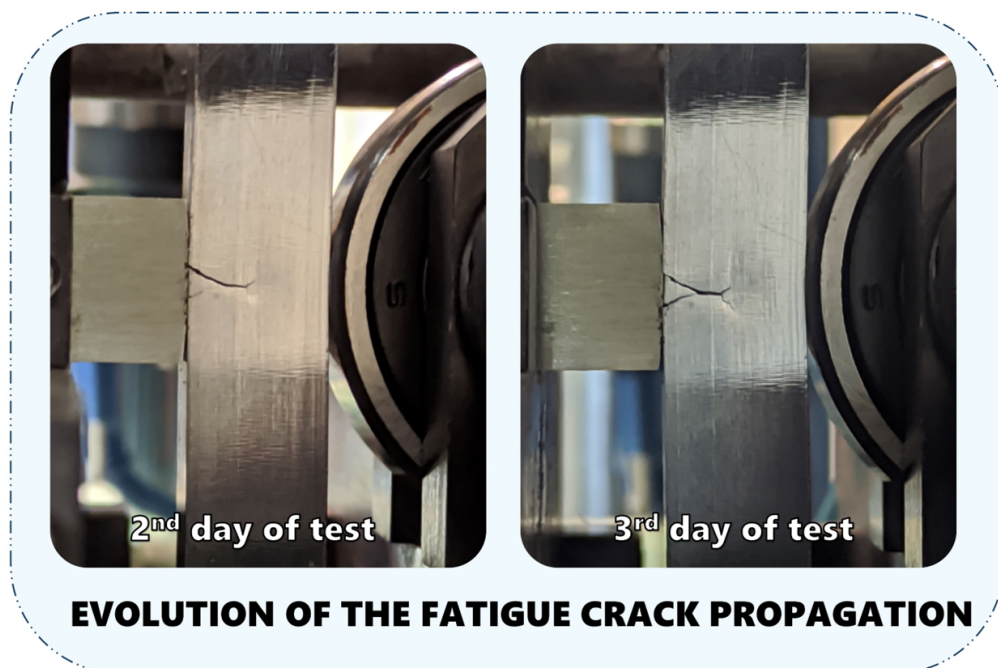


**Figure 6.7.** Highlighting the evolution of crack propagation pattern over time of test T05.

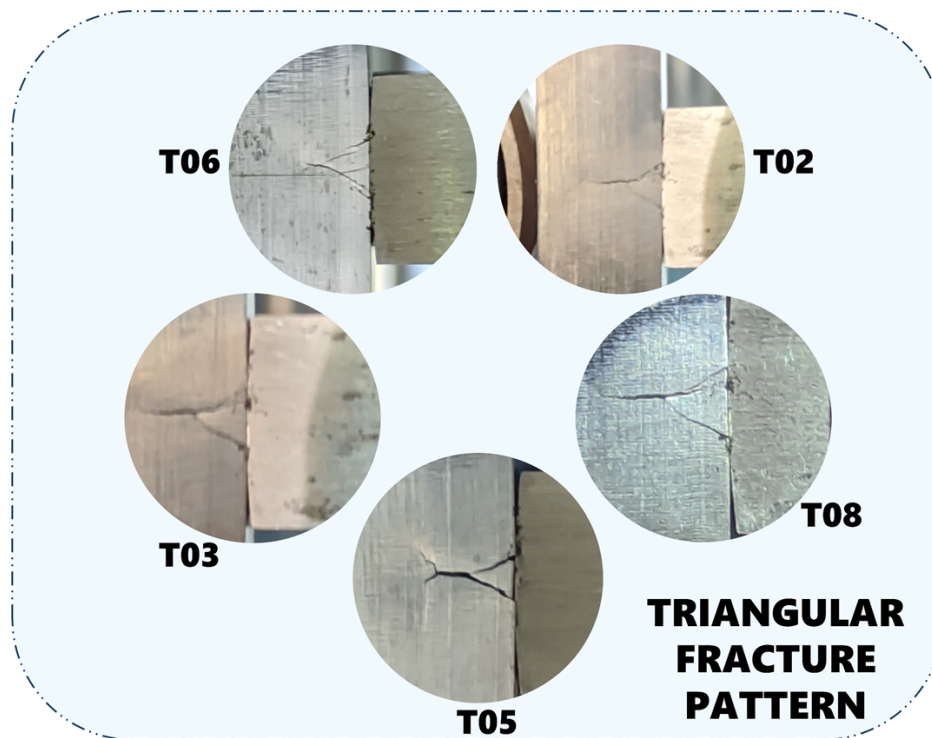


**Figure 6.8.** Triangular pattern of crack propagation observed across selected specimens.

tern, the cracks tend to align themselves with the center of the pad (midpoint of the contact) and propagate together until they reach approximately the mid-thickness of the test specimen, which then progresses to final fracture. Thus, a discussion arises concerning these experimental results, regarding the significant difference in mechanical behavior between classically performed fretting fatigue tests in laboratories and the ones conducted in this work. In classical tests, such behavior has been not observed, and when a small crack has been detected, it has been expected that the specimen would soon fracture. However, the behavior of these new experiments diverges considerably from this expectation, as even with cracks observed near the midpoint of the specimen, such specimens still endured a considerable amount of time before final fracture.

### 6.3.3 Post-failure analysis

Figure 6.9 illustrates the components under analysis after the complete fracture of the specimen. In it, the detached triangular fracture pattern can be observed, a phenomenon that occurred in some specimens, while in others, the triangle body resulting from the merging of the two main cracks did not detach from the specimen. Additionally, wear on the pad can be observed, along with the macroscopic fracture region, with emphasis on the crack propagation

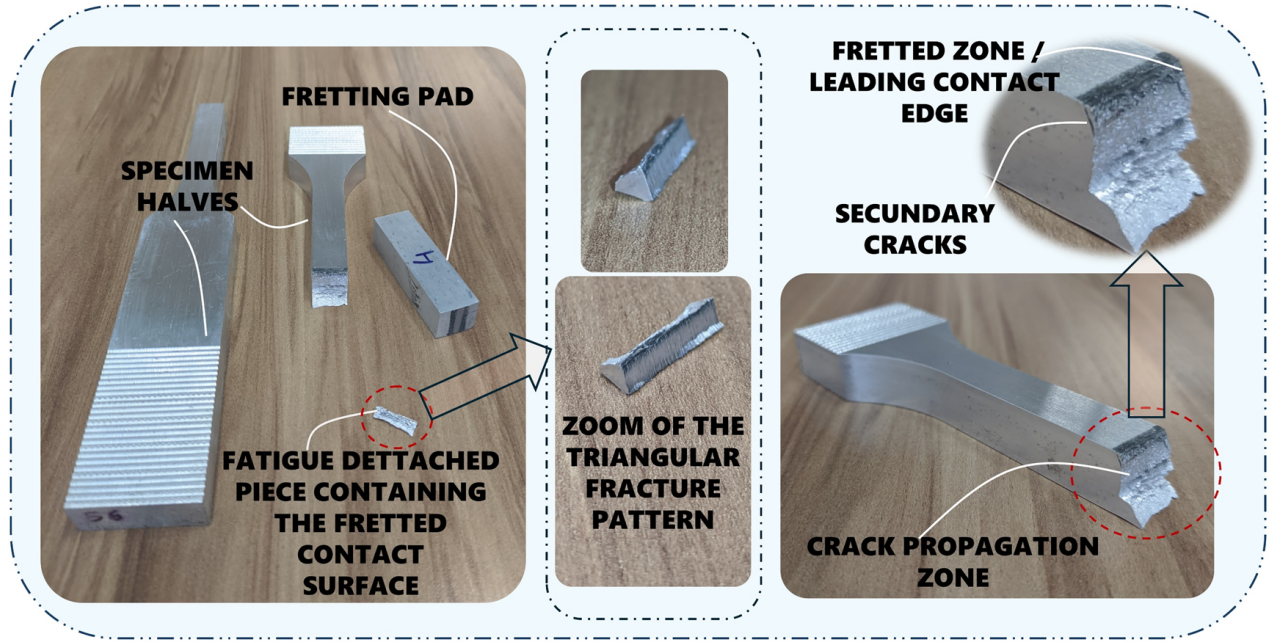


**Figure 6.9.** Post-failure analysis, featuring both parts of the fractured specimen, the fretting pad, and the fatigue-detached triangular piece. Macroscopic details of the fracture are also depicted.

zone. Secondary cracks near the fretted region in the slip zone are also visible.

### 6.3.3.1 Confocal and SEM analysis

More specific analyses were performed with a confocal laser and scanning electron microscope (SEM). In Fig. 6.10, photos and its respective observations under confocal laser microscope of T06 are shown, highlighting the lateral face of the sliced fractured specimen for analysis, with the appearance of the crack originating from both the trailing edge and the leading edge of the contact (crack initial angle of  $33^\circ$ ). Secondary cracks are clearly visible. This figure also emphasizes the fractured slice of the specimen, viewed from the front, from the perspective of the contact, where it is possible to visualize the fretted region at the slip zone and to estimate the value of the stick zone size ( $2c$ ). This value aligns with analytical predictions, where the maximum size of  $c$  can be computed from the following equation:

$$c = a \sqrt{1 - \frac{Q}{fP}} = \sqrt{\frac{8PR(1 - \nu^2)}{\pi E} \left(1 - \frac{Q}{fP}\right)} \quad (6.1)$$

where  $a$  is the contact half-size, which is given in terms of the force  $P$ , the radius of the pad,  $R$ , the Poisson's ratio  $\nu$ , and the modulus of elasticity,  $E$ . Based on the values of  $Q$  and  $P$  for the test T06, as the ones provided in Table 1, and considering that the pad has a radius of 70

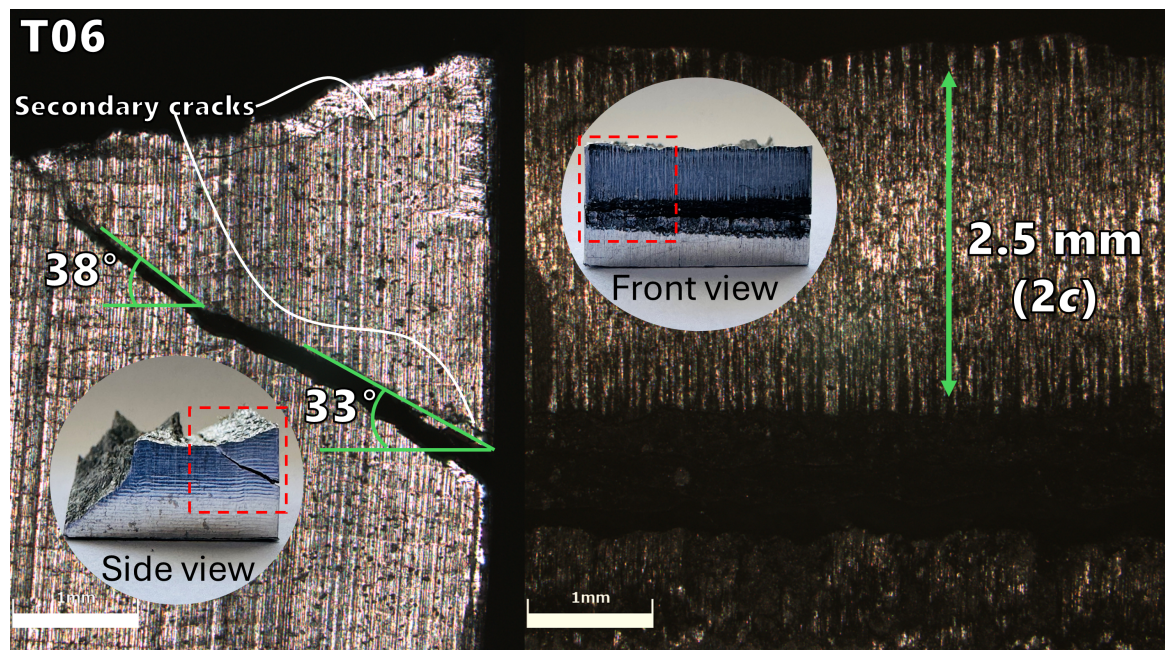


**Figure 6.10.** Confocal laser microscopic images showing the cracked specimen T06, highlighting the crack initiation angles, secondary cracks, and the fretted region.

mm, the size of  $2c$  is calculated to be 2.37 mm, which is reasonably close to the experimental measurement of 2.5 mm.

In the confocal analysis shown in Fig. 6.11, the angles and triangle heights of various specimens are highlighted, and these values are presented in Table 6.3. It is notable that the crack emerging at angle  $\beta_2$  is the most prominent, to the extent that in some cases, it grows to the point of fracturing the specimen before meeting the crack initiated under angle  $\beta_1$ . In Fig. 10, with the growth of the crack, the angle  $\beta_2$  located near the trailing edge tends towards 90 degrees, meaning it approaches the characteristic angle of mode I failure. On the other hand, the angle  $\beta_1$ , approximately from halfway up the triangle's height ( $h_t$ ), exhibits a decreasing pattern, causing the crack to direct itself towards the main crack. This results in the distorted pattern at the head of the triangle, where, in many cases, fusion of the cracks occurred. Additionally, it is interesting to observe that the heights of these triangles are very close, suggesting a proportional relationship to the loading  $P$  across the analyzed specimens (same value used). Another noteworthy observation is that, regardless of the intensity of loading  $Q$ , the average angles values are quite similar at approximately 64 degrees.

In an alternative approach to measuring these angles, internal measurements within the contact region were taken instead of just at the ends (Fig. 6.11), as demonstrated in Fig. 6.12.

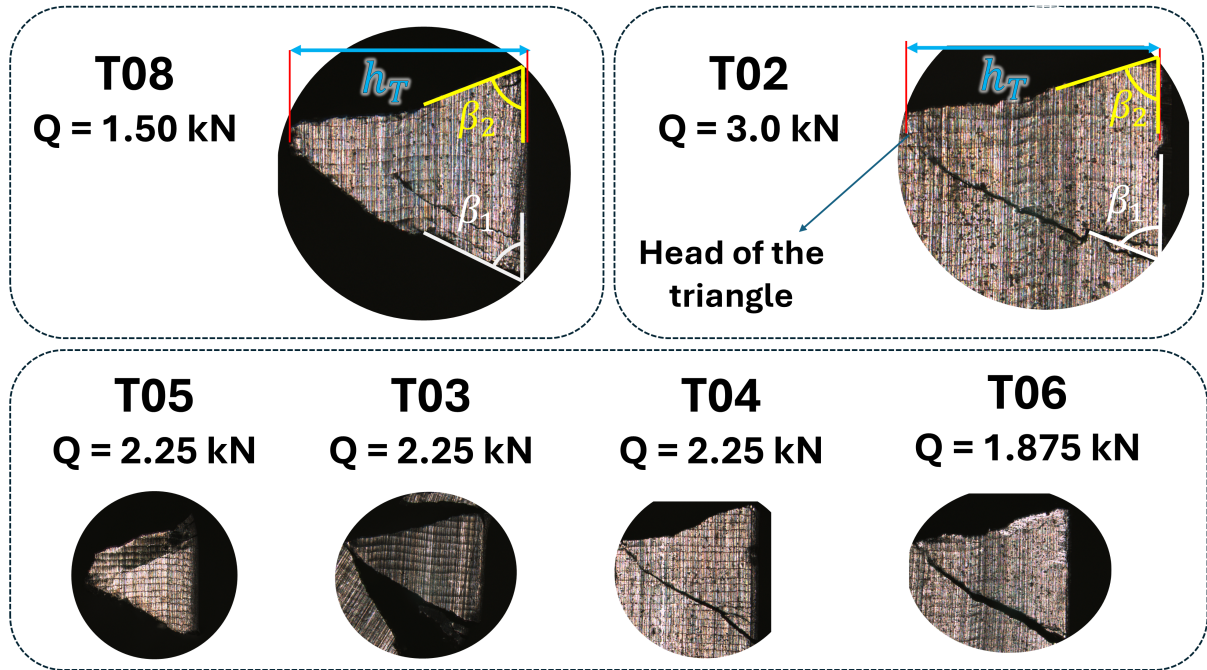


**Figure 6.11.** Highlighted confocal images of the fracture of T06, in lateral and frontal views.

**Table 6.3.** Dimensions of the heights of the triangles, the angles  $\beta_1$  and  $\beta_2$ , and their mean value.

TEST ID	$h_t$ (mm)	Crack angle $\beta_1$ (°)	Crack angle $\beta_2$ (°)	Mean crack angle $\beta$ (°)
T02	3.4	68	72	70
T03	3.6	61	67	64
T04	3.4	53	75	64
T05	3.2	57	62	59
T06	3.6	57	74	65
T08	3.6	63	65	64

The figure displays the fractured surface of specimen T06, illustrating the boundary between the crack propagation region and the fast fracture region. Using the confocal microscope, five angle measurements were conducted along the crack propagation region, and consistently, these measurements remained around 64 degrees, as anticipated. Similar measurements conducted on the other test specimens also exhibited this behavior, as reported in Table 6.4. Furthermore, with the assistance of scanning electron microscopy (SEM), a 1000x magnification of the fracture region revealed the presence of dimples, a characteristic of fracture commonly observed in such rapid fracture zones.

Figures 6.13, and 6.14 depict observations obtained via SEM for various test specimens. In Fig. 6.13, the observation of T02 is presented, showing an inclined top-view perspective highlighting the contact region with a view of the slip zone and secondary cracks. Additionally,

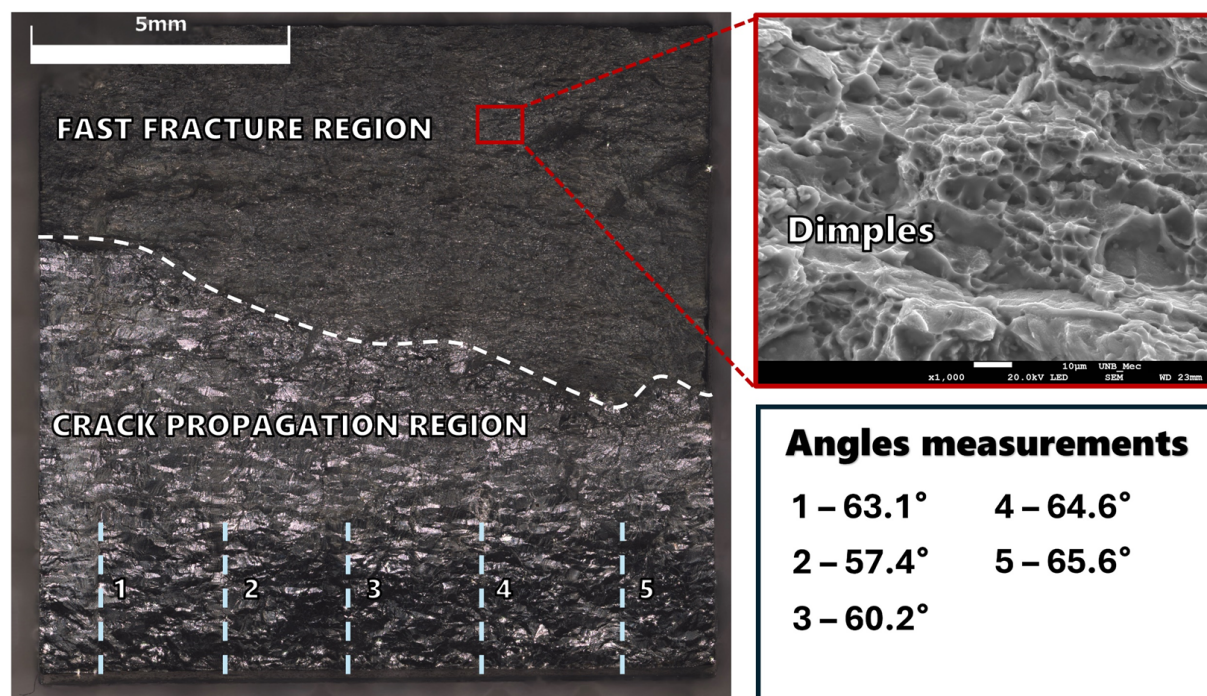


**Figure 6.12.** Fractography of the specimen T06 from a top-view perspective using confocal microscopy.

**Table 6.4.** Measurements of angles for other specimens.

TEST ID	Measurements					Mean Angle
	1	2	3	4	5	
T02	74.8	71.6	72.1	73.2	69.4	72.2
T03	66.7	65.7	55.7	62.4	64.4	63.0
T04	62.7	61.1	58.1	58.4	59.8	60.0
T06	63.1	57.4	60.2	64.6	65.6	62.2
T08	54.9	57.2	54.8	58.3	59.8	57.0

the three-dimensional position of the  $\beta_1$  measurement is emphasized. In Fig. 6.14a, the fast fracture region of T03 reveals the characteristic abrupt change in crack direction during the rapid fracture process, which is observed in almost all specimens. Fig. 6.14b displays the triangular cylindrical piece detached from T05, showing both propagation regions and secondary cracks. Further, Fig. 6.14c, 6.14d, 6.14e, and 6.14f exhibit potential crack initiation zones in T06, near one of the corners where contact with the pad has been established. Notably, at approximately 400x magnification, beach marks in this region are discernible. In Fig. 6.14f, the size of these 'waves' in the region has been measured, with dimensions on the order of 5 microns.

The analysis presented in Fig. 6.15 effectively distinguishes the slip zone from the stick zone using an energy dispersive spectroscopy (EDS) mapping technique on specimen T04. In Fig.

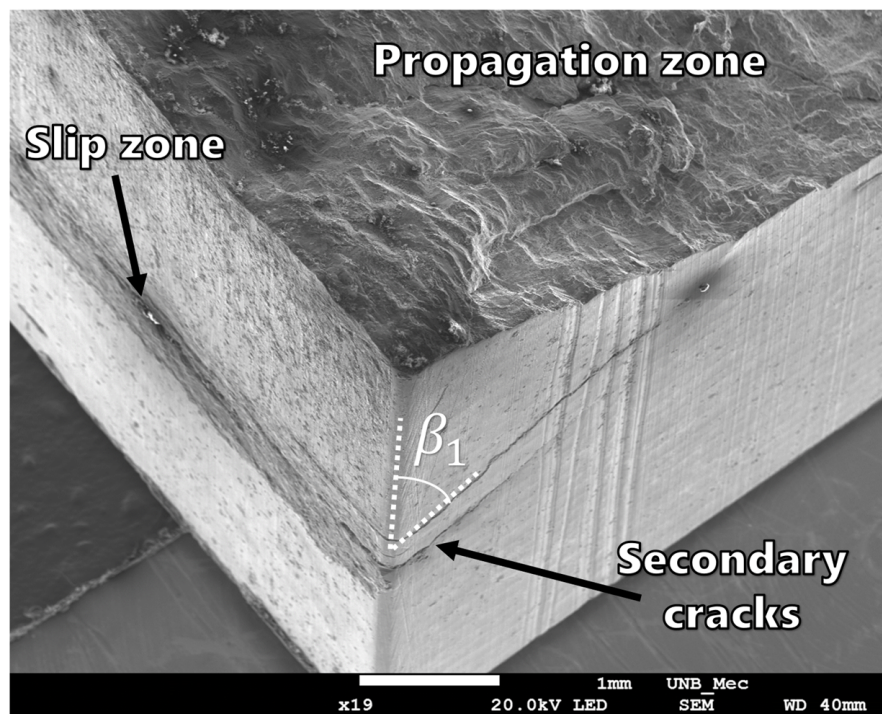


**Figure 6.13.** SEM observations of the test specimen T02 at the inclined top view near contact.

6.15(a), both zones' locations are identified by quantifying Aluminum and Oxygen individually using EDS. The slip region, where material wear is typically observed, is expected to contain a significant amount of aluminum oxide, whereas the stick zone will not (GARCIA *et al.*, 2024). As expected, a small amount of oxide is observed in the stick region (5%), while a high amount (72%) is present in the slip region. Figure 6.15b displays the color-coded result of this mapping, depicting the surface distribution of the main chemical elements, Oxygen and Aluminum. This analysis clarifies that the fretting cracks originate within the slip zone.

## 6.4 ANALYTICAL AND NUMERICAL FRAMEWORKS

This section provides an overview of the methodologies employed for fatigue life prediction. It is worthy to note that the analysis pertains to an atypical loading regime characterized by variable amplitude loading effects. Consequently, the Miner's damage rule has been selected as the method of choice to quantify the cumulative damage within a load block and extrapolate it to determine the fretting fatigue total life. Two approaches are tested: one based on classical multiaxial fatigue models and the other utilizing data-driven methodology. All loading conditions are numerically simulated using the Finite Element Method (FEM) to assess the stress-state. It is noteworthy that critical plane approaches are adopted in both classical fati-

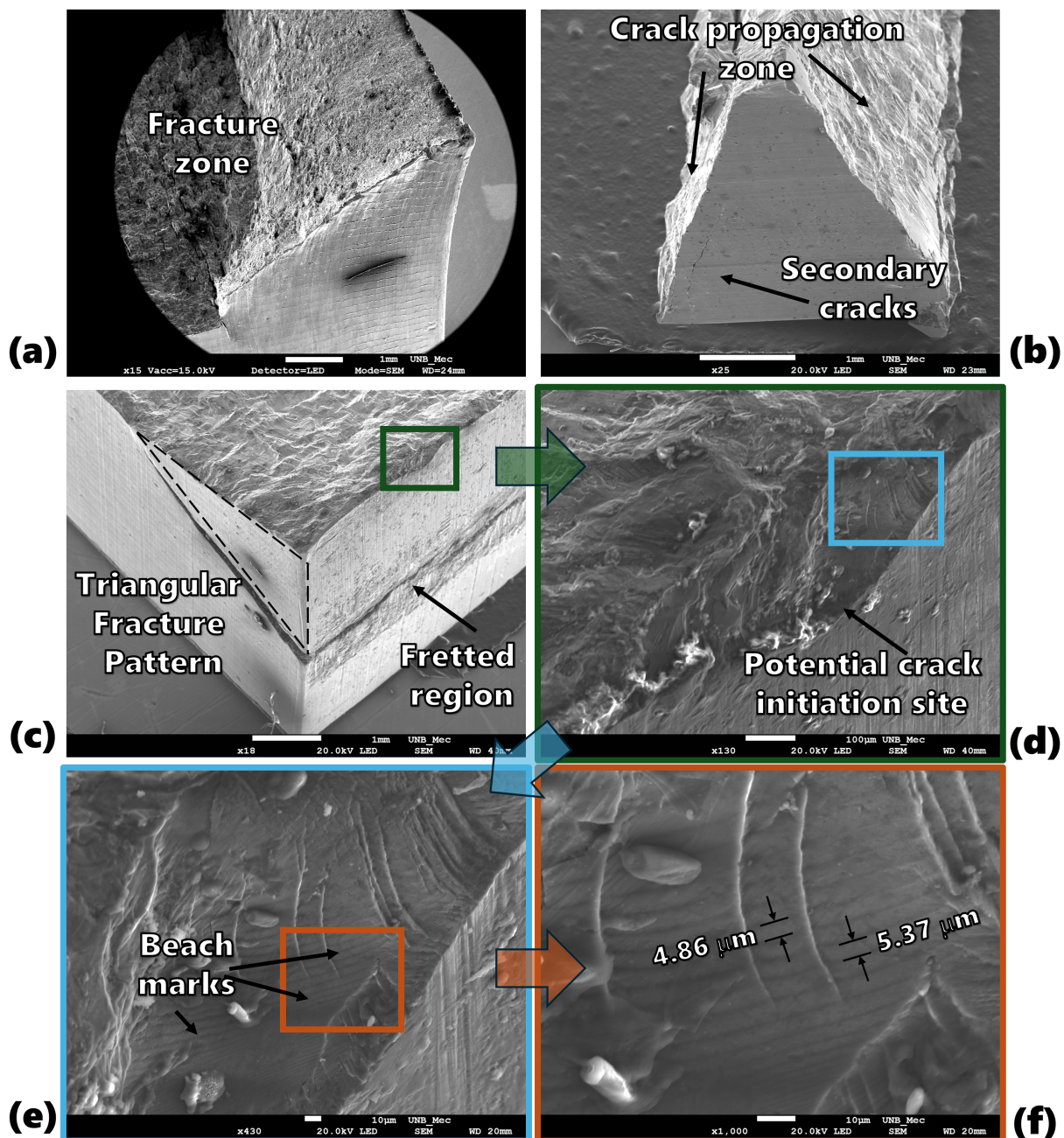


**Figure 6.14.** SEM observations of the test specimens: (a) T03 (fast fracture surface), (b) T05 (triangular detached fretted piece), (c) T06 (inclined top view), (d) T06 (130x magnification), (e) T06 (430x magnification), and (f) T06 (1000x magnification).

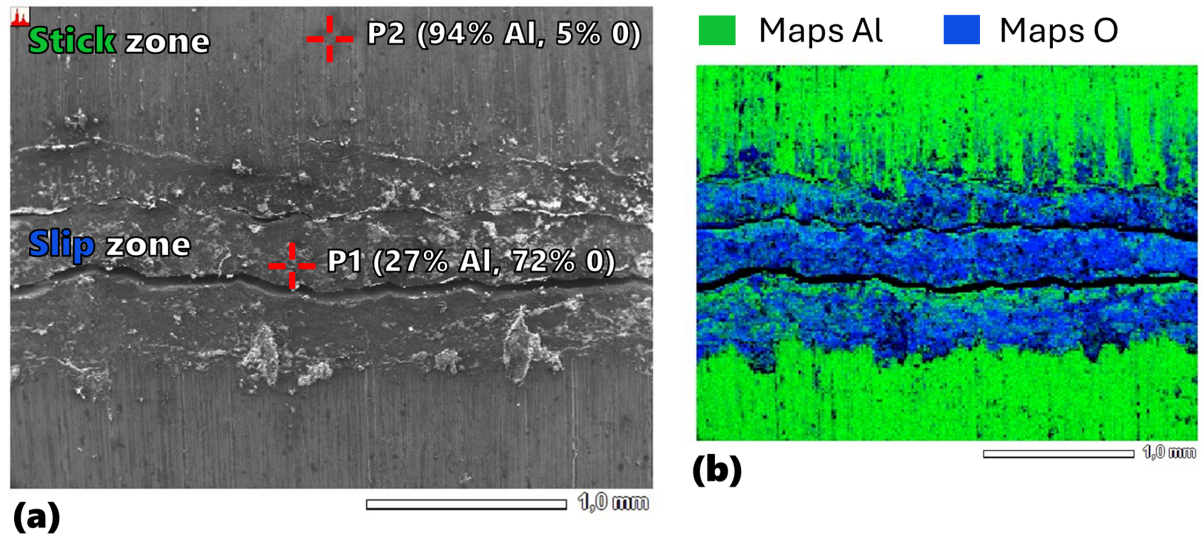


**Figure 6.15.** Mapping using EDS, highlighting the quantity of aluminum and oxygen present at specific points (a) and across the entire analyzed surface (b) of the contact of specimen T04.

gauge models and the machine learning model. Furthermore, it is emphasized that a non-local approach is also applicable in such analyses involving fretting fatigue. Thus, stress extraction has been conducted based on the theory of critical distances (TCD) using the point method (MEN *et al.*, 2024; BRITO OLIVEIRA *et al.*, 2023a; BARBOSA *et al.*, 2020), widely employed in fretting problems (WANG *et al.*, 2022a; ROSSINO *et al.*, 2009; DOCA *et al.*, 2022; HOJJATI-TALEMI; WAHAB, 2013; OLIVEIRA *et al.*, 2024).

#### 6.4.1 Multiaxial fatigue models calibration

The first approach employed involves classical multiaxial fatigue models. Two models were selected: the Modified Wohler Curve Method (MWCM), based on shear stress effects, and the Smith, Watson, and Topper (SWT) model, which considers normal stress effects (see Chapter 2, section 2.1.3). Both models rely on critical plane concepts. These models have been extensively utilized in the fretting fatigue literature (ZOU *et al.*, 2023; ARAÚJO *et al.*, 2008; FOUVRY *et al.*, 2014; BHATTI *et al.*, 2019; MORENO-RUBIO *et al.*, 2023; INFANTE-GARCÍA *et al.*, 2022; SUSMEL, 2022). To apply these models, a calibration process using plain and/or torsional fatigue data for the specific material under study is necessary (Al 7075-T651). Axial and torsional fatigue data have been collected (PINTO, 2022), such that Wöhler curves were established for at least two load conditions to fulfill the calibration requirements of the MWCM model, as illustrated in Fig. 6.15a. As observed, the torsional ( $\tau_{-1}$ ) and axial ( $\sigma_{-1}$ ) fatigue

limits for this material are 168 and 204 MPa, respectively.

It is important to highlight that the application of the MWCM for high values of  $\rho$  results in conservative outcomes (SUSMEL, 2008). Therefore, the validity of the MWCM formulation persists as long as  $\rho$  remains below a critical threshold  $\rho_{\text{crit}}$ , which is mathematically represented as follows (SUSMEL; TAYLOR, 2008; SUSMEL, 2009):

$$\rho_{\text{crit}} = \frac{\tau_{-1}}{2\tau_{-1} - \sigma_{-1}} \quad (6.2)$$

In cases where  $\rho$  exceeds  $\rho_{\text{crit}}$ , it is constrained to  $\rho_{\text{crit}}$  to ensure the integrity of the model. Hence, considering the collected data for the material in question depicted in Fig. 6.15a, it is feasible to calibrate the model for the material under study using the curves shown in Fig. 6.15b. It is worth noting that the calculation of shear stress amplitude in this study follows the Maximum Rectangular Hull (MRH) approach (see Fig. 2.4), similar to previous works (BRITO OLIVEIRA *et al.*, 2022; BRITO OLIVEIRA *et al.*, 2023a). Therefore, the final equation for life calculation is given as:

$$N_f = 10^7 \left[ \frac{-50.748\rho + 139.687}{\tau_{a,\text{max}}} \right]^{-3.571\rho + 11.905} \quad (6.3)$$

The calibration of the SWT model exclusively considers uniaxial fatigue data. Upon calibration, the resulting equation for Al 7075-T651 is as follows:

$$\sqrt{\sigma_{n,\text{max}}\sigma_{n,a}} = 1230.62N_f^{-0.12} \quad (6.4)$$

## 6.4.2 Data-driven model

The data-driven model considered in this study has been previously utilized and validated in recent literature (BRITO OLIVEIRA *et al.*, 2023a; OLIVEIRA *et al.*, 2024). Such models rely on real-world data and employ algorithms to discern patterns and make predictions. Specifically, the model under consideration is based on artificial neural networks (ANNs), trained with real fatigue fretting experiment data conducted by various authors across different loading conditions, geometries, and aeronautical aluminum alloys (OLIVEIRA *et al.*, 2024). It is worth noting that this approach was initially validated by applying it to two aluminum alloys not

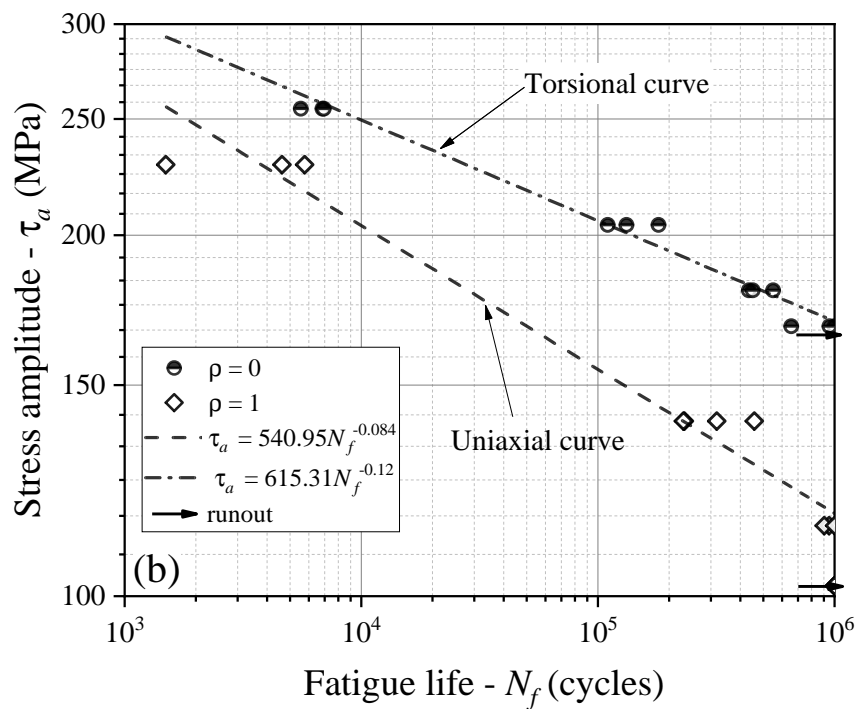
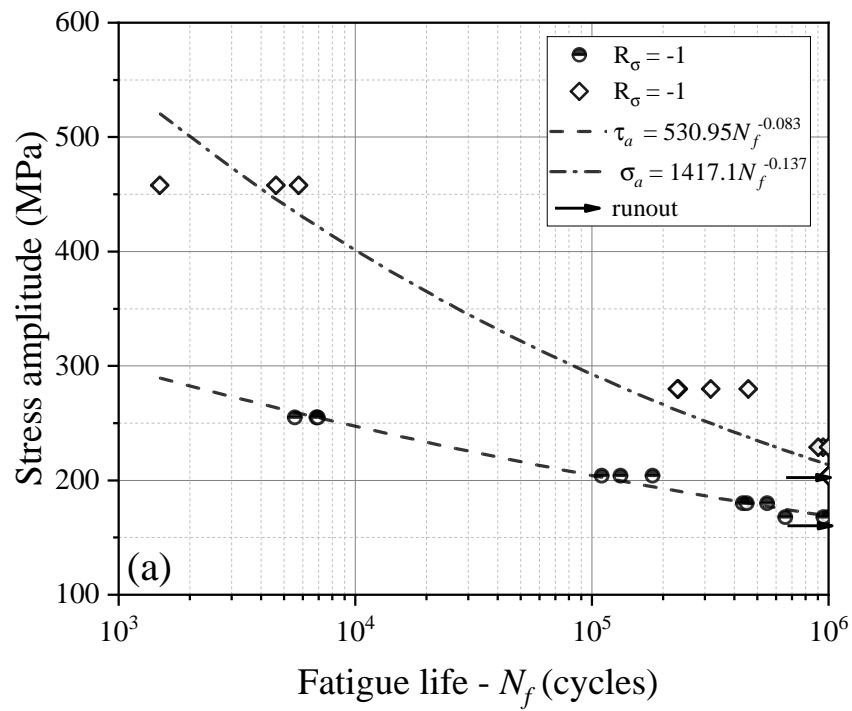


**Figure 6.16.** Wöhler curves for torsional and uniaxial fatigue under fully reversed loading ( $R_\sigma = -1$ ) (a) and modified Wöhler diagram for the same fatigue curves (b).

included in its training dataset (BRITO OLIVEIRA *et al.*, 2023a). Subsequently, the authors further tested these models on entirely different alloys not utilized in training, such as Ti-6Al-4V titanium alloys and ASTM A743 CA6NM steel alloys, highlighting the significant generalization capabilities of these models (OLIVEIRA *et al.*, 2024). More recently, applications of these models in fatigue fretting tests conducted on aeronautical aluminum under variable amplitude bulk load conditions have also shown promising results (OLIVEIRA *et al.*, 2024b). Additionally, it is noteworthy that these models have been also successfully tested in fretting fatigue tests on Inconel 718 alloys, considering the effects of high temperatures (CARDOSO *et al.*, 2024). Further elaboration on this methodology is documented in (OLIVEIRA *et al.*, 2024). However, an outline of its fundamental operation is presented here for clarity. This methodology can be conceptualized as a hybrid framework, integrating various processes and considerations beyond the mere application of specific parameters within a neural network model. Hence, it can be divided into two principal segments: data preprocessing and subsequent utilization of this processed data within the neural network model for life prediction. The preprocessing phase follows a chain of reasoning based on established methodologies within the fretting literature, takes into account the mechanics of the problem itself. This is essential for advancing the model's potential for broad generalization, given the inherent sensitivity of such data-driven models to the quality and nature of input-output datasets (BRITO OLIVEIRA *et al.*, 2022; HAYKIN, 2008; GORJI *et al.*, 2022; NOWELL; NOWELL, 2020).

Initially, the experimental tests are simulated numerically to ascertain stress distributions within the test specimen. Subsequently, equivalent stresses ( $\sigma_{n,\max}$ ,  $\tau_{a,\max}$ ) are computed at a specific point and on the critical plane. Herein, the material critical distance, employing the point method ( $L/2$ ), and the critical plane established based on the MWCM criterion are considered. Once this is done, the next step is to normalize these stresses with respect to their ultimate stress ( $\sigma_{\text{ult}}$ ). The ratio of yield stress ( $\sigma_y$ ) to ultimate stress ( $\sigma_{\text{ult}}$ ) is also considered in the inputs of the ANN model. Furthermore, incorporation of this stress ratio as an input parameter serves to differentiate materials and enriches the model's input data complexity. This strategy also facilitates the model's assimilation of four distinct parameters through a rationalized three-input interface. Finally, in the model's output stage, life estimation is yielded in a normalized form relative to conventionally accepted runout life standards ( $N_{f,\max} = 10^8$  cycles). In essence, this model can be understood as a function ( $f(x_1, x_2, x_3)$ ), encapsulating

the workflow outlined above, as follows:

$$f \left( \frac{\tau_{a,\max}}{\sigma_{\text{ult}}}, \frac{\sigma_{n,\max}}{\sigma_{\text{ult}}}, \frac{\sigma_y}{\sigma_{\text{ult}}} \right) = \frac{\log_{10} N_f}{\log_{10} N_{f,\max}} \quad (6.5)$$

### 6.4.3 Finite element analysis

In order to numerically compute the equivalent stresses for all aforementioned models, the finite element method (FEM) is applied using the ABAQUS commercial finite element (FE) software. Accordingly, a cylindrical contact model is constructed based on the dimensions depicted in Fig. 6.1 and the loading conditions in Fig. 6.3. We emphasize that we initially proposed a model similar to the one created in Chapter 4, with only one pad and half of the specimen. However, it was observed that the presence of the bearing significantly affects the stress distribution, so it has been decided to create a model closer to the experiment, including the bearing (see Fig. 6.18b). The bearing is fixed prior to analysis. The FE model, in accordance with the experiments, encompasses five main steps. In the first one, the load  $P$  is applied until reaching its minimum value, set at 10% of the maximum load (5 kN and 10 kN) in the pad. Subsequently, in the second step, both loads  $P$  and  $B$  are incrementally increased to their maximum values. In the third step, the fretting load is imposed on the pad, considering only 2 cycles for stabilization. In the fourth step, the loads  $P$  and  $B$  are reduced to their minimum values, completing a block of full loading cycle, as depicted in Fig. 6.3. Finally, in the fifth step, a new loading cycle is initiated, incrementally increasing the loads  $P$  and  $B$  to their maximum values, following the pattern from step 3.

During the simulation, the stress components directly at the material critical distance is illustrated in Fig. 6.17. The imposition of load  $P$  until its minimum value is set from time 1.0 to 2.0, and the increase of both  $P$  and  $B$  to their maximum values from 2.0 to 3.0, indicating the onset of the fretting cycle. As seen, two time-ranges of stresses within the loading are highlighted. The first pertains to the corresponding damage experienced by the rise and fall of loads  $P$  and  $B$  during a complete loading cycle. The second range is associated with the fretting loading ( $Q$ ), point out the equivalent of just one cycle out of the 8000 cycles conducted in the flight fretting fatigue test. For damage calculation, the Miner's rule is employed, wherein  $n_1$  and  $n_2$  represent the cycles applied during that specific sub-block under analysis, here considered

as 1 and 8000, respectively. On the other hand,  $N_1$  and  $N_2$  denote the life estimates from the models, corresponding to if the specimen had been subjected to the loading highlighted in each of the demarcated stresses ranges, thereby calculating damage 1 and 2, respectively.

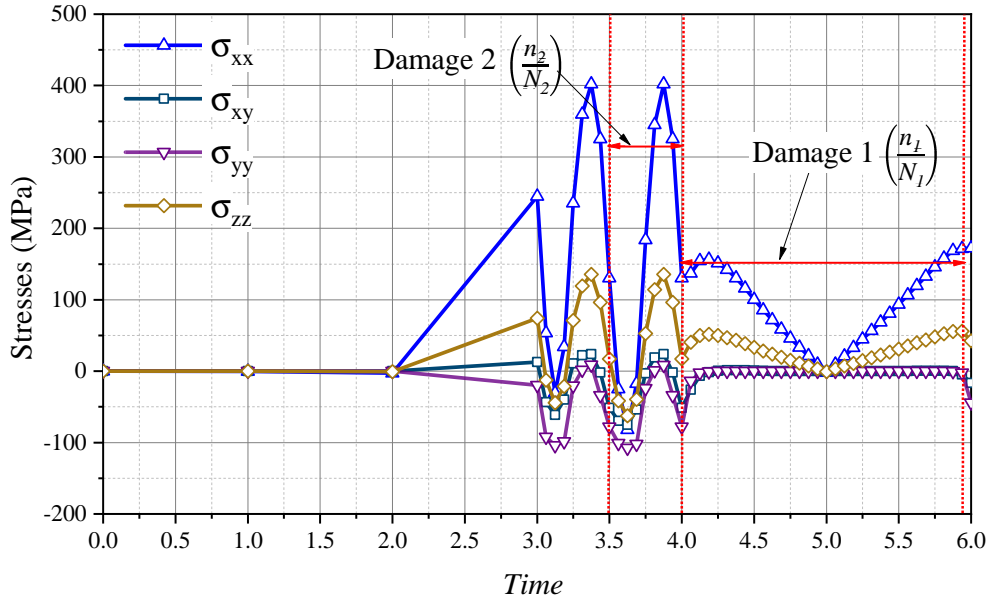


**Figure 6.17.** Numerical analysis of stress distribution for the test configuration T03.

In terms of model discretization, the setups feature a finely meshed region near the contact surface, as depicted in Fig. 6.18b. This refined area consists of quadrangular elements while a coarser mesh of triangular elements is situated away from the contact region. Linear elements are employed across all analyses, with the use of 2D plane strain elements. Friction contact constraints are implemented using the penalty formulation, with primary and secondary nodes defined in the mesh refinement region. The latter is positioned on the pad's contact surface, while the former is situated on the specimen. The frictionless steel bearing is positioned aligned with the pad and fixed underneath (Fig. 6.18b). Additionally, multipoint constraints are applied to the pad's upper surface to avoid rotation. To summarize the entire modeling approach outlined in this section, Fig. 6.18 provides a step-by-step overview, for the calculation of both fretting fatigue lives:  $N_{f,B}$  and  $N_{f,Q}$ .

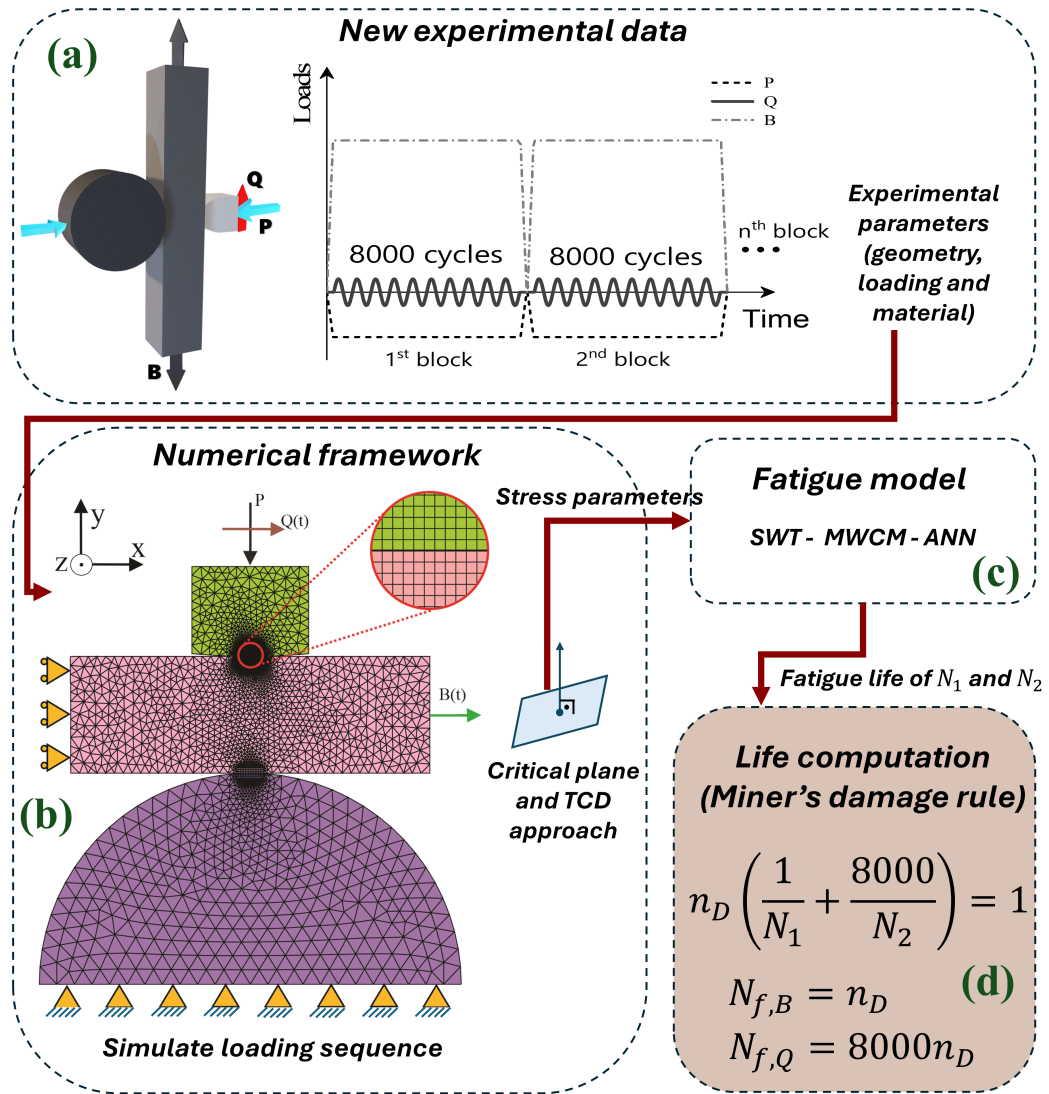


Figure 6.18. Flowchart illustrating all the modelling proposed and conducted.

## 6.5 RESULTS AND DISCUSSIONS

Before presenting the results, let us delve into the two error analysis methodologies employed to interpret these findings. The first originates from the equation of error measured during the training of the ANN model, known as the Empirical Risk Error (Eq. 3.1). Essentially, this equation represents half of the Mean Squared Error (MSE), a commonly utilized metric for such analyses, thereby yielding a similar interpretation. The second error is the Band Mean Error Factor (BMEF), as defined in Eq. 4.3.

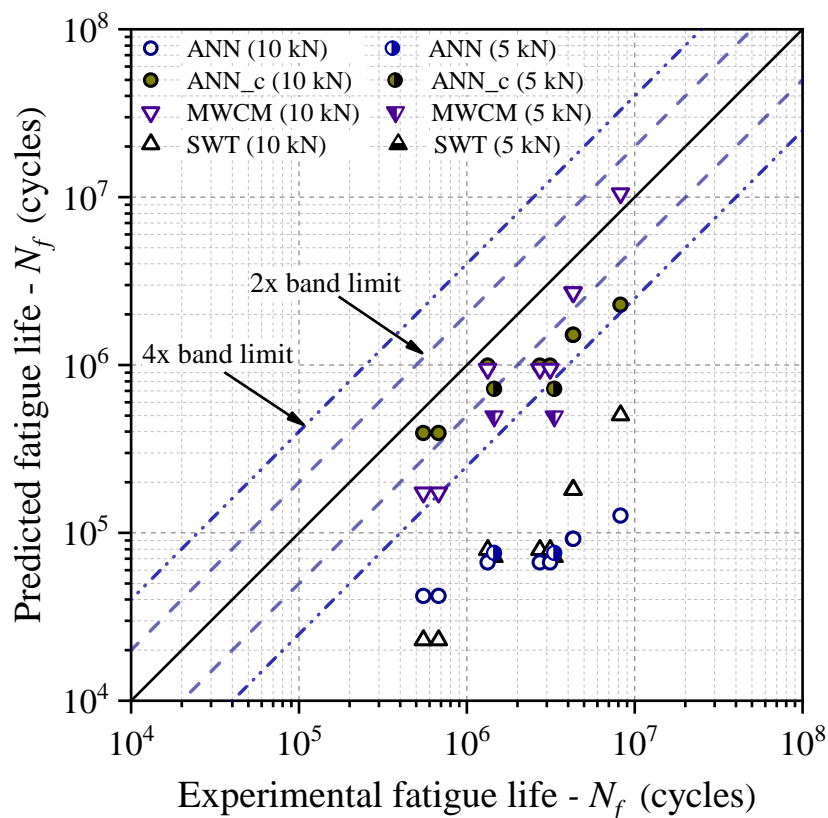


Figure 6.19. Estimated vs. fatigue life for all testing conditions

### 6.5.1 Life estimates

In light of the methodology outlined in the preceding section and all conducted analyses, the results of life predictions for all referenced models are depicted in Fig. 6.19. The Miner's damage rule analysis revealed that, across all models, the damage attributed to Damage 1 (Fig. 6.17) is near negligible, with Damage 2 predominating in the life calculations. First, one address the SWT model, which yielded highly conservative results (black upward triangles). This may be attributed to the significant influence of the mean stress presented in all experiments. While previous studies have explored the effect of mean stress in fretting fatigue tests (VANTADORI *et al.*, 2020; FADEL *et al.*, 2012; ROSSINO *et al.*, 2009), the configurations of the tests under examination are distinct, featuring a notably pronounced mean stress, which, under the SWT analysis, has not been observed in classical fretting experiments.

The initial outcomes obtained by the ANN model (blue circle) exhibited a similar trend to those of the SWT model. In other words, their results have been highly conservative. Even at a considerable distance from the hotspot (TCD approach), the equivalent stress parameters identified on the critical planes have been notably high, particularly concerning the maximum

normal stress ( $\sigma_{n,max}$ ), which accounts for the nonzero mean stress effect. This circumstance led both the SWT and ANN models to predict values significantly below the experimental life. When the MWCM model was applied directly, a mathematical error was noted, and the results failed to converge to a life value. Thus, the problem has been directed towards the critical  $\rho$  value (Eq. 6.2), revealing that, particularly under Damage 2 related loading,  $\rho$  values ranged from 2.4 to 3.8, significantly higher than the critical value ( $\rho_{criti}$ ) calculated based on fatigue limits (Eq. 6.2), yielding 1.3. Consequently,  $\rho$  was considered equal to the critical  $\rho_{criti}$ , emphasizing the notion that when micro/meso cracks are fully open, an increase in the normal mean stress does not lead to further fatigue damage (SUSMEL, 2008).

One must acknowledge that the MWCM approach posits that fatigue damage centers on the values of  $\tau_a$  and  $\rho$ , rather than  $\tau_a$  and  $\sigma_{n,max}$ , hence the critical  $\rho$  value directly influences the final  $\sigma_{n,max}$  value. This adjustment rendered the model estimates highly promising, even though conservative (purple downward triangle), with most estimates falling within the band of 4 (Fig. 6.19). Nevertheless, to apply a similar correction in the ANN model, whose parameters were inspired by the MWCM model, the authors constrained the maximum normal stress input parameter by  $\sigma_{n,max} = \rho_{crit}\tau_a$  whenever  $\rho > \rho_{crit}$ . Such approach is supported given that, although the model has been 'exposed' to this type of material during training, such loading conditions were never presented. Examining the values used in its training for this material (7075-T651), the average of all experiment values floated around 1.4, close to the critical value (1.3). Despite the model being trained with some values surpassing the critical value ( $\rho_{crit}$ ), it never encountered experiments with such intense mean stress, resulting in exceedingly high  $\rho$  values (3.8), unaccounted for in its training and therefore incapable of providing coherent estimates. Thus, with the corrected  $\sigma_{n,max}$  values, the model estimates, as aforementioned,  $ANN_c$ , emerged as the most accurate (dark grey circles). As we will discuss in the next subsection, these still conservative results suggest that an approach to crack initiation and propagation life may be necessary. Prior to such a discussion, it is pertinent to highlight the calculation of the band error factors ( $\psi$ ) pertaining to each experimental data, as reported in Table 6.5, in terms of the number of the loading block obtained ( $N_{f,B}$ ). The  $ANN_c$  model yielded its most accurate estimates for values with lower lives, whereas the MWCM model performed better for data with longer lives. Table 6.6 presents a compilation of BMEF and ER errors for all models under study, emphasizing that the two most effective models have been the  $ANN_c$  and

**Table 6.5.** Fatigue life in terms of loading blocks and the error  $\psi$  values of each test.

Test ID	Q (kN)	$N_{f,B}$ (cycles)				Band error factor ( $\psi$ )		
		Exp	ANN <sub>c</sub>	SWT	MWCM	ANN <sub>c</sub>	SWT	MWCM
T01	3	85	49	3	22	1.7	29.6	3.9
T02	3	69	49	3	22	1.4	24.0	3.2
T03	2.25	166	124	10	118	1.3	16.9	1.4
T04	2.25	340	124	10	118	2.7	34.5	2.9
T05	2.25	393	124	10	118	3.2	39.8	3.3
T06	1.875	536	189	23	339	2.8	23.7	1.6
T07	1.875	539	189	23	339	2.8	23.9	1.6
T08	1.5	1031	285	63	1315	3.6	16.5	1.3
T09	2.25	183	90	9	62	2.0	20.3	3.0
T10	2.25	415	90	9	62	4.6	46.1	6.7

**Table 6.6.** Error values (ER and BMEF) for all models in study.

Model	ER*	BMEF
ANN	17.98	42.31
ANN <sub>c</sub>	1.4	2.79
SWT	15.82	23.95
MWCM	1.64	2.91

\* Values must be multiplied by  $10^{-5}$ .

the MWCM.

## 6.5.2 The stress intensity factor range response

It is worth noting that the models used in this work are crack initiation life prediction criteria, as they are commonly employed in cases where crack initiation life closely approximates total fatigue life. Furthermore, the ANN-based model was trained using experiments under these aforementioned conditions, making it practically impossible for it to generalize its values to situations that are physically distinct. This underscores the necessity of maintaining a critical evaluation in such circumstances. As previously mentioned, upon observing failure behavior in the tests here conducted, it is noticeable that cracks approaching mid-thickness through the specimen remain visible for a considerable period before final failure. This suggests the existence of a substantial crack propagation time period until unstable crack propagation and ultimate rupture. As previously reported nearly all life estimates yielded conservative values. This suggests that the addition of crack propagation life estimates to compute a total life (initiation plus propagation) could in principle enhance the estimates. Nonetheless, the development of

a crack propagation model to estimate life considering the complexity of the physics involved in such an experimental program, wherein two primary inclined cracks propagate and merge near the mid-thickness of the specimen, would require a more robust analysis involving the existence of inclined cracks, friction between crack faces, simultaneous crack propagation to form a detached element, etc. This will not be pursued here, but a discussion about the behavior of the mode I stress intensity factor range considering an idealized straight crack under these complex loadings can help to qualitatively understand the fracture behavior and the level of conservativeness yielded by the life initiation models.

Figure 6.20 illustrates the variation of the stress intensity factor range,  $\Delta K$ , for a straight crack originating from the contact edge and propagating perpendicular to the contact surface (mode I) under fretting conditions. The calculation of  $\Delta K$  was performed utilizing a non-intrusive post-processing approach based on the distributed dislocation technique (DDT) (NOWELL *et al.*, 1987; CARDOSO *et al.*, 2018). This simplification tends to overestimate the  $\Delta K$  calculation since the actual crack propagated at an inclined angle and friction between the crack faces tends to reduce the effective stress intensity factor range. The present analysis reveals a diminishing influence of the fretting loading (Damage 2) on crack propagation as it grows. Hence, beyond a certain distance, the fretting loading becomes less significant in crack propagation, with control shifting to the loading associated with Damage 1, i.e., the low cycles fatigue regime due to the normal  $P$  and bulk  $B$ , loads. This seems to be a reasonable explanation to the long crack propagation stage observed, given that the interval between consecutive Damage 1 loading cycles is about 8 minutes.

## 6.6 PARTIAL CONCLUSIONS

Based on the analyses and tests carried out in this work, one has concluded that fretting fatigue experiments performed under more complex loading conditions exhibited significantly different fatigue behavior compared to those commonly reported in the literature. Unlike classical fretting fatigue experiments, the observed cracks in our study showed a notably slow propagation stage due to the nature of the loadings. These loadings included the presence of bulk, normal, and fretting loads with different frequencies and waveforms. This shift in the physics of the problem significantly alters the analysis, leading to the recognition that

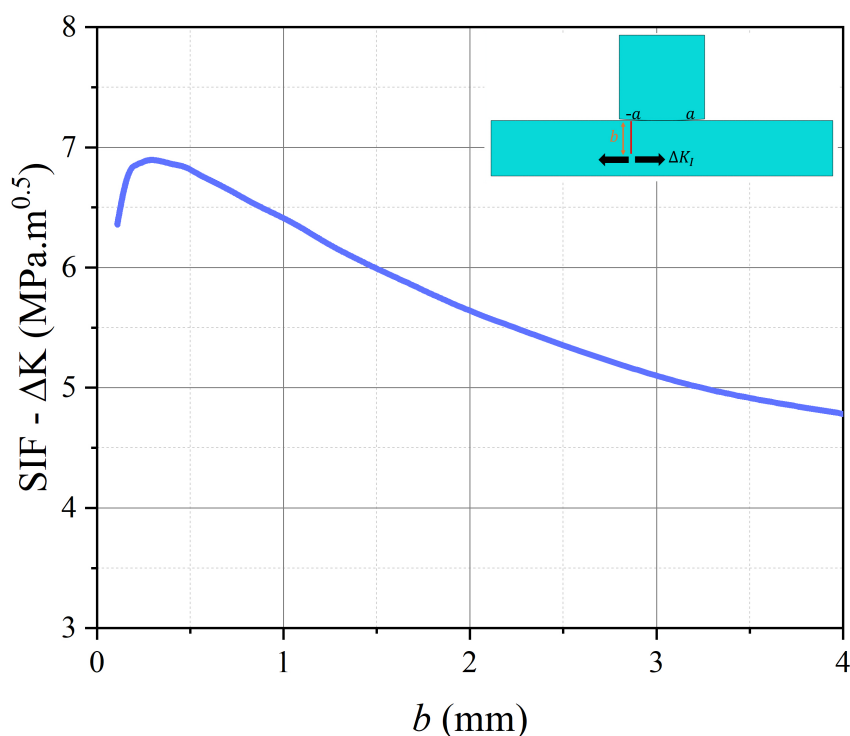


**Figure 6.20.** Depth ( $b$ ) vs. stress intensity factor range ( $\Delta K$ ) for the fretting cycle loading (see the Damage 2 range in Fig. 6.17) for the test configuration T06.

multiaxial fatigue models commonly applied in the literature to estimate life (or endurance) did not demonstrate the same level of accuracy as typically observed.

In contrast to classical experiments, where crack initiation life closely approximates total fatigue life, our analysis revealed a significant time period in crack propagation. During this stage, propagating inclined cracks originating simultaneously from both contact edges were clearly observed, eventually leading to the formation of a triangular-shaped detached body, which is a unique fracture behavior. Finally, fracture of the specimens was observed after the slow propagation of a dominant mode I straight crack. Furthermore, a preliminary theoretical analysis using fracture mechanics showed that the stress intensity factor range caused by the fretting loads decreases as the crack grows. This suggests that, after a certain point, crack propagation is governed by the low cycle fatigue loads  $P$  and  $B$ , helping to explain the dominant crack propagation phase observed in the tests.

The life estimation methodology considering the MWCM and ANN<sub>c</sub> models demonstrated that, from a mechanical perspective, the influence of very high mean stresses must be

limited in such models to be consistent with the fact that time-varying loads are more relevant for producing fatigue. The surprising accuracy of the estimated fatigue lives, falling within a 4x error-band, demonstrated the robustness of the ANN<sub>c</sub> model. Precision could certainly be increased should more elaborate crack propagation estimates be considered. Additionally, it is clear that ANN models cannot be applied indiscriminately without a strong mechanical understanding of the problem under consideration. These new experiments clearly showed that the crack propagation stage played a significant role in the fatigue response. Therefore, an ANN that was trained with fretting data where crack initiation was dominant could not detect such aspects. This interpretation of the physical phenomenon must be conducted by the researcher before applying any model, whether data-driven or empirical. Finally, we emphasize that the new experimental data provided in this work stimulates further investigations in the field, encouraging the adoption of more robust approaches to address the complexities of real-world problems.

# Chapter 7

## Conclusions

*"In this chapter, one presents a summary of the main conclusions drawn from each chapter, along with a final section on future work."*

## 7.1 MAIN CONCLUSIONS

The new ANN fretting fatigue proposed models were based on theories such as the critical distance theory, multiaxial fatigue models, and contact mechanics theory, among others. Another significant aspect is the application of numerical modeling for extracting stress parameters (Chapter 4), which allowed us to expand the perspectives of the first work (Chapter 3), which had been restricted to analytically solved fretting fatigue cases. Various other applications were discussed in Chapters 5 and 6, including cases in overhead conductors. All chapters highlighted the generalization capabilities of the neural network models, which, primarily due to the choice of their input and output parameters, faced challenging test datasets that differed considerably from those used as training datasets. Although not presented in this thesis, related studies conducted in collaboration with other authors have shown that this ANN methodology can also handle the effects of high temperatures and variable normal loads in materials even more resistant than titanium, as discussed in Chapter 4, specifically Inconel 718 (CARDOSO *et al.*, 2024).

Machine learning models typically use test datasets that adhere to the following guidelines: 'Ensure that the conditions for your test set are met: it needs to be large enough (despite the lack of final scientific consensus on this) to ensure statistically significant results and should be representative of the entire dataset. Specifically, do not select a test set whose characteristics differ from those of the training set'. However, we went beyond this criterion by introducing nonlinear inputs that not only incorporated the effects of geometry and loading types but also facilitated material identification. This approach exposed the model to entirely new and significantly different data from those used in training, even though resulting in accurate estimates. Thus, our methodology not only expanded the capabilities of an already innovative model in the field of fretting fatigue by introducing nonlinear variables, thereby enhancing its generalization capabilities but also marked the onset of a new phase in fretting fatigue life prediction, facilitated by data-driven models.

Finally, it can be concluded that the new experiments discussed in Chapter 6 clearly demonstrate that experiments involving complex loadings, inspired by real-world conditions, can reveal previously unseen particularities due to the simplifications typically made in classical fretting fatigue tests. With the new loading conditions, driven by the loads experienced by

aircraft fuselages, it has been observed that the crack propagation phase increased considerably. This complexity has been such that even the new ANN models, which had successfully addressed all previously proposed challenges, struggled with this situation. It became necessary to make previously unrequired considerations to achieve reasonable estimates. The key takeaway from these analyses is the importance of thoroughly understanding the physics of the phenomenon under study. This understanding is crucial for proposing machine learning models capable of accurately predicting future behavior.

## 7.2 FUTURE WORKS

A promising proposal for future research is to enhance the fatigue analysis presented in Chapter 6, where the crack propagation process have been not considered. Although the results obtained have been satisfactory, a more numerically detailed analysis aimed to better representing the experimental observations—such as the appearance of inclined cracks and the corresponding calculation of propagation life—certainly warrants further study.

Another suggestion would be to analyse and create other data-driven models with other types of input, such as strains parameters or even the slip amplitude, to find more accurate models that can be applied in other contexts, such as with the presence of plastic flow.

Another idea for future work involves the fact that nearly all the data-driven models proposed in this study utilized stress parameters extracted at the critical distance as inputs, taking into account the stress gradient effect on the material. However, this can also be seen as a limitation in the model's application, since extracting the stress requires prior knowledge of this critical distance value. Despite being a parameter extensively studied in the literature, with values for various materials readily available and relatively easy to obtain, this may not always be accessible, particularly for new materials. Additionally, there is some variability in this material parameter, with different sources sometimes reporting distinct values for the same material. Furthermore, many researchers are beginning to apply the concept of variable critical distance, as discussed in Chapter 2. Therefore, it would be worthwhile to develop a model that is more independent of this parameter. One idea could be to train a new model that considers both local and non-local parameters, incorporating a standard stress reduction for all materials, allowing the model itself to determine the critical distance.

Another interesting idea would be to test the proposed modeling in this study in other fatigue contexts, such as in notched materials or brittle materials, shifting the focus away from fretting fatigue. This would aim to further expand the model's generalization capabilities.

# References

ABBASI, F.; MAJZOobi, G. H.; MENDIGUREN, J. A review of the effects of cyclic contact loading on fretting fatigue behavior. *Advances in Mechanical Engineering*, v. 12, n. 9, p. 1–17, 2020. ISSN 16878140. Cited in page 21.

ADRIANO, V. S.; MARTÍNEZ, J. M.; FERREIRA, J. L.; ARAÚJO, J. A.; SILVA, C. R. da. The influence of the fatigue process zone size on fatigue life estimations performed on aluminum wires containing geometric discontinuities using the Theory of Critical Distances. *Theoretical and Applied Fracture Mechanics*, Elsevier, v. 97, n. April, p. 265–278, 2018. ISSN 01678442. Disponível em: <<https://doi.org/10.1016/j.tafmec.2018.09.002>>. Cited 2 times in pages 37 and 163.

ALBERT, W. A. J. Uber treibseile am harz. archiv fur mineralogie, geognosie. *Bergbau und Huttenkunde*, v. 10, p. 215, 1837. Cited in page 18.

ALMEIDA, G.; CARDOSO, R.; CHASSAING, G.; POMMIER, S.; ARAÚJO, J. Fretting fatigue of Inconel 718 at room and elevated temperatures considering both constant and cyclic normal contact loads. *Tribology International*, Elsevier Ltd, v. 183, n. March, p. 108382, may 2023. ISSN 0301679X. Disponível em: <<https://linkinghub.elsevier.com/retrieve/pii/S0301679X2300169X>>. Cited 5 times in pages 7, 12, 23, 36, and 194.

ALMEIDA, G. M.; CARDOSO, R. A.; GARCIA, M. A.; CHASSAING, G.; POMMIER, S.; ARAÚJO, J. A. Four actuators fretting fatigue rig and tests with cyclic normal load for Ti-6Al-4V. *Theoretical and Applied Fracture Mechanics*, Elsevier Ltd, v. 119, n. February, p. 103292, 2022. ISSN 01678442. Disponível em: <<https://doi.org/10.1016/j.tafmec.2022.103292>>. Cited 5 times in pages v, 12, 62, 63, and 64.

ALMEIDA, G. M.; PESSOA, G. C.; CARDOSO, R. A.; CASTRO, F. C.; ARAÚJO, J. A. Investigation of crack initiation path in AA7050-T7451 under fretting conditions. *Tribology International*, Elsevier Ltd, v. 144, n. July 2019, p. 106103, 2020. ISSN 0301679X. Disponível em: <<https://doi.org/10.1016/j.triboint.2019.106103>>. Cited 2 times in pages 23 and 29.

ALPAYDIN, E. *Introduction to machine learning*. [S.l.]: MIT press, 2020. Cited in page 69.

ANJUM, Z.; QAYYUM, F.; KHUSHNOOD, S.; AHMED, S.; SHAH, M. Prediction of non-propagating fretting fatigue cracks in Ti6Al4V sheet tested under pin-in-dovetail configuration: Experimentation and numerical simulation. *Materials and Design*, Elsevier Ltd, v. 87, p. 750–758, 2015. ISSN 18734197. Disponível em: <<http://dx.doi.org/10.1016/j.matdes.2015.08.070>>. Cited in page 5.

ARAÚJO, J.; NOWELL, D. The effect of rapidly varying contact stress fields on fretting fatigue. *International Journal of Fatigue*, v. 24, n. 7, p. 763–775, jul 2002. ISSN 01421123. Cited 3 times in pages 7, 23, and 33.

- ARAÚJO, J.; NOWELL, D. Mixed high low fretting fatigue of ti6al4v: Tests and modelling. *Tribology international*, Elsevier, v. 42, n. 9, p. 1276–1285, 2009. Cited in page 196.
- ARAÚJO, J. A. *On the initiation and arrest fretting fatigue cracks*. Tese (Doutorado) — University of Oxford, 2000. Disponível em: <<https://ethos.bl.uk/OrderDetails.do?uin=uk.bl.ethos.342243>>. Cited 9 times in pages xii, 4, 15, 108, 109, 112, 117, 119, and 120.
- ARAÚJO, J. A.; CASTRO, F. C. A comparative analysis between multiaxial stress and  $\Delta K$ -based short crack arrest models in fretting fatigue. *Engineering Fracture Mechanics*, v. 93, p. 34–47, 2012. ISSN 00137944. Cited 13 times in pages vi, xi, 22, 88, 89, 92, 95, 100, 101, 108, 112, 115, and 119.
- ARAÚJO, J. A.; CASTRO, F. C.; MATOS, I. M.; CARDOSO, R. A. Life prediction in multiaxial high cycle fretting fatigue. *International Journal of Fatigue*, Elsevier, v. 134, n. October 2019, p. 105504, 2020. ISSN 01421123. Disponível em: <<https://doi.org/10.1016/j.ijfatigue.2020.105504>>. Cited 6 times in pages 5, 7, 65, 88, 163, and 170.
- ARAÚJO, J. A.; DANTAS, A. P.; CASTRO, F. C.; MAMIYA, E. N.; FERREIRA, J. L. On the characterization of the critical plane with a simple and fast alternative measure of the shear stress amplitude in multiaxial fatigue. *International Journal of Fatigue*, v. 33, n. 8, p. 1092–1100, 2011. ISSN 01421123. Cited 6 times in pages 27, 30, 86, 88, 101, and 107.
- ARAÚJO, J. A.; NOWELL, D. Analysis of pad size effects in fretting fatigue using short crack arrest methodologies. *International Journal of Fatigue*, v. 21, n. 9, p. 947–956, 1999. ISSN 01421123. Cited in page 6.
- ARAÚJO, J. A.; SUSMEL, L.; PIRES, M. S.; CASTRO, F. C. A multiaxial stress-based critical distance methodology to estimate fretting fatigue life. *Tribology International*, Elsevier, v. 108, n. May 2016, p. 2–6, 2017. ISSN 0301679X. Disponível em: <<http://dx.doi.org/10.1016/j.triboint.2016.07.028>>. Cited 4 times in pages 23, 36, 37, and 106.
- ARAÚJO, J. A.; SUSMEL, L.; TAYLOR, D.; FERRO, J. C.; MAMIYA, E. N. On the use of the Theory of Critical Distances and the Modified Wöhler Curve Method to estimate fretting fatigue strength of cylindrical contacts. *International Journal of Fatigue*, v. 29, n. 1, p. 95–107, 2007. ISSN 01421123. Cited 3 times in pages 6, 37, and 106.
- ARAÚJO, J. A.; SUSMEL, L.; TAYLOR, D.; FERRO, J. C.; FERREIRA, J. L. On the prediction of high-cycle fretting fatigue strength: Theory of critical distances vs. hot-spot approach. *Engineering Fracture Mechanics*, v. 75, n. 7, p. 1763–1778, 2008. ISSN 00137944. Cited 8 times in pages 30, 36, 86, 88, 89, 101, 119, and 210.
- ARULKUMARAN, K.; DEISENROTH, M. P.; BRUNDAGE, M.; BHARATH, A. A. Deep reinforcement learning: A brief survey. *IEEE Signal Processing Magazine*, IEEE, v. 34, n. 6, p. 26–38, 2017. Cited in page 71.
- ASTM. Standard Guide for Fretting Fatigue Testing. *E2789 - 10*, v. 10, n. Reapproved, p. 1–10, 2015. Cited 2 times in pages 60 and 61.
- ATTIA, M. H.; WATERHOUSE, R. B. *Standardization of fretting fatigue test methods and equipment*. [S.l.]: ASTM International, 1992. Cited in page 60.

- AZEVEDO, C. R.; CESCÓN, T. Failure analysis of aluminum cable steel reinforced (ACSR) conductor of the transmission line crossing the Paraná River. *Engineering Failure Analysis*, v. 9, n. 6, p. 645–664, 2002. ISSN 13506307. Cited in page 162.
- AZEVEDO, C. R. d. F.; HENRIQUES, A.; FILHO, A. R. P.; FERREIRA, J.; ARAÚJO, J. Fretting fatigue in overhead conductors: Rig design and failure analysis of a grosbeak aluminium cable steel reinforced conductor. *Engineering Failure Analysis*, Elsevier, v. 16, n. 1, p. 136–151, 2009. Cited 3 times in pages 6, 63, and 162.
- BADIBANGA, R. K. *Evaluation of the fatigue resistance of power line conductors function of the H/w parameter*. Tese (Doutorado) — Universidade de Brasília, 2017. Cited 6 times in pages viii, 65, 183, 184, 189, and 190.
- BARBER, D. *Bayesian reasoning and machine learning*. [S.l.]: Cambridge University Press, 2012. Cited in page 69.
- BARBOSA, J. F.; CORREIA, J.; JÚNIOR, R.; ESUS, A. M. P. D. Fatigue life prediction of metallic materials considering mean stress effects by means of an artificial neural network. *International Journal of Fatigue*, Elsevier Ltd, Federal University of Rio Grande do Norte, Natal, Brazil, v. 135, 2020. ISSN 01421123 (ISSN). Disponível em: <<https://www.scopus.com/inward/record.uri?eid=2-s2.0-85079326265&doi=10.1016%2Fj.ijfatigue.2020.105527&partnerID=40&md5=93aef5fe674eae85bfdd5451441314dd>>. Cited in page 210.
- BARTOSZ, J.; BEATA, S.; MALGORZATA, Z.; KRYSZTIAN, F.; PAWEL, S. The researches of influence of strengthening on fatigue strength of aluminium wires for ohl conductors. *Archives of Civil and Mechanical Engineering*, Springer, v. 19, p. 862–870, 2019. Cited in page 163.
- BASQUIN, O. H. The exponential law of endurance tests. In: *Proc Am Soc Test Mater*. [S.l.: s.n.], 1910. v. 10, p. 625–630. Cited in page 19.
- BELLECAVE, J. *Stress gradients in fretting fatigue*. 1 p. Tese (Doutorado) — University of Brasília, 2015. Cited 7 times in pages xii, 108, 109, 112, 117, 119, and 120.
- BHATTI, N. A.; Abdel Wahab, M. Fretting fatigue crack nucleation: A review. *Tribology International*, Elsevier Ltd, v. 121, n. December 2017, p. 121–138, 2018. ISSN 0301679X. Disponível em: <<https://doi.org/10.1016/j.triboint.2018.01.029>>. Cited in page 6.
- BHATTI, N. A.; PEREIRA, K.; WAHAB, M. A. *A comparison between critical-plane and stress-invariant approaches for the prediction of fretting fatigue crack nucleation*. Springer Singapore, 2019. 530–538 p. ISSN 21954364. ISBN 9789811304101. Disponível em: <[http://dx.doi.org/10.1007/978-981-13-0411-8\\_47](http://dx.doi.org/10.1007/978-981-13-0411-8_47)>. Cited 2 times in pages 29 and 210.
- BISHOP, C. M.; NASRABADI, N. M. *Pattern recognition and machine learning*. [S.l.]: Springer, 2006. v. 4. Cited 3 times in pages 68, 69, and 77.
- BRAMHALL, R. *Studies in fretting fatigue*. Tese (Doutorado) — Oxford University, 1973. Cited 2 times in pages 4 and 5.
- BREIMAN, L. Random forests. *Machine learning*, Springer, v. 45, p. 5–32, 2001. Cited in page 173.

- BRITO OLIVEIRA, G. A.; CARDOSO, R. A.; FREIRE JÚNIOR, R. C. S.; ARAÚJO, J. A. A generalized ANN-multi-axial fatigue nonlocal approach to compute fretting fatigue life for aeronautical Al alloys. *Tribology International*, v. 180, n. November 2022, p. 108250, feb 2023. ISSN 0301679X. Disponível em: <<https://linkinghub.elsevier.com/retrieve/pii/S0301679X23000373>>. Cited 28 times in pages 9, vi, 14, 17, 103, 104, 105, 106, 108, 109, 119, 120, 125, 127, 128, 131, 137, 152, 154, 163, 164, 170, 171, 174, 194, 210, 211, and 213.
- BRITO OLIVEIRA, G. A.; FREIRE JÚNIOR, R. C. S.; BARBOSA, J. F.; CORREIA, J. A. F. O. An approach to predict ultimate transverse tensile strength based on mixed ANN models for a composite lamina. *Journal of Materials Research and Technology*, v. 23, p. 2719–2729, 2023. ISSN 22387854. Cited in page 73.
- BRITO OLIVEIRA, G. A.; FREIRE JÚNIOR, R. C. S.; Conte Mendes Veloso, L. A.; ARAÚJO, J. A. A hybrid ANN-multi-axial fatigue nonlocal model to estimate fretting fatigue life for aeronautical Al alloys. *International Journal of Fatigue*, v. 162, n. November 2021, p. 107011, 2022. ISSN 01421123. Cited 9 times in pages 9, 13, 17, 85, 86, 106, 163, 211, and 213.
- CÂMARA, E. C. B.; FREIRE, R. C. S. Using neural networks to modeling the transverse elasticity modulus of unidirectional composites. *Composites Part B: Engineering*, v. 42, n. 7, p. 2024–2029, 2011. ISSN 13598368. Cited in page 73.
- CÂMARA, E. C. B.; KALOMBO, R. B.; FERREIRA, J. L.; ARAÚJO, J. A.; Freire Júnior, R. C. S. Estimating the fatigue behavior of a family of aluminum conductor cables using ANNs applying the Poffenberger-Swart formula. *International Journal of Fatigue*, v. 159, n. September 2021, 2022. ISSN 01421123. Cited 3 times in pages 3, 7, and 10.
- CÂMARA, E. C. B.; KALOMBO, R. B.; FERREIRA, J. L. A.; ARAÚJO, J. A.; Freire Júnior, R. C. S. Estimating fatigue behavior of a family of aluminum overhead conductors using ANNs. *Fatigue and Fracture of Engineering Materials and Structures*, Blackwell Publishing Ltd, Welding Department, Federal Institut of Alagoas, CEP: 57230-000, Coruripe, Alagoas, Brazil, v. 44, n. 4, p. 983–996, 2021. ISSN 8756758X (ISSN). Disponível em: <<https://www.scopus.com/inward/record.uri?eid=2-s2.0-85099092590&doi=10.1111%2Fffe.13408&partnerID=40&md5=e407126dd30b6798e0393007d935d20e>>. Cited 2 times in pages 10 and 65.
- CAMPBELL, F. C. *Elements of Metallurgy and Engineering Alloys*. [S.l.]: ASM International, 2008. Cited in page 20.
- CARBONI, M.; ZAMORANO, M. On monitoring fretting fatigue damage in solid railway axles by acoustic emission with unsupervised machine learning and comparison to non-destructive testing techniques. *Proceedings of the Institution of Mechanical Engineers, Part F: Journal of Rail and Rapid Transit*, SAGE Publications Sage UK: London, England, p. 09544097231193186, 2023. Cited in page 10.
- CARDOSO, R.; OLIVEIRA, G.; ALMEIDA, G.; ARAÚJO, J. A simple linear regression strategy for fretting fatigue life estimates. *Tribology International*, Elsevier, p. 109852, 2024. Cited 3 times in pages 163, 213, and 224.
- CARDOSO, R. A.; CAMPOS, E. R. S.; FERREIRA, J. L.; WANG, D.; ARAÚJO, J. A. A crack arrest methodology based on Bazant's parameter to fretting fatigue. *Theoretical and Applied Fracture Mechanics*, Elsevier, v. 95, n. February, p. 208–217, 2018. ISSN 01678442.

Disponível em: <<https://doi.org/10.1016/j.tafmec.2018.03.001>>. Cited 2 times in pages 6 and 220.

CARDOSO, R. A.; DOCA, T.; NÉRON, D.; POMMIER, S.; ARAÚJO, J. A. Wear numerical assessment for partial slip fretting fatigue conditions. *Tribology International*, Elsevier Ltd, v. 136, n. March, p. 508–523, 2019. ISSN 0301679X. Disponível em: <<https://doi.org/10.1016/j.triboint.2019.03.074>>. Cited 4 times in pages 5, 23, 29, and 135.

CARDOSO, R. A.; FERRY, B.; MONTEBELLO, C.; MERIAUX, J.; POMMIER, S.; ARAÚJO, J. A. Study of size effects in fretting fatigue. *Tribology International*, Elsevier Ltd, v. 143, n. July 2019, p. 106087, 2020. ISSN 0301679X. Disponível em: <<https://doi.org/10.1016/j.triboint.2019.106087>>. Cited 2 times in pages 119 and 120.

CARDOSO, R. A.; NÉRON, D.; POMMIER, S.; ARAÚJO, J. A. An enrichment-based approach for the simulation of fretting problems. *Computational Mechanics*, Springer, v. 62, p. 1529–1542, 2018. Cited 2 times in pages 5 and 7.

CARDOU, A.; CLOUTIER, L.; ST-LOUIS, M.; LEBLOND, A. Acsr electrical conductor fretting fatigue at spacer clamps. In: *Standardization of fretting fatigue test methods and equipment*. [S.l.]: ASTM International, 1992. Cited in page 63.

CARPINTERI, A.; VANTADORI, S.; ZANICHELLI, A. Lifetime estimation of mechanical assemblies under constant amplitude fretting fatigue loading. *Fatigue & Fracture of Engineering Materials & Structures*, Wiley Online Library, v. 42, n. 9, p. 1927–1936, 2019. Cited in page 22.

CASTRO, F. C.; ARAÚJO, J. A.; MAMIYA, E. N.; ZOUAIN, N. Remarks on multiaxial fatigue limit criteria based on prismatic hulls and ellipsoids. *International Journal of Fatigue*, Elsevier Ltd, v. 31, n. 11-12, p. 1875–1881, 2009. ISSN 01421123. Disponível em: <<http://dx.doi.org/10.1016/j.ijfatigue.2009.01.004>>. Cited 2 times in pages 27 and 31.

CASTRO, F. C.; ARAÚJO, J. A.; ZOUAIN, N. On the application of multiaxial high-cycle fatigue criteria using the theory of critical distances. *Engineering Fracture Mechanics*, Elsevier Ltd, v. 76, n. 4, p. 512–524, 2009. ISSN 00137944. Disponível em: <<http://dx.doi.org/10.1016/j.engfracmech.2008.10.014>>. Cited 2 times in pages 36 and 37.

CATTANEO, C. Sul contatto di due corpi elastici: distribuzione locale degli sforzi. *rendiconti dell'accademia nazionale dei lincci*. *Rendiconti dell'Accademia nazionale dei Lincei*, v. 27, p. 342–348, 1938. Cited 2 times in pages 6 and 39.

CHABOCHE, J.-L. Continuum damage mechanics: Part ii—damage growth, crack initiation, and crack growth. *Journal of applied mechanics*, p. 65–72, 1988. Cited in page 24.

CHAMBON, L.; JOURNET, B. Modelling of fretting fatigue in a fracture-mechanics framework. *Tribology International*, v. 39, n. 10, p. 1220–1226, 2006. ISSN 0301679X. Cited in page 4.

CHEN, D.; LI, Y.; LIU, K.; LI, Y. A physics-informed neural network approach to fatigue life prediction using small quantity of samples. *International Journal of Fatigue*, Elsevier, v. 166, p. 107270, 2023. Cited 2 times in pages 73 and 105.

- CHEN, T.; GUESTRIN, C. XGBoost: A Scalable Tree Boosting System. In: *Proceedings of the 22nd ACM SIGKDD International Conference on Knowledge Discovery and Data Mining*. New York, NY, USA: ACM, 2016. p. 785–794. ISBN 9781450342322. Disponível em: <<https://dl.acm.org/doi/10.1145/2939672.2939785>>. Cited in page 173.
- CIAVARELLA, M.; DEMELIO, G. A review of analytical aspects of fretting fatigue , with extension to damage paraCiavarella, M. Demelio, G., 2001. A review of analytical aspects of fretting fatigue , with extension to damage parameters , and application to dovetail joints q. Internat. *International Journal of Solids and Structures*, v. 38, n. January 1999, 2001. Cited in page 3.
- CIAVARELLA, M.; DINI, D.; DEMELIO, G. Fretting fatigue, surface damage or fatigue phenomonon. In: *10th International Conference on Fracture, Honolulu*. [S.l.: s.n.], 2001. Cited in page 5.
- CIAVARELLA, M.; DINI, D.; DEMELIO, G. P. A critical assessment of damage parameters for fretting fatigue. *ASTM SPECIAL TECHNICAL PUBLICATION*, AMERICAN TECHNICAL PUBLISHERS LTD, v. 1425, p. 108–120, 2003. Cited in page 6.
- CRISTIANINI, N.; SHAWE-TAYLOR, J. *An introduction to support vector machines and other kernel-based learning methods*. [S.l.]: Cambridge university press, 2000. Cited in page 69.
- CROCCOLO, D.; AGOSTINIS, M. D.; FINI, S.; OLMI, G.; ROBUSTO, F.; SCAPECCHI, C. Fretting fatigue in mechanical joints: A literature review. *Lubricants*, MDPI, v. 10, n. 4, p. 53, 2022. Cited in page 6.
- CROSSLAND, B. Effect of large hydrostatic pressures on the torsional fatigue strength of an alloy steel. v. 138, p. 12–12, 1956. Cited 3 times in pages 24, 31, and 105.
- CYBENKO, G. Approximation by superpositions of a sigmoidal function. *Mathematics of control, signals and systems*, Springer, v. 2, n. 4, p. 303–314, 1989. Cited in page 76.
- DALPÉ, C.; GOUDREAU, S.; CLOUTIER, L.; CARDO, A. Use of eddy current technology to assist in the evaluation of the fatigue damage of electrical conductors. *Research in Nondestructive Evaluation*, The American Society for Nondestructive Testing, v. 19, n. 4, p. 181–201, 2008. Cited in page 6.
- DANG-VAN, K.; GRIVEAU, B.; MESSAGE, O. On a new multiaxial fatigue limit criterion : theory and application, biaxial and multiaxial fatigue. *EGF Publication*, v. 3, p. 479–496, jan 1982. Cited in page 37.
- DIETTERICH, T. G. Ensemble methods in machine learning. In: SPRINGER. *International workshop on multiple classifier systems*. [S.l.], 2000. p. 1–15. Cited in page 69.
- DING, J.; HOUGHTON, D.; WILLIAMS, E.; LEEN, S. Simple parameters to predict effect of surface damage on fretting fatigue. *International Journal of Fatigue*, Elsevier, v. 33, n. 3, p. 332–342, 2011. Cited in page 24.
- DINI, D.; NOWELL, D.; DYSON, I. N. The use of notch and short crack approaches to fretting fatigue threshold prediction: Theory and experimental validation. *Tribology international*, Elsevier, v. 39, n. 10, p. 1158–1165, 2006. Cited in page 6.

- DINIZ, B. d. C.; FREIRE JÚNIOR, R. C. S. Study of the fatigue behavior of composites using modular ANN with the incorporation of a posteriori failure probability. *International Journal of Fatigue*, Elsevier, v. 131, n. July 2019, p. 105357, 2020. ISSN 01421123. Disponível em: <<https://doi.org/10.1016/j.ijfatigue.2019.105357>>. Cited in page 8.
- DOBROMIRSKI, J. Variables of Fretting Process: Are There 50 of Them? In: *Standardization of Fretting Fatigue Test Methods and Equipment*. 100 Barr Harbor Drive, PO Box C700, West Conshohocken, PA 19428-2959: ASTM International, 2009. p. 60–60–7. Disponível em: <<http://www.astm.org/doiLink.cgi?STP25816S>>. Cited in page 21.
- DOCA, T.; LOYOLA, F. M.; ALBUQUERQUE, E. L. Numerical frameworks for fretting fatigue life analysis: Modeling, validation and experimental comparison. *Theoretical and Applied Fracture Mechanics*, Elsevier Ltd, v. 121, n. May, p. 103479, 2022. ISSN 01678442. Disponível em: <<https://doi.org/10.1016/j.tafmec.2022.103479>>. Cited 2 times in pages 5 and 210.
- DOMINGOS, P. A few useful things to know about machine learning. *Communications of the ACM*, ACM New York, NY, USA, v. 55, n. 10, p. 78–87, 2012. Cited 2 times in pages 69 and 72.
- DOMÍNGUEZ, J. Cyclic variations in friction forces and contact stresses during fretting fatigue. *Wear*, v. 218, n. 1, p. 43–53, 1998. ISSN 00431648. Cited 3 times in pages 47, 48, and 124.
- DOMÍNGUEZ, J.; NAVARRO, C. Analysis of fretting fatigue with spherical contact in 7075-T6 aluminum alloy. *TMS Annual Meeting*, n. February, p. 45–58, 2002. Cited in page 7.
- DOWLING, N. *Mechanical Behavior of Materials*. Fourth edition. [S.l.]: Pearson, 2013. ISBN 0131395068. Cited 4 times in pages 20, 21, 22, and 35.
- EDEN, E.; ROSE, W.; CUNNINGHAM, P. The endurance of metals: experiments on rotating beams at university college, london. *Proceedings of the Institution of Mechanical Engineers*, SAGE Publications Sage UK: London, England, v. 81, n. 1, p. 839–974, 1911. Cited in page 3.
- EDWARDS, P.; RYMAN, R.; COOK, R. *Fracture mechanics prediction of fretting fatigue under constant amplitude loading*. [S.l.]: Royal Aircraft Establishment, 1977. Cited in page 4.
- EKBERG, A. Fretting fatigue of railway axles - A review of predictive methods and an outline of a finite element model. *Proceedings of the Institution of Mechanical Engineers, Part F: Journal of Rail and Rapid Transit*, v. 218, n. 4, p. 299–316, 2004. ISSN 09544097. Cited in page 29.
- ENDO, K.; GOTO, H. Initiation and propagation of fretting fatigue cracks. *Wear*, Elsevier, v. 38, n. 2, p. 311–324, 1976. Cited in page 4.
- FADEL, A. A.; ROSA, D.; MURÇA, L. B.; FERREIRA, J. L.; ARAÚJO, J. A. Effect of high mean tensile stress on the fretting fatigue life of an Ibis steel reinforced aluminium conductor. *International Journal of Fatigue*, Elsevier Ltd, v. 42, p. 24–34, 2012. ISSN 01421123. Disponível em: <<http://dx.doi.org/10.1016/j.ijfatigue.2011.03.007>>. Cited 4 times in pages 6, 63, 162, and 217.

- FARRIS, T. N.; HARISH, G.; TIECHE, C.; SAKAGAMI, T.; SZOLWINSKI, M. P. Experimental tools for characterizing fretting contacts. *JSME International Journal Series A Solid Mechanics and Material Engineering*, The Japan Society of Mechanical Engineers, v. 43, n. 4, p. 374–383, 2000. Cited 2 times in pages 5 and 7.
- FATEMI, A.; SOCIE, D. F. A Critical Plane Approach To Multiaxial Fatigue Damage Including Out-of-Phase Loading. *Fatigue Fracture of Engineering Materials Structures*, v. 11, n. 3, p. 149–165, 1988. ISSN 14602695. Cited 2 times in pages 24 and 28.
- FELLOWS, L. J.; NOWELL, D.; HILLS, D. A. Contact stresses in a moderately thin strip (with particular reference to fretting experiments). *Wear*, v. 185, n. 1-2, p. 235–238, 1995. ISSN 00431648. Cited 2 times in pages 57 and 120.
- FENNER, A.; FIELD, J. Fatigue of an aluminium alloy under conditions of friction. *Rev. de Metallurgie*, v. 55, n. 2, p. 475–485, 1958. Cited 2 times in pages 3 and 4.
- FERJAOUI, A.; YUE, T.; Abdel Wahab, M.; HOJJATI-TALEMI, R. Prediction of fretting fatigue crack initiation in double lap bolted joint using Continuum Damage Mechanics. *International Journal of Fatigue*, Elsevier Ltd, v. 73, p. 66–76, 2015. ISSN 01421123. Disponível em: <<http://dx.doi.org/10.1016/j.ijfatigue.2014.11.012>>. Cited in page 33.
- FERRY, B. *Study of the stress gradient effect and the size effect in fretting fatigue*. Tese (Doutorado) — L'Université Paris-Saclay, 2017. Cited 7 times in pages xii, 108, 109, 112, 117, 119, and 120.
- FERRY, B.; ARAÚJO, J. A.; POMMIER, S.; DEMMOU, K. Life of a Ti-6Al-4V alloy under fretting fatigue: Study of new nonlocal parameters. *Tribology International*, Elsevier, v. 108, n. November 2016, p. 23–31, 2017. ISSN 0301679X. Disponível em: <<http://dx.doi.org/10.1016/j.triboint.2016.11.003>>. Cited 2 times in pages 30 and 36.
- FINDLEY, W. N.; COLEMAN, J. J.; HANLEY, B. C. *Theory for combined bending and torsion fatigue with data for SAE 4340 steel. Technical Report No. 1 On basic research on fatigue failures under combined stress*. United States, 1956. Disponível em: <<https://www.osti.gov/biblio/4370559https://www.osti.gov/servlets/purl/4370559>>. Cited 5 times in pages 24, 28, 86, 88, and 101.
- FONTES DO RÊGO, E. M.; ANTUNES, M. A.; de Oliveira Miranda, A. C. A methodology for fretting fatigue life estimation using strain-based fracture mechanics. *Engineering Fracture Mechanics*, Elsevier, v. 194, n. December 2017, p. 24–41, 2018. ISSN 00137944. Disponível em: <<https://doi.org/10.1016/j.engfracmech.2018.02.033>>. Cited in page 4.
- FOUVRY, S.; GALLIEN, H.; BERTHEL, B. From uni- to multi-axial fretting-fatigue crack nucleation: Development of a stress-gradient-dependent critical distance approach. *International Journal of Fatigue*, Elsevier Ltd, v. 62, p. 194–209, 2014. ISSN 01421123. Disponível em: <<http://dx.doi.org/10.1016/j.ijfatigue.2013.05.016>>. Cited 4 times in pages 30, 31, 36, and 210.
- FOUVRY, S.; KAPSA, P.; VINCENT, L. Quantification of fretting damage. *Wear*, Elsevier, v. 200, n. 1-2, p. 186–205, 1996. Cited in page 7.
- FOUVRY, S.; NOWELL, D.; KUBIAK, K.; HILLS, D. Prediction of fretting crack propagation based on a short crack methodology. *Engineering Fracture Mechanics*, Elsevier, v. 75, n. 6, p. 1605–1622, 2008. Cited in page 6.

- FREIRE JÚNIOR, R. C. S.; NETO, A. D. D.; AQUINO, E. M. F. D. Comparative study between ann models and conventional equations in the analysis of fatigue failure of grfp. *International journal of fatigue*, Elsevier, v. 31, n. 5, p. 831–839, 2009. Cited in page 8.
- GAILLIEGUE, T. *Effects of phase-angle between the fretting and the bulk fatigue loads on the life of the AL 7050-T7451 and ASTM 743 CA6NM*. 128 p. Tese (Doutorado) — University of Brasilia, 2018. Cited 6 times in pages xii, 109, 112, 118, 119, and 120.
- GAILLIEGUE, T.; DOCA, T.; ARAÚJO, J. A.; FERREIRA, J. L. Fretting life of the Al7050-T7451 under out-of-phase loads: Numerical and experimental analysis. *Theoretical and Applied Fracture Mechanics*, Elsevier, v. 106, n. July 2019, p. 102492, 2020. ISSN 01678442. Disponível em: <<https://doi.org/10.1016/j.tafmec.2020.102492>>. Cited in page 30.
- GAN, L.; WU, H.; ZHONG, Z. Fatigue life prediction considering mean stress effect based on random forests and kernel extreme learning machine. *International Journal of Fatigue*, Elsevier Ltd, v. 158, n. December 2021, p. 106761, 2022. ISSN 0142-1123. Disponível em: <<https://doi.org/10.1016/j.ijfatigue.2022.106761>>. Cited in page 173.
- GANDIOLLE, C.; FOUVRY, S. Fretting fatigue crack propagation rate under variable loading conditions. *Frattura ed Integrità Strutturale*, v. 10, n. 35, p. 232–241, 2016. Cited in page 7.
- GARCIA, M. A.; BADIBANGA, R. K.; ARAÚJO, J. A.; FERREIRA, J. L.; SILVA, C. R. M. da. Fretting fatigue tests on 6201-t81 aluminum alloy conductor wires at room temperature and 75° c. *Wear*, Elsevier, p. 205321, 2024. Cited 2 times in pages 163 and 208.
- GARCIA, M. A.; Mendes Veloso, L. A.; Comes de Castro, F.; ARAÚJO, J. A.; FERREIRA, J. L.; Moreira da Silva, C. R. Experimental device for fretting fatigue tests in 6201 aluminum alloy wires from overhead conductors. *Wear*, v. 460-461, n. August, 2020. ISSN 00431648. Cited 4 times in pages 65, 66, 163, and 176.
- GAßNER, E. Zur gestaltung eines dauerbruchsicheren tragschrauben-holmanschlusses. *DVL-Bericht, VM 466*, 1937. Cited in page 19.
- GAßNER, E. Festigkeitsversuche mit wiederholter beanspruchung im flugzeugbau. *Deutsche Luftwacht, Ausg. Luftwissen*, v. 6, p. 61–64, 1939. Cited in page 19.
- GAßNER, E. Ergebnisse aus betriebsfestigkeits-versuchen mit stahl- und leichtmetallbauteilen. In: *Bericht, Vol. 152*. Jena, Lilienthalgesellschaft für Luftfahrtforschung, Berlin: [s.n.], 1942. Cited in page 19.
- GERBER, W. Relation between the superior and inferior stresses of a cycle of limiting stress. *Zeit. Bayerischen Arch. Ing.-Vereins*, 1874. Cited in page 19.
- GIANNAKOPOULOS; SURESH; CHENUT. Similarities of stress concentrations in contact at round punches and fatigue at notches: implications to fretting fatigue crack initiation. *Fatigue & fracture of engineering materials & structures*, Wiley Online Library, v. 23, n. 7, p. 561–571, 2000. Cited in page 6.
- GIANNAKOPOULOS, A.; SURESH, S. A three-dimensional analysis of fretting fatigue. *Acta Materialia*, Elsevier, v. 46, n. 1, p. 177–192, 1998. Cited 2 times in pages 5 and 6.

- GLODEK, G.; NAZABAL, A.; LLAVORI, I.; TALEMI, R. Numerical modelling of microstructure inhomogeneity to reproduce experimentally observed scatter in fretting fatigue lifetimes. *Tribology International*, v. 185, n. April, 2023. ISSN 0301679X. Cited 4 times in pages 5, 23, 29, and 36.
- GLODEK, G.; TALEMI, R. An applied approach for estimating fretting fatigue lifetime of dovetail joints using coupon scale test data. *Theoretical and Applied Fracture Mechanics*, Elsevier Ltd, v. 121, n. April, p. 103455, 2022. ISSN 0167-8442. Disponível em: <<https://doi.org/10.1016/j.tafmec.2022.103455>>. Cited 2 times in pages 3 and 55.
- GLOROT, X.; BENGIO, Y. Understanding the difficulty of training deep feedforward neural networks. *Journal of Machine Learning Research*, v. 9, p. 249–256, 2010. ISSN 15324435. Cited 2 times in pages 82 and 129.
- GOLDEN, P. J.; GRANDT, A. F. Fracture mechanics based fretting fatigue life predictions in Ti-6Al-4V. *Engineering Fracture Mechanics*, v. 71, n. 15, p. 2229–2243, 2004. ISSN 00137944. Cited in page 4.
- GOLLER, C.; KUCHLER, A. Learning task-dependent distributed representations by backpropagation through structure. In: IEEE. *Proceedings of International Conference on Neural Networks (ICNN'96)*. [S.l.], 1996. v. 1, p. 347–352. Cited in page 74.
- GOMES, R. C.; ARAÚJO, J. A.; CARDOSO, R. A.; FERREIRA, J. L.; SILVA, C. R. Fatigue life prediction using critical distance on aluminum alloy wire containing indentation produced marks. *Theoretical and Applied Fracture Mechanics*, Elsevier, v. 128, p. 104135, 2023. Cited in page 163.
- GOODMAN, J. Mechanics applied to engineering longmans. *Green and Co., London*, 1899. Cited 2 times in pages 19 and 22.
- GORJI, M. B.; PANNEMAECKER, A. de; SPEVACK, S. Machine learning predicts fretting and fatigue key mechanical properties. *International Journal of Mechanical Sciences*, Elsevier Ltd, v. 215, n. November 2021, p. 106949, 2022. ISSN 00207403. Disponível em: <<https://doi.org/10.1016/j.ijmecsci.2021.106949>>. Cited 2 times in pages 24 and 213.
- GRIFFITH, A. A. The phenomena of rupture and flow in solids. *Philosophical Transactions of the Royal Society A: Mathematical, Physical and Engineering Sciences*, v. 221, p. 163–198, 1921. Cited in page 33.
- HADDAD, M. E.; DOWLING, N.; TOPPER, T.; SMITH, K. J integral applications for short fatigue cracks at notches. *International Journal of Fracture*, Springer, v. 16, p. 15–30, 1980. Cited in page 34.
- HAFID, F.; GUEGUIN, M.; LAURENT, V.; MOUGEOT, M.; VAYATIS, N.; YANG, C.; GHIDAGLIA, J.-M. Hybrid modelling for lifetime prediction. In: SPRINGER. *Engineering Assets and Public Infrastructures in the Age of Digitalization: Proceedings of the 13th World Congress on Engineering Asset Management*. [S.l.], 2020. p. 387–395. Cited in page 9.
- HAIGH, B. A new machine for alternating load tests. *Engineering*, v. 24, p. 721–723, 1912. Cited in page 19.
- HAIGH, B. The endurance of metals under alternating stresses. *JW Scot. Iron St. Inst*, v. 23, p. 17–56, 1915. Cited in page 19.

- HALAMKA, J.; BARTOŠÁK, M.; ŠPANIEL, M. Using hybrid physics-informed neural networks to predict lifetime under multiaxial fatigue loading. *Engineering Fracture Mechanics*, Elsevier, v. 289, p. 109351, 2023. Cited 2 times in pages 73 and 105.
- HAMILTON, G. M. Explicit equations for the stresses beneath a sliding spherical contact. *Proceedings of the Institution of Mechanical Engineers, Part C: Journal of Mechanical Engineering Science*, v. 197, n. 1, p. 53–59, 1983. ISSN 20412983. Cited 3 times in pages 47, 48, and 124.
- HAMILTON, G. M.; GOODMAN, L. The stress field created by a circular sliding contact. *Journal of Applied Mechanics*, ASME International, v. 33, n. 2, p. 371–376, 1966. Cited in page 47.
- HAN, S.; KHATIR, S.; Abdel Wahab, M. A deep learning approach to predict fretting fatigue crack initiation location. *Tribology International*, Elsevier Ltd, v. 185, n. January, p. 108528, 2023. ISSN 0301679X. Disponível em: <<https://doi.org/10.1016/j.triboint.2023.108528>>. Cited 3 times in pages 10, 24, and 154.
- HAN, S.; KHATIR, S.; WANG, C.; Abdel Wahab, M. An improved Artificial Neural Network for the direct prediction of fretting fatigue crack initiation lifetime. *Tribology International*, Elsevier Ltd, v. 183, n. February, p. 108411, 2023. ISSN 0301679X. Disponível em: <<https://doi.org/10.1016/j.triboint.2023.108411>>. Cited in page 10.
- HASTIE, T.; TIBSHIRANI, R.; FRIEDMAN, J. H.; FRIEDMAN, J. H. *The elements of statistical learning: data mining, inference, and prediction*. [S.l.]: Springer, 2009. v. 2. Cited 2 times in pages 68 and 70.
- HATTORI, T.; NAKAMURA, M.; WATANABE, T. Simulation of fretting-fatigue life by using stress-singularity parameters and fracture mechanics. *Tribology international*, Elsevier, v. 36, n. 2, p. 87–97, 2003. Cited in page 24.
- HAYKIN, S. *Neural Networks and Learning Machines Haykin*. Pearson; 3. [S.l.: s.n.], 2008. 936 p. Cited 13 times in pages 68, 69, 72, 73, 75, 77, 81, 93, 96, 129, 173, 174, and 213.
- HENG, J.; ZHOU, Z.; ZOU, Y.; KAEWUNRUEN, S. GPR-assisted evaluation of probabilistic fatigue crack growth in rib-to-deck joints in orthotropic steel decks considering mixed failure models. *Engineering Structures*, Elsevier Ltd, v. 252, n. May 2021, p. 113688, 2022. ISSN 18737323. Disponível em: <<https://doi.org/10.1016/j.engstruct.2021.113688>>. Cited 2 times in pages 173 and 174.
- HERTZ, H. Ueber die berührung fester elastischer körper. Walter de Gruyter, Berlin/New York Berlin, New York, 1882. Cited 2 times in pages 6 and 38.
- HILLS, D.; NOWELL, D. *Mechanics of Fretting Fatigue*. [S.l.: s.n.], 1993. 246 p. Cited 2 times in pages 6 and 45.
- HILLS, D.; NOWELL, D.; O'CONNOR, J. On the mechanics of fretting fatigue. *Wear*, Elsevier, v. 125, n. 1-2, p. 129–146, 1988. Cited in page 5.
- HILLS, D.; NOWELL, D.; SACKFIELD, A. *Mechanics of Elastic Contacts*. [S.l.]: Butterworth-Heinemann Ltd, 1993. Cited 3 times in pages 7, 38, and 47.

- HILLS, D. A.; DINI, D. The use of asymptotic solution in fretting fatigue. *The 15th European Conference of Fracture*, 2004. Disponível em: <[/home/bellecave/THESIS/Biblio/BIBLIOGRAPHY/Hills2004-Theuseofasumptoticsolutioninfrettingfatigue..pdf](#)>. Cited in page 6.
- HILLS, D. A.; NOWELL, D. Fretting Fatigue Tests. v. 37, n. 2, p. 153–167, 1994. Cited in page 38.
- HILLS, D. A.; NOWELL, D. Mechanics of fretting fatigue - Oxford's contribution. *Tribology International*, Elsevier, v. 76, p. 1–5, 2014. ISSN 0301679X. Disponível em: <<http://dx.doi.org/10.1016/j.triboint.2013.09.015>>. Cited in page 7.
- HOEPPNER, D.; GOSS, G. Research on the mechanism of fretting fatigue. *Corrosion fatigue: Chemistry, mechanics and microstructure*, National Association of Corrosion Engineers, 1972. Cited in page 4.
- HOEPPNER, D. W. Comments on “initiation and propagation of fretting fatigue cracks”. *Wear*, Elsevier, v. 43, n. 2, p. 267–268, 1977. Cited in page 4.
- HOJJATI-TALEMI, R.; Abdel Wahab, M.; De Pauw, J.; De Baets, P. Prediction of fretting fatigue crack initiation and propagation lifetime for cylindrical contact configuration. *Tribology International*, Elsevier, v. 76, p. 73–91, 2014. ISSN 0301679X. Disponível em: <<http://dx.doi.org/10.1016/j.triboint.2014.02.017>>. Cited 5 times in pages xi, 108, 112, 115, and 119.
- HOJJATI-TALEMI, R.; WAHAB, M. A. Fretting fatigue crack initiation lifetime predictor tool: Using damage mechanics approach. *Tribology International*, Elsevier, v. 60, p. 176–186, 2013. ISSN 0301679X. Disponível em: <<http://dx.doi.org/10.1016/j.triboint.2012.10.028>>. Cited 4 times in pages 4, 7, 29, and 210.
- HORŇAS, J.; BĚHAL, J.; HOMOLA, P.; SENCK, S.; HOLZLEITNER, M.; GODJA, N.; PÁSZTOR, Z.; HEGEDŮS, B.; DOUBRAVA, R.; RŽEK, R. *et al.* Modelling fatigue life prediction of additively manufactured ti-6al-4v samples using machine learning approach. *International Journal of Fatigue*, Elsevier, v. 169, p. 107483, 2023. Cited in page 173.
- HORNIK, K.; STINCHCOMBE, M.; WHITE, H. Multilayer feedforward networks are universal approximators. *Neural networks*, Elsevier, v. 2, n. 5, p. 359–366, 1989. Cited in page 76.
- HU, D.; SU, X.; LIU, X.; MAO, J.; SHAN, X.; WANG, R. Bayesian-based probabilistic fatigue crack growth evaluation combined with machine-learning-assisted GPR. *Engineering Fracture Mechanics*, Elsevier, v. 229, n. October 2019, p. 106933, 2020. ISSN 00137944. Disponível em: <<https://doi.org/10.1016/j.engfracmech.2020.106933>>. Cited 2 times in pages 173 and 174.
- INFANTE-GARCÍA, D.; DÍAZ-ÁLVAREZ, A.; BELDA, R.; DÍAZ-ÁLVAREZ, J.; CANTERO, J. L.; GINER, E.; MIGUÉLEZ, M. H. Influence of machining parameters on fretting fatigue life of Inconel 718. *International Journal of Fatigue*, v. 162, n. March, 2022. ISSN 01421123. Cited 2 times in pages 33 and 210.
- INFANTE-GARCIA, D.; ZABALA, A.; GINER, E.; LLAVORI, I. On the use of the theory of critical distances with mesh control for fretting fatigue life assessment in complete and nearly complete contacts. *Theoretical and Applied Fracture Mechanics*,

- Elsevier Ltd, v. 121, n. May, p. 103476, 2022. ISSN 01678442. Disponível em: <<https://doi.org/10.1016/j.tafmec.2022.103476>>. Cited in page 36.
- INGLIS, C. Stresses in a plate due to the presence of cracks and sharp corners. *Trans Inst Naval Archit*, v. 55, p. 219–241, 1913. Cited in page 33.
- IRWIN, G. R. *Elasticity and Plasticity / Elastizität und Plastizität*. Berlin, Heidelberg: Springer Berlin Heidelberg, 1958. v. 3 / 6. (Handbuch der Physik / Encyclopedia of Physics, v. 3 / 6). Cited 2 times in pages 33 and 34.
- JAIN, A. K.; DUBES, R. C. *Algorithms for clustering data*. [S.l.]: Prentice-Hall, Inc., 1988. Cited in page 69.
- JAMES, G.; WITTEN, D.; HASTIE, T.; TIBSHIRANI, R. *et al. An introduction to statistical learning*. [S.l.]: Springer, 2013. v. 112. Cited 2 times in pages 68 and 72.
- JIMENEZ-MARTINEZ, M.; ALFARO-PONCE, M. Fatigue damage effect approach by artificial neural network. *International Journal of Fatigue*, v. 124, n. 2901, p. 42–47, 2019. ISSN 01421123. Cited in page 8.
- JOHNSON, K. *Contact Mechanics*. Cambridge University Press, 1985. ISBN 9781139171731. Disponível em: <<https://doi.org/10.1017/CBO9781139171731>>. Cited 3 times in pages 6, 7, and 38.
- JOHNSON, K. L.; KENDALL, K.; ROBERTS, a. Surface energy and the contact of elastic solids. *Proceedings of the royal society of London. A. mathematical and physical sciences*, The Royal Society London, v. 324, n. 1558, p. 301–313, 1971. Cited in page 7.
- JURKIEWICZ, B.; SMYRAK, B. Studies on the evolution of fatigue strength of aluminium wires for overhead line conductors. *Materials*, MDPI, v. 17, n. 11, p. 2537, 2024. Cited in page 163.
- JUSTNN. *Neural Planner Software*. ‘JustNN – free neural network software’. [S.l.], 2015. Accessed date: 3 March 2021. Disponível em: <[www.justnn.com](http://www.justnn.com)>. Cited in page 100.
- KALLMEYER, A. R.; KRGO, A.; KURATH, P. Evaluation of multiaxial fatigue life prediction methodologies for Ti-6Al-4V. *Journal of Engineering Materials and Technology*, v. 124, n. 2, p. 229–237, 2002. ISSN 00944289. Cited in page 112.
- KALOMBO, R.; MARTÍNEZ, J.; FERREIRA, J.; SILVA, C. D.; ARAÚJO, J. Comparative fatigue resistance of overhead conductors made of aluminium and aluminium alloy: tests and analysis. *Procedia Engineering*, Elsevier, v. 133, p. 223–232, 2015. Cited 4 times in pages 6, 63, 65, and 162.
- KALOMBO, R.; PESTANA, M.; FERREIRA, J.; SILVA, C. da; ARAÚJO, J. Influence of the catenary parameter (h/w) on the fatigue life of overhead conductors. *Tribology International*, Elsevier, v. 108, p. 141–149, 2017. Cited 2 times in pages 6 and 162.
- KALOMBO, R. B.; PESTANA, M. S.; Freire Júnior, R. C.; FERREIRA, J. L.; SILVA, C. R.; VELOSO, L. A.; CÂMARA, E. C.; ARAÚJO, J. A. Fatigue life estimation of an all aluminium alloy 1055 MCM conductor for different mean stresses using an artificial neural network. *International Journal of Fatigue*, Elsevier, v. 140, n. July, p. 105814, 2020. ISSN 01421123. Disponível em: <<https://doi.org/10.1016/j.ijfatigue.2020.105814>>. Cited 3 times in pages 3, 7, and 9.

- KANTIMATHI, A.; ALIC, J. The effects of periodic high loads on fretting fatigue. *Journal of Engineering Materials and Technology* 103, p. 223–228, 1981. Cited in page 7.
- KINYON, S. E.; HOEPFNER, D. W. Spectrum load effects on the fretting behavior of ti-6al-4v. *ASTM SPECIAL TECHNICAL PUBLICATION*, AMERICAN TECHNICAL PUBLISHERS LTD, v. 1367, p. 100–118, 2000. Cited in page 7.
- KIRKPATRICK, G. *Fretting fatigue analysis and palliatives*. Tese (Doutorado) — Massachusetts Institute of Technology, 1999. Disponível em: <<http://oai.dtic.mil/oai/oai?verb=getRecord&metadataPrefix=html&identifier=ADA372220>>. Cited 8 times in pages xii, 108, 109, 112, 115, 118, 119, and 120.
- KITAGAWA, H.; TAKAHASHI, S. Applicability of fracture mechanics to very small cracks or the cracks in the early stage. In: *Proc. 2nd Int. Conf. on Mechanical Behaviour of Materials*. [S.l.: s.n.], 1976. p. 627–631. Cited in page 20.
- KOHONEN, T. Self-organized formation of topologically correct feature maps. *Biological cybernetics*, Springer, v. 43, n. 1, p. 59–69, 1982. Cited in page 74.
- KONDO, Y.; SAKAE, C.; KUBOTA, M.; KITAHARA, H.; YANAGIHARA, K. Fretting fatigue under variable loading below fretting fatigue limit. *Fatigue & Fracture of Engineering Materials & Structures*, Wiley Online Library, v. 29, n. 3, p. 191–199, 2006. Cited in page 7.
- KOUANGA, C. T.; JONES, J. D.; REVILL, I.; WORMALD, A.; NOWELL, D.; DWYER-JOYCE, R. S.; ARAÚJO, J. A.; SUSMEL, L. On the estimation of finite lifetime under fretting fatigue loading. *International Journal of Fatigue*, Elsevier, v. 112, n. December 2017, p. 138–152, 2018. ISSN 01421123. Disponível em: <<https://doi.org/10.1016/j.ijfatigue.2018.03.013>>. Cited 2 times in pages 30 and 120.
- KOUANGA, C. T.; JONES, J. D.; REVILL, I.; WORMALD, A.; NOWELL, D.; DWYER-JOYCE, R. S.; SUSMEL, L. A variable amplitude fretting fatigue life estimation technique: Formulation and experimental validation. *Tribology International*, Elsevier Ltd, v. 178, n. PA, p. 108055, 2023. ISSN 0301679X. Disponível em: <<https://doi.org/10.1016/j.triboint.2022.108055>>. Cited 4 times in pages 7, 30, 36, and 154.
- LALONDE, S.; GUILBAULT, R.; LANGLOIS, S. Numerical analysis of acsr conductor–clamp systems undergoing wind-induced cyclic loads. *IEEE Transactions on Power Delivery*, IEEE, v. 33, n. 4, p. 1518–1526, 2017. Cited 2 times in pages 6 and 162.
- LALONDE, S.; GUILBAULT, R.; LANGLOIS, S. Numerical analysis of ACSR conductor-clamp systems undergoing wind-induced cyclic loads. *IEEE Transactions on Power Delivery*, IEEE, v. 33, n. 4, p. 1518–1526, 2018. ISSN 08858977. Cited 2 times in pages 163 and 172.
- LALONDE, S.; GUILBAULT, R.; LÉGERON, F. Modeling multilayered wire strands, a strategy based on 3D finite element beam-to-beam contacts - Part I: Model formulation and validation. *International Journal of Mechanical Sciences*, Elsevier Ltd, v. 126, n. December 2016, p. 281–296, 2017. ISSN 00207403. Disponível em: <<http://dx.doi.org/10.1016/j.ijmecsci.2016.12.014>>. Cited 2 times in pages 172 and 186.
- LANTEIGNE, J.; CLOUTIER, L.; CARDOU, A. *Fatigue life of aluminum wires in all aluminum and ACSR conductors*. [S.l.], 1986. Cited in page 6.

- LEMAITRE, J. A continuous damage mechanics model for ductile fracture. p. 83–89, 1985. Cited in page 24.
- LÉVESQUE, F.; GOUDREAU, S.; CARDOU, A.; CLOUTIER, L. Strain measurements on acsr conductors during fatigue tests i—experimental method and data. *IEEE Transactions on Power Delivery*, IEEE, v. 25, n. 4, p. 2825–2834, 2010. Cited 2 times in pages 6 and 162.
- LI, A.; HU, W.; ZHAN, Z.; MENG, Q. A novel continuum damage mechanics-based approach for thermal corrosion fatigue (tcf) life prediction of aluminum alloys. *International Journal of Fatigue*, Elsevier, v. 163, p. 107065, 2022. Cited in page 24.
- LI, X.; ZUO, Z.; QIN, W. A fretting related damage parameter for fretting fatigue life prediction. *International Journal of Fatigue*, Elsevier Ltd, v. 73, p. 110–118, 2015. ISSN 01421123. Disponível em: <<http://dx.doi.org/10.1016/j.ijfatigue.2014.12.003>>. Cited in page 5.
- LINDSTRÖM, S. B. Continuous-time, high-cycle fatigue model for nonproportional stress with validation for 7075-T6 aluminum alloy. *International Journal of Fatigue*, Elsevier, v. 140, n. July, p. 105839, 2020. ISSN 01421123. Disponível em: <<https://doi.org/10.1016/j.ijfatigue.2020.105839>>. Cited in page 109.
- LISKIEWICZ, T.; DINI, D. *Fretting Wear and Fretting Fatigue: Fundamental Principles and Applications*. 3. ed. Elsevier, 2023. ISBN 978-0-12-824096-0. Disponível em: <<https://www.elsevier.com/books/fretting-wear-and-fretting-fatigue/liskiewicz/9780128240960>>. Cited in page 66.
- LIU, W.; CHEN, Z.; HU, Y. XGBoost algorithm-based prediction of safety assessment for pipelines. *International Journal of Pressure Vessels and Piping*, Elsevier Ltd, v. 197, n. May 2021, p. 104655, jun 2022. ISSN 03080161. Disponível em: <<https://doi.org/10.1016/j.ijpvp.2022.104655><https://linkinghub.elsevier.com/retrieve/pii/S0308016122000473>>. Cited in page 173.
- LIU, Y.; YUAN, H. A hierarchical mechanism-informed neural network approach for assessing fretting fatigue of dovetail joints. *International Journal of Fatigue*, Elsevier Ltd, v. 168, n. June 2022, p. 107453, 2023. ISSN 01421123. Disponível em: <<https://doi.org/10.1016/j.ijfatigue.2022.107453>>. Cited 5 times in pages 6, 11, 33, 154, and 163.
- LOBATO DA SILVA, B.; de ALMEIDA FERREIRA, J. L.; OLIVEIRA, F.; ARAÚJO, J. A. Influence of mean stress on the fatigue strength of ASTM A743 CA6NM alloy steel. *Frattura ed Integrità Strutturale*, v. 4, n. 14, p. 17–26, 2010. Cited 2 times in pages 109 and 112.
- LYKINS, C. D.; MALL, S.; JAIN, V. A shear stress-based parameter for fretting fatigue crack initiation. *Fatigue and Fracture of Engineering Materials and Structures*, v. 24, n. 7, p. 461–473, 2001. ISSN 8756758X. Cited in page 29.
- MADGE, J.; LEEN, S.; MCCOLL, I.; SHIPWAY, P. Contact-evolution based prediction of fretting fatigue life: Effect of slip amplitude. *Wear*, Elsevier, v. 262, n. 9-10, p. 1159–1170, 2007. Cited in page 5.
- MADGE, J. J.; LEEN, S. B.; SHIPWAY, P. H. A combined wear and crack nucleation-propagation methodology for fretting fatigue prediction. *International Journal of Fatigue*, v. 30, n. 9, p. 1509–1528, 2008. ISSN 01421123. Cited in page 4.

MAJZOBI, G. H.; KAZEMI, M. A. A New Investigation on the Effect of Re-shot Peening on Fretting Fatigue Behavior of A17075-T6 A New Investigation on the Effect of Re-shot Peening on Fretting Fatigue Behavior of A17075-T6. *Tribology Transactions*, v. 56, p. 943–952, 2013. ISSN 1040-2004. Disponível em: <<https://doi.org/10.1080/10402004.2013.812761>>. Cited 3 times in pages 6, 8, and 24.

MALEKI, E.; UNAL, O.; Reza Kashyzadeh, K. Fatigue behavior prediction and analysis of shot peened mild carbon steels. *International Journal of Fatigue*, Elsevier Ltd, Mechanical Engineering Department, Sharif University of Technology-International Campus Kish Island, Iran, v. 116, p. 48–67, 2018. ISSN 01421123 (ISSN). Disponível em: <<https://www.scopus.com/inward/record.uri?eid=2-s2.0-85048422014&doi=10.1016%2Fj.ijfatigue.2018.06.004&partnerID=40&md5=b46b94949c3a12aa0e681de0ba146783>>. Cited in page 8.

MAMIYA, E. N.; ARAÚJO, J. A. Fatigue limit under multiaxial loadings: On the definition of the equivalent shear stress. *Mechanics Research Communications*, v. 29, n. 2-3, p. 141–151, 2002. ISSN 00936413. Cited in page 31.

MAMIYA, E. N.; ARAÚJO, J. A.; CASTRO, F. C. Prismatic hull: A new measure of shear stress amplitude in multiaxial high cycle fatigue. *International Journal of Fatigue*, Elsevier Ltd, v. 31, n. 7, p. 1144–1153, 2009. ISSN 01421123. Disponível em: <<http://dx.doi.org/10.1016/j.ijfatigue.2008.12.010>>. Cited in page 31.

MAMIYA, E. N.; CASTRO, F. C.; ARAÚJO, J. A. Recent developments on multiaxial fatigue: The contribution of the University of Brasília. *Theoretical and Applied Fracture Mechanics*, Elsevier Ltd, v. 73, p. 48–59, 2014. ISSN 01678442. Disponível em: <<http://dx.doi.org/10.1016/j.tafmec.2014.06.007>>. Cited in page 32.

MARQUARDT, C.; ZENNER, H. Lifetime calculation under variable amplitude loading with the application of artificial neural networks. *International Journal of Fatigue*, v. 27, n. 8, p. 920–927, 2005. ISSN 01421123. Cited in page 8.

MARTÍN, V.; VÁZQUEZ, J.; NAVARRO, C.; DOMÍNGUEZ, J. Effect of shot peening residual stresses and surface roughness on fretting fatigue strength of Al 7075-T651. *Tribology International*, v. 142, n. July 2019, 2020. ISSN 0301679X. Cited 9 times in pages vii, xii, 57, 108, 112, 116, 119, 138, and 139.

MASSINGHAM, M.; IRVING, P. The effect of variable amplitude loading on stress distribution within a cylindrical contact subjected to fretting fatigue. *Tribology international*, Elsevier, v. 39, n. 10, p. 1084–1091, 2006. Cited in page 7.

MATOS, I.; ROCHA, P.; KALOMBO, R.; VELOSO, L.; ARAÚJO, J.; CASTRO, F. Fretting fatigue of 6201 aluminum alloy wires of overhead conductors. *International Journal of Fatigue*, Elsevier, v. 141, p. 105884, 2020. Cited 4 times in pages 6, 163, 166, and 176.

MATOS, I. M.; ARAÚJO, J. A.; CASTRO, F. C. Fretting fatigue performance and life prediction of 1120 aluminum alloy wires of overhead conductors. *Theoretical and Applied Fracture Mechanics*, Elsevier Ltd, v. 121, n. April, p. 103521, 2022. ISSN 01678442. Disponível em: <<https://doi.org/10.1016/j.tafmec.2022.103521>>. Cited 11 times in pages xii, 29, 65, 163, 164, 166, 167, 168, 170, 175, and 176.

- MATOS, I. M.; ARAÚJO, J. A.; CASTRO, F. C. Life prediction of 6201-T81 aluminum alloy wires under fretting fatigue and variable amplitude loading. *Tribology International*, Elsevier Ltd, v. 183, n. January, p. 108407, 2023. ISSN 0301-679X. Disponível em: <<https://doi.org/10.1016/j.triboint.2023.108407>>. Cited 12 times in pages [xiii](#), [23](#), [36](#), [55](#), [154](#), [163](#), [164](#), [166](#), [167](#), [168](#), [170](#), and [176](#).
- MATSUISHI, M.; ENDO, T. Fatigue of metals subjected to varying stress. *Japan Society of Mechanical Engineers, Fukuoka, Japan*, v. 68, n. 2, p. 37–40, 1968. Cited in page [24](#).
- MCDIARMID, D. L. A General Criterion for High Cycle Multiaxial Fatigue Failure. *Fatigue Fracture of Engineering Materials Structures*, v. 14, n. 4, p. 429–453, 1991. ISSN 14602695. Cited 2 times in pages [24](#) and [28](#).
- MCDOWELL, J. R. Fretting corrosion tendencies of several combinations of materials. *Symposium on Fretting Corrosion*, ASTM, p. 24–39, 1953. Cited in page [3](#).
- MEGGIOLARO, M. A.; CASTRO, J. T. P. D. The moment of inertia method to calculate equivalent ranges in non-proportional tension-torsion histories. *Journal of Materials Research and Technology*, Korea Institute of Oriental Medicine, v. 4, n. 3, p. 229–234, 2015. ISSN 22387854. Disponível em: <<http://dx.doi.org/10.1016/j.jmrt.2015.01.004>>. Cited in page [27](#).
- MEGUID, S.; KANTH, P.; CZEKANSKI, A. Finite element analysis of fir-tree region in turbine discs. *Finite elements in analysis and design*, Elsevier, v. 35, n. 4, p. 305–317, 2000. Cited in page [55](#).
- MEN, H.; ZHOU, W.; HUANG, H.; WANG, M.; FU, X. Study of the point method for fretting fatigue life prediction. *International Journal of Mechanical Sciences*, Elsevier, v. 275, p. 109297, 2024. Cited in page [210](#).
- MINDLIN, R. Compliance of elastic bodies in contact. *Journal of Applied Mechanics*, v. 16, p. 259–268, 1949. Cited in page [39](#).
- MINER, M. A. Cumulative damage in fatigue. *Journal of Applied Mechanics*, American Society of Mechanical Engineers, 1945. Cited in page [23](#).
- MOËS, N.; DOLBOW, J.; BELYTSCHKO, T. A finite element method for crack growth without remeshing. *International journal for numerical methods in engineering*, v. 46, n. 1, p. 131–150, 1999. Cited in page [57](#).
- MONTALVO, S.; FOUVRY, S.; MARTINEZ, M. A hybrid analytical-fem 3d approach including wear effects to simulate fretting fatigue endurance: application to steel wires in crossed contact. *Tribology International*, Elsevier, p. 108713, 2023. Cited in page [65](#).
- MOORE, H.; KOMMERS, J. Fatigue of metals under repeated stress. *Chemical and Metallurgical Engineering*, v. 25, n. 25, p. 1141–1144, 1921. Cited in page [19](#).
- MORENO-RUBIO, M.; VÁZQUEZ, J.; NAVARRO, C.; DOMÍNGUEZ, J. Experimental study on the fretting fatigue of Inconel 718 superalloy. *Tribology International*, v. 186, n. May, 2023. Cited in page [210](#).
- MUÑOZ, S.; NAVARRO, C.; DOMÍNGUEZ, J. Application of fracture mechanics to estimate fretting fatigue endurance curves. *Engineering Fracture Mechanics*, v. 74, n. 14, p. 2168–2186, 2007. ISSN 00137944. Cited 9 times in pages [vii](#), [xii](#), [61](#), [108](#), [112](#), [116](#), [119](#), [138](#), and [139](#).

- MUSKHELISHVILI, N. I. *Some Basic Problems of the Mathematical Theory of Elasticity*. [S.l.]: Springer Netherlands, 1977. Cited 3 times in pages 6, 43, and 86.
- MUTOH, Y. Mechanisms of fretting fatigue. *JSME international journal. Ser. A, Mechanics and material engineering*, The Japan Society of Mechanical Engineers, v. 38, n. 4, p. 405–415, 1995. Cited in page 7.
- MUTOH, Y.; TANAKA, K.; KONDOH, M. Fretting fatigue in sup9 spring steel under random loading. *JSME international journal. Ser. 1, Solid mechanics, strength of materials*, The Japan Society of Mechanical Engineers, v. 32, n. 2, p. 274–281, 1989. Cited in page 7.
- MUTOH, Y.; XU, J.-Q. Fracture mechanics approach to fretting fatigue and problems to be solved. *Tribology International*, Elsevier, v. 36, n. 2, p. 99–107, 2003. Cited in page 5.
- NAVARRO, C.; MUÑOZ, S.; DOMÍNGUEZ, J. On the use of multiaxial fatigue criteria for fretting fatigue life assessment. *International Journal of Fatigue*, v. 30, n. 1, p. 32–44, 2008. ISSN 01421123. Cited 2 times in pages 7 and 29.
- NAVARRO, C.; VÁZQUEZ, J.; DOMÍNGUEZ, J. A general model to estimate life in notches and fretting fatigue. *Engineering Fracture Mechanics*, Elsevier Ltd, v. 78, n. 8, p. 1590–1601, 2011. ISSN 00137944. Disponível em: <<http://dx.doi.org/10.1016/j.engfracmech.2011.01.011>>. Cited 5 times in pages 4, 88, 89, 108, and 119.
- NAWROCKI, A.; LABROSSE, M. A finite element model for simple straight wire rope strands. *Computers & Structures*, Elsevier, v. 77, n. 4, p. 345–359, 2000. Cited in page 172.
- NESLÁDEK, M.; ŠPANIEL, M.; JURENKA, J.; RŮŽIČKA, J.; KUŽELKA, J. Fretting fatigue - Experimental and numerical approaches. *International Journal of Fatigue*, v. 44, p. 61–73, 2012. ISSN 01421123. Cited in page 5.
- NEU, R. W. Progress in standardization of fretting fatigue terminology and testing. *Tribology International*, Elsevier, v. 44, n. 11, p. 1371–1377, 2011. ISSN 0301679X. Disponível em: <<http://dx.doi.org/10.1016/j.triboint.2010.12.001>>. Cited in page 60.
- NEU, R. W.; PAPE, J. A.; SWALLA, D. R. Methodologies for linking nucleation and propagation approaches for predicting life under fretting fatigue. In: *Fretting fatigue: current technology and practices*. [S.l.]: ASTM International, 2000. Cited in page 5.
- NEUBER, H. Theorie der technischen formzahl. *Forschung auf dem Gebiet des Ingenieurwesens A*, Springer, v. 7, p. 271–274, 1936. Cited in page 34.
- NEWMAN, J. C.; PHILLIPS, E. P.; SWAIN, M. H. Fatigue-life prediction methodology using small-crack theory. *International Journal of Fatigue*, v. 21, n. 2, p. 109–119, 1999. ISSN 01421123. Cited in page 109.
- NISHIOKA, K.; HIRAKAWA, K. Fundamental investigations of fretting fatigue: Part 3, some phenomena and mechanisms of surface cracks. *Bulletin of JSME*, The Japan Society of Mechanical Engineers, v. 12, n. 51, p. 397–407, 1969. Cited 2 times in pages 3 and 4.
- NISHIOKA, K.; HIRAKAWA, K. Fundamental investigations of fretting fatigue: part 4, the effect of mean stress. *Bulletin of JSME*, The Japan Society of Mechanical Engineers, v. 12, n. 51, p. 408–414, 1969. Cited 2 times in pages 3 and 4.

- NISHIOKA, K.; HIRAKAWA, K. Fundamental investigations of fretting fatigue:(part 2, fretting fatigue testing machine and some test results). *Bulletin of JSME*, The Japan Society of Mechanical Engineers, v. 12, n. 50, p. 180–187, 1969. Cited 2 times in pages 3 and 4.
- NISHIOKA, K.; HIRAKAWA, K. Fundamental investigations of fretting fatigue:(part 5, the effect of relative slip amplitude). *Bulletin of JSME*, The Japan Society of Mechanical Engineers, v. 12, n. 52, p. 692–697, 1969. Cited 2 times in pages 3 and 4.
- NISHIOKA, K.; KENJI, H. Fundamental investigations of fretting fatigue: Part 6, effects of contact pressure and hardness of materials. *Bulletin of JSME*, The Japan Society of Mechanical Engineers, v. 15, n. 80, p. 135–144, 1972. Cited 2 times in pages 3 and 4.
- NISHIOKA, K.; NISHIMURA, S.; HIRAKAWA, K. Fundamental investigations of fretting fatigue: Part 1, on the relative slip amplitude of press-fitted axle assemblies. *Bulletin of JSME*, The Japan Society of Mechanical Engineers, v. 11, n. 45, p. 437–445, 1968. Cited 2 times in pages 3 and 4.
- NOWELL, D. *An analysis of fretting fatigue*. Tese (Doutorado) — University of Oxiford, 1988. Cited 12 times in pages xi, 4, 46, 57, 88, 89, 90, 93, 108, 112, 113, and 119.
- NOWELL, D.; DAI, D. Analysis of surface tractions in complex fretting fatigue cycles using quadratic programming. *ASME Journal of Tribology*, v. 120, p. 744–749, 1998. Cited in page 43.
- NOWELL, D.; DINI, D.; HILLS, D. A. Recent developments in the understanding of fretting fatigue. *Engineering Fracture Mechanics*, v. 73, n. 2, p. 207–222, 2006. ISSN 00137944. Cited 3 times in pages 33, 60, and 61.
- NOWELL, D.; HILLS, D. Mechanics of fretting fatigue tests. *International Journal of Mechanical Sciences*, Elsevier, v. 29, n. 5, p. 355–365, 1987. Cited in page 43.
- NOWELL, D.; HILLS, D. Crack initiation criteria in fretting fatigue. *Wear*, Elsevier, v. 136, n. 2, p. 329–343, 1990. Cited in page 7.
- NOWELL, D.; HILLS, D. A.; O'CONNOR, J. J. Analysis of Fretting Fatigue. *I Mech E Conference Publications (Institution of Mechanical Engineers)*, p. 965–973, 1987. ISSN 01440799. Cited in page 220.
- NOWELL, D.; NOWELL, P. W. A machine learning approach to the prediction of fretting fatigue life. *Tribology International*, Elsevier Ltd, v. 141, n. August 2019, p. 105913, 2020. ISSN 0301679X. Disponível em: <<https://doi.org/10.1016/j.triboint.2019.105913>>. Cited 10 times in pages vi, 9, 24, 87, 93, 97, 100, 101, 163, and 213.
- O'HALLORAN, S. M.; CONNAIRE, A. D.; HARTE, A. M.; LEEN, S. B. Modelling of fretting in the pressure armour layer of flexible marine risers. *Tribology International*, Elsevier, v. 100, p. 306–316, 2016. ISSN 0301679X. Disponível em: <<http://dx.doi.org/10.1016/j.triboint.2016.02.040>>. Cited in page 29.
- OLIVEIRA, G. A.; CARDOSO, R. A.; JÚNIOR, R. C. F.; ARAÚJO, J. A. A hybrid ann multiaxial fatigue model for the assessment of fretting fatigue under variable amplitude shear loading. *Procedia Structural Integrity*, Elsevier, v. 57, p. 228–235, 2024b. Cited 3 times in pages 10, 153, and 213.

- OLIVEIRA, G. A. B.; CÂMARA, E. C. B.; Freire Júnior, R. C. S. Obtaining G12 and Xt using mixed ANNs based on matrix and fiber properties. *Composites Part B: Engineering*, v. 175, p. 107171, oct 2019. ISSN 13598368. Disponível em: <<https://linkinghub.elsevier.com/retrieve/pii/S1359836819320542>>. Cited in page 73.
- OLIVEIRA, G. A. B.; CARDOSO, R. A.; JÚNIOR, R. C. S. F.; DOCA, T.; ARAÚJO, J. A. On the generalization capability of artificial neural networks used to estimate fretting fatigue life. *Tribology International*, Elsevier, p. 109222, 2024. Cited 25 times in pages 9, vii, 14, 103, 105, 107, 108, 112, 119, 120, 125, 127, 128, 131, 138, 149, 152, 154, 163, 164, 168, 171, 210, 211, and 213.
- OMRANI, A.; LANGLOIS, S.; DYKE, P. V.; LALONDE, S.; KARGANROUDI, S. S.; DIENG, L. Fretting fatigue life assessment of overhead conductors using a clamp/conductor numerical model and biaxial fretting fatigue tests on individual wires. *Fatigue & Fracture of Engineering Materials & Structures*, Wiley Online Library, v. 44, n. 6, p. 1498–1514, 2021. Cited 2 times in pages 65 and 168.
- ORBANIĆ, P.; FAJDIGA, M. A neural network approach to describing the fretting fatigue in aluminium-steel couplings. *International Journal of Fatigue*, v. 25, n. 3, p. 201–207, 2003. Cited 2 times in pages 6 and 8.
- PALMGREN, A. Die lebensdauer von kugellagernzeitschrift des. *Vereines Deutscher Ingenieure*, v. 68, n. 14, p. 339–341, 1924. Cited in page 23.
- PAPADOPOULOS, I. V.; DAVOLI, P.; GORLA, C.; FILIPPINI, M.; BERNASCONI, A. A comparative study of multiaxial high-cycle fatigue criteria for metals. *International Journal of Fatigue*, v. 19, n. 3, p. 219–235, 1997. ISSN 01421123. Cited in page 31.
- PARIS, P.; ERDOGAN, F. A critical analysis of crack propagation laws. 1963. Cited 2 times in pages 34 and 35.
- PESTANA, M. S.; KALOMBO, R. B.; Freire Júnior, R. C. S.; FERREIRA, J. L. A.; SILVA, C. R. M. da; ARAÚJO, J. A. Use of artificial neural network to assess the effect of mean stress on fatigue of overhead conductors. *Fatigue and Fracture of Engineering Materials and Structures*, Blackwell Publishing Ltd, Mechanical Engineering, University of Brasilia, Federal District, Brasília, Brazil, v. 41, n. 12, p. 2577–2586, 2018. ISSN 8756758X (ISSN). Disponível em: <<https://www.scopus.com/inward/record.uri?eid=2-s2.0-85055987786&doi=10.1111%2Fffe.12858&partnerID=40&md5=278975f18aa65d7ed71266e8f7afb16a>>. Cited 4 times in pages 7, 9, 24, and 65.
- PETERSON, R. E. Notch sensitivity. *Metal fatigue*, McGraw Hill, p. 293–306, 1959. Cited in page 34.
- PINTO, A. L. *Fretting fatigue under variable amplitude loading*. Tese (Doutorado) — KU Leuven and University of Brasilia, 2022. Cited 2 times in pages 194 and 210.
- PINTO, A. L.; ALMEIDA, G. M.; TALEMI, R.; ARAÚJO, J. A. Fretting fatigue under variable amplitude shear loading blocks considering partial slip regime: Experimental/numerical analysis. *Tribology International*, Elsevier Ltd, v. 182, n. February, p. 108367, 2023. ISSN 0301679X. Disponível em: <<https://doi.org/10.1016/j.triboint.2023.108367>>. Cited 6 times in pages 7, 12, 23, 154, 158, and 161.

- PINTO, A. L.; ARAÚJO, J. A.; TALEMI, R. Effects of fretting wear process on fatigue crack propagation and life assessment. *Tribology International*, Elsevier Ltd, v. 156, n. October 2020, p. 106787, 2021. ISSN 0301679X. Disponível em: <<https://doi.org/10.1016/j.triboint.2020.106787>>. Cited in page 5.
- PINTO, A. L.; CARDOSO, R. A.; TALEMI, R.; ARAÚJO, J. A. Fretting fatigue under variable amplitude loading considering partial and gross slip regimes: Numerical analysis. *Tribology International*, Elsevier Ltd, v. 146, n. August 2019, p. 106199, 2020. ISSN 0301679X. Disponível em: <<https://doi.org/10.1016/j.triboint.2020.106199>>. Cited 3 times in pages 23, 29, and 88.
- PINTO, A. L.; CARDOSO, R. A.; TALEMI, R.; ARAÚJO, J. A. Early crack orientation prediction methods under fretting fatigue loading including wear effects. *International Journal of Fatigue*, Elsevier Ltd, v. 161, n. April, p. 106893, 2022. ISSN 01421123. Disponível em: <<https://doi.org/10.1016/j.ijfatigue.2022.106893>>. Cited in page 119.
- PINTO, A. L.; TALEMI, R.; ARAÚJO, J. A. Fretting fatigue total life assessment including wear and a varying critical distance. *International Journal of Fatigue*, Elsevier Ltd, v. 156, n. October 2021, p. 106589, 2022. ISSN 01421123. Disponível em: <<https://doi.org/10.1016/j.ijfatigue.2021.106589>>. Cited 3 times in pages 36, 37, and 108.
- PLEUNE, T. T.; CHOPRA, O. K. Using artificial neural networks to predict the fatigue life of carbon and low-alloy steels. *Nuclear Engineering and Design*, v. 197, n. 1, p. 1–12, 2000. ISSN 00295493. Cited in page 8.
- POFFENBERGER, J.; SWART, R. Differential displacement and dynamic conductor strain. *IEEE Transactions on Power Apparatus and Systems*, IEEE, v. 84, n. 4, p. 281–289, 1965. Cited in page 10.
- POOVAKAUD, V. V.; JIMÉNEZ-PEÑA, C.; TALEMI, R.; COPPIETERS, S.; DEBRUYNE, D. Assessment of fretting fatigue in high strength steel bolted connections with simplified Fe modelling techniques. *Tribology International*, v. 143, n. July 2019, 2020. ISSN 0301679X. Cited in page 31.
- QUINLAN, J. R. *C4. 5: programs for machine learning*. [S.l.]: Elsevier, 2014. Cited in page 69.
- RAJASEKARAN, R.; NOWELL, D. Fretting fatigue in dovetail blade roots: Experiment and analysis. *Tribology international*, Elsevier, v. 39, n. 10, p. 1277–1285, 2006. Cited in page 62.
- RANGEL, D.; ERENA, D.; VÁZQUEZ, J.; ARAÚJO, J. A. Prediction of initiation and total life in fretting fatigue considering kinked cracks. *Theoretical and Applied Fracture Mechanics*, v. 119, n. April, 2022. ISSN 01678442. Cited 3 times in pages 4, 29, and 37.
- RAO, J.; KISHORE, C.; MAHADEVAPPA, V. Weight optimization of turbine blades. In: *Proceedings 12th International Symposium on Transport Phenomena and Dynamics of Rotating Machinery*. [S.l.: s.n.], 2008. Cited in page 55.
- RASMUS, A. *Semi-Supervised Learning*. MIT Press, 2015. Disponível em: <<https://mitpress.mit.edu/9780262514125/semi-supervised-learning/>>. Cited in page 70.

- ROCHA, P. H.; DÍAZ, J. I.; SILVA, C. R.; ARAÚJO, J. A.; CASTRO, F. C. Fatigue of two contacting wires of the ACSR Ibis 397.5 MCM conductor: Experiments and life prediction. *International Journal of Fatigue*, Elsevier, v. 127, n. April, p. 25–35, 2019. ISSN 01421123. Disponível em: <<https://doi.org/10.1016/j.ijfatigue.2019.05.033>>. Cited 2 times in pages 163 and 168.
- ROCHA, P. H.; LANGLOIS, S.; LALONDE, S.; ARAÚJO, J. A.; CASTRO, F. C. A general life estimation method for overhead conductors based on fretting fatigue behavior of wires. *Theoretical and Applied Fracture Mechanics*, Elsevier Ltd, v. 121, n. March, p. 103443, 2022. ISSN 01678442. Disponível em: <<https://doi.org/10.1016/j.tafmec.2022.103443>>. Cited 9 times in pages 6, 55, 170, 172, 175, 181, 183, 186, and 188.
- ROCHA, P. H. C.; LANGLOIS, S.; LALONDE, S.; ARAÚJO, J. A.; CASTRO, F. C. Influence of 1350 and 6201 aluminum alloys on the fatigue life of overhead conductors – A finite element analysis. *Tribology International*, Elsevier Ltd, v. 186, n. June, p. 108661, 2023. ISSN 0301-679X. Disponível em: <<https://doi.org/10.1016/j.triboint.2023.108661>>. Cited 7 times in pages 163, 172, 175, 183, 184, 186, and 188.
- ROSSINO, L. S.; CASTRO, F. C.; Bose Filho, W. W.; ARAÚJO, J. A. Issues on the mean stress effect in fretting fatigue of a 7050-T7451 Al alloy posed by new experimental data. *International Journal of Fatigue*, Elsevier Ltd, v. 31, n. 11-12, p. 2041–2048, 2009. ISSN 01421123. Disponível em: <<http://dx.doi.org/10.1016/j.ijfatigue.2008.12.011>>. Cited 16 times in pages vi, xi, 22, 30, 88, 89, 92, 95, 100, 101, 108, 112, 115, 119, 210, and 217.
- ROUSSEAU, G.; MONTEBELLO, C.; GUILHEM, Y.; POMMIER, S. A novel approach to model fretting-fatigue in multiaxial and non-proportional loading conditions. *International Journal of Fatigue*, Elsevier, v. 126, n. April, p. 79–89, 2019. ISSN 01421123. Disponível em: <<https://doi.org/10.1016/j.ijfatigue.2019.04.022>>. Cited in page 154.
- RUIZ, C.; BODDINGTON, P.; CHEN, K. An investigation of fatigue and fretting in a dovetail joint. *Experimental mechanics*, Springer, v. 24, p. 208–217, 1984. Cited 3 times in pages 5, 24, and 62.
- SACKFIELD, A.; HILLS, D. A note on the hertz contact problem: A correlation of standard formulae. *The Journal of Strain Analysis for Engineering Design*, v. 18, n. 3, p. 195–197, 1983. ISSN 20413130. Cited 3 times in pages 47, 48, and 124.
- SAID, J.; FOUVRY, S.; CAILLETAUD, G.; BASSEVILLE, S.; COULANGEON, M.; BROCARD, J.; YANG, C.; HAFID, F. A global–local approach to predict the fretting-fatigue failure of clamped aluminum powerline conductors: From mono-contact crossed wires to full conductor vibrational tests. *Engineering Failure Analysis*, v. 146, n. November 2022, 2023. ISSN 13506307. Cited 3 times in pages 6, 29, and 55.
- SAID, J.; GARCIN, S.; FOUVRY, S.; CAILLETAUD, G.; YANG, C.; HAFID, F. A multi-scale strategy to predict fretting-fatigue endurance of overhead conductors. *Tribology International*, Elsevier Ltd, v. 143, n. July 2019, p. 106053, mar 2020. ISSN 0301679X. Disponível em: <<https://doi.org/10.1016/j.triboint.2019.106053><https://linkinghub.elsevier.com/retrieve/pii/S0301679X19305687>>. Cited in page 172.
- SATO, K. Determination and control of contact pressure distribution in fretting fatigue. *ASTM SPECIAL TECHNICAL PUBLICATION*, AMERICAN TECHNICAL PUBLISHERS LTD, v. 1159, p. 85–85, 1992. Cited in page 5.

- SCHILLAI, K. *Enhanced fretting fatigue resistance of conductors for high voltage overhead lines*. Tese (Doutorado) — ETH Zurich, 2019. Cited in page 172.
- SCHÜTZ, W. A history of fatigue. *Engineering Fracture Mechanics*, v. 54, n. 2, p. 263–300, 1996. ISSN 00137944. Cited in page 19.
- SEEGER, M. Gaussian Processes for Machine Learning. *International Journal of Neural Systems*, v. 14, n. 02, p. 69–106, apr 2004. ISSN 0129-0657. Disponível em: <<https://www.worldscientific.com/doi/abs/10.1142/S0129065704001899>>. Cited 2 times in pages 173 and 174.
- SENAVIRATHNA, S. K.; UDAWATTE, H.; HARISCHANDRA, N.; FERNANDO, M.; EKANAYAKE, C. Image-based condition monitoring of transmission line conductors using image processing and deep neural networks. In: IEEE. *2023 IEEE 17th International Conference on Industrial and Information Systems (ICIIS)*. [S.l.], 2023. p. 388–393. Cited in page 10.
- SINES, G. *Failure of materials under combined repeated stresses with superimposed static stresses*. [S.l.], 1955. Cited in page 24.
- SMITH, J. A fatigue testing machine. *Engineering*, v. 88, p. 105–107, 1908. Cited 3 times in pages 19, 105, and 135.
- SMITH, J. Some experiments on fatigue of metals. *J. Iron Steel Inst*, v. 82, n. 2, p. 246–318, 1910. Cited in page 19.
- SMITH, R.; WATSON, P.; TOPPER, T. A stress–strain function for the fatigue of metals (stress-strain function for metal fatigue including mean stress effect). *J Materials*, v. 5, n. January 1970, p. 767–778, 1970. ISSN 0039-6265. Cited 3 times in pages 24, 28, and 29.
- SOCHER, R.; MANNING, C. D.; NG, A. Y. Learning continuous phrase representations and syntactic parsing with recursive neural networks. In: VANCOUVER. *Proceedings of the NIPS-2010 deep learning and unsupervised feature learning workshop*. [S.l.], 2010. v. 2010, p. 1–9. Cited in page 74.
- SONG, H.; LIU, J.; ZHANG, H.; DU, J. Multi-source data driven fatigue failure analysis and life prediction of pre-corroded aluminum – lithium alloy 2050-T8. *Engineering Fracture Mechanics*, Elsevier Ltd, v. 292, n. January, p. 109626, 2023. ISSN 0013-7944. Disponível em: <<https://doi.org/10.1016/j.engfracmech.2023.109626>>. Cited in page 173.
- SPANGENBERG, L. *Über das verhalten der metalle bei wiederholten anstrengungen, etc*. [S.l.]: Ernst & Korn, 1875. Cited in page 19.
- SPANGENBERG, L. Ober festigkeits-versuche mit eisen und stahl. *Glaser's Ann. Gew*, v. 5, p. 6–15, 1879. Cited in page 19.
- STEIER, V. F.; BADIBANGA, R. K.; SILVA, C. R. M. da; NOGUEIRA, M. M.; ARAÚJO, J. A. Effect of chromium nitride coatings and cryogenic treatments on wear and fretting fatigue resistance of aluminum. *Electric power systems research*, Elsevier, v. 116, p. 322–329, 2014. Cited in page 6.
- STOVER, R. J.; MABIE, H.; FUREY, M. A finite element investigation of a bearing/cartridge interface for a fretting corrosion study. *Journal of Tribology*, p. 157, 1985. Cited in page 5.

- STROHMANN, T.; STAROSTIN-PENNER, D.; BREITBARTH, E.; REQUENA, G. Automatic detection of fatigue crack paths using digital image correlation and convolutional neural networks. *Fatigue and Fracture of Engineering Materials and Structures*, Blackwell Publishing Ltd, German Aerospace Center (DLR), Institute of Materials Research, Cologne, Germany, v. 44, n. 5, p. 1336–1348, 2021. ISSN 8756758X (ISSN). Disponível em: <<https://www.scopus.com/inward/record.uri?eid=2-s2.0-85100904100&doi=10.1111%2Fffe.13433&partnerID=40&md5=b41fae999a82e7c3bfd679ba6e339722>>. Cited 2 times in pages 8 and 9.
- SUNDE, S. L.; HAUGEN, B.; BERTO, F. Experimental and numerical fretting fatigue using a new test fixture. *International Journal of Fatigue*, v. 143, n. July 2020, 2021. ISSN 01421123. Cited in page 62.
- SUSMEL, L. A unifying approach to estimate the high-cycle fatigue strength of notched components subjected to both uniaxial and multiaxial cyclic loadings. *Fatigue and Fracture of Engineering Materials and Structures*, v. 27, n. 5, p. 391–411, 2004. ISSN 8756758X. Cited in page 37.
- SUSMEL, L. Multiaxial fatigue limits and material sensitivity to non-zero mean stresses normal to the critical planes. *Fatigue & Fracture of Engineering Materials & Structures*, Wiley Online Library, v. 31, n. 3-4, p. 295–309, 2008. Cited 2 times in pages 211 and 218.
- SUSMEL, L. *Multiaxial notch fatigue*. [S.l.]: Elsevier, 2009. Cited in page 211.
- SUSMEL, L. A simple and efficient numerical algorithm to determine the orientation of the critical plane in multiaxial fatigue problems. *International Journal of Fatigue*, Elsevier Ltd, v. 32, n. 11, p. 1875–1883, 2010. ISSN 01421123. Disponível em: <<http://dx.doi.org/10.1016/j.ijfatigue.2010.05.004>>. Cited in page 27.
- SUSMEL, L. Notches, nominal stresses, fatigue strength reduction factors and constant/variable amplitude multiaxial fatigue loading. *International Journal of Fatigue*, Elsevier Ltd, v. 162, n. January, p. 106941, 2022. ISSN 01421123. Disponível em: <<https://doi.org/10.1016/j.ijfatigue.2022.106941>>. Cited in page 210.
- SUSMEL, L.; LAZZARIN, P. A bi-parametric Wöhler curve for high cycle multiaxial fatigue assessment. *Fatigue and Fracture of Engineering Materials and Structures*, v. 25, n. 1, p. 63–78, 2002. ISSN 8756758X. Cited 8 times in pages 24, 28, 30, 86, 87, 88, 101, and 105.
- SUSMEL, L.; TAYLOR, D. A novel formulation of the theory of critical distances to estimate lifetime of notched components in the medium-cycle fatigue regime. *Fatigue & Fracture of Engineering Materials & Structures*, Wiley Online Library, v. 30, n. 7, p. 567–581, 2007. Cited in page 37.
- SUSMEL, L.; TAYLOR, D. The modified wöhler curve method applied along with the theory of critical distances to estimate finite life of notched components subjected to complex multiaxial loading paths. *Fatigue & Fracture of Engineering Materials & Structures*, Wiley Online Library, v. 31, n. 12, p. 1047–1064, 2008. Cited 2 times in pages 37 and 211.
- SUTTON, R. S.; BARTO, A. G. *Reinforcement learning: An introduction*. [S.l.]: MIT press, 2018. Cited 2 times in pages 68 and 71.
- SZOLWINSKI, M. P.; FARRIS, T. N. Mechanics of fretting fatigue crack formation. *Wear*, Elsevier, v. 198, n. 1-2, p. 93–107, 1996. Cited in page 7.

- SZOLWINSKI, M. P.; FARRIS, T. N. *Observation, analysis and prediction of fretting fatigue in 2024-T351 aluminum alloy*. [S.l.], 1998. v. 221, 24–36 p. Cited 12 times in pages xi, 5, 10, 33, 88, 89, 91, 94, 108, 112, 114, and 119.
- TANAKA, K. Engineering formulae for fatigue strength reduction due to crack-like notches. *International Journal of Fracture*, Springer, v. 22, p. R39–R46, 1983. Cited in page 34.
- TAYLOR, D. Geometrical effects in fatigue: a unifying theoretical model. *International Journal of Fatigue*, v. 21, n. 5, p. 413–420, 1999. ISSN 01421123. Cited 9 times in pages 34, 35, 36, 86, 88, 101, 106, 163, and 164.
- THUM, A. Querbrüche an kardanwellen. *Deutsche Kraftfahrtforschung*, VDI-Verlag Berlin, n. Heft 6, 1938. Cited in page 19.
- THUM, A. Der werkstoff in der konstruktiven berechnung. *Vortrag Eisenhüttentag 1938, Stahl und Eisen*, v. 59, p. 252–263, 1939. Cited in page 19.
- THUM, A.; BAUTZ, W. Zeitfestigkeit. *VDI-Zeitschrift*, v. 81, p. 1407–1412, 1937. Cited in page 19.
- THUM, A.; RÜTTGER, R. Das verhalten von rohrverbindungen bei verschiedener oberflächenbeschaffenheit und formgebung. *Mitt. Ver. Großkesselbes.*, n. Nr. 53, p. 127–133, 1935. Cited in page 19.
- THUM, A.; WEIß, H. Dauerverdrehversuche an kurbelwellenstählen. *Zentr. f. wiss. Berichtswes. über Luftfahrtforschung F.B.*, n. Nr. 966, 1938. Cited in page 19.
- TOMLINSON, G. The rusting of steel surfaces in contact. *Proceedings of the Royal Society of London. Series A, Containing Papers of a Mathematical and Physical Character*, The Royal Society London, v. 115, n. 771, p. 472–483, 1927. Cited in page 3.
- TUR, M.; FUENMAYOR, J.; RÓDENAS, J. J.; GINER, E. 3D analysis of the influence of specimen dimensions on fretting stresses. *Finite Elements in Analysis and Design*, v. 39, n. 10, p. 933–949, 2003. ISSN 0168874X. Cited in page 122.
- VALLELLANO, C.; DOMÍNGUEZ, J.; NAVARRO, A. Predicting the fretting fatigue limit for spherical contact. *Engineering Failure Analysis*, v. 11, n. 5, p. 727–736, 2004. ISSN 13506307. Cited 2 times in pages 33 and 119.
- VANTADORI, S.; ZANICHELLI, A.; ARAÚJO, J. A. Fretting fatigue of 7050-T7451 Al alloy: the influence of bulk mean stress. *International Journal of Fatigue*, Elsevier, v. 140, n. July, p. 105816, 2020. ISSN 01421123. Disponível em: <<https://doi.org/10.1016/j.ijfatigue.2020.105816>>. Cited 3 times in pages 7, 22, and 217.
- VÁZQUEZ, J.; NAVARRO, C.; DOMÍNGUEZ, J. Experimental results in fretting fatigue with shot and laser peened al 7075-t651 specimens. *International journal of fatigue*, Elsevier, v. 40, p. 143–153, 2012. Cited in page 7.
- VÁZQUEZ, J.; NAVARRO, C.; DOMÍNGUEZ, J. Analytical solution for a cylindrical contact with reverse slip. *Journal of Strain Analysis for Engineering Design*, v. 48, n. 3, p. 189–197, 2013. ISSN 03093247. Cited 2 times in pages 43 and 122.

- VENKATESH, T. A.; CONNER, B. P.; SURESH, S.; GIANNAKOPOULOS, A. E.; LINDLEY, T. C.; LEE, C. S. An experimental investigation of fretting fatigue in Ti-6Al-4V: The role of contact conditions and microstructure. *Metallurgical and Materials Transactions A: Physical Metallurgy and Materials Science*, v. 32, n. 5, p. 1131–1146, 2001. ISSN 10735623. Cited 7 times in pages [xii](#), [108](#), [109](#), [112](#), [118](#), [119](#), and [120](#).
- VIEIRA, E. R. *Análise comparativa do efeito da fadiga por fretting nos fios de cabos condutores formados pelas ligas de alumínio 1120 e AA 6201*. Tese (Doutorado) — Universidade de Brasília, 2020. Cited 6 times in pages [xii](#), [163](#), [164](#), [166](#), [167](#), and [176](#).
- VINGSBO, O.; SÖDERBERG, S. On fretting maps. *Wear*, v. 126, n. 2, p. 131–147, 1988. ISSN 00431648. Cited in page [23](#).
- WAHAB, M. A. A data-assisted physics informed neural network (da-pinn) for fretting fatigue lifetime prediction. *Available at SSRN 4518531*, 2023. Cited in page [10](#).
- WANG, C.; LI, C.; LING, Y.; Abdel Wahab, M. Investigation on fretting fatigue crack initiation in heterogenous materials using a hybrid of multiscale homogenization and direct numerical simulation. *Tribology International*, Elsevier Ltd, v. 169, n. February, p. 107470, 2022. ISSN 0301679X. Disponível em: <https://doi.org/10.1016/j.triboint.2022.107470>. Cited 2 times in pages [5](#) and [210](#).
- WANG, C.; LI, Y.; TRAN, N. H.; WANG, D.; KHATIR, S.; WAHAB, M. A. Artificial neural network combined with damage parameters to predict fretting fatigue crack initiation lifetime. *Tribology International*, Elsevier Ltd, v. 175, n. August, p. 107854, 2022. ISSN 0301679X. Disponível em: <https://doi.org/10.1016/j.triboint.2022.107854>. Cited 2 times in pages [10](#) and [163](#).
- WANG, C.; WANG, D.; Abdel Wahab, M. Fretting Fatigue Lifetime Estimation for Heterogeneous material using Critical Distance with Mesh Control. *Engineering Fracture Mechanics*, Elsevier Ltd, v. 281, n. January, p. 109092, 2023. ISSN 00137944. Disponível em: <https://doi.org/10.1016/j.engfracmech.2023.109092>. Cited in page [23](#).
- WANG, H.; LI, B.; GONG, J.; XUAN, F.-Z. Machine learning-based fatigue life prediction of metal materials: Perspectives of physics-informed and data-driven hybrid methods. *Engineering Fracture Mechanics*, Elsevier, p. 109242, 2023. Cited 4 times in pages [v](#), [24](#), [67](#), and [72](#).
- WANG, Y.; GANG, L.; LIU, S.; CUI, Y. Coupling Fractal Model for Fretting Wear on Rough Contact Surfaces. *Journal of Tribology*, v. 143, n. 9, p. 1–13, 2021. ISSN 15288897. Cited in page [8](#).
- WARLOW-DAVIES, E. Fretting corrosion and fatigue strength: brief results of preliminary experiments. *Proceedings of the Institution of Mechanical Engineers*, SAGE Publications Sage UK: London, England, v. 146, n. 1, p. 32–38, 1941. Cited in page [3](#).
- WATERHOUSE, R. *Fretting Fatigue*. Edited by RB Waterhouse. [S.l.]: Applied Science Publishers, UK, 1981. 244 p. Cited in page [4](#).
- WATERHOUSE, R. Fretting wear. *ASM handbook*, ASM International, v. 18, p. 242–256, 1992. Cited 2 times in pages [7](#) and [23](#).

WATERHOUSE, R.; ALLERY, M. The effect of non-metallic coatings on the fretting corrosion of mild steel. *Wear*, Elsevier, v. 8, n. 2, p. 112–120, 1965. Cited 2 times in pages 3 and 4.

WITTKOWSKY, B. U.; BIRCH, P. R.; DOMÍNGUEZ, J.; SURESH, S. Experimental investigation of fretting fatigue with spherical contact in 7075-T6 aluminum alloy. *ASTM Special Technical Publication*, n. 1367, p. 213–227, 2000. ISSN 10403094. Cited 7 times in pages xii, 29, 61, 108, 112, 115, and 119.

WRIGHT, K. Discussion and communication on an investigation of fretting corrosion. *Proceedings of the Institution of Mechanical Engineers*, SAGE Publications Sage UK: London, England, v. 1b, p. 571–574, 1953. Cited in page 3.

WRIGHT, K. An investigation of fretting corrosion. *Proceedings of the Institution of Mechanical Engineers*, SAGE Publications Sage UK: London, England, v. 1b, p. 556–571, 1953. Cited in page 3.

YANG, J.; KANG, G.; KAN, Q. A novel deep learning approach of multiaxial fatigue life-prediction with a self-attention mechanism characterizing the effects of loading history and varying temperature. *International Journal of Fatigue*, Elsevier Ltd, v. 162, n. March, p. 106851, 2022. ISSN 01421123. Disponible em: <<https://doi.org/10.1016/j.ijfatigue.2022.106851>>. Cited in page 173.

ZABALA, A.; INFANTE-GARCÍA, D.; GINER, E.; GOEL, S.; ENDRINO, J. L.; LLAVORI, I. On the use of the theory of critical distances with mesh control for fretting fatigue lifetime assessment. *Tribology International*, Elsevier Ltd, v. 142, n. October 2019, p. 105985, 2020. ISSN 0301679X. Disponible em: <<https://doi.org/10.1016/j.triboint.2019.105985>>. Cited in page 36.

ZHAN, Z.; LI, H. A novel approach based on the elastoplastic fatigue damage and machine learning models for life prediction of aerospace alloy parts fabricated by additive manufacturing. *International Journal of Fatigue*, Elsevier Ltd, School of Aeronautic Science and Engineering, Beihang University, Beijing, 100191, China, v. 145, 2021. ISSN 01421123 (ISSN). Disponible em: <<https://www.scopus.com/inward/record.uri?eid=2-s2.0-85098466998&doi=10.1016%2Fj.ijfatigue.2020.106089&partnerID=40&md5=e6f9b1391136108e405ada0f51d8b3d3>>. Cited in page 173.

ZHAN, Z.; LI, H.; LAM, K. Y. Development of a novel fatigue damage model with am effects for life prediction of commonly-used alloys in aerospace. *International Journal of Mechanical Sciences*, Elsevier, v. 155, p. 110–124, 2019. Cited in page 24.

ZHOU, T.; JIANG, S.; HAN, T.; ZHU, S.-P.; CAI, Y. A physically consistent framework for fatigue life prediction using probabilistic physics-informed neural network. *International Journal of Fatigue*, Elsevier, v. 166, p. 107234, 2023. Cited 2 times in pages 73 and 105.

ZOU, L.; LU, L.; LI, Y.; YANG, K.; ZHAO, H.; DONG, Y.; ZENG, D. Experimental and numerical study on press-fitted railway axles: Fretting fatigue behaviour in the very high cycle regime. *International Journal of Fatigue*, Elsevier, v. 166, p. 107243, 2023. Cited in page 210.